INFORMATION TO USERS

This manuscript has been reproduced from the microfilm master. UMI films the text directly from the original or copy submitted. Thus, some thesis and dissertation copies are in typewriter face, while others may be from any type of computer printer.

The quality of this reproduction is dependent upon the quality of the copy submitted. Broken or indistinct print, colored or poor quality illustrations and photographs, print bleedthrough, substandard margins, and improper alignment can adversely affect reproduction.

In the unlikely event that the author did not send UMI a complete manuscript and there are missing pages, these will be noted. Also, if unauthorized copyright material had to be removed, a note will indicate the deletion.

Oversize materials (e.g., maps, drawings, charts) are reproduced by sectioning the original, beginning at the upper left-hand corner and continuing from left to right in equal sections with small overlaps. Each original is also photographed in one exposure and is included in reduced form at the back of the book.

Photographs included in the original manuscript have been reproduced xerographically in this copy. Higher quality 6" x 9" black and white photographic prints are available for any photographs or illustrations appearing in this copy for an additional charge. Contact UMI directly to order.

U·M·I

University Microfilms International
A Bell & Howell Information Company
300 North Zeeb Road, Ann Arbor, MI 48106-1346 USA
313/761-4700 800/521-0600

Reproduced with permission of the copyright owner. Further reproduction prohibited without permission.

Reproduced with permission of the copyright owner. Further reproduction prohibited without permission.

Order Number 9320756

Structure of reconnection layers in the magnetosphere

Lin, Yu, Ph.D.

University of Alaska Fairbanks, 1993

U·M·I
300 N. Zeeb Rd.
Ann Arbor, MI 48106

Reproduced with permission of the copyright owner. Further reproduction prohibited without permission.

Reproduced with permission of the copyright owner. Further reproduction prohibited without permission.

STRUCTURE OF RECONNECTION LAYERS IN THE MAGNETOSPHERE

A

THESIS

Presented to the Faculty of the University of Alaska Fairbanks

in Partial Fulfillment of the Requirements

for the Degree of

DOCTOR OF PHILOSOPHY

By

Yu Lin, B. S., M. S.

Fairbanks, Alaska

May, 1993

Reproduced with permission of the copyright owner. Further reproduction prohibited without permission.

STRUCTURE OF RECONNECTION LAYERS IN THE MAGNETOSPHERE

by

Yu Lin

RECOMMENDED:

J. G. Hawkins

D. D. Sentman

R. W. Smith

D. W. Swift

L. C. Lee, Chairman, Advisory Committee

J. L. Morack, Head, Physics Department

APPROVED:

P. Reichardt, Dean, College of Natural Sciences

E. C. Murphy, Chancellor's Faculty Associate for Graduate Studies

21 April 1993

Date

Reproduced with permission of the copyright owner. Further reproduction prohibited without permission.

Abstract

Magnetic reconnection can lead to the formation of observed boundary layers at the dayside magnetopause and in the nightside plasma sheet of the magnetosphere. In this thesis, the structure of these reconnection layers is studied by solving the one-dimensional Riemann problem for the evolution of a current sheet. Analytical method, resistive MHD simulations, and hybrid simulations are used.

Based on the ideal MHD formulation, rotational discontinuities, slow shocks, slow expansion waves, and contact discontinuity are present in the dayside reconnection layer. Fast expansion waves are also present in the solution of the Riemann problem, but they quickly propagate out of the reconnection layer. Our study provides a coherent picture for the transition from the reconnection layer with two slow shocks in Petschek's model to the reconnection layer with a rotational discontinuity and a slow expansion wave in Levy et al's model.

In the resistive MHD simulations, the rotational discontinuities are replaced by intermediate shocks or time-dependent intermediate shocks. In the hybrid simulations, the time-dependent intermediate shock quickly evolves to a steady rotational discontinuity, and the contact discontinuity does not exist.

The magnetotail reconnection layer consists of two slow shocks. Hybrid simulations of slow shocks indicate that there exists a critical number, M_c, such that for slow shocks with an intermediate Mach number $M_I \geq M_c$, a large-amplitude rotational wavetrain is present in the downstream region. For slow shocks with $M_I < M_c$, the downstream wavetrain does not exist. Chaotic ion orbits in the downstream wave provide an efficient mechanism for ion heating and wave damping and explain the existence of the critical number M_c in slow shocks.

Reproduced with permission of the copyright owner. Further reproduction prohibited without permission.

Table of Contents

Reproduced with permission of the copyright owner. Further reproduction prohibited without permission.

Reproduced with permission of the copyright owner. Further reproduction prohibited without permission.

List of Figures

Reproduced with permission of the copyright owner. Further reproduction prohibited without permission.

Reproduced with permission of the copyright owner. Further reproduction prohibited without permission.

Reproduced with permission of the copyright owner. Further reproduction prohibited without permission.

Reproduced with permission of the copyright owner. Further reproduction prohibited without permission.

Reproduced with permission of the copyright owner. Further reproduction prohibited without permission.

Reproduced with permission of the copyright owner. Further reproduction prohibited without permission.

Reproduced with permission of the copyright owner. Further reproduction prohibited without permission.

List of Tables

Reproduced with permission of the copyright owner. Further reproduction prohibited without permission.

Acknowledgments

I would like to thank Professor L. C. Lee, my thesis advisor and the chairman of my graduate advisory committee. His continuous advice and encouragement made the completion of this thesis possible. In guidance for my research work, he himself set an excellent example for me. I learnt to be open-minded, deep-thinking, and hard-working. I would always feel fortunate to have spent five years working with him.

My sincere appreciation also goes to the other members of my graduate advisory committee, Professors J. G. Hawkins, D. D. Sentman, R. W. Smith, and D. W. Swift. Their concerns and helpful suggestions improved my research work and the quality of my thesis. The hybrid code which I used in part of my thesis was developed by Prof. Swift.

I am indebt to Professors K. K. Tschu and T. Y. Tu, who opened the door of Space Physics for me when I was younger. Had it not for them I could never start to work in Space Physics.

My gratitude also extends to my fellow graduate students. It was through discussions with them that I could broad my view and think deeply. In particular, Ms. A. L. LaBelle-Hamer and Dr. D. Q. Ding have been working in the same office with me for years. Our friendship made these years of my graduate study unforgettable.

This thesis work was supported by grants from the National Aeronautics and Space Administration, the National Science Foundation, and the Department of Energy to the Unicersity of Alaska Fairbanks. The computer work was supported by the computer Service Center of the Geophysical Institute and the Pittsburge Supercomputer Center.

Finally, I would like to thank my parents Mr. Jin-Lian Lin and Ms. Hui-Ji Xu, my husband Dr. Sen-Wei Huang, and my sisters Ms. Yun Lin and Ms. Shan Lin. Their love, support and expectation encouraged me to finish this thesis with my greatest effort.

Reproduced with permission of the copyright owner. Further reproduction prohibited without permission.

Chapter 1 Introduction

The concept of magnetic reconnection was first introduced into magnetospheric physics by Dungey [1961]. Reconnection of magnetic field lines takes place between two plasma regions with antiparallel magnetic field components. Through magnetic reconnection, magnetic energy can be efficiently converted into kinetic energy, leading to the ejection of high-speed plasma. Layered structure which contains several magnetohydrodynamic (MHD) discontinuities and expansion waves is formed in the high-speed outflow region [e.g., Petschek, 1964; Levy et al., 1964; Shi and Lee, 1990; Lin et al., 1992]. This layered plasma structure is called the reconnection layer. In the earth's magnetosphere, magnetic reconnection usually takes place at the dayside magnetopause, which is the interface between the solar wind and the magnetosphere, and in the nightside plasma sheet. As a result, layered structures are formed at the dayside magnetopause and in the magnetotail [e.g., Paschmann et al., 1979; Sonnerup et al., 1981; Gosling et al., 1990b, c; Feldman et al., 1984].

Theoretical models of magnetic reconnection have been proposed by many authors [Petschek, 1964; Levy et al., 1964; Sonnerup, 1970; Yeh and Axford, 1970; Priest and Forbes, 1986; Priest and Lee, 1991]. In these ideal models, the reconnection layer has a simple structure with only one or two discontinuities. However, the observed layered structures in the dayside magnetopause boundary layer are complicated [e.g., Paschmann et al., 1979; Gosling et al., 1990b] and cannot be explained by the above ideal models.

The purpose of this thesis is to study systematically the structure of the reconnection layer at the dayside magnetopause and in the magnetotail. The results obtained will be compared with satellite observations. In this thesis, an analytical method, fluid simulations, and particle simulations are used to study the evolution of the current sheet after the onset of magnetic reconnection. It is found that five discontinuities and expansion waves may be developed in a

Reproduced with permission of the copyright owner. Further reproduction prohibited without permission.

reconnection layer. These discontinuities and expansion waves include rotational discontinuities, intermediate shocks, slow shocks, slow expansion waves, and contact discontinuity. A detailed description of MHD discontinuities and waves will be given in Chapter 2.

In this chapter, we introduce the concept of magnetic reconnection and the reconnection layer. The outline of the thesis is presented at the end of the chapter.

1.1 Reconnection Layer in the Magnetosphere

1.1.1 Basic Concept of Magnetic Reconnection

Magnetic reconnection usually takes place at the current sheet that separates two plasma regions which have antiparallel magnetic field components. Figure 1.1 illustrates the basic concept of magnetic reconnection. As shown in the figure, plasmas and magnetic field lines in Region 1 and Region 2 are initially separated by a thin current sheet denoted by the vertical dashed line. Magnetic reconnection can be triggered by impinging plasma flows toward the initial current sheet from the two sides. At $t = t_1 > 0$, the magnetic field lines are bent toward the plasma sheet due to the plasma inflow. At $t = t_2 > t_1$, the two bent field lines contact each other at point X. As a result of magnetic diffusion, the original field lines are cut and reconnected at $t = t_3$ to form two new field lines. The newly reconnected field lines are highly bent and the magnetic tension force accelerates plasma away from point X to high speed. Consequently, the magnetic energy is converted into plasma kinetic energy and the topology of field lines is also changed. In addition, plasmas in Region 1 and Region 2 can be transported directly through the reconnected field lines to the outflow region.

1.1.2 Simple Models of Magnetic Reconnection

The formation of layered structure in the plasma outflow region of magnetic reconnection is illustrated in Figure 1.2a. The initial current sheet, which separates antiparallel magnetic fields, is

Reproduced with permission of the copyright owner. Further reproduction prohibited without permission.

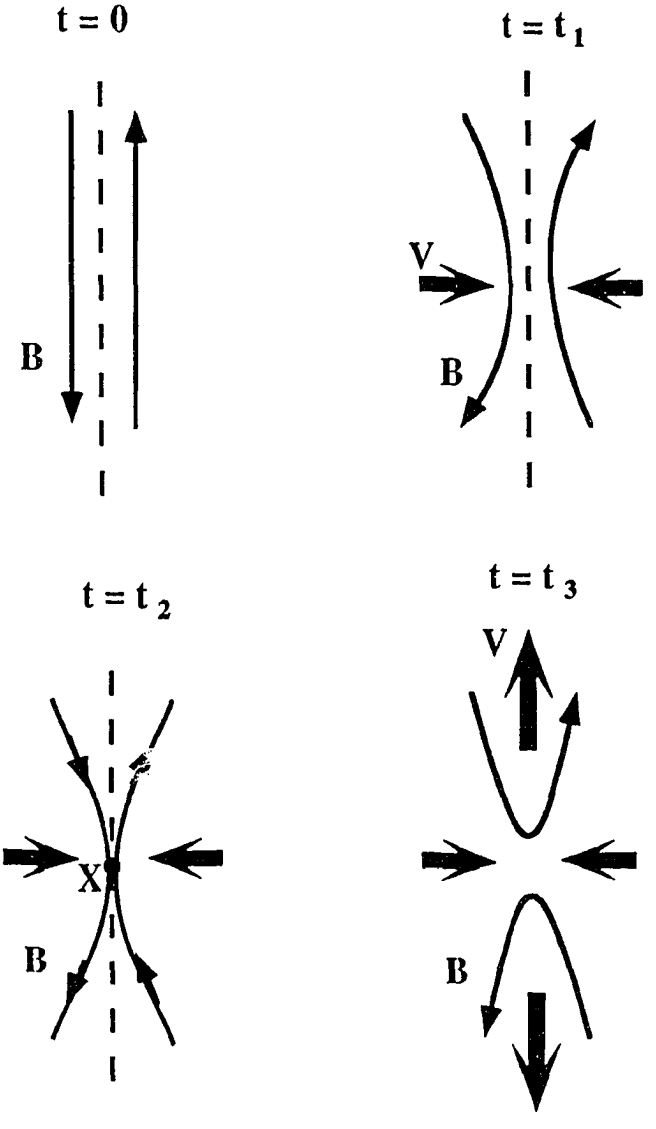

Figure 1.1 A schematic sketch of the magnetic reconnection process. The dashed lines indicates the position of initial current sheet, which separates two plasma regions with antiparallel magnetic fields ($t = 0$). At $t = t_1$, the two field lines approach each other. At $t = t_2$, reconnection takes place at point X of the current sheet. At $t = t_3$, high-speed plasma flows are present in the outflow region.

Reproduced with permission of the copyright owner. Further reproduction prohibited without permission.

located along the z axis. After the onset of magnetic reconnection, a reconnected magnetic field line is formed at $t = 0$. This field line is highly bent at point X, the place where the reconnection takes place. This field line will be convected in the $+z$ direction by the high-speed flow. The field line positions at t_1 and t_2 are shown in Figure 1.2a. As the field line is convected in the z direction, the disturbance associated with highly bent field at the point X will propagate as waves toward the two sides of the initial current sheet. In the xz plane, two wave fronts are formed along XC and XD, respectively, as indicated in Figure 1.2a. Therefore, the formation of reconnection layer can be considered as a result of the evolution of initial current sheet. Note that in Figure 1.2a, we consider for simplicity the propagation of only one wave mode toward each side of the current sheet. In general cases, there are three wave modes propagating to each side.

The existence of layered structure in the plasma outflow region of magnetic reconnection was first pointed out by Petschek [1964]. The conversion of energy is mainly through the MHD discontinuities in the reconnection layer. In the following we briefly describe two basic models of magnetic reconnection, which are proposed by Petschek [1964] and Levy et al. [1964]. Petschek's [1964] reconnection model is a symmetric model, and the model of Levy et al. [1964] deals with asymmetric magnetic fields and plasma densities on the two sides of the current layer.

(A) Petschek's [1964] Symmetric Model

Petschek's [1964] reconnection model describes the symmetric case with equal plasma density, equal magnetic field strength, and antiparallel magnetic fields on the two sides of the current layer. In this model, the reconnection configuration consists of three parts: the inflow region, the outflow region, and the small central diffusion region, as illustrated in Figure 1.3a. The magnetic field lines in the inflow region are convected from the two sides toward the dark central diffusion region. The outflow region has two parts; the reconnection layer in each part consists of a pair of slow shocks emanating from the central diffusion region. Plasmas are accelerated through slow shocks, leading to the presence of high-speed flow in the downstream region of slow shocks.

Reproduced with permission of the copyright owner. Further reproduction prohibited without permission.

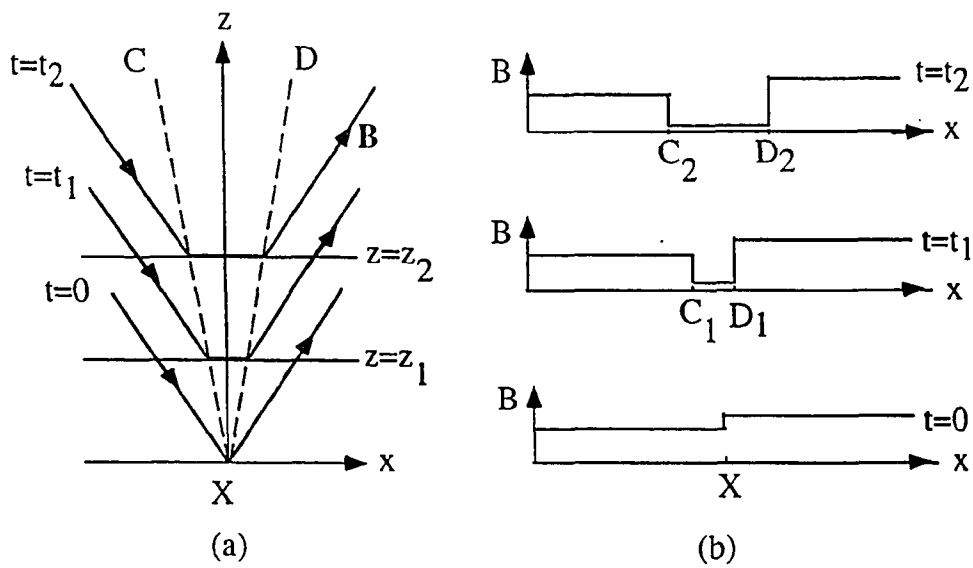

Figure 1.2 (a) An illustration for the formation of reconnection layer in the outflow region of magnetic reconnection in the xz plane. The reconnection layer consists of two discontinuities XC and XD which emanate from the point X. (b) Time evolution of magnetic field profile in the 1-D initial value problem which corresponds to the 2-D configuration of reconnection layer. The magnetic field line in the outflow region is convected to z_1 and z_2 at time t_1 and t_2, respectively.

Reproduced with permission of the copyright owner. Further reproduction prohibited without permission.

The symmetric reconnection in Petschek's [1964] model was recently simulated by Yan et al., [1992]. Figure 1.3b shows the magnetic field lines and the streamlines of plasma flow obtained in the simulation. Two pairs of slow shocks are present in the region where the streamlines are highly bent. It is apparent from the spacing between magnetic field lines in the downstream region that the magnetic energy is considerably reduced through the slow shocks. The reduced magnetic field and accelerated plasma flow in the downstream regions of slow shocks indicate that the magnetic energy is converted to the plasma kinetic energy. Symmetric reconnection models have also been studied by other authors [Sonnerup, 1970; Yeh and Axford 1970; Priest and Forbes, 1986; Priest and Lee, 1991].

(B) Asymmetric Reconnection Model of Levy et al. [1964]

Levy et al. [1964] provided an asymmetric model for magnetic reconnection. In this model, the magnetic field strength on one side of the current sheet is larger than that on the other side, and the plasma mass density on the high field side is set to zero. As a result, each pair of slow shocks in Petschek's [1964] model are replaced by an intermediate wave (rotational discontinuity) and a narrow slow expansion fan, as illustrated in Figure 1.4. The rotational discontinuity accomplishes the change of magnetic field direction and also leads to the presence of high speed flow along the current layer. Across the slow expansion wave downstream of the rotational discontinuity, the plasma mass density decreases slowly to zero.

1.1.3 Reconnection Layers at the Dayside Magnetopause and in the Magnetotail

The earth's magnetosphere is the cavity carved in the solar wind by the geomagnetic field. Figure 1.5 sketches the geomagnetic field and associated plasma regions in the noon-midnight meridian plane of the magnetosphere. As indicated by the dashed line, the magnetopause is the interface between the magnetosphere and the solar wind. The part of solar wind surrounding the magnetosphere is called the magnetosheath. The geomagnetic field lines are dragged by the solar

Reproduced with permission of the copyright owner. Further reproduction prohibited without permission.

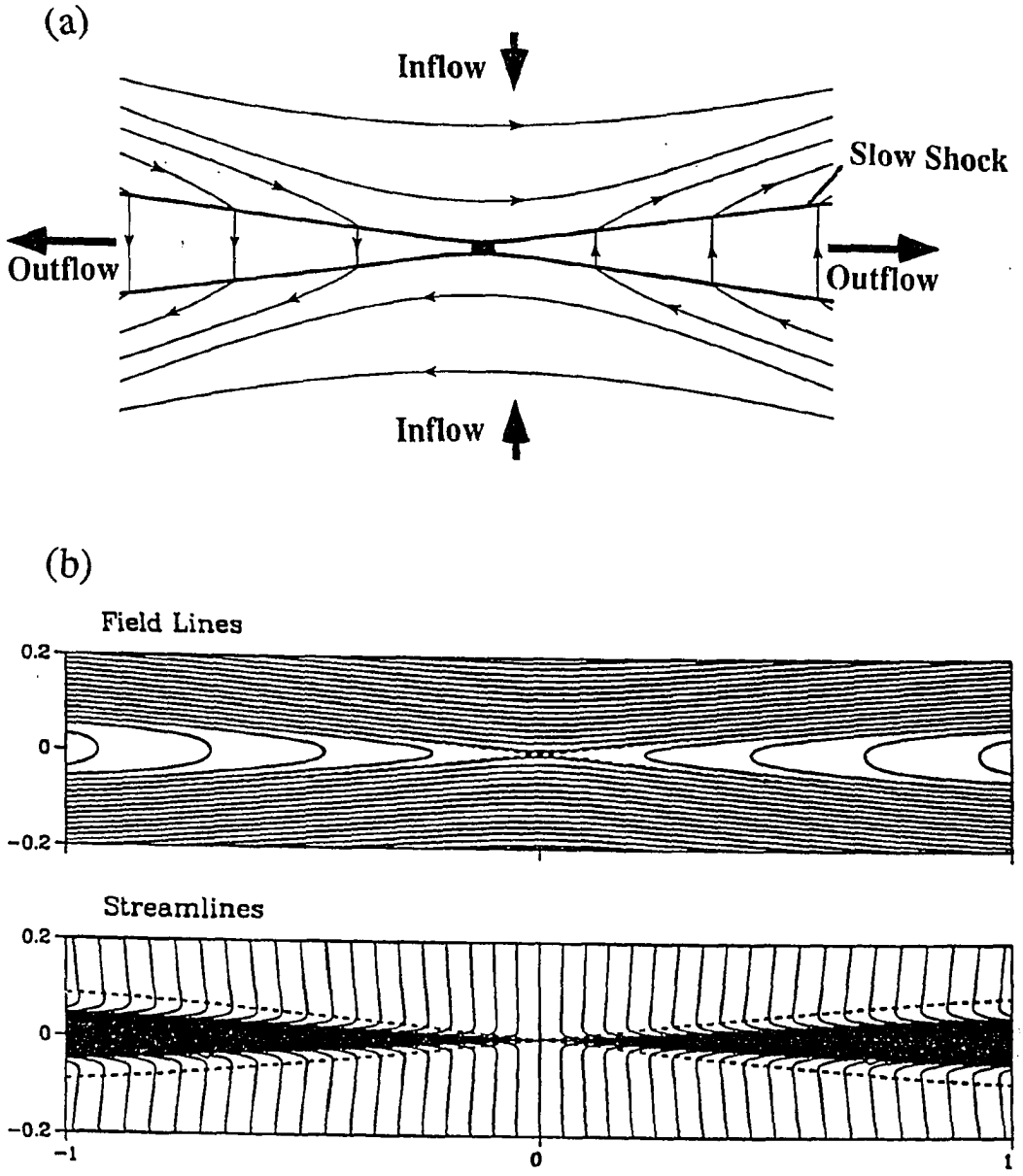

Figure 1.3 (a) Petschek's [1964] symmetric reconnection model which consists of the inflow region, the outflow region, and the small central diffusion region as shown by the dark area. A pairs of slow shocks are present in each part of the outflow region. (b) Magnetic field lines and streamlines of plasma flow obtained in the MHD simulation by Yan et al. [1992]. The dashed lines are the separatrices. Slow shocks are located downstream of the separatrices.

Reproduced with permission of the copyright owner. Further reproduction prohibited without permission.

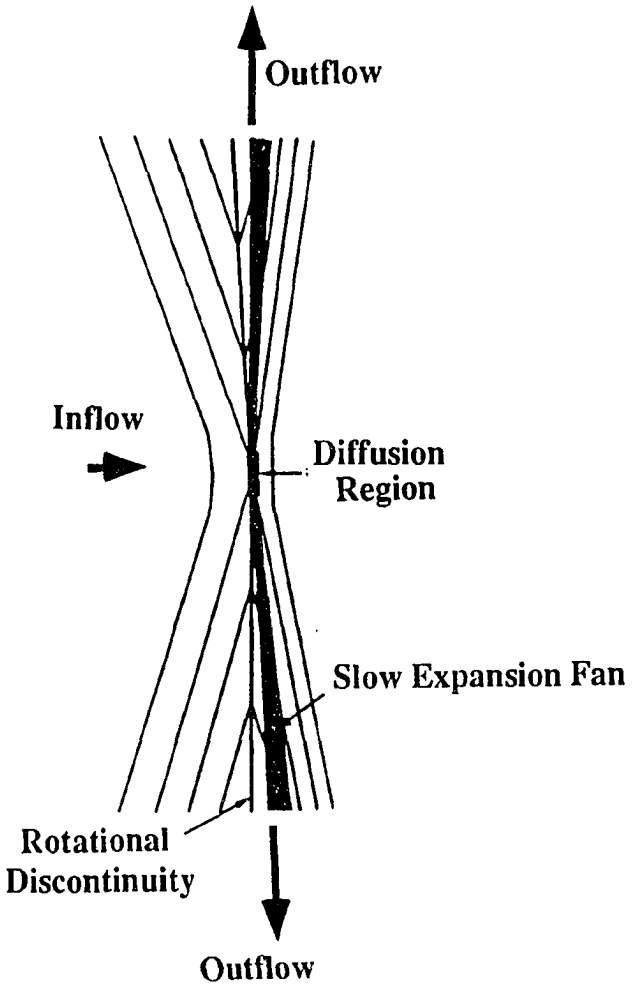

Figure 1.4 Levy et al.'s [1964] asymmetric reconnection model. A rotational discontinuity and a slow expansion wave are present in the reconnection layer.

Reproduced with permission of the copyright owner. Further reproduction prohibited without permission.

wind to form a long magnetotail. The magnetotail consists of two regions: the lobes and the plasma sheet. The plasma sheet is located near the equatorial plane and contains a plasma population with high density. The lobes are located between the plasma sheet and the magnetopause and have a low plasma density. Magnetic field strength in the magnetosheath is usually smaller than that in the magnetosphere, and the plasma density in the magnetosheath is higher than that in the magnetosphere.

As shown in Figure 1.5, the geomagnetic field has a northward component at the dayside magnetopause. In the presence of a southward interplanetary magnetic field (IMF), the magnetosheath and magnetospheric magnetic fields on the two sides of the magnetopause current sheet have antiparallel components, and magnetic reconnection can take place at the subsolar point X of the dayside magnetopause. As a result, high-speed flows are present in the dayside boundary layer which is shown by the shaded area earthward of the magnetopause. The reconnected magnetic field lines at the dayside magnetopause are convected with plasma flows toward the magnetotail. In the distant magnetotail, the magnetic fields in the lobes are antiparallel, and magnetic reconnection can take place at point N in the tail plasma sheet, as shown in Figure 1.5. High-speed plasma flows are then present in the plasma sheet, as shown by the shaded area in the magnetotail, and the magnetic field lines are convected earthward and tailward.

As a result of the magnetic reconnections at the dayside magnetopause and in the magnetotail, reconnection layers can be formed in the dayside boundary layer and in the tail plasma sheet.

1.2 Evolution of the Current Sheet Associated with Magnetic Reconnection – the Riemann Problem

Although attempts have been made to study the two-dimensional (2-D) configuration of the reconnection layer by using MHD simulations [e.g., Scholer, 1989; Shi and Lee, 1990], the discontinuities and expansion waves obtained in 2-D simulations have not been clearly identified

Reproduced with permission of the copyright owner. Further reproduction prohibited without permission.

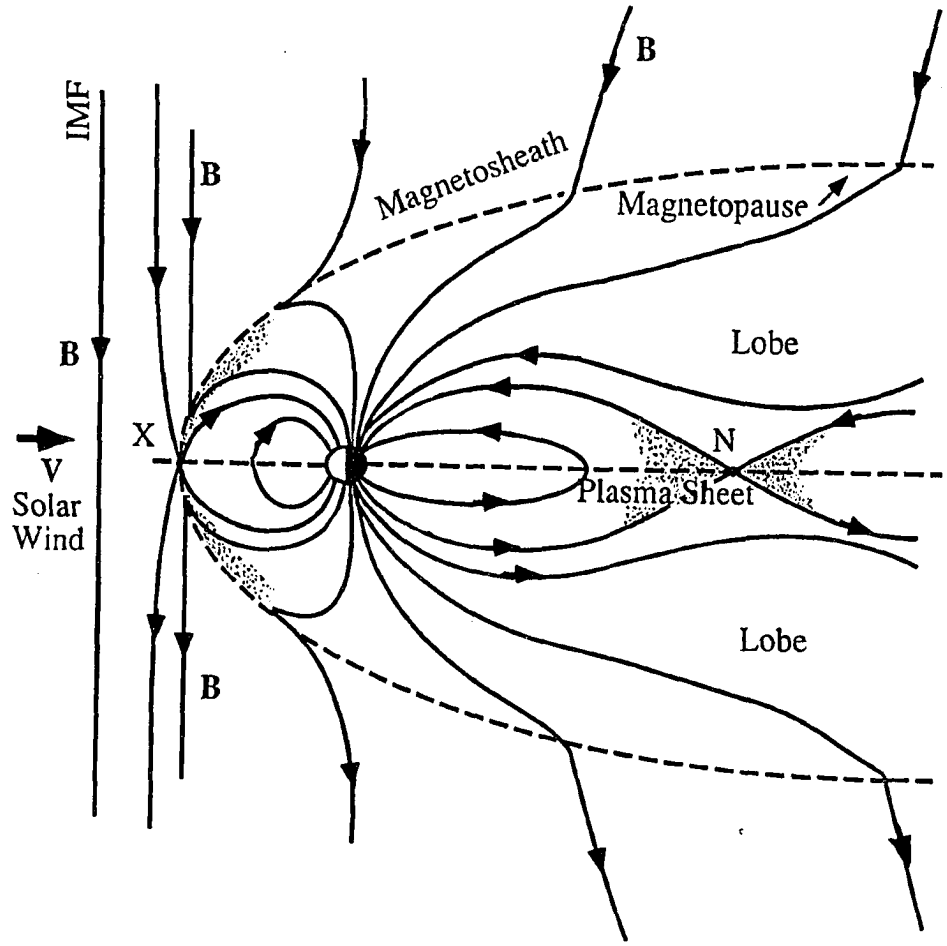

Figure 1.5 A sketch of the geomagnetic field and associated plasma regions in the noon-midnight meridian plane of the magnetosphere. In the presence of a southward IMF, magnetic reconnections can take place at point X of the dayside magnetopause and at point N in the tail plasma sheet.

Reproduced with permission of the copyright owner. Further reproduction prohibited without permission.

and studied due to low spatial resolution and small simulation domain. Clear separation between discontinuities usually requires a long simulation time and thus a very long simulation domain along the z direction in Figure 1.2a. In order to identify clearly the discontinuities and expansion waves in the reconnection layer, we can simplify the 2-D problem to a one-dimensional (1-D) initial value problem by assuming that the z coordinate of the discontinuity fronts in Figure 1.2a is related to the time t by $z = \bar{v}_z t$, where $\bar{v}_z$ is a constant plasma flow speed. The physical quantities in the 1-D initial value problem are functions of x and t.

Figure 1.2b illustrates the time evolution of the magnetic field profile in the 1-D initial value problem, which corresponds to the 2-D reconnection configuration in Figure 1.2a. Initially a thin current sheet exists at position X on the x axis. After the onset of magnetic reconnection at $t = 0$, the initial profile of magnetic field starts to evolve. At $t = t_1$, the discontinuity XC in Figure 1.2a propagates to the position indicated by C_1 along the x axis in Figure 1.2b. At the same time, the discontinuity XD propagates to the position indicated by D_1. At a later time $t = t_2$ which corresponds to $z = z_2$, the two discontinuities propagate to C_2 and D_2, respectively. Therefore the reconnection configuration in the xz plane corresponds to the 1-D evolution of the initial current sheet as shown in Figure 1.2b. Such an initial value problem is called the Riemann problem, which concerns the evolution of a 1-D system initially with two constant states separated by a transition layer [e.g., Jeffrey and Taniuti, 1966].

In this thesis, we study the structure of the reconnection layer in the magnetosphere by solving the Riemann problem for the evolution of an initial current sheet.

1.3 Previous Work on the Structure of the Reconnection Layer in the Magnetosphere

As mentioned earlier, Petschek's [1964] model is a symmetric model with equal plasma densities, equal magnetic field strengths, and exactly antiparallel magnetic fields on the two sides of the

Reproduced with permission of the copyright owner. Further reproduction prohibited without permission.

current layer. Two pairs of slow shocks are formed in the reconnection layer. This model can be applied to the reconnection in the tail plasma sheet, where the current sheet in the equatorial plane separates equal plasma densities and antiparallel magnetic fields. Similar symmetric reconnection models have also been proposed by Sonnerup [1970], Yeh and Axford [1970], Priest and Forbes [1986], and Priest and Lee [1991].

On the other hand, Levy et al. [1964] provided an asymmetric reconnection model for the dayside magnetopause, which separates the magnetosheath from the magnetosphere. They considered only the extreme case in which the plasma density on the magnetospheric side is zero. In the reconnection layer obtained by Levy et al. [1964], a rotational discontinuity exists at the magnetopause, and a slow expansion fan forms the boundary layer earthward of the magnetopause. This model was later further elaborated by Yang and Sonnerup [1977]. However, in general cases at the dayside magnetopause, the plasma density in the magnetosphere is finite, and the structure of reconnection layer is more complicated.

Based on the ideal (non-dissipative and non-dispersive) MHD formulation, the structure of the reconnection layer at the dayside magnetopause was studied by solving the Riemann problem [Heyn et al., 1988; Biernat et al., 1988]. It is found that rotational discontinuities, slow shocks, slow expansion waves, and contact discontinuity may be present in the reconnection layer. However, in these studies, the total pressure (magnetic pressure plus plasma thermal pressure) is assumed constant everywhere in the reconnection layer for simplicity, and the existence of the fast mode waves in the solution of the Riemann problem are completely ignored. Rijnbeek et al. [1988] compared the results from Heyn et al. [1988] with satellite observations at the dayside magnetopause. They found that the observations are different from the results of the ideal MHD formulation in many aspects.

On the other hand, 2-D MHD simulations were also carried out to study the structure of the reconnection layer in the magnetosphere [Sato, 1979; Ugai, 1984; Scholer, 1989; Shi and Lee, 1990]. Slow shocks were obtained in the Petschek-like symmetric reconnection layer [Sato, 1979;

Reproduced with permission of the copyright owner. Further reproduction prohibited without permission.

Ugai 1984]. On the other hand, Shi and Lee [1990] used a 2-D resistive MHD code to study the reconnection layer under different symmetry conditions. It is found that the intermediate shocks may be present in the reconnection layer. The presence of intermediate shock was also found by Scholer [1989]. However, in these simulations, the initial magnetic fields on the two sides of the current sheet are assumed exactly antiparallel.

1.4 Observations of the Reconnection Layer in the Magnetosphere

Satellite observations of plasma and field signatures at the earth's magnetopause and in the magnetotail have provided a large amount of observational evidence for the existence of the reconnection layer. Evidence for the existence of rotational discontinuity and high-speed plasma flows at the dayside magnetopause have been reported by Paschmann et al. [1979; 1986], Sonnerup [1979], Sonnerup et al. [1981], Berchem and Russell [1982], and Gosling et al. [1990a, b, c]. Observations of the ion and electron distributions in the dayside boundary layer region also indicate the presence of layered structure, which is associated with magnetic reconnection [Gosling et al., 1990a, b; c; Smith and Rogers, 1991; Fuselier et al., 1991]. On the other hand, ISEE deep-tail observations of plasma and the magnetic field at the lobe-plasma sheet boundaries indicated the presence of slow mode shocks [Feldmann et al., 1984, 1985; Smith et al., 1984; Schwartz et al., 1987].

Observations of reconnection layer at the dayside magnetopause will be given and compared with our simulation results in Chapter 4. Observations of slow shocks in the magnetotail will be discussed in Chapter 5.

1.5 Objectives and Outline of the Thesis

In this thesis, we use an analytical method, fluid simulation, and particle simulation to study the evolution of the current sheet associated with magnetic reconnection. The purposes of this

Reproduced with permission of the copyright owner. Further reproduction prohibited without permission.

thesis are: (1) to study systematically the structure of the reconnection layer at the dayside magnetopause and in the magnetotail; (2) to understand the roles of intermediate shocks and rotational discontinuities in the reconnection layer; and (3) to study the structures of individual discontinuities (shocks and waves) in the reconnection layer.

In Chapter 2, we study the structure of the reconnection layer by analytically solving the 1-D Riemann problem associated with magnetic reconnection on the basis of the ideal MHD formulation. Fast expansion waves, rotational discontinuities, slow shocks, slow expansion waves, and contact discontinuities are obtained in the solution of the Riemann problem.

In Chapter 3, the structure of the reconnection layer is studied using 1-D resistive MHD simulations. In the presence of a finite resistivity, the steady-state rotational discontinuities cannot exist, and steady intermediate shocks or time-dependent intermediate shocks (TDIS) are present in the reconnection layer. The steady intermediate shocks and time-dependent intermediate shocks play the role of rotational discontinuities in the reconnection layer.

In Chapter 4, we study the structure of reconnection layer based on 1-D hybrid simulations, in which the ions are treated as particles and the electrons are treated as a fluid. It is found that the structure of the reconnection layer obtained in the hybrid simulations is different from that in the resistive MHD simulations. In particular, the time-dependent intermediate shock evolves quickly to a steady rotational discontinuity with a constant width because of the particle kinetic effects. In addition, the contact discontinuity does not appear in the reconnection layer. The layered structure at the magnetopause and in the magnetotail plasma sheet obtained from the simulation will be compared with the ISEE satellite observations.

In Chapter 5, we study the structure of slow shocks in a collisionless plasma. The structure of slow shocks is simulated by using the 1-D hybrid code. It is also found that chaotic ion motion in the downstream wave of slow shocks can provide a very efficient mechanism for ion heating and for the damping of wavetrain downstream of the slow shocks. The simulation results can explain the lack of coherent wavetrains downstream of slow shocks observed in the deep magnetotail.

Reproduced with permission of the copyright owner. Further reproduction prohibited without permission.

The summary and discussion of this thesis are given in Chapter 6.

Reproduced with permission of the copyright owner. Further reproduction prohibited without permission.

Chapter 2 Ideal MHD Solutions of the Riemann Problem Associated with the Structure of Reconnection Layers

In this chapter, we study the structure of reconnection layers at the dayside magnetopause and in the tail plasma sheet based on the ideal MHD formulation. We solve the 1-D Riemann problem for the evolution of an initial current sheet after the onset of magnetic reconnection. In order to understand the existence and roles of MHD discontinuities in the reconnection layers, the properties of MHD waves and discontinuities will be briefly reviewed. The equations for solving the Riemann problem are derived from the jump conditions of physical quantities across the MHD discontinuities and expansion waves. The structures of reconnection layers at the dayside magnetopause and in the magnetotail are then solved.

It should be pointed out that the term ideal MHD used in the Riemann problem has a special meaning [e.g., Wu, 1990; Lin et al., 1992; Wu and Kennel, 1992]. The MHD discontinuities obtained in the ideal MHD approximation are considered as a structureless, thin layer. The effects of dissipation due to a finite resistivity or viscosity on the stability and evolution of these discontinuities are ignored.

2.1 Magnetohydrodynamic (MHD) Discontinuities

2.1.1 Linear MHD Modes and the Related Nonlinear MHD Discontinuities

It has been known for decades that there exist four types of magnetohydrodynamic discontinuities: Contact discontinuity, tangential discontinuity, rotational discontinuity, and MHD shocks [Landau and Lifshitz, 1960]. All of these MHD discontinuities are related to small-amplitude MHD linear modes. We begin our discussions with the MHD linear wave modes.

Reproduced with permission of the copyright owner. Further reproduction prohibited without permission.

An ideal MHD fluid is completely described by its velocity $\mathbf{V}$, density ρ, pressure P, specific-heat ratio γ, and magnetic field $\mathbf{B}$. The behavior of the fluid is governed by the following complete set of ideal (non-dispersive and non-dissipative) MHD fluid equations:

$$\frac{\partial \rho}{\partial t} + \nabla \cdot (\rho \mathbf{V}) = 0 \tag{2.1a}$$

$$\frac{\partial (\rho \mathbf{V})}{\partial t} + \nabla \cdot [(P + \frac{B^2}{2\mu_0})\mathbf{I} + \rho \mathbf{V}\mathbf{V} - \frac{\mathbf{B}\mathbf{B}}{\mu_0}] = 0 \tag{2.1b}$$

$$\frac{\partial \epsilon_T}{\partial t} + \nabla \cdot [(\frac{\rho V^2}{2} + \frac{P}{\gamma - 1} + P)\mathbf{V} + \mathbf{E} \times \mathbf{B}] = 0 \tag{2.1c}$$

$$\frac{\partial \mathbf{B}}{\partial t} = -\nabla \times \mathbf{E} \tag{2.1d}$$

$$\nabla \cdot \mathbf{B} = 0 \tag{2.1e}$$

with

$$\epsilon_T = \frac{1}{2}\rho V^2 + \frac{1}{\gamma - 1}p + \frac{1}{2\mu_0}B^2 \tag{2.2}$$

and

$$\mathbf{E} = -\mathbf{V} \times \mathbf{B} \tag{2.3}$$

where $\mathbf{E}$ and μ_0 are, respectively, the electric field and the permeability of free space. The specific-heat ratio is chosen to be $\gamma = 5/3$.

The 1-D form of equations (2.1) -- (2.3) can be expressed as

$$\frac{\partial \rho}{\partial t} + V_x \frac{\partial \rho}{\partial x} + \rho \frac{\partial V_x}{\partial x} = 0 \tag{2.4a}$$

$$\rho \frac{\partial V_x}{\partial t} + \rho V_x \frac{\partial V_x}{\partial x} + \frac{\partial}{\partial x}(P + \frac{B_t^2}{8\pi}) = 0 \tag{2.4b}$$

$$\rho \frac{\partial \mathbf{V}_t}{\partial t} + \rho V_x \frac{\partial \mathbf{V}_t}{\partial x} = \frac{B_x}{4\pi} \frac{\partial \mathbf{B}_t}{\partial x} \tag{2.4c}$$

$$\partial \mathbf{B}_t / \partial t + V_x \frac{\partial \mathbf{B}_t}{\partial x} = B_x \frac{\partial \mathbf{V}_t}{\partial x} - \mathbf{B}_t \frac{\partial V_x}{\partial x} \tag{2.4d}$$

$$\frac{\partial P}{\partial t} + V_x \frac{\partial P}{\partial x} = C_S^2 (\frac{\partial \rho}{\partial t} + V_x \frac{\partial \rho}{\partial x}) \tag{2.4e}$$

where x is the direction of wave propagation, $C_S \equiv (\gamma P/\rho)^{1/2}$ is the speed of sound, and the subscript "t" represents the components transverse to the x direction, with $\mathbf{B}_t = (0, B_y, B_z)$ and

Reproduced with permission of the copyright owner. Further reproduction prohibited without permission.

$\mathbf{V}_t = (0, V_y, V_z)$. Equations (2.4) consists of seven component equations in seven unknowns. The ideal MHD equations do not provide a characteristic length or time.

Let the subscript "0" denote the homogeneous background state. Since equations (2.4) are symmetric with respect to rotations about the x axis, B_{z0} may be set to zero without loss of generality. We may also choose the upstream tangential velocity $\mathbf{V}_{t0} = 0$ since the tangential velocity can be removed by a Galilean transformation. The small-amplitude waves can be obtained by linearizing equations (2.4a) -- (2.4e). Assume that the physical quantities in a small-amplitude linear wave vary as $\sim e^{-i(kx-\omega t)}$, where k is the wavenumber and ω is the wave frequency. By solving the linearized equations, we arrive at the dispersion relation for MHD waves

$$C(C^2 - C_I^2)[C^4 - C^2(C_A^2 + C_S^2) + C_S^2 C_I^2] = 0 \tag{2.5}$$

where $C = \omega/k$ is the wave speed, the Alfven speed C_A is defined as

$$C_A \equiv B_0/\sqrt{\mu\rho_0} \tag{2.6}$$

and the intermediate speed C_I is defined as

$$C_I \equiv C_A cos\theta \tag{2.7}$$

Here, θ is the wave propagation angle with respect to the background magnetic field.

Seven independent linear waves, corresponding to four distinct MHD modes, can be obtained from the dispersion relation (2.5). These MHD modes include:

Reproduced with permission of the copyright owner. Further reproduction prohibited without permission.

(a) one non-propagating entropy wave with phase speed

$$C = 0 \tag{2.8}$$

(b) two fast magnetosonic waves with

$$C = \pm C_F \equiv \pm\{\frac{1}{2}[(C_S^2 + C_A^2) + \sqrt{(C_S^2 + C_A^2)^2 - 4C_S^2 C_I^2}]\}^{1/2} \tag{2.9}$$

(c) two intermediate waves with

$$C = \pm C_I \tag{2.10}$$

(d) two slow magnetosonic waves with

$$C = \pm C_{SL} \equiv \pm\{\frac{1}{2}[(C_S^2 + C_A^2) - \sqrt{(C_S^2 + C_A^2)^2 - 4C_S^2 C_I^2}]\}^{1/2} \tag{2.11}$$

Note that $C_F^2 > C_I^2 > C_{SL}^2$. The non-propagating entropy wave with $C = 0$ remains stationary in the frame of the fluid. In the entropy mode structure, adjacent elements of the fluid have different specific entropies. On the other hand, there is no change in specific entropy in all three small-amplitude linear propagating waves. The fast mode waves and slow mode waves are compressible, while the intermediate wave leaves the pressure and density unchanged.

Figure 2.1 shows the Friedrich diagrams for three MHD waves, in which the wave speed is plotted as a function of the wave propagation angle relative to the background magnetic field $\mathbf{B_0}$. Cases with $\beta < 1$ and $\beta > 1$ are shown, where β is the ratio of background plasma pressure to magnetic pressure. As shown in the figure, the diagram is divided into four regions by the three MHD wave speeds. Region 1 is the super-fast region, region 2 is the sub-fast and

Reproduced with permission of the copyright owner. Further reproduction prohibited without permission.

super-intermediate region, region 3 is the sub-intermediate and super-slow region, and region 4 is the sub-slow region.

An MHD discontinuity is a stationary thin layer through which the magnetic field, plasma density, pressure, and flow velocity may have a significant jump. There exist four types of MHD discontinuities: contact discontinuity, tangential discontinuity, rotational discontinuity, and MHD shocks. As mentioned at the beginning of this section, all the discontinuities are related to the MHD linear wave modes. The contact discontinuity is related to the entropy wave and moves with the fluid. The tangential discontinuity is a special case of the entropy mode discontinuity in which the component of magnetic field normal to the discontinuity front is equal to zero. Both the contact discontinuity and tangential discontinuity are non-propagating structures: they convect with the plasma fluid. The rotational discontinuity is a nonlinear intermediate mode structure through which the normal component of plasma flow velocity relative to the discontinuity is constant and equal to the normal component of Alfven velocity, which is defined as $\mathbf{V}_A = \mathbf{B}/\sqrt{\mu_0 \rho}$.

MHD shocks are associated with the propagating MHD wave modes. The shock formation process can be described as follows. For a nonlinear compressional wave, local wave speed increases with the local wave amplitude. The high pressure parts in the wave propagate faster than the low pressure parts. As a result, the fast propagating part of the wave may catch up and overtake the slower part, leading to steepening of the wave. As long as this steepening process is balanced by damping due to dissipation in the plasma, a shock with a finite width is formed. Since a shock is steepened from compressional waves, a characteristic feature of the shock is the increase of the plasma density downstream of the shock. Correspondingly, the normal component of plasma flow velocity decreases. The shock can exist only if the normal plasma flow speed in the upstream region exceeds the corresponding wave mode speed and the normal flow speed in downstream region is less than the local wave speed. There is a dissipation process in the shock transition layer, in which the plasma is heated. The jump relations of physical quantities have been studied usually by assuming that there is no heat flux across the shock [e.g., Landau and Lifshitz,

Reproduced with permission of the copyright owner. Further reproduction prohibited without permission.

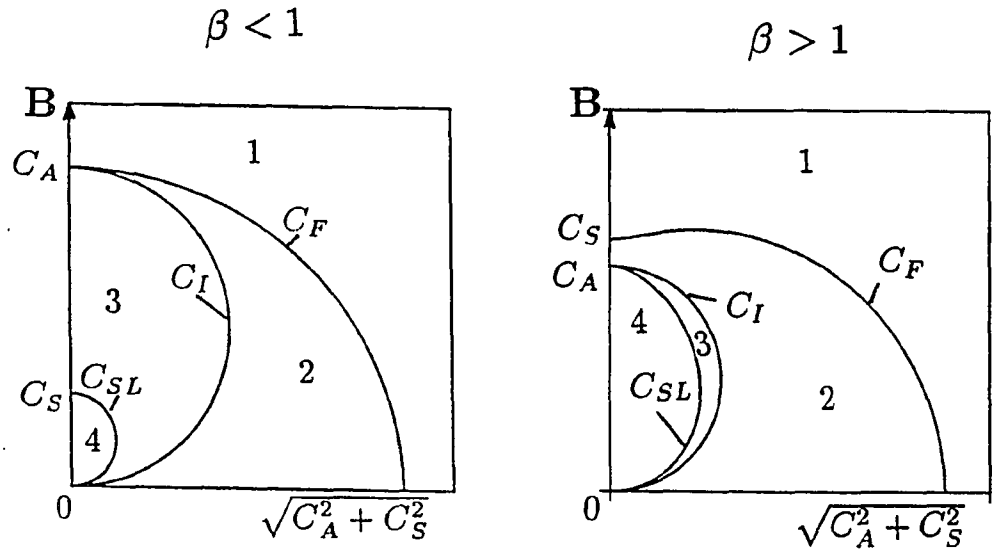

Figure 2.1 Friedrich diagrams for three MHD wave modes, in which the wave speed is plotted as a function of the wave propagation angle relative to the background magnetic field $\mathbf{B}_0$. The diagram is divided into four regions by the three MHD waves.

Reproduced with permission of the copyright owner. Further reproduction prohibited without permission.

1960; Kantrowitz and Petschek, 1966]. The second law of thermodynamics requires the entropy to increase across a shock [de Hoffman and Teller, 1950].

There exist three types of MHD shocks: fast shock, intermediate shock, and slow shock. The fast shock is steepened from the MHD fast mode compressional wave, intermediate shock from the intermediate wave, and slow shock from the slow mode compressional wave. The plasma density increases across MHD shocks, and the normal component of plasma flow velocity decreases. For the fast shock, the shock stability condition requires that the normal component of upstream plasma flow velocity is in Region 1 (super-fast) of Figure 2.1 and the downstream normal flow speed is in Region 2 (sub-fast and super-intermediate). Therefore the fast shock is also called the 1-2 shock. For the slow shock, the normal component of upstream flow velocity is sub-intermediate and super-slow (Region 3), and the downstream normal flow speed is sub-slow (Region 4). Thus the slow shock is also called the 3-4 shock. Similarly, the intermediate shock by definition is the shock with upstream normal flow speed super-intermediate and downstream normal flow speed sub-intermediate. Thus the intermediate shock can be 1-3, 2-3, 1-4, or 2-4 shocks. However, based on the shock evolutionary condition of the ideal MHD, Akhiezer et al. [1958] and Taniuti [1962] argued that the MHD intermediate shocks are not structurally stable and are physically unrealizable. On the other hand, Wu [1987, 1988, 1990] recently showed that in the dissipative MHD formulation all the four types of intermediate shocks can be formed by the steepening of the nonlinear transverse MHD waves.

2.1.2 Rankine-Hugoniot Jump Conditions of MHD Discontinuities

The discontinuity can be considered as a thin transition region between a pair of uniform stationary plasma regions. The jumps of physical quantities across the MHD discontinuities can be described by the conservation laws in the MHD formulation. Since the MHD discontinuity is stationary ($\partial/\partial t = 0$) and one dimensional, we can integrate the equations in (2.1) along x and set $\partial/\partial t = 0$ to obtain the jump conditions. The resulting jump conditions are related to the

Reproduced with permission of the copyright owner. Further reproduction prohibited without permission.

conservation of mass, momentum, and energy flux in the discontinuity frame, the conservation of the normal magnetic field component B_x, and the conservation of the tangential electric field component. These conservation laws, which are called the Rankine-Hugoniot (RH) jump conditions, can be written in the discontinuity frame as

$$[\rho v_n] = 0 \tag{2.12a}$$

$$[\rho v_n \mathbf{v_t} - B_n \mathbf{B}_t/\mu_0] = 0 \tag{2.12b}$$

$$[\rho V_n^2 + p + B^2/2\mu_0 - B_n^2/\mu_0] = 0 \tag{2.12c}$$

$$[(\rho v^2/2 + \epsilon_T + p + B^2/\mu_0)v_n - B_n^2 v_n/\mu_0 - B_n(\mathbf{B}_t \cdot \mathbf{v}_t)/\mu_0] = 0 \tag{2.12d}$$

$$[B_n] = 0 \tag{2.12e}$$

$$[B_n \mathbf{v}_t - v_n \mathbf{B}_t] = 0 \tag{2.12f}$$

where the subscripts n (along x) and t denote the components normal and tangential to the discontinuity surface, respectively, and the square brackets denote the difference between the values on the two sides of the discontinuity, i.e., $[A] = A_2 - A_1$. The subscripts "1" and "2" denote the quantities upstream and downstream of the discontinuity, respectively. The RH jump conditions only relate the upstream and downstream asymptotic states and do not describe the structure inside the discontinuity, which is determined by dissipation. From equations (2.12a) -- (2.12f), the jump relations for each MHD discontinuity can be obtained as follows [e.g., Landau and Lifshitz, 1960].

Reproduced with permission of the copyright owner. Further reproduction prohibited without permission.

(i) Contact Discontinuity:

$$v_n = 0, B_n \neq 0, [\mathbf{B}_t] = 0, [\mathbf{v}_t] = 0, [\rho] \neq 0, [P] = 0. \tag{2.13}$$

(ii) Tangential Discontinuity:

$$v_n = 0, B_n = 0, [\mathbf{B}_t] \neq 0, [\mathbf{v}_t] \neq 0, [\rho] \neq 0, [P + B^2/2\mu_0] = 0. \tag{2.14}$$

(iii) Rotational Discontinuity:

$$v_n = B_n/\sqrt{\mu_0\rho} \neq 0, [\mathbf{v}_t] = s[\mathbf{B}_t]/\sqrt{\mu_0\rho} = s[\mathbf{V}_{At}] \neq 0, [\rho] = 0, [P] = 0. \tag{2.15}$$

where $s = sgn(v_n B_n)$. The relation $[\mathbf{v}] = s[\mathbf{B}/\sqrt{\mu_0\rho}] = s[\mathbf{V}_A]$ is also called the Walen relation for the rotational discontinuity.

(iv) MHD Shocks:

The jump conditions are different for different MHD shocks. The conservation of tangential electric field in equation (2.12f) requires that MHD shocks satisfy the shock coplanarity condition, which states that the upstream magnetic field, downstream magnetic field, and shock normal are in the same plane. Therefore, the tangential magnetic fields in upstream and downstream regions are either in the same direction or exactly antiparallel. To solve for the changes in the physical quantities across an MHD shock, we can use a frame in which the upstream flow velocity is parallel (or antiparallel) to the upstream magnetic field, i.e., the tangential component of the electric field in the upstream region is transformed away. The tangential flow velocity in the new frame is

$$\mathbf{v}_t' = \mathbf{v}_t + \mathbf{u}_t^{HT} \quad , \tag{2.16}$$

where $\mathbf{u}_t^{HT}$ is the transformation velocity which is also transverse to the shock normal. The conservation of tangential electric field then requires that the tangential component of electric field in the downstream region is also zero. Thus, in the new frame, the downstream flow velocity is

Reproduced with permission of the copyright owner. Further reproduction prohibited without permission.

also aligned with the downstream magnetic field. This new frame is called the de Hoffmann-Teller frame (HT frame). The normal component of flow velocity in the HT frame is the same as that in the old frame.

We now use the HT frame to solve the RH jump conditions for MHD shocks. For convenience, we still use $\mathbf{v}_t$ to represent the tangential flow velocities in the HT frame. Without losing generality of the results, we assume $B_y = 0$ and $v_y = 0$. Let $R_\rho = \rho_2/\rho_1$, $R_{v_n} = v_{n2}/v_{n1}$, $R_{B_t} = B_{t2}/B_{t1}$, $R_P = P_2/P_1$, and $R_{v_t} = v_{t2}/v_{t1}$. We obtain from the equations in (2.12) the following relations for MHD shocks:

$$a_3 R_\rho^3 + a_2 R_\rho^2 + a_1 R_\rho + a_0 = 0 \tag{2.17a}$$

$$R_{v_n} = 1/R_\rho \tag{2.17b}$$

$$R_{B_t} = \frac{R_\rho(1 - M_I^2)}{R_\rho - M_I^2} \tag{2.17c}$$

$$\frac{\beta_1}{2M_I^2 cos^2\theta_{nB1}}(R_P - 1) + (1/R_\rho - 1) + \frac{R_{B_t}^2}{2M_I^2} tan^2\theta_{nB1} - \frac{tan^2\theta_{nB1}}{2M_I^2} = 0 \tag{2.17d}$$

$$R_{v_t} = R_{B_t}/R_\rho \tag{2.17e}$$

with

$$a_3 = -(1 + \frac{5\beta_1}{2M_I^2})/cos^2\theta_{nB1} \tag{2.18a}$$

$$a_2 = 2M_I^2 - \frac{1}{2}M_I^2 tan^2\theta_{nB1} + 4 + \frac{5\beta_1}{cos^2\theta_{nB1}} + 4tan^2\theta_{nB1} \tag{2.18b}$$

$$a_1 = -M_I^4 - 8M_I^2 - \frac{5\beta_1}{2\cos^2\theta_{nB1}}M_I^2 - \frac{5}{2}M_I^2 tan^2\theta_{nB1} \tag{2.18c}$$

$$a_0 = 4M_I^4 \tag{2.18d}$$

where the upstream intermediate Mach number $M_I \equiv v_{n1}/C_{I1}$, C_{I1} is the upstream intermediate mode speed, $\beta_1 = P/(B_1^2/2\mu_0)$ is the upstream plasma beta, and θ_{nB1} is the upstream shock normal angle which is defined as the angle between the upstream magnetic field and the shock

Reproduced with permission of the copyright owner. Further reproduction prohibited without permission.

normal direction. In general, equation (2.17a) has three independent roots, which may correspond to the fast shock, intermediate shock, and slow shock.

Across the fast shocks with $v_{n1} > C_{F1}$ and $C_{I2} < v_{n2} < C_{F2}$, the tangential magnetic field does not change direction, and

$$[\rho] > 0, [P] > 0, [|\mathbf{B}_t|] > 0, [v_n] < 0. \tag{2.19}$$

Across the intermediate shocks, the tangential magnetic field changes direction by 180°, and

$$[\rho] > 0, [P] > 0, [|\mathbf{B}_t|] \neq 0, [v_n] < 0. \tag{2.20}$$

As mentioned earlier, the intermediate shocks have four types: 1-3, 2-3, 1-4, and 2-4 shocks.

For the slow shocks with $C_{SL1} < v_{n1} < C_{I1}$ and $v_{n2} > C_{SL2}$, the tangential magnetic field does not change direction, and

$$[\rho] > 0, [P] > 0, [|\mathbf{B}_t|] < 0, [v_n] < 0. \tag{2.21}$$

Slow shocks with a Mach number $M_I = 1$ are called switch-off shocks, in which the downstream tangential magnetic field in equation (2.17c) is "switched off" with $B_{t2} = 0$. For given θ_{nB} and β_1, the switch-off shock can be considered as the strongest slow shock based on the jump of tangential magnetic field across the shock.

2.1.3 Modification of the Rankine-Hugoniot Jump Conditions in Anisotropic Plasma

In our hybrid simulations which will be presented in Chapter 4, the plasma pressure anisotropy with $P_{\|} \neq P_{\perp}$ is found to be present, where $P_{\|}$ and $P_{\perp}$ are, respectively, the components of plasma thermal pressure parallel and perpendicular to local magnetic field. The pressure anisotropy has also been observed by satellites in the magnetosheath and magnetosphere [e.g., Tsurutani et

Reproduced with permission of the copyright owner. Further reproduction prohibited without permission.

al., 1981; Sonnerup et al., 1981]. In the presence of pressure anisotropy, the RH conditions of discontinuities are modified and can be written as

$$[\rho v_n] = 0 \tag{2.22a}$$

$$[\rho v_n \mathbf{v}_t - \frac{B_n \mathbf{B}_t}{\mu_0} + \frac{B_n \mathbf{B}_t}{2\mu_0}(\beta_\parallel - \beta_\perp)] = 0 \tag{2.22b}$$

$$[\rho v_n^2 + P_\perp + \frac{B^2}{2\mu_0} + \frac{B_n^2}{2\mu_0}(\beta_\parallel - \beta_\perp)] = 0 \tag{2.22c}$$

$$[(\frac{1}{2}\rho v^2 + \frac{5}{2}P + \frac{B^2}{\mu_0} - \frac{B^2}{6\mu_0}(\beta_\parallel - \beta_\perp))v_n - (1 - \frac{1}{2}(\beta_\parallel - \beta_\perp))\frac{B_n \mathbf{B}_t}{\mu_0} \cdot \mathbf{v}_t -$$
$$(1 - \frac{1}{2}(\beta_\parallel - \beta_\perp))\frac{B_n^2}{\mu_0} v_n] = 0 \tag{2.22d}$$

$$[B_n \mathbf{v}_t - v_n \mathbf{B}_t] = 0 \tag{2.22e}$$

where $\beta_\parallel$ is the plasma beta parallel to the local magnetic field, $\beta_\perp$ is the plasma beta perpendicular to the magnetic field, and the total plasma thermal pressure $P = (P_\parallel + 2P_\perp)/3$.

(i) Contact Discontinuity:

From equations (2.22), we obtain the jump relations for a contact discontinuity

$$v_n = 0, B_n \neq 0, [\mathbf{v}_t] = 0, [\mathbf{B}_t] \neq 0, [\rho] \neq 0, [P] \neq 0. \tag{2.23}$$

Thus in the presence of pressure anisotropy, the magnetic field, plasma density and pressure may not be constant across the contact discontinuity. This is different from the situation with an isotropic plasma pressure.

(ii) Tangential Discontinuity:

For a tangential discontinuity,

$$v_n = 0, B_n = 0, [\mathbf{B}_t] \neq 0, [\mathbf{v}_t] \neq 0, [\rho] \neq 0, [P_\perp + B_t^2] = 0 \tag{2.24}$$

(iii) Rotational Discontinuity:

Reproduced with permission of the copyright owner. Further reproduction prohibited without permission.

For a rotational discontinuity,

$$[\mathbf{v}] = [(\mathbf{B}/\sqrt{\mu_0\rho})(1 - \frac{\beta_{\|} - \beta_{\perp}}{2})^{1/2}] \neq 0, [B] \neq 0, [\rho] \neq 0, [P] \neq 0. \qquad (2.25)$$

The other jump relations across the rotational discontinuity can be written as [e.g., Hudson, 1971]

$$\rho_2/\rho_1 = (1 - \alpha_1)/(1 - \alpha_2) \qquad (2.26a)$$

$$(P_{\perp 2} - P_{\perp 1}) + (B_1^2 - B_2^2)/8\pi = 0 \qquad (2.26b)$$

$$(P_{\|1} + \frac{3}{2}P_{\perp 1} + \frac{B_1^2}{8\pi})/\rho_1 = (P_{\|2} + \frac{3}{2}P_{\perp 2} + \frac{B_2^2}{8\pi})/\rho_2 \qquad (2.26c)$$

where $\xi = 1 - \alpha$, with $\alpha = (\beta_{\|} - \beta_{\perp})/2$. Therefore, unlike the isotropic plasma, the magnetic field, plasma density, pressure, and flow velocity across the rotational discontinuity may not be constant.

(iv) MHD Shocks:

For MHD shocks, the jump relations are also modified in the presence of the pressure anisotropy. The jump relations of MHD shocks in anisotropic plasma will be discussed in Chapter 4.

2.2 Variation of Physical Quantities Across Expansion Waves

In addition to the MHD discontinuities discussed above, MHD expansion waves may also be present in the reconnection layer. There are two types of expansion waves: fast mode expansion waves and slow mode expansion waves. The expansion waves are different from MHD shocks in that the plasma density decreases through the expansion waves. The compressional waves can steepen to form a shock. The expansion waves do not form a stationary structure but expand with time. For the fast (slow) expansion wave, the upstream normal flow speed is equal to or less than

Reproduced with permission of the copyright owner. Further reproduction prohibited without permission.

the MHD fast (slow) mode speed. The tangential component of magnetic field does not change direction through the expansion simple wave. In particular, we have

$$[v_n] > 0, [|\mathbf{B}_t|] < 0, [\rho] < 0, [P] < 0 \tag{2.27}$$

for the fast expansion wave, and

$$[v_n] > 0, [|\mathbf{B}_t|] > 0, [\rho] < 0, [P] < 0 \tag{2.28}$$

for the slow expansion wave. The expansion waves can be described as a non-linear simple wave. A general expansion wave solution was given by Akhiezer et al. [1975]. Heyn et al. [1988] derived the variations of physical quantities through the slow expansion wave by assuming that the entropy and total pressure are conserved.

On the other hand, if the expansion wave is weak and thus $|C_{SL1} - C_{SL2}|$ is less than or equal to v_{n1}, the jump conditions across an expansion wave can be obtained by assuming that the mass, momentum, and entropy are conserved across the expansion wave. Thus the jump conditions across a slow or fast expansion wave can be obtained approximately by replacing the energy equation (2.12d) with the entropy conservation equation

$$[P\rho^{-\gamma}] = 0 \tag{2.29}$$

Although an expansion wave may not strictly be a steady structure with $\partial/\partial t = 0$, the usage of equations (2.12) and (2.29) is found to be a very good approximation for weak expansion waves in the Riemann problem. Therefore, the jumps of physical quantities across the slow or fast expansion

Reproduced with permission of the copyright owner. Further reproduction prohibited without permission.

wave can be obtained from the following relations

$$a_6' R_\rho^{\gamma+3} + a_5' R_\rho^{\gamma+2} + a_4' R_\rho^{\gamma+1} + a_3' R_\rho^3 + a_2' R_\rho^2 + a_1' R_\rho + a_0' = 0 \qquad (2.30a)$$

$$R_{v_n} = 1/R_\rho \qquad (2.30b)$$

$$R_{B_t} = R_\rho(1 - M_I^2)/(\rho - M_I^2) \qquad (2.30c)$$

$$R_P = R_\rho^\gamma \qquad (2.30d)$$

$$R_{v_t} = R_{B_t}/R_\rho \qquad (2.30e)$$

where

$$a_6' = \beta_1/(2M_I^2 cos^2\theta_{nB1}) \qquad (2.31a)$$

$$a_5' = -\beta_1/cos^2\theta_{nB1} \qquad (2.31b)$$

$$a_4' = \beta_1 M_I^2/(2cos^2\theta_{nB1}) \qquad (2.31c)$$

$$a_3' = -1/cos^2\theta_{nB1} - \beta_1/(2M_I^2 cos^2\theta_{nB1}) + tan^2\theta_{nB1} M_I^2/2 \qquad (2.31d)$$

$$a_2' = 1 + 2M_I^2 + \beta_1/cos^2\theta_{nB1} + tan^2\theta_{nB1} \qquad (2.31e)$$

$$a_1' = -[M_I^4 + 2M_I^2 + \beta_1 M_I^2/(2cos^2\theta_{nB1}) + tan^2\theta_{nB1} M_I^2/2] \qquad (2.31f)$$

$$a_0' = M_I^4 \qquad (2.31g)$$

We have checked the variations of physical quantities across the expansion waves obtained in our numerical simulations to be presented in the next chapter and found that the above jump conditions are well satisfied for the fast expansion waves. The slow expansion waves can also be described by the above jump conditions if the asymmetry of physical quantities on the two sides of the initial current sheet is not very large, i.e., $\rho_s/\rho_m < 30$. We have also used the above jump conditions to construct an expansion wave and simulated the evolution of such structure. It

Reproduced with permission of the copyright owner. Further reproduction prohibited without permission.

is found that the physical quantities in the upstream and downstream regions remain the same as those initially imposed.

2.3 Formulation of the Riemann Problem

After obtaining the jump relations across each discontinuity and expansion wave, we now derive the equations for solving the 1-D Riemann problem associated with the structure of the reconnection layer.

In our study, the initial physical quantities on the two sides of the current layer are given, and the initial plasma flow velocities on the two sides are zero. At the dayside magnetopause, the magnetic fields and plasma densities in the magnetosheath and the magnetosphere are different. In general, for an MHD system of n quantities, the solution of the Riemann problem consists of n discontinuities or waves, and the solution is unique [Jeffrey and Tanuiti, 1966]. The physical system is governed by the MHD equations in (2.1) with seven quantities (B_y, B_z, ρ, P, V_x, V_y, V_z), and thus $n = 7$. Therefore, there exist seven discontinuities or expansion waves in the solution of Riemann problem associated with magnetic reconnection.

As shown earlier, among the four types of MHD discontinuities, the tangential discontinuity may only be present when $B_n = 0$, while the contact discontinuity, rotational discontinuity, and MHD shocks require $B_n \neq 0$. Applied to the earth's magnetosphere, the quiet-time magnetopause is usually identified as a tangential discontinuity when the earth's magnetic field is closed [e.g., Van Allen and Adnan, 1992]. On the other hand, the contact discontinuity, rotational discontinuity and MHD shocks may be present at the magnetopause-boundary layer region with magnetic reconnection. The rotational discontinuity may change the direction of magnetic field. The slow shock and fast shock may change the magnitude of magnetic field, plasma density, and pressure. The contact discontinuity links two regions with different plasma densities but conserves pressure, magnetic field, and plasma flow velocity. The intermediate shock may not only change the

Reproduced with permission of the copyright owner. Further reproduction prohibited without permission.

magnitude of field, density and pressure but also change the direction of tangential magnetic field by 180°. However, they do not exist in the ideal MHD formulation. In addition, the fast expansion wave and slow expansion wave may also be present. Both expansion waves change the magnitude of magnetic field, plasma density, pressure, and flow velocity.

Among the MHD wave modes involved, the fast mode quickly propagates away from the initial current sheet. They are not considered as a permanent part of the reconnection layer, although they appear in the Riemann problem. In the main reconnection layer, the rotational discontinuities propagate fastest, and thus they bound the reconnection layer on the magnetosheath side and/or the magnetospheric side. Following them are the slow shocks or slow expansion waves. Since the contact discontinuity is a non-propagating structure, it stays at the center of the reconnection layer, separating the propagating discontinuities on the two sides. Physically speaking, the rotational discontinuity on either side of the reconnection layer plays the role of changing the direction of magnetic field. The slow shocks and slow expansion waves change the magnetic field strength and plasma density, and the contact discontinuity is required at the center of the reconnection layer to link different plasma densities on its two sides.

Assume that the total pressure $(P + B^2/2\mu_0)$ is constant across the initial current sheet. Our calculations indicate that the fast shock is present only if the shear flows on the two sides of the initial current sheet is large. Thus the solutions in this section do not contain the fast shocks. Only five different types of discontinuities need to be taken into consideration: fast expansion waves, rotational discontinuities, slow shocks, slow expansion waves, and contact discontinuities. Note that in the resistive MHD formulation to be presented in the next chapter, the intermediate shocks may be present and the structure of reconnection layer obtained from the above method is modified.

Figure 2.2 schematically shows the solution of the Riemann problem: an initial current sheet evolves into a system of MHD discontinuities based on the ideal MHD formulation. The initial current sheet exists at $x = 0$, and the profile of plasma density has a jump at the initial current

Reproduced with permission of the copyright owner. Further reproduction prohibited without permission.

sheet. At $t > 0$, seven discontinuities and expansion waves are present. Let CD denote the contact discontinuity. Three wave modes propagate to the left side of the discontinuity CD. These three discontinuities and expansion waves are the fast expansion wave F, the rotational discontinuity RD, and the slow mode SL. The slow mode SL can be a slow shock (SS) or a slow expansion wave (SE). There are also three discontinuities and expansion waves that propagate to the right side of the contact discontinuity CD, including the fast expansion wave F', the rotational discontinuity RD', and the slow mode SL', as shown in Figure 2.2. Region 1 and Region 8 in the figure are the plasma regions on the two sides of the initial current sheet, and Regions 2 through 7 indicate other 6 uniform regions between the discontinuities. In the following, we use the subscripts 1 through 8 to denote physical quantities in these eight regions.

We now derive the equations to obtain the seven discontinuities or waves shown in Figure 2.2. The physical quantities in Regions 1 and 8 are given. For each of the other six plasma regions, there are seven unknowns in the MHD formulation. In addition, the propagation speeds of the seven discontinuities are also unknown. Therefore, the Riemann problem contains forty-nine unknowns. On the other hand, there are seven component equations in the RH jump conditions of each discontinuity or expansion wave, and thus there are forty-nine equations in the Riemann problem. Therefore, the Riemann problem can be completely solved.

In the following, we first derive the jump relations for the discontinuities and expansion waves on the left side of the contact discontinuity, and then derive those for the discontinuities and expansion waves on the right side. Finally, the set of equations for solving the Riemann problem are obtained from the jump relations across the contact discontinuity. As shown in the following formulation, the forty-nine equations for the forty-nine unknowns are simplified to a final set of only thirteen coupled equations.

(1) Formulation at the Fast Expansion Wave F:

We now derive equations for the fast expansion wave F. First, we transfer the flow velocity relative to the fast wave to a HT frame with $\mathbf{v}_1 \parallel \mathbf{B}_1$. Let M_{IF} be the intermediate Mach number

Reproduced with permission of the copyright owner. Further reproduction prohibited without permission.

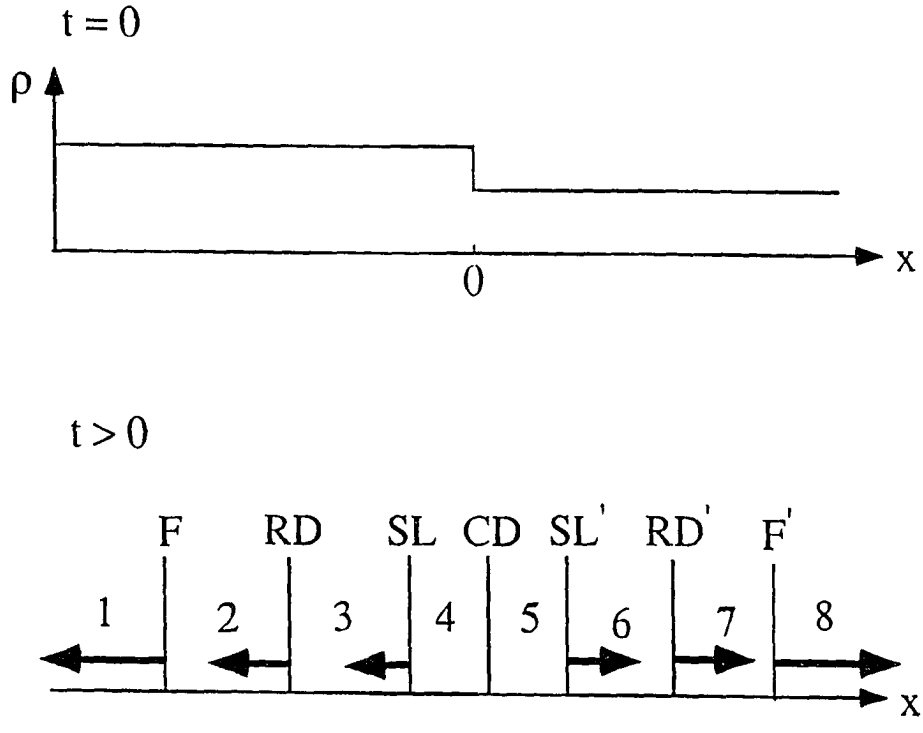

Figure 2.2 An illustration for the Riemann problem. The initial current sheet located at $x = 0$ evolves into seven discontinuities and expansion waves. The fast mode wave F, rotational discontinuity RD, and slow mode wave SL propagate to the left side of the contact discontinuity CD, while F', RD', and SL' propagate to the righthand side.

Reproduced with permission of the copyright owner. Further reproduction prohibited without permission.

of the fast wave. Since $V_{x1} = 0$, the propagation speed of the fast expansion wave, V_F, can be written as

$$V_F = -M_{IF} C_{I1} \tag{2.32}$$

where

$$C_{I1} = B_x / \sqrt{\mu_0 \rho_1} \tag{2.33}$$

is the intermediate mode speed in Region 1. The normal component of flow velocity in Region 1 relative to the fast wave is

$$v_{n1F} = V_{x1} - V_F = -V_F = M_{IF} C_{I1} \tag{2.34}$$

Since $\mathbf{V}_{t1} = 0$, the transformation velocity at the fast expansion wave is then

$$\mathbf{u}^{HTF} = v_{n1F} \mathbf{B}_{t1} / B_x = M_{IF} C_{I1} \mathbf{B}_{t1} / B_x \tag{2.35}$$

Thus in the HT frame, the flow velocity at the fast shock is

$$\mathbf{v}^{HTF} = \mathbf{V} + M_{IF} C_{I1} \mathbf{B}_{t1} / B_x \tag{2.36}$$

At the fast expansion wave, the jump relations are

$$a'_6 R_{\rho F}^{\gamma+3} + a'_5 R_{\rho F}^{\gamma+2} + a'_4 R_{\rho F}^{\gamma+1} + a'_3 R_{\rho F}^{3} + a'_2 R_{\rho F}^{2} + a'_1 R_{\rho F} + a'_0 = 0 \tag{2.37}$$

$$R_{v_n F} = 1 / R_{\rho F} \tag{2.38}$$

$$R_{B_t F} = R_{\rho F} (1 - M_{IF}^2) / (R_{\rho F} - M_{IF}^2) \tag{2.39}$$

$$R_{PF} = R_{\rho F}^{\gamma} \tag{2.40}$$

$$R_{v_t F} = R_{B_t F} / R_{\rho F} \tag{2.41}$$

where $R_{\rho F}$, $R_{v_n F}$, $R_{B_t F}$, R_{PF}, and $R_{v_t F}$ are respectively the ratios of downstream to upstream quantities ρ, v_n, B_t, P, and v_t of the fast wave, and the quantities a'_6 through a'_0 are expressed

Reproduced with permission of the copyright owner. Further reproduction prohibited without permission.

by (2.30) with M_I replaced by M_{IF}. The plasma density, pressure, and strength of tangential magnetic field in Region 2 can be written as

$$\rho_2 = R_{\rho F}\rho_1 \tag{2.42}$$

$$P_2 = R_{PF}P_1 \tag{2.43}$$

$$B_{t2} = R_{B_t F}B_{t1} \tag{2.44}$$

Insert equation (2.39) into (2.44) and equation (2.40) into (2.43). We have

$$B_{t2} = R_{\rho F}(1 - M_{IF}^2)(B_{y1}^2 + B_{z1}^2)^{1/2}/(R_{\rho F} - M_{IF}^2) \tag{2.45}$$

$$P_2 = \beta_1 R_{\rho F}^{\gamma}(B_x^2 + B_{y1}^2 + B_{z1}^2)/2 \tag{2.46}$$

where β_1 is the plasma beta in Region 1. According to the coplanarity of the fast expansion wave, $\mathbf{B_{t2}}/B_{t2} = \mathbf{B_{t1}}/B_{t1}$. It is obtained

$$B_{y2} = R_{B_t F}B_{y1} \tag{2.47}$$

$$B_{z2} = R_{B_t F}B_{z1} \tag{2.48}$$

Let v_{n2F} be the normal flow velocity in Region 2 relative to the fast wave. Since

$$v_{n2F} = R_{v_n F}v_{n1F} \tag{2.49}$$

$$V_{x2} = v_{n2F} + V_F \tag{2.50}$$

where V_{x2} is the x-component flow velocity in Region 2, it is then obtained with the help of equations (2.32), (2.34), and (2.38)

$$V_{x2} = M_{IF}C_{I1}(1 - /R_{\rho F})/R_{\rho F} \tag{2.51}$$

In the HT frame of the fast wave F, the upstream and downstream flow velocities are parallel to

Reproduced with permission of the copyright owner. Further reproduction prohibited without permission.

the magnetic fields. The Region 2 tangential flow velocity in the HT frame can be written as

$$\mathbf{v}_{t2}^{HTF} = R_{v_t F}\mathbf{v}_{t1}^{HTF} \tag{2.52}$$

Since the Region 2 tangential flow velocity $\mathbf{V}_{t2}$ is related to $\mathbf{v}_{t2}^{HTF}$ by

$$\mathbf{V}_{t2} = \mathbf{v}_{t2}^{HTF} - \mathbf{u}^{HTF} \tag{2.53}$$

we obtain from equations (2.52), (2.53), and (2.35)

$$V_{y2} = (R_{v_t F} - 1)M_{IF}C_{I1}B_{y1}/B_x \tag{2.54}$$

$$V_{z2} = (R_{v_t F} - 1)M_{IF}C_{I1}B_{z1}/B_x \tag{2.55}$$

(2) Formulation at the Rotational Discontinuity RD:

Across the rotational discontinuity RD, the plasma density, pressure, and magnetic field strength are conserved, and the variation of flow velocity obeys the Walen relation of the rotational discontinuity. Thus the physical quantities in Region 3 can be written as

$$\rho_3 = \rho_3 \tag{2.56}$$

$$P_3 = P_2 \tag{2.57}$$

$$B_{t3} = B_{t2} \tag{2.58}$$

$$V_{x3} = V_{x2} \tag{2.59}$$

$$V_{y3} = V_{y2} + (B_{y3} - B_{y2})/\sqrt{\mu_0\rho_3} \tag{2.60}$$

$$V_{z3} = V_{z2} + (B_{z3} - B_{z2})/\sqrt{\mu_0\rho_3} \tag{2.61}$$

Since $B_{y3} = B_{t3}sin\Phi_{B3}$ and $B_{z3} = B_{t3}cos\Phi_{B3}$, where Φ_{B3} is the azimuthal angle of the

Reproduced with permission of the copyright owner. Further reproduction prohibited without permission.

tangential magnetic field in Region 3, we have

$$B_{y3} = B_{t2} sin\Phi_{B3} \tag{2.62}$$

$$B_{z3} = B_{t2} cos\Phi_{B3} \tag{2.63}$$

We insert equations (2.44), (2.47), (2.59), (2.56), (2.58), and (2.62) into (2.60) to obtain

$$V_{y3} = (R_{v_t F} - 1) M_{IF} B_{y1} / \sqrt{\mu_0 \rho_1} + R_{B_t F} (B_{t1} sin\Phi_{B3} - B_{y1}) / \sqrt{\mu_o \rho_1 R_{\rho F}} \tag{2.64}$$

Similarly,

$$V_{z3} = (R_{v_t F} - 1) M_{IF} B_{z1} / \sqrt{\mu_0 \rho_1} + R_{B_t F} (B_{t1} cos\Phi_{B3} - B_{z1}) / \sqrt{\mu_o \rho_1 R_{\rho F}} \tag{2.65}$$

(3) Formulation at the Slow Mode SL:

The slow mode SL in Figure 2.2 can be a slow shock (SS) or a slow expansion wave (SE) under different conditions of magnetic field and plasma quantities on the two sides of the initial current sheet. We first derive equations for the slow shock, and then discuss the formulation for the slow expansion wave.

At the slow shock SS,

$$cos^2\theta_{nB3} = B_x^2 / (B_x^2 + B_{t2}^2) \tag{2.66}$$

$$tan^2\theta_{nB3} = B_{t2}^2 / B_x^2 \tag{2.67}$$

$$\beta_3 = 2\mu_0 P_2 / (B_x^2 + B_{t2}^2) \tag{2.68}$$

where θ_{nB3} is the upstream shock normal angle of the slow shock and β_3 is the upstream plasma beta. Note that the jump conditions across the rotational discontinuity RD have been used to

Reproduced with permission of the copyright owner. Further reproduction prohibited without permission.

obtain equations (2.66) -- (2.68). The jump relations at the slow shock can be written as

$$a_3 R_{\rho SL}^3 + a_2 R_{\rho SL}^2 + a_1 R_{\rho SL} + a_0 = 0 \tag{2.69}$$

$$R_{v_n SL} = 1/R_{\rho SL} \tag{2.70}$$

$$R_{B_t SL} = \frac{R_{\rho SL}(1 - M_{ISL}^2)}{R_{\rho SL} - M_{ISL}^2} \tag{2.71}$$

$$R_{PSL} = 1 - \frac{2M_{ISL}^2 cos^2\theta_{nB3}}{\beta_3}[(1/R_{\rho SL} - 1) + \frac{R_{B_t SL}^2}{2M_{ISL}^2} tan^2\theta_{nB3} - \frac{tan^2\theta_{nB3}}{2M_{ISL}^2}] \tag{2.72}$$

$$R_{v_t SL} = R_{B_t SL}/R_{\rho SL} \tag{2.73}$$

where M_{ISL} is the upstream Mach number of the slow shock, $R_{\rho SL}$, $R_{v_n SL}$, $R_{B_t SL}$, R_{PSL}, and $R_{v_t SL}$ are respectively the jumps of plasma density, normal flow speed, magnitude of tangential magnetic field, pressure, and magnitude of tangential flow velocity across the slow shock, and a_0 through a_3 are given by equation (2.18) with the help of equations (2.66) -- (2.68). The plasma density, pressure, and magnetic field in Region 3 can be expressed as

$$\rho_4 = R_{\rho SL}\rho_3 \tag{2.74}$$

$$P_4 = R_{PSL}P_3 \tag{2.75}$$

$$\mathbf{B}_{t4} = R_{B_t SL}\mathbf{B}_{t3} \tag{2.76}$$

Through some algebraic procedures, we then obtain

$$P_4 = \frac{\beta_1}{2}(B_x^2 + B_{y1}^2 + B_{z1}^2)R_{\rho F}^{\gamma}\{1 - \frac{1}{P_2}[\frac{B_x^2 M_{ISL}^2}{R_{\rho SL}}(1 - R_{\rho SL}) + \frac{B_{t2}^2 R_{\rho SL}^2 (1 - M_{ISL}^2)^2}{2(R_{\rho SL} - M_{ISL}^2)^2} - \frac{B_{t2}^2}{2}]\} \tag{2.77}$$

$$B_{t4} = \sqrt{B_{y1}^2 + B_{z1}^2} R_{\rho F} R_{\rho SL}(1 - M_{IF}^2)(1 - M_{ISL}^2)/[(R_{\rho F} - M_{IF}^2)(R_{\rho SL} - M_{ISL}^2)] \tag{2.78}$$

Since the upstream flow speed relative to the slow shock is

$$v_{n3SL} = M_{ISL} C_{I3} \tag{2.79}$$

where $C_{I3} = B_x/\sqrt{\mu_0 \rho_3}$ is the intermediate speed in Region 3, the propagation speed of the

Reproduced with permission of the copyright owner. Further reproduction prohibited without permission.

slow shock, V_{SL}, can be written as

$$V_{SL} = V_{x3} - M_{ISL}B_x/\sqrt{\mu_0\rho_1 R_{\rho F}} \tag{2.80}$$

Since the downstream normal flow speed relative to the slow shock can be expressed by

$$v_{n4SL} = R_{v_n SL} v_{n3SL} \tag{2.81}$$

$$v_{n4SL} = V_{x4} - V_{SL} \tag{2.82}$$

we then obtain

$$V_{x4} = R_{v_n SL} V_{x3} + (1 - R_{v_n SL}) V_{SL} \tag{2.83}$$

With the help of equations (2.51), (2.59), (2.69), and (2.79), we have from equation (2.83)

$$V_{x4} = \frac{B_x M_{IF}}{R_{\rho F}\sqrt{\mu_0\rho_1}}(1 - R_{\rho F}) + \frac{B_x M_{ISL}}{R_{\rho SL}\sqrt{\mu_0\rho_1 R_{\rho F}}}(1 - R_{\rho SL}) \tag{2.84}$$

In HT frame at the slow shock SS, the transformation velocity can be written as

$$\mathbf{u}^{HTSL} = v_{n3SL}\mathbf{B}_{t3}/B_x - \mathbf{V}_{t3} \tag{2.85}$$

The tangential flow velocity upstream of the slow shock in the HT frame is

$$\mathbf{v}_{t3}^{HTSL} = \mathbf{V}_{t3} + \mathbf{u}^{HTSL} \tag{2.86}$$

Downstream of the slow shock, the tangential flow velocity in the HT frame is

$$\mathbf{v}_{t4}^{HTSL} = R_{v_t SL}\mathbf{v}_{t3}^{HTSL} \tag{2.87}$$

Since $\mathbf{V}_{t4} = \mathbf{v}_{t4}^{HTSL} - \mathbf{u}^{HTSL}$, we then obtain

$$\mathbf{V}_{t4} = \mathbf{V}_{t3} + (R_{v_t SL} - 1)\mathbf{u}^{HTSL} \tag{2.88}$$

Through some algebraic procedures we then obtain

Reproduced with permission of the copyright owner. Further reproduction prohibited without permission.

$$V_{y4} = (R_{v_t F} - 1)M_{IF}B_{y1}/\sqrt{\mu_0\rho_1} + R_{B_t F}(\sqrt{B_{y1}^2 + B_{z1}^2}sin\Phi_{B3} - B_{y1})/\sqrt{\mu_0\rho_1 R_{\rho F}}$$

$$+M_{ISL}(R_{v_t SL} - 1)\sqrt{B_{y1}^2 + B_{z1}^2}R_{B_t F}sin\Phi_{B3}/\sqrt{\mu_0\rho_1 R_{\rho F}} \qquad (2.89)$$

$$V_{z4} = (R_{v_t F} - 1)M_{IF}B_{z1}/\sqrt{\mu_0\rho_1} + R_{B_t F}(\sqrt{B_{y1}^2 + B_{z1}^2}cos\Phi_{B3} - B_{z1})/\sqrt{\mu_0\rho_1 R_{\rho F}}$$

$$+M_{ISL}(R_{v_t SL} - 1)\sqrt{B_{y1}^2 + B_{z1}^2}R_{B_t F}cos\Phi_{B3}/\sqrt{\mu_0\rho_1 R_{\rho F}} \qquad (2.90)$$

Note that $\Phi_{B4} = \Phi_{B3}$ according to the coplanarity condition across the slow shock.

If the slow mode structure SL is a slow expansion wave, the magnetic field and flow velocity in Region 4 can still be expressed by equations (2.78), (2.84), (2.89), and (2.90), except that $R_{\rho SL}$ satisfies

$$a_6' R_{\rho SL}^{\gamma+3} + a_5' R_{\rho SL}^{\gamma+2} + a_4' R_{\rho SL}^{\gamma+1} + a_3' R_{\rho SL}^3 + a_2' R_{\rho SL}^2 + a_1' R_{\rho SL} + a_0' = 0 \qquad (2.91)$$

where a_6' -- a_0' are expressed by equations (2.31) for the Region 3 quantities M_{ISL}, θ_{nB3}, and β_3. The plasma pressure in Region 4 can be written as

$$P_4 = \beta_1(B_x^2 + B_{y1}^2 + B_{z1}^2)(R_{\rho F}R_{\rho SL})^\gamma/2 \qquad (2.92)$$

(4) Formulation from F', RD', and SL':

We now write down equations obtained from the jump relations across the discontinuities and expansion waves on the right side of the contact discontinuity CD, which are shown in Figure 2.2. The procedure is similar to that for the discontinuities and expansion waves on the left side. We only write down the simplified equations for physical quantities in Region 5 which is adjacent to the central contact discontinuity CD.

Reproduced with permission of the copyright owner. Further reproduction prohibited without permission.

The strength of tangential magnetic field and plasma pressure in Region 5 can be written as

$$B_{t5} = \sqrt{B_{y8}^2 + B_{z8}^2} R_{\rho F'} R_{\rho SL'} (1 - M_{IF'}^2)(1 - M_{ISL'}^2) / [(R_{\rho F'} - M_{IF'}^2)(R_{\rho SL'} - M_{ISL'}^2)] \tag{2.93}$$

$$P_5 = \frac{\beta_8}{2}(B_x^2 + B_{y8}^2 + B_{z8}^2) R_{\rho F'}^{\gamma} \{1 - \frac{1}{P_7}[\frac{B_x^2 M_{ISL'}^2}{R_{\rho SL'}}(1 - R_{\rho SL'}) + \frac{B_{t7}^2 R_{\rho SL'}^2 (1 - M_{ISL'}^2)^2}{2(R_{\rho SL'} - M_{ISL'}^2)^2} - \frac{B_{t7}^2}{2}]\} \tag{2.94}$$

where the quantities B_{t7} and P_7 of Region 7 satisfy

$$B_{t7} = R_{\rho F'}(1 - M_{IF'}^2)(B_{y8}^2 + B_{z8}^2)^{1/2} / (R_{\rho F'} - M_{IF'}^2) \tag{2.95}$$

$$P_7 = beta_8 R_{\rho F'}^{\gamma} (B_x^2 + B_{y8}^2 + B_{z8}^2)/2 \tag{2.96}$$

and the density ratios at the fast expansion wave ($R_{\rho F'}$) and the slow shock $R_{\rho SL'}$ satisfy

$$a_6' R_{\rho F'}^{\gamma+3} + a_5' R_{\rho F'}^{\gamma+2} + a_4' R_{\rho F'}^{\gamma+1} + a_3' R_{\rho F'}^3 + a_2' R_{\rho F'}^2 + a_1' R_{\rho F'} + a_0' = 0 \tag{2.97}$$

$$a_3 R_{\rho SL'}^3 + a_2 R_{\rho SL'}^2 + a_1 R_{\rho SL'} + a_0 = 0 \tag{2.98}$$

where a_6' -- a_0' are a function of the upstream intermediate Mach number $M_{IF'}$ at the fast wave F' and a_3 -- a_0 are a function of the upstream intermediate Mach number $M_{ISL'}$ at the slow shock SL'.

Let Φ_{B6} be the azimuthal angle of tangential magnetic field in Region 6. The components of flow velocity in Region 5 can be written as

$$V_{x5} = -\frac{B_x M_{IF'}}{R_{\rho F'}\sqrt{\mu_0 \rho_8}}(1 - R_{\rho F'}) - \frac{B_x M_{ISL'}}{R_{\rho SL'}\sqrt{\mu_0 \rho_8 R_{\rho F'}}}(1 - R_{\rho SL'}) \tag{2.99}$$

$$V_{y5} = (1 - R_{v_t F'}) M_{IF'} B_{y8} / \sqrt{\mu_0 \rho_8} - R_{B_t F'} (\sqrt{B_{y8}^2 + B_{z8}^2} sin\Phi_{B6} - B_{y8}) / \sqrt{\mu_0 \rho_8 R_{\rho F'}} - M_{ISL'}(R_{v_t SL'} - 1)\sqrt{B_{y8}^2 + B_{z8}^2} R_{B_t F'} sin\Phi_{B6} / \sqrt{\mu_0 \rho_8 R_{\rho F'}} \tag{2.100}$$

$$V_{z5} = (1 - R_{v_t F'}) M_{IF'} B_{z8} / \sqrt{\mu_0 \rho_8} - R_{B_t F'} (\sqrt{B_{y8}^2 + B_{z8}^2} cos\Phi_{B6} - B_{z8}) / \sqrt{\mu_0 \rho_8 R_{\rho F'}} - M_{ISL'}(R_{v_t SL'} - 1)\sqrt{B_{y8}^2 + B_{z8}^2} R_{B_t F'} cos\Phi_{B6} / \sqrt{\mu_0 \rho_8 R_{\rho F'}} \tag{2.101}$$

(5) Final Equations for Solving the Riemann Problem:

Reproduced with permission of the copyright owner. Further reproduction prohibited without permission.

We now derive the final set of equations for solving the Riemann problem. For quantities on the left side of CD, we can use nine equations (2.78), (2.77), (2.84), (2.89), (2.90), (2.37), (2.69), (2.47), and (2.48) to express twelve unknowns B_{t4}, P_4, V_{x4}, V_{y4}, V_{z4}, Φ_{B3}, P_2, B_{t2}, $R_{\rho F}$, $R_{\rho SL}$, M_{IF}, and M_{ISL}. Other physical quantities can be obtained from these twelve unknowns. Similarly for quantities on the right of the contact discontinuity CD, we can also use nine equations (2.93) -- (2.101) to express twelve unknowns. Therefore, at this stage, we have eighteen equations for twenty-four unknowns.

The magnetic field and plasma quantities in Region 4 are related to those in Region 5 by using the jump conditions at the contact discontinuity CD. The jump relations across the contact discontinuity CD are

$$B_{t4} = B_{t5} \tag{2.102}$$

$$\Phi_{B3} = \Phi_{B6} \tag{2.103}$$

$$P_4 = P_5 \tag{2.104}$$

$$V_{x4} = V_{x5} \tag{2.105}$$

$$V_{y4} = V_{y5} \tag{2.106}$$

$$V_{z4} = V_{z5} \tag{2.107}$$

With the help of these six equations, we now have twenty-four equations for the twenty-four unknowns. Through algebraic manipulations, we can further simplify these twenty-four equations to thirteen equations which contains thirteen unknowns.

Let the physical quantities be normalized to the quantities in Region 8, with $\rho^* \equiv \rho/\rho_8$, $\mathbf{B}^* \equiv \mathbf{B}/B_{z8}$, $P^* \equiv P/(B_8^2/\mu_0)$, and $\mathbf{V}^* \equiv \mathbf{V}/V_{Az8}$, where $V_{Az8} = B_{z8}/\sqrt{\mu_0\rho_8}$ is the z component of Alfven velocity in Region 8. Define the thirteen variables $w_1 \equiv M_{IF}$, $w_2 \equiv R_{\rho F}$, $w_3 \equiv B^*_{t2}$, $w_4 \equiv P^*_2$, $w_5 \equiv R_{\rho SL}$, $w_6 \equiv M_{ISL}$, $w_7 \equiv \Phi_{B3}$, $w_8 \equiv M_{IF'}$, $w_9 \equiv R_{\rho F'}$, $w_{10} \equiv B^*_{t7}$, $w_{11} \equiv P^*_7$, $w_{12} \equiv R_{\rho SL'}$, and $w_{13} \equiv M_{ISL'}$. By using equations (2.102) --

Reproduced with permission of the copyright owner. Further reproduction prohibited without permission.

(2.107) to relate the physical quantities in Region 4 and Region 5, which have been discussed earlier, we obtain the following final set of equations for variables w_1 -- w_{13}

$$\frac{\beta_1}{2w_1^2cos^2\theta_{nB1}}w_2^{\gamma+3}-\frac{\beta_1}{cos^2\theta_{nB1}}w_2^{\gamma+2}+\frac{\beta_1 w_1^2}{2cos^2\theta_{nB1}}w_2^{\gamma+1}+(-\frac{1}{cos^2\theta_{nB1}}-\frac{\beta_1}{2w_1^2cos^2\theta_{nB1}}$$

$$+\frac{1}{2}w^2tan^2\theta_{nB1})w_2^3+(1+2w_1^2+\frac{\beta_1}{cos^2\theta_{nB1}}+tan^2\theta^2\theta_{nB1})w_2^2-(w_1^4+2w_1^2+$$

$$\frac{\beta_1}{2\cos^2\theta_{nB1}}w_1^2+\frac{1}{2}w_1^2tan^2\theta_{nB1})w_2+w_1^4=0 \qquad (2.108a)$$

$$w_3-w_2(1-w_1^2)\sqrt{B_{z1}^{*2}+B_{y1}^{*2}}/(w_2-w_1^2)=0 \qquad (2.108b)$$

$$w_4-\frac{1}{2}\beta_1 w_2^{\gamma}(B_{z1}^{*2}+B_{y1}^{*2}+B_x^{*2})=0 \qquad (2.108c)$$

$$\frac{w_4}{w_6^2}w_5^{\gamma+3}-2w_4w_5^{\gamma+2}+w_4w_6^2w_5^{\gamma+1}+(-w_3^2-B_x^{*2}-\frac{w_4}{w_6^2}+\frac{1}{2}w_3^2w_6^2)w_5^3+[B_x^{*2}(1+2w_6^2)$$

$$+2w_4+w_3^2]w_5^2-[B_x^{*2}(w_6^4+2w_6^2)+w_4w_6^2+\frac{1}{2}w_3^2w_6^2]w_5+B_x^{*2}w_6^4=0 \qquad (2.108d)$$

$$\frac{\beta_8}{2w_8^2cos^2\theta_{nB8}}w_9^{\gamma+3}-\frac{\beta_8}{cos^2\theta_{nB8}}w_9^{\gamma+2}+\frac{\beta_8 w_8^2}{2cos^2\theta_{nB8}}w_9^{\gamma+1}+(-\frac{1}{cos^2\theta_{nB8}}-\frac{\beta_8}{2w_8^2cos^2\theta_{nB8}}$$

$$+\frac{1}{2}w_9^2tan^2\theta_{nB8})w_9^3+(1+2w_8^2$$

$$+\frac{\beta_8}{cos^2\theta_{nB8}}+tan^2\theta_{nB8})w_9^2-(w_8^4+2w_8^2+\frac{\beta_8}{2\cos^2\theta_{nB8}}w_8^2+\frac{1}{2}w_8^2tan^2\theta_{nB8})w_9+w_8^4=0 \qquad (2.108e)$$

$$w_{10}-w_9(1-w_8^2)\sqrt{B_{z8}^{*2}+B_{y8}^{*2}}/(w_9-w_8^2)=0 \qquad (2.108f)$$

$$w_{11}-\frac{1}{2}\beta_8 w_9^{\gamma}(B_{z8}^{*2}+B_{y8}^{*2}+B_x^{*2})=0 \qquad (2.108g)$$

$$\frac{w_{11}}{w_{13}^2}w_{12}^{\gamma+3}-2w_{11}w_{12}^{\gamma+2}+w_{11}w_{13}^2w_{12}^{\gamma+1}+(-w_{10}^2-B_x^{*2}-\frac{w_{11}}{w_{13}^2}+\frac{1}{2}w_{10}^2w_{13}^2)w_{12}^3+[B_x^{*2}(1+2w_{13}^2)$$

$$+2w_{11}+w_{10}^2]w_{12}^2-[B_x^{*2}(w_{13}^4+2w_{13}^2)+w_{11}w_{13}^2+\frac{1}{2}w_{10}^2w_{13}^2]w_{12}+B_x^{*2}w_{13}^4=0 \qquad (2.108h)$$

$$\frac{1}{w_2w_5\sqrt{\rho_1^*}}[w_5w_1(1-w_2)+w_6\sqrt{w_2}(1-w_5)]+\frac{1}{w_9w_{12}\sqrt{\rho_8^*}}[w_8w_{12}(1-w_9)$$

$$+w_{13}\sqrt{w_9}(1-w_{12})]=0 \qquad (2.108i)$$

Reproduced with permission of the copyright owner. Further reproduction prohibited without permission.

$$\frac{1}{(w_2-w_1^2)\sqrt{\rho_1^*}}[B_{y1}^* w_1(1-w_2)+\sqrt{w_2}(1-w_1^2)(sinw_7\sqrt{B_{y1}^{*2}+B_{z1}^{*2}}-B_{y1}^*)$$
$$+w_6\sqrt{w_2}\sqrt{B_{y1}^{*2}+B_{z1}^{*2}}(1-w_1^2)\frac{(1-w_5)}{(w_5-w_6^2)}sinw_7]$$
$$+\frac{1}{(w_9-w_8^2)\sqrt{\rho_8^*}}[B_{y8}^* w_8(1-w_9)+\sqrt{w_9}(1-w_8^2)(sinw_7\sqrt{B_{y8}^{*2}+B_{z8}^{*2}}-B_{y8}^*)$$
$$+w_{13}\sqrt{w_9}\sqrt{B_{y8}^{*2}+B_{z8}^{*2}}(1-w_8^2)\frac{(1-w_{12})}{(w_{12}-w_{13}^2)}sinw_7]=0 \qquad (2.108j)$$

$$\frac{1}{(w_2-w_1^2)\sqrt{\rho_1^*}}[B_{z1}^* w_1(1-w_2)+\sqrt{w_2}(1-w_1^2)(cosw_7\sqrt{B_{y1}^{*2}+B_{z1}^{*2}}-B_{z1}^*)$$
$$+w_6\sqrt{w_2}\sqrt{B_{y1}^{*2}+B_{z1}^{*2}}(1-w_1^2)\frac{(1-w_5)}{(w_5-w_6^2)}cosw_7]$$
$$+\frac{1}{(w_9-w_8^2)\sqrt{\rho_8^*}}[B_{z8}^* w_8(1-w_9)+\sqrt{w_9}(1-w_8^2)(cosw_7\sqrt{B_{y8}^{*2}+B_{z8}^{*2}}-B_{z8}^*)$$
$$+w_{13}\sqrt{w_9}\sqrt{B_{y8}^{*2}+B_{z8}^{*2}}(1-w_8^2)\frac{(1-w_{12})}{(w_{12}-w_{13}^2)}cosw_7]=0 \qquad (2.108k)$$

$$\sqrt{B_{y1}^{*2}+B_{z1}^{*2}}\frac{w_2w_5(1-w_1^2)(1-w_6^2)}{(w_2-w_1^2)(w_5-w_6^2)}-\sqrt{B_{y8}^{*2}+B_{z8}^{*2}}\frac{w_9w_{12}(1-w_8^2)(1-w_{13}^2)}{(w_9-w_8^2)(w_{12}-w_{13}^2)}=0 \qquad (2.108l)$$

$$\beta_1(B_{z1}^{*2}+B_{y1}^{*2}+B_x^{*2})w_2^\gamma\{1-\frac{1}{w_4}[\frac{B_x^{*2}w_6^2}{w_5}(1-w_5)+\frac{w_3^2w_5^2(1-w_6^2)^2}{2(w_5-w_6^2)^2}-\frac{w_3^2}{2}]\}$$
$$-\beta_8(B_{z8}^{*2}+B_{y8}^{*2}+B_x^{*2})w_9^\gamma\{1-\frac{1}{w_{11}}[\frac{B_x^{*2}w_{13}^2}{w_{12}}(1-w_{12})+\frac{w_{10}^2w_{12}^2(1-w_{13}^2)^2}{2(w_{12}-w_{13}^2)^2}-\frac{w_{10}^2}{2}]\}=0 \qquad (2.108m)$$

Note that (2.108m) is obtained when one assumes that the slow mode on both sides of the contact discontinuity are slow shocks, and it will be replaced by an adequate equation if slow expansion waves are needed in the solution. For example, if the slow mode SL is a slow expansion wave and the slow mode SL' is a slow shock, (2.108m) should be replaced by

$$\beta_1(B_{z1}^{*2}+B_{y1}^{*2}+B_x^{*2})(w_2w_5)^\gamma-\beta_8(B_{z8}^{*2}+B_{y8}^{*2}+B_x^{*2})w_9^\gamma\{1$$
$$-\frac{1}{w_{11}}[\frac{B_x^{*2}w_{13}^2}{w_{12}}(1-w_{12})+\frac{w_{10}^2w_{12}^2(1-w_{13}^2)^2}{2(w_{12}-w_{13}^2)^2}-\frac{w_{10}^2}{2}]\}=0 \qquad (2.109)$$

The physical quantities in the eight regions in Figure 2.2 can be obtained by solving equations in (2.108) for thirteen unknowns w_1 through w_{13}. The set of final equations can be completely

Reproduced with permission of the copyright owner. Further reproduction prohibited without permission.

solved by using a FORTRAN subroutine in IMSL libraries, which solves the non-linear equations by using modified Powell hybrid algorithm and a finite-difference approximation to the Jacobian.

2.4 Structure of the Reconnection Layer in Cases with $B_y = 0$

In the following we solve the Riemann problem for cases with $B_y = 0$. The total pressure balance condition, $(P + B^2/2\mu_0) = const$, is used across the initial current sheet. For the dayside magnetopause, we assume that an initial current sheet exists at $x = 0$, as shown in Figure 2.2, the magnetosheath is in the region with $x < 0$, and the magnetosphere is in the region with $x > 0$. The antiparallel magnetic field components are in the z direction. Cases with $B_s < B_m$ and $\rho_s > \rho_m$ are studied. It is found that in general, rotational discontinuities, slow shocks, slow expansion waves, and contact discontinuity may be present in the dayside reconnection layer. The slow mode on the magnetospheric side of the resulting reconnection layer is a slow shock, and the slow mode on the magnetosheath side may be a slow shock or a slow expansion wave. For the nightside plasma sheet, we assume equal plasma densities and equal magnetic field strengths on the two sides of an initial current sheet.

The structure of the reconnection layers in the magnetosphere is determined by solving equations (2.108) and (2.109). In our calculations, $B_x > 0$ and $B_{zm} > 0$ are used. We present three cases with different symmetry properties as listed in Table 2.1, which also summarizes the results obtained in this chapter.

2.4.1 Symmetric Case with $B_y = 0$

We first present a case with equal plasma densities and exactly antiparallel magnetic fields on the two sides of the initial current sheet. In this case, $\rho_1 = \rho_8$, $B_{z1} = -B_{z8}$, and $B_{y1} = B_{y1} = 0$. Therefore $\rho_1^* = \rho_8^* = 1$, $B_{z1}^* = -B_{z8}^* = -1$, and $B_{y1}^* = B_{y8}^* = 0$. We

Reproduced with permission of the copyright owner. Further reproduction prohibited without permission.

Table 2.1 Structure of Reconnection Layer

Symmetry Property \ B_y	$B_y = 0$	$B_y \neq 0$
Symmetric	SS+SS'	RD+SS+SS'+RD'
Weakly Asymmetric	RD+SS+CD+SS'	RD+SS+CD+SS'+RD'
Highly Asymmetric	RD+SE+CD+SS'	RD+SE+CD+SS'+RD'

Note: (1) RD: Rotational Discontinuity

SS: Slow Shock

SE: Slow Expansion Wave

CD: Contact Discontinuity

(2) In addition, two fast expansion waves are also present, but they quickly propagate out of the reconnection layer.

Table 2.1 Structure of reconnection layer.

Reproduced with permission of the copyright owner. Further reproduction prohibited without permission.

have also chosen $\beta_1 = 0.2$ and $B_x^* = 0.25$. This symmetric case can be applied to the tail plasma sheet.

According to equation (2.1), the resulting discontinuities are symmetric on the two sides of the initial current sheet. Thus we have $w_8 = w_1, w_9 = w_2, w_{10} = w_3, w_{11} = w_4, w_{12} = w_5$, and $w_{13} = w_6$. From (2.108j) and (2.108k), we obtain

$$[\frac{\sqrt{w_2}(1-w_1^2)}{(w_2-w_1^2)} + w_6\sqrt{w_2}\frac{(1-w_1^2)}{(w_2-w_1^2)}\frac{(1-w_5)}{(w_5-w_6^2)}]sinw_7 = 0 \qquad (2.110)$$

$$[\frac{\sqrt{w_2}(1-w_1^2)}{(w_2-w_1^2)} + w_6\sqrt{w_2}\frac{(1-w_1^2)}{(w_2-w_1^2)}\frac{(1-w_5)}{(w_5-w_6^2)}]cosw_7 = 0 \qquad (2.111)$$

Combining these two equations we have

$$\frac{\sqrt{w_2}(1-w_1^2)}{(w_2-w_1^2)} + w_6\sqrt{w_2}\frac{(1-w_1^2)}{(w_2-w_1^2)}\frac{(1-w_5)}{(w_5-w_6^2)} = 0 \qquad (2.112)$$

Since the azimuthal angle w_7 of tangential magnetic field upstream of the slow mode is not present in other equations of (2.108), multiple solutions with various values of x_7 can be obtained. Therefore, we cannot obtain unique a solution for this special case by using equations (2.108).

The symmetric case with $B_y = 0$ is a singular case in which the rotational discontinuity does not exist. Since $B_y = 0$ and $V_y = 0$ and the configuration is symmetric, there are only four discontinuities in the result. Because of the symmetry in plasma density and magnetic field, the contact discontinuity does not exist and the components B_z and V_x are equal to zero at the center of the resulting reconnection layer. The slow modes are two slow shocks. The discontinuities in the resulting reconnection layer are (F, SS, SS', F'). For such a symmetric configuration, we only calculate the physical quantities for the discontinuities F and SS by using the conditions $B_z = 0$ and $V_x = 0$ at the center of the reconnection layer. The discontinuities on the righthand side can be determined from the result on the lefthand side. Since $B_t = 0$ downstream of the slow shock, it is obtained that $M_{ISL} = 1$ at the slow shock. Therefore the slow shocks are two switch-off shocks.

Reproduced with permission of the copyright owner. Further reproduction prohibited without permission.

The result of the Riemann problem is obtained as

$$(\rho_3^*, P_3^*, B_{y3}^*, B_{z3}^*, V_{x3}^*, V_{y3}^*, V_{z3}^*) = (0.883, 0.0864, 0, -0.877, 0.134, 0, 0.031)$$

$$(\rho_4^*, P_4^*, B_{y4}^*, B_{z4}^*, V_{x4}^*, V_{y4}^*, V_{z4}^*) = (1.777, 0.502, 0, 0, 0, 0, 0.964)$$

The fast expansion wave is weak with a downstream to upstream density ratio ~ 0.883. At the slow shock, $\theta_{nB2} = 74.1^o$ and $\beta_2 = 0.208$. The propagation speed of the slow shock is $V_{SL}^* = -0.132$. The left column of Figure 2.3 shows the spatial profiles of B_z, ρ, P, and V_x in the ideal MHD solution. The fast expansion waves F and F', across which the plasma density and magnetic field strength decrease by $\sim 12\%$, are not shown because they quickly propagate out of the reconnection layer. Across the slow shock, the density increases to 2.012 times of the upstream value, the downstream to upstream ratio of plasma pressure is 5.810, and the tangential magnetic field decreases to zero. The velocity component V_z increases to the tangential Alfven speed downstream of the slow shock. The positions of the slow shocks are plotted in the column figure of Figure 2.3 as a function of the time t. In the figure, the x coordinate is normalized to a scale length x_0, and the time t is normalized to $t_0 \equiv x_0/V_{Az8}$.

In Chapter 3, we will show that for this symmetric case with $B_y = 0$, the result obtained from the resistive MHD formulation is the same as the ideal MHD solution shown above.

2.4.2 Weakly Asymmetric Case with $B_y = 0$

For cases in which the guide fields B_{ys} and B_{ym} equal zero and the magnetic field and plasma quantities in the magnetosheath and magnetosphere are asymmetric, equations (2.108j) and

Reproduced with permission of the copyright owner. Further reproduction prohibited without permission.

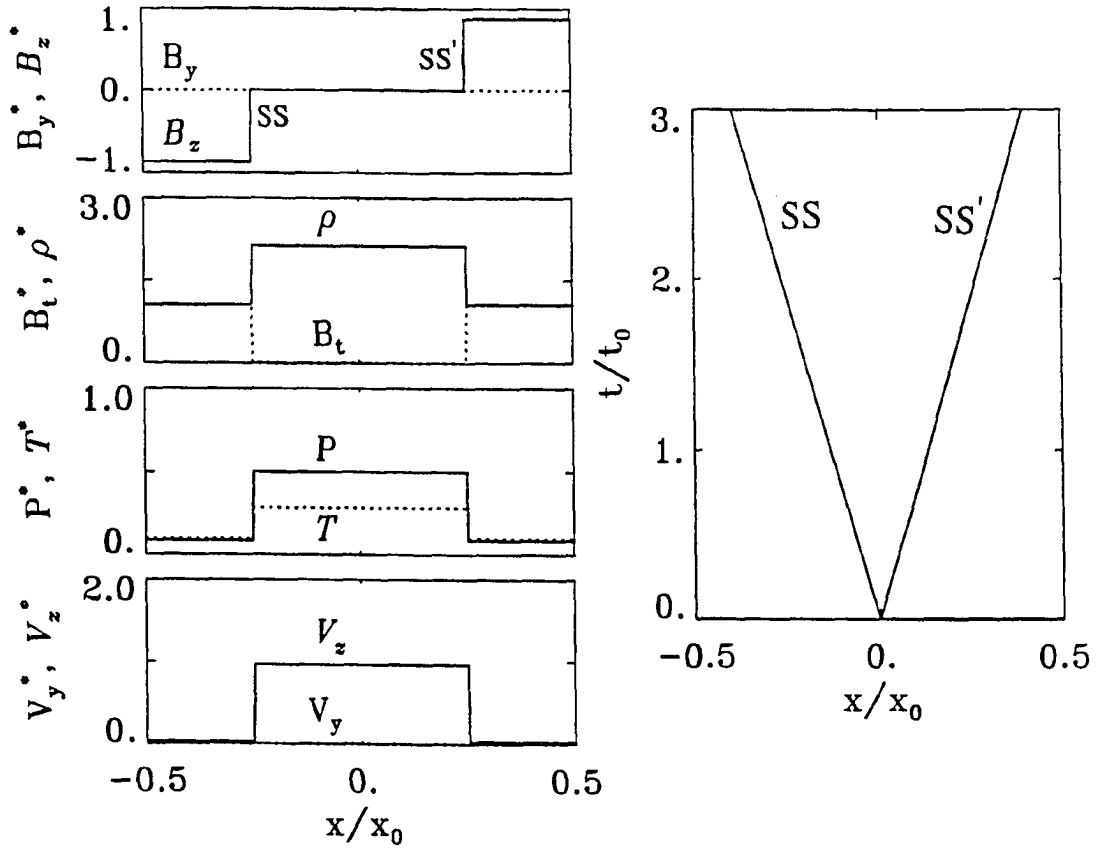

Figure 2.3 Structure of the reconnection layer in symmetric case with $B_y = 0$. The left column show spatial profiles of the normalized tangential magnetic field components (B_y^* and B_z^*), tangential magnetic field strength B_t^*, plasma density ρ^*, pressure P^*, temperature T^*, and components of tangential flow velocity (V_y^* and V_z^*), respectively. The right plot shows positions of the slow shocks as a function of time t.

Reproduced with permission of the copyright owner. Further reproduction prohibited without permission.

(2.108k) become

$$[\frac{\sqrt{w_2}(1-w_1^2)}{\sqrt{\rho_1^*}(w_2-w_1^2)}|B_{z1}^*| + w_6\sqrt{w_2}\frac{(1-w_1^2)(1-w_5)}{\sqrt{\rho_1^*}(w_5-w_6^2)(w_2-w_1^2)}|B_{z1}^*|$$

$$+\frac{\sqrt{w_9}(1-w_8^2)}{\sqrt{\rho_8^*}(w_9-w_8^2)}|B_{z8}^*| + w_{13}\sqrt{w_9}\frac{(1-w_8^2)(1-w_12)}{\sqrt{\rho_8^*}(w_9-w_8^2)(w_{12}-w_{13}^2)}|B_{z8}^*|]sinw_7 = 0 \tag{2.113}$$

$$\frac{1}{\sqrt{\rho_1^*}(w_2-w_1^2)}[B_{z1}^* w_1(1-w_2) + \sqrt{w_2}(1-w_1^2)(|B_{z1}^*|cosw_7 - B_{z1}^*)$$

$$+w_6\sqrt{w_2}(1-w_1^2)\frac{(1-w_5)}{(w_5-w_6^2)}|B_{z1}^*|cosw_7]$$

$$+\frac{1}{\sqrt{\rho_8^*}(w_9-w_8^2)}[B_{z8}^* w_8(1-w_9) + \sqrt{w_9}(1-w_8^2)(|B_{z8}^*|cosw_7 - B_{z8}^*)$$

$$+w_{13}\sqrt{w_9}(1-w_8^2)\frac{(1-w_{12})}{(w_{12}-w_{13}^2)}|B_{z8}^*|cosw_7] = 0 \tag{2.114}$$

From our numerical solutions, we find $w_7 = 0^o$. Note that w_7 is the rotation angle of tangential magnetic field across the rotational discontinuity RD', and the rotational angle of tangential magnetic field across RD is $(180^o - w_7)$. Therefore in this case, the tangential magnetic field rotates 180^o across the discontinuity RD and rotates 0^o across RD'. Thus the rotational discontinuity RD' does not exist. On the dayside, the rotational discontinuity RD on the magnetosheath side of the reconnection layer is usually identified as the magnetopause.

We now show the result of a case with $\beta_m = 0.2$, $B_{zs} = -B_{zm}$, $B_x = 0.25B_{zm}$, and $\rho_s = 2\rho_m$. Note that $\beta_s = 0.2$ in this case. The given quantities in Region 1 and Region 8, as indicated in Figure 2.2, are

$$(\rho_1^*, P_1^*, B_{y1}^*, B_{z1}^*, V_{x1}^*, V_{y1}^*, V_{z1}^*) = (2, 0.10625, 0, -1, 0, 0, 0)$$

$$(\rho_8^*, P_8^*, B_{y8}^*, B_{z8}^*, V_{x8}^*, V_{y8}^*, V_{z8}^*) = (1, 0.106, 0, 1, 0, 0, 0)$$

The obtained discontinuities in the layer are (F, RD, SS, CD, SS', F'). The obtained magnetic

Reproduced with permission of the copyright owner. Further reproduction prohibited without permission.

field and plasma quantities in Regions 2 through 6 are

$$(\rho_2^*, P_2^*, B_{y2}^*, B_{z2}^*, V_{x2}^*, V_{y2}^*, V_{z2}^*) = (1.534, 0.0684, 0, -0.753, 0.197, 0, 0.0477)$$

$$(\rho_3^*, P_3^*, B_{y3}^*, B_{z3}^*, V_{x3}^*, V_{y3}^*, V_{z3}^*) = (1.534, 0.0684, 0, 0.753, 0.197, 0, 1.264)$$

$$(\rho_4^*, P_4^*, B_{y4}^*, B_{z4}^*, V_{x4}^*, V_{y4}^*, V_{z4}^*) = (3.251, 0.347, 0, 0.248, 0.102, 0, 0.807)$$

$$(\rho_5^*, P_5^*, B_{y5}^*, B_{z5}^*, V_{x5}^*, V_{y5}^*, V_{z5}^*) = (1.821, 0.347, 0, 0.248, 0.102, 0, 0.807)$$

$$(\rho_6^*, P_6^*, B_{y6}^*, B_{z6}^*, V_{x6}^*, V_{y6}^*, V_{z6}^*) = (0.999, 0.106, 0, 0.706, -0.000251, 0, 0.334)$$

At the slow shock SS, $M_{ISL} = 0.892$, and at the slow shock SS', $M_{ISL'} = 0.897$. The propagation speeds of the discontinuities in resulting reconnection layer are $V_R^* = -0.005$, $V_{SL}^* = 0.017$, $V_C^* = 0.102$ for the contact discontinuity, and $V_{SL}'^* = 0.225$. Figure 2.4 shows the solution of this case with the same format as in Figure 2.3. At the rotational discontinuity RD, B_z component changes sign but conserves magnitude. Across the slow shocks SS and SS' from upstream to downstream, the plasma density increases and magnetic field decreases. The density ratio at the slow shock SS is $R_{\rho SL} = 2.119$, and that at the slow shock SS' is $R_{\rho SL'} = 1.826$.

2.4.3 *Highly Asymmetric Case with* $B_y = 0$

Figure 2.5 shows a large asymmetric case for the dayside reconnection with $\beta_m = 0.08$, $B_x = 0.05B_{zm}$, $B_{zs} = -0.5B_{zm}$, and $\rho_s = 10\rho_m$. In this case, $\beta_s = 3.32$. We have parameters on the two sides of the initial current sheet as

$$(\rho_1^*, P_1^*, B_{y1}^*, B_{z1}^*, V_{x1}^*, V_{y1}^*, V_{z1}^*) = (10, 0.419, 0, -0.5, 0, 0, 0)$$

$$(\rho_8^*, P_8^*, B_{y8}^*, B_{z8}^*, V_{x8}^*, V_{y8}^*, V_{z8}^*) = (1, 0.0401, 0, 1, 0, 0, 0)$$

It is found that the slow shocks SS in weakly asymmetric case is replaced by a slow expansion wave SE. The resulting discontinuities for the Riemann problem are (F, RD, SE, CD, SS', F').

Reproduced with permission of the copyright owner. Further reproduction prohibited without permission.

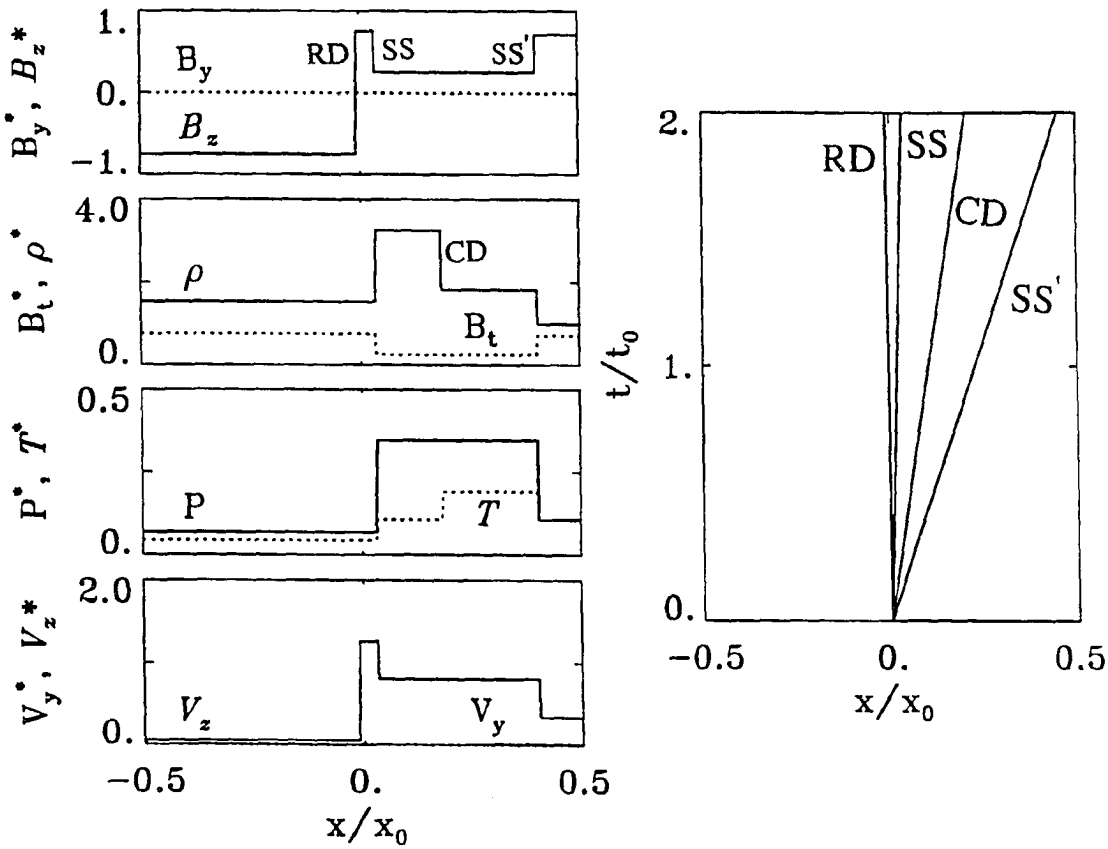

Figure 2.4 Same as Figure 2.3 with $B_y = 0$, except for a case with a small asymmetry in plasma density.

Reproduced with permission of the copyright owner. Further reproduction prohibited without permission.

The magnetic field and plasma quantities in the solution are

$$(\rho_2^*, P_2^*, B_{y2}^*, B_{z2}^*, V_{x2}^*, V_{y2}^*, V_{z2}^*) = (9.58, 0.386, 0, -0.479, 0.0131, 0, 0.0004)$$

$$(\rho_3^*, P_3^*, B_{y3}^*, B_{z3}^*, V_{x3}^*, V_{y3}^*, V_{z3}^*) = (9.58, 0.386, 0, 0.479, 0.0131, 0, 0.310)$$

$$(\rho_4^*, P_4^*, B_{y4}^*, B_{z4}^*, V_{x4}^*, V_{y4}^*, V_{z4}^*) = (7.070, 0.233, 0, 0.733, 0.0171, 0, 0.427)$$

$$(\rho_5^*, P_5^*, B_{y5}^*, B_{z5}^*, V_{x5}^*, V_{y5}^*, V_{z5}^*) = (2.381, 0.233, 0, 0.733, 0.0171, 0, 0.427)$$

$$(\rho_6^*, P_6^*, B_{y6}^*, B_{z6}^*, V_{x6}^*, V_{y6}^*, V_{z6}^*) = (1.000, 0.0401, 0, 0.959, 0.0000, 0, 0.0000)$$

At the slow expansion wave SE, $M_{ISL} = 0.703$. At the slow shock SS', $M_{ISL'} = 0.591$. The propagation speeds of the discontinuities are $V_R^* = -0.003$, $V_{SL}^* = 0.002$, $V_C^* = 0.0171$, and $V_{SL'}^* = 0.03$. As shown in Figure 2.5, the plasma density decreases across the slow expansion wave SE, and the density ratio is $R_{\rho SL} = 0.738$. For the case with $\rho_s/\rho_m \to \infty$, the discontinuities SS' and CD become insignificant, and the reconnection layer consists of only the rotational discontinuity RD and the slow expansion wave SE as predicted in Levy et al.' model [1964].

2.4.4 Parameter Search

In order to see the variation of reconnection layer structure with the change of asymmetry in magnetic field and plasma quantities, we calculate the density jump $R_{\rho SL}$ across the slow mode SL and $R_{\rho SL'}$ across SL' as a function of ρ_s/ρ_m, as shown in Figure 2.6. The parameters used are $\beta_m = 0.1$, $B_x = 0.1B_{zm}$, and $B_{ym} = B_{ys} = 0$. In this calculation, we assume $(T_s/T_m) = (\rho_s/\rho_m)^{1/2}$ for simplicity by noting that $T_m > T_s$ and $\rho_m < \rho_s$ at the dayside magnetopause. Since the total pressure balance are used across the initial current layer, the ratio B_s/B_m decreases as ρ_s/ρ_m increases. It is seen from Figure 2.6 at $\rho_s/\rho_m = 1$, which corresponds to the symmetric case with $B_y = 0$, the two identical slow shocks have the same

Reproduced with permission of the copyright owner. Further reproduction prohibited without permission.

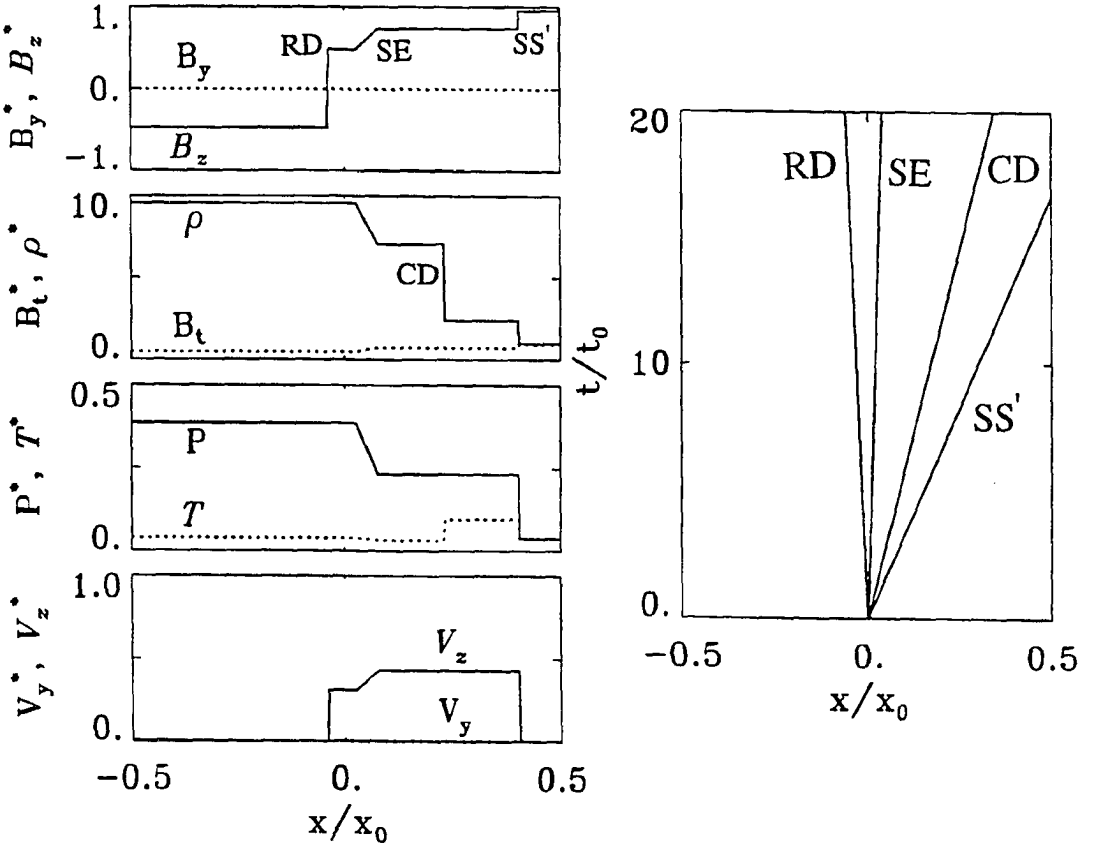

Figure 2.5 Same as Figure 2.3 with $B_y = 0$, except for a case with a large asymmetry in plasma density and magnetic field.

Reproduced with permission of the copyright owner. Further reproduction prohibited without permission.

density jumps. The ratio $R_{\rho SL}$ decreases as ρ_s/ρ_m increases, and $R_{\rho SL} < 1$ as $\rho_s/\rho_m > 16.5$. The case with $R_{\rho SL} > 1$ corresponds to the slow shock on the magnetosheath side of the reconnection layer, while $R_{\rho SL} < 1$ indicates the presence of a slow expansion wave. On the other hand, the jump ratio $R_{\rho SL'}$ across the slow shock remains relatively constant as ρ_s/ρ_m increases.

Note that in Levy et al.'s [1964] model, $\rho_s/\rho_m \rightarrow \infty$ and a slow expansion wave SE is present in the reconnection layer. The slow shock SS' does not exist in their model because the magnetospheric plasma density $\rho_m = 0$ is assumed. Figure 2.6 provides a transition from the symmetric Petschek's [1964] model to the highly asymmetric model of Levy et al. [1964].

2.5 Structure of the Reconnection Layer in Cases with $B_y \neq 0$

We now study the cases with $B_y \neq 0$. In these cases, two rotational discontinuities are present in the reconnection layer. Three specific cases are presented in the following.

2.5.1 Symmetric Case with $B_y \neq 0$

We first study a symmetric case with $\beta_m = \beta_m = 0.2$, $\rho_s = \rho_m$, $B_x = 0.25B_{zm}$, $B_{zs} = -B_{zm}$, and $B_{ys} = B_{ym} = B_{zm}$. Since the plasma density and magnetic field strength are symmetric, the contact discontinuity does not exist in this case. The solution contains only six discontinuities and expansion waves (F, RS, SS, SS', RD', F'), as shown in Figure 2.7. In this

Reproduced with permission of the copyright owner. Further reproduction prohibited without permission.

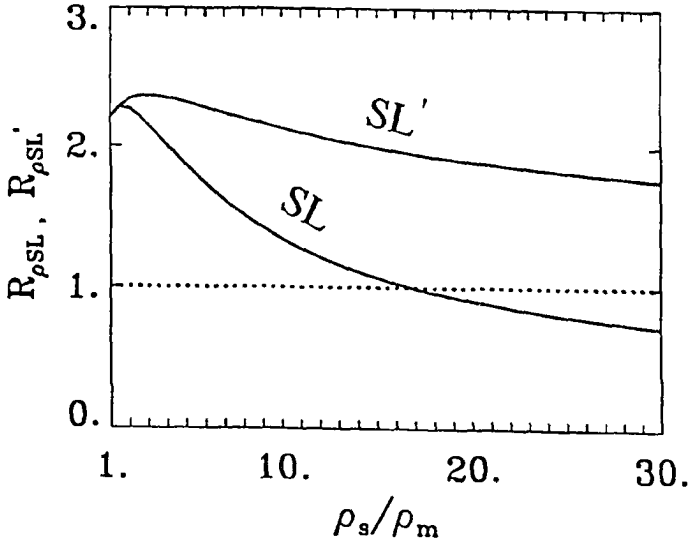

Figure 2.6 The density jump $R_{\rho SL}$ across the slow mode SL and $R_{\rho SL'}$ across the slow expansion wave SL' as a function of ρ_s/ρ_m for the case with $B_y = 0$. The case with $\rho_s/\rho_m = 1$ corresponds to the symmetric case. The case with $R_{\rho SL} > 1$ corresponds to the slow shock on the magnetosheath side of the reconnection layer, while the case with $R_{\rho SL} < 1$ corresponds to the slow expansion wave.

Reproduced with permission of the copyright owner. Further reproduction prohibited without permission.

case, we have

$$(\rho_1^*, P_1^*, B_{y1}^*, B_{z1}^*, V_{x1}^*, V_{y1}^*, V_{z1}^*) = (1, 0.206, 1, -1, 0, 0, 0)$$

The magnetic field and plasma quantities in Regions 2, 3, and 4 are obtained as

$$(\rho_2^*, P_2^*, B_{y2}^*, B_{z2}^*, V_{x2}^*, V_{y2}^*, V_{z2}^*) = (0.96, 0.19, 0.96, -0.96, 0.059, -0.0065, 0.0065)$$

$$(\rho_3^*, P_3^*, B_{y3}^*, B_{z3}^*, V_{x3}^*, V_{y3}^*, V_{z3}^*) = (0.962, 0.193, 1.359, 0, 0.0594, 0.399, 0.986)$$

$$(\rho_4^*, P_4^*, B_{y4}^*, B_{z4}^*, V_{x4}^*, V_{y4}^*, V_{z4}^*) = (1.612, 0.482, 1.134, 0, 0, 0, 0.986)$$

The intermediate Mach number at the slow shock SS is $M_{IS} = 0.574$. The azimuthal angle of tangential magnetic field in Region 3, Region 4, and Region 5 is 90^o, and thus the rotation angle of tangential magnetic field across the rotational discontinuity RD is 45^o. The density ratio $R_{\rho SL} = 1.676$ at the slow shock. The propagation speed of the rotational discontinuity is $V_R^* = -0.195$, and that of the slow shock is $V_S^* = -0.087$.

2.5.2 Weakly Asymmetric Case with $B_y \neq 0$

We now study an asymmetric case with $\beta_m = 0.2$, $B_x = 0.25 B_{zm}$, $B_{zs} = -B_{zm}$, $B_{ys} = B_{ym} = B_{zm}$, and $\rho_s = 2\rho_m$. In this case, $\beta_s = 0.2$. The physical quantities in Region 1 and Region 8 as shown in Figure 2.2a are, respectively,

$$(\rho_1^*, P_1^*, B_{y1}^*, B_{z1}^*, V_{x1}^*, V_{y1}^*, V_{z1}^*) = (2, 0.206, 1, -1, 0, 0, 0)$$

$$(\rho_8^*, P_8^*, B_{y8}^*, B_{z8}^*, V_{x8}^*, V_{y8}^*, V_{z8}^*) = (1, 0.206, 1, 1, 0, 0, 0)$$

The resulting discontinuities in this case are $(F, RD, SS, CD, SS', RD', F')$. The magnetic

Reproduced with permission of the copyright owner. Further reproduction prohibited without permission.

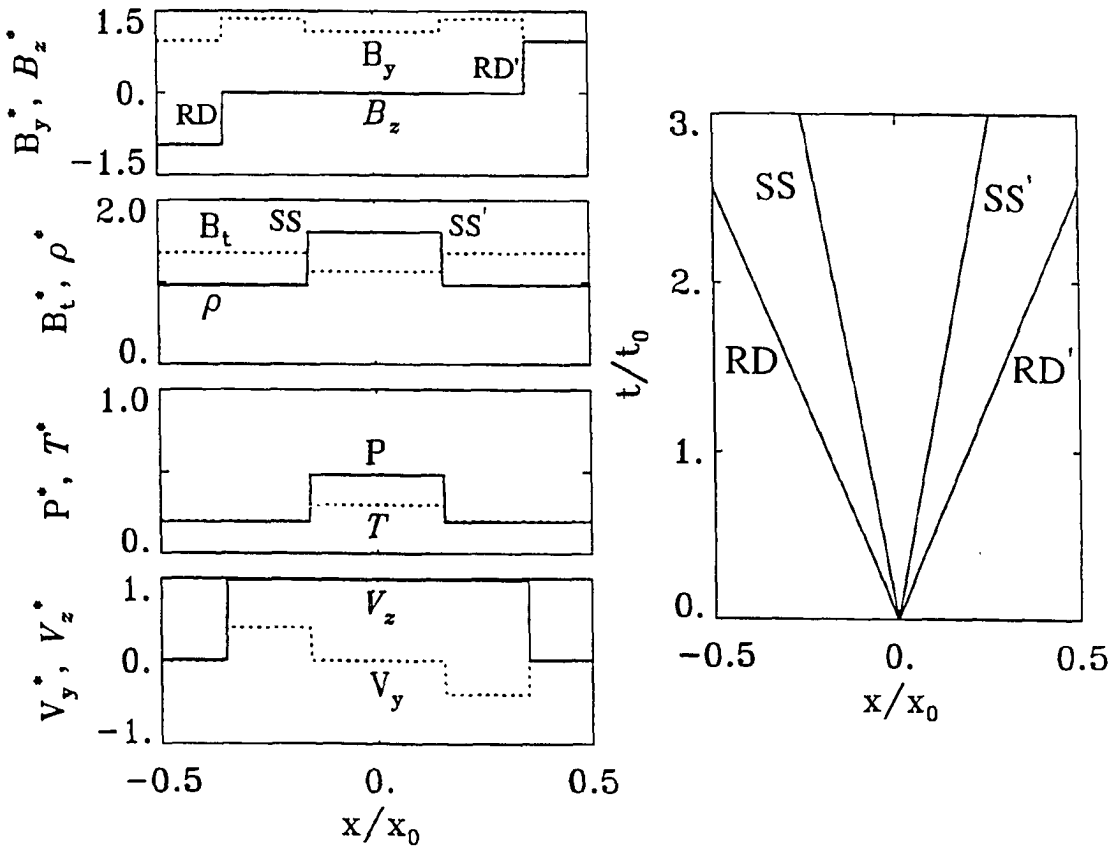

Figure 2.7 Same as Figure 2.3, except for a symmetric case with $B_y \neq 0$.

Reproduced with permission of the copyright owner. Further reproduction prohibited without permission.

field and plasma quantities in Regions 2 through 7 are

$$(\rho_2^*, P_2^*, B_{y2}^*, B_{z2}^*, V_{x2}^*, V_{y2}^*, V_{z2}^*) = (1.998, 0.206, 0.931, -0.931, 0., -0.0787, 0.0787)$$

$$(\rho_3^*, P_3^*, B_{y3}^*, B_{z3}^*, V_{x3}^*, V_{y3}^*, V_{z3}^*) = (1.998, 0.206, 1.300, 0.210, 0.0002, 0.182, 0.886)$$

$$(\rho_4^*, P_4^*, B_{y4}^*, B_{z4}^*, V_{x4}^*, V_{y4}^*, V_{z4}^*) = (3.08, 0.44, 1.12, 0.18, -0.035, -0.046, 0.85)$$

$$(\rho_5^*, P_5^*, B_{y5}^*, B_{z5}^*, V_{x5}^*, V_{y5}^*, V_{z5}^*) = (1.53, 0.44, 1.12, 0.18, -0.035, -0.046, 0.85)$$

$$(\rho_6^*, P_6^*, B_{y6}^*, B_{z6}^*, V_{x6}^*, V_{y6}^*, V_{z6}^*) = (0.94, 0.19, 1.31, 0.21, -0.09, -0.37, 0.76)$$

$$(\rho_7^*, P_7^*, B_{y7}^*, B_{z7}^*, V_{x7}^*, V_{y7}^*, V_{z7}^*) = (0.94, 0.19, 0.94, 0.94, -0.09, 0.0099, 0.068)$$

The result of this case is shown in Figure 2.8. At the slow shock SS, $M_{ISL} = 0.561$, and the density ratio $R_{\rho SL} = 1.543$. At the slow shock SS', $M_{ISL'} = 0.558$, and $R_{\rho SL'} = 1.623$. The rotation angle of tangential magnetic field across the rotational discontinuity RD is 54.168^o, and that across the rotational discontinuity RD' is 35.832^o. The propagation speeds of the discontinuities in the resulting reconnection layer are $V_R^* = -0.177$, $V_{SL}^* = -0.099$, $V_C^* = -0.0347$, $V_{SL}'^* = 0.054$, and $V_R'^* = 0.168$.

2.5.2 Highly Asymmetric Case with $B_y = 0$

We now present a case with $B_y \neq 0$ and with a large asymmetry in magnetic field and plasma density on the two sides of initial current sheet. In this case, $\beta_m = 0.08$, $\beta_s = 3.256$, $B_x = 0.05B_{zm}$, $B_{zs} = -0.5B_{zm}$, $B_{ys} = B_{ym} = 0.05B_{zm}$, and $\rho_s = 10\rho_m$. The parameters on the two sides of the initial current sheet are

$$(\rho_1^*, P_1^*, B_{y1}^*, B_{z1}^*, V_{x1}^*, V_{y1}^*, V_{z1}^*) = (10, 0.415, 0.05, -1, 0, 0, 0)$$

$$(\rho_8^*, P_8^*, B_{y8}^*, B_{z8}^*, V_{x8}^*, V_{y8}^*, V_{z8}^*) = (1, 0.0402, 0.05, 1, 0, 0, 0)$$

A slow expansion wave, instead of a slow shock, is present on the magnetosheath side of the resulting reconnection layer. The obtained discontinuities in this case are $(F, RD, SE, CD, SS', RD', F')$.

Reproduced with permission of the copyright owner. Further reproduction prohibited without permission.

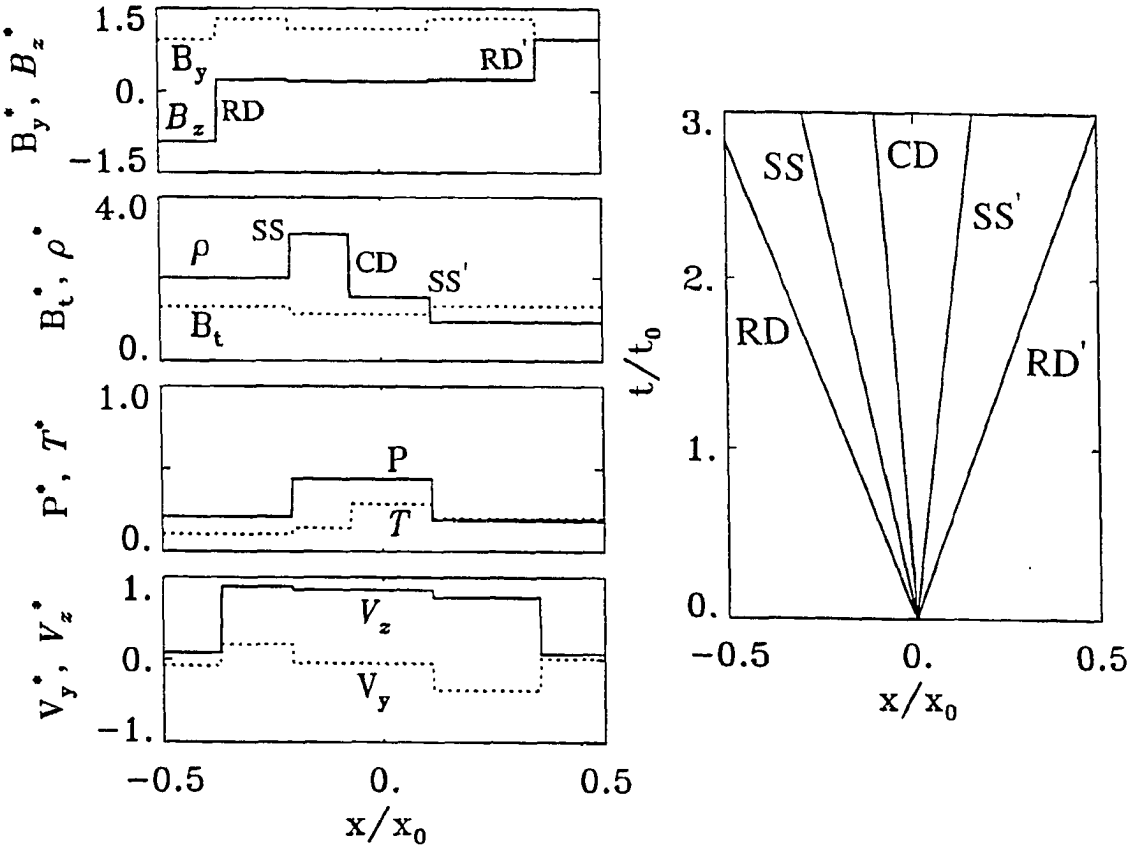

Figure 2.8 Same as Figure 2.3, except for a weakly asymmetric case with $B_y \neq 0$.

Reproduced with permission of the copyright owner. Further reproduction prohibited without permission.

The magnetic field and plasma quantities in Regions 2 through 7 as shown in Figure 2.2a are obtained as

$$(\rho_2^*, P_2^*, B_{y2}^*, B_{z2}^*, V_{x2}^*, V_{y2}^*, V_{z2}^*) = (9.58, 0.387, 0.0477, -0.477, 0.0131, -0.0, 0.0)$$

$$(\rho_3^*, P_3^*, B_{y3}^*, B_{z3}^*, V_{x3}^*, V_{y3}^*, V_{z3}^*) = (9.58, 0.387, 0.0372, 0.480, 0.0131, -0.0034, 0.310)$$

$$(\rho_4^*, P_4^*, B_{y4}^*, B_{z4}^*, V_{x4}^*, V_{y4}^*, V_{z4}^*) = (7.070, 0.233, 0.0566, 0.730, 0.0171, 0.0055, 0.425)$$

$$(\rho_5^*, P_5^*, B_{y5}^*, B_{z5}^*, V_{x5}^*, V_{y5}^*, V_{z5}^*) = (2.237, 0.233, 0.0566, 0.730, 0.0171, 0.0055, 0.425)$$

$$(\rho_6^*, P_6^*, B_{y6}^*, B_{z6}^*, V_{x6}^*, V_{y6}^*, V_{z6}^*) = (1.0, 0.040, 0.074, 0.96, 0.0, -0.026, 0.0017)$$

$$(\rho_7^*, P_7^*, B_{y7}^*, B_{z7}^*, V_{x7}^*, V_{y7}^*, V_{z7}^*) = (1.0, 0.040, 0.048, 0.96, 0.0, 0.0, 0.0)$$

The result of this case is shown in Figure 2.9. At the slow expansion wave SE, $M_{ISL} = 0.701$, and at the slow shock SS', $M_{ISL'} = 0.590$. The rotation angle of tangential magnetic fields across the rotational discontinuity RD is 169.855^o, and that across the rotational discontinuity RD' is 1.572^o. The propagation speeds of the discontinuities are $V_R^* = -0.003$, $V_{SL}^* = 0.0018$, $V_C^* = 0.0171$, $V_{SL'}^* = 0.0295$, and $V_R'^* = 0.05$.

2.5.4 Parameter Search

Figure 2.10a shows the ratios $R_{\rho SL}$ and $R_{\rho SL'}$ as a function of ρ_s/ρ_m for cases with $\beta_m = 0.1$, $B_x = 0.1B_{xm}$, $\Phi_{Bm} = 0^o$, $\Phi_{Bs} = 120^o$, and $T_s/T_m = (\rho_s/\rho_m)^{1/2}$. It is seen that the slow mode on the magnetosheath side of the reconnection layer is a slow shock as $\rho_s/\rho_m < 12.5$ and is a slow expansion wave as $\rho_s/\rho_m > 12.5$. Figure 2.10b shows the rotation angles of tangential magnetic fields across the rotational discontinuities at the magnetopause (Φ_{BR}) in the boundary layer ($\Phi_{BR'}$). It is seen that $\Phi_{BR'}$ decreases as ρ_s/ρ_m increases, and Φ_{BR} increases with ρ_s/ρ_m. The total angle $(\Phi_{BR} + \Phi_{BR'}) = 120^o$, and the two curves in Figure 2.10b are symmetric about 60^o.

Reproduced with permission of the copyright owner. Further reproduction prohibited without permission.

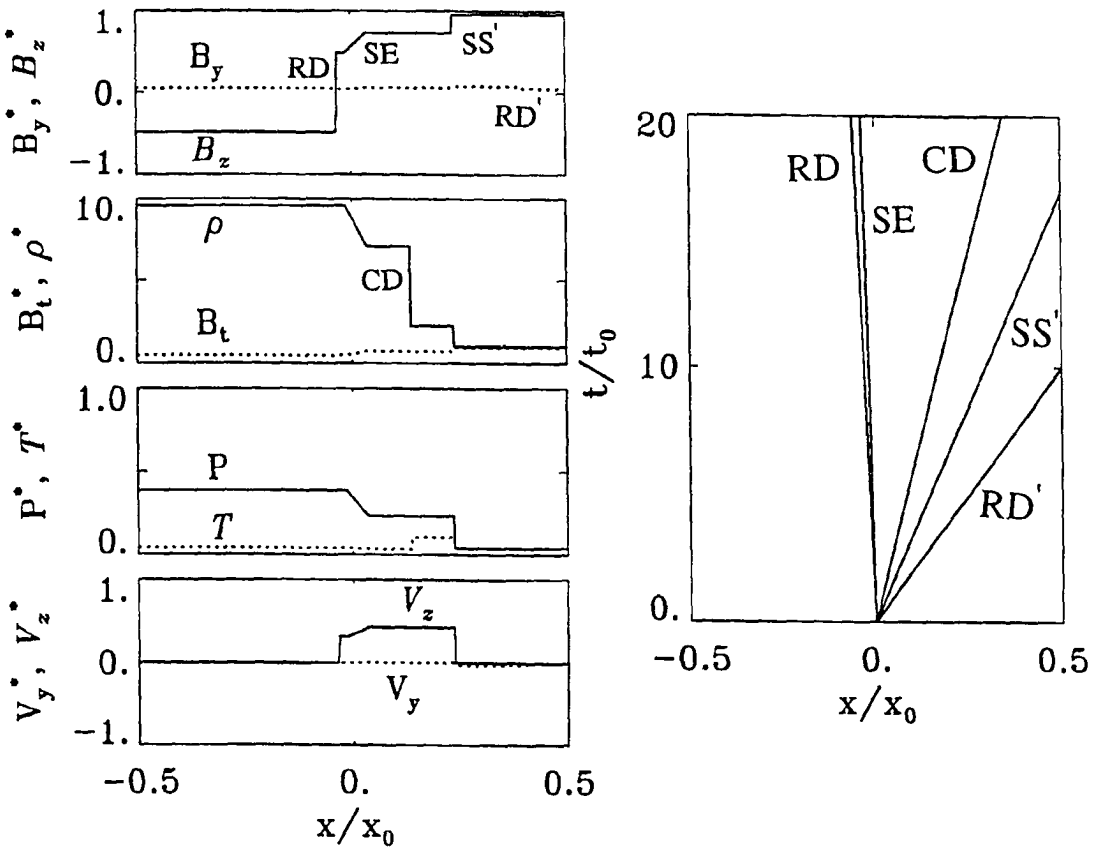

Figure 2.9 Same as Figure 2.3, except for a highly asymmetric case with $B_y \neq 0$.

Reproduced with permission of the copyright owner. Further reproduction prohibited without permission.

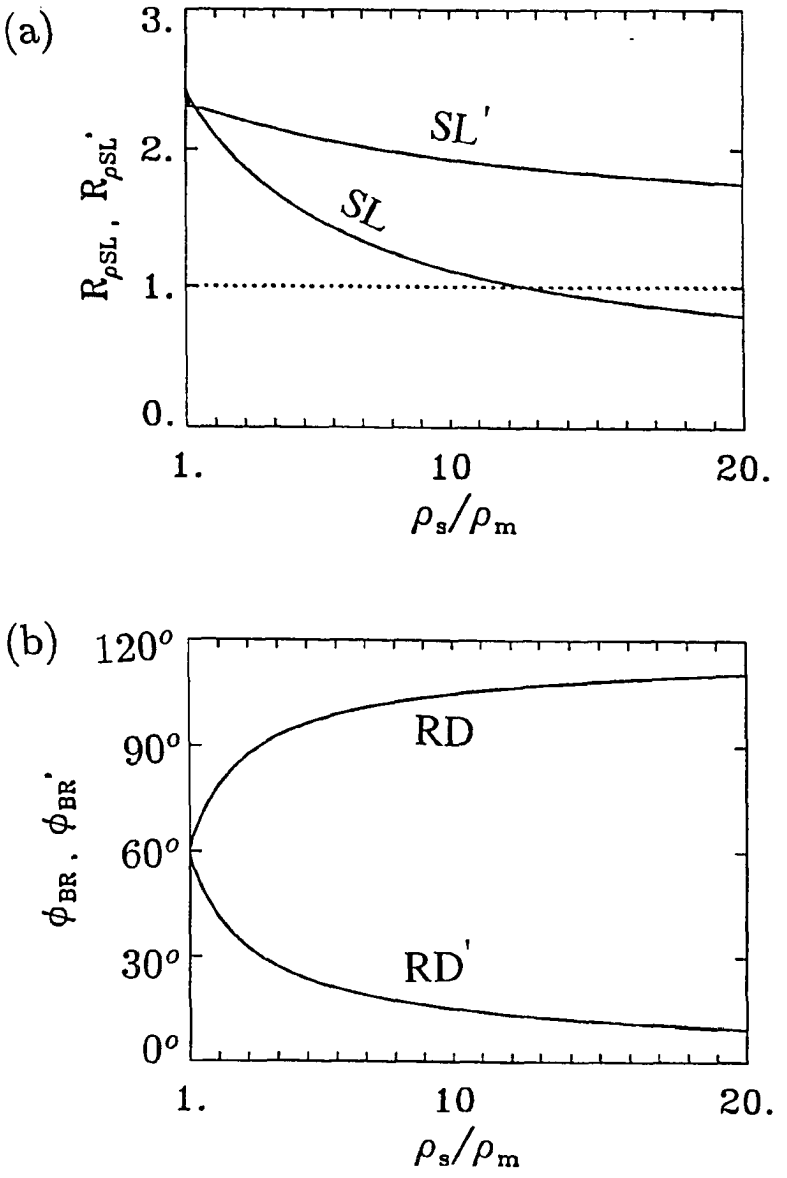

Figure 2.10 (a) Density ratios $R_{\rho SL}$ and $R_{\rho SL'}$ across SL and SL' as a function of ρ_s/ρ_m for the case with $B_y = 0$. (b) Rotation angle Φ_{BR} ($\Phi_{BR'}$) across the rotational discontinuity RD (RD').

Reproduced with permission of the copyright owner. Further reproduction prohibited without permission.

2.6 Summary

In summary, we have shown that on the basis of ideal MHD formulation, rotational discontinuities, slow shocks, slow expansion waves, and a contact discontinuity may be present in the reconnection layer. In addition, two fast expansion waves are also present in the solution of Riemann problem. But they quickly propagate out of the reconnection layer. A summary is given in Table 2.1.

(a) Cases with $B_y = 0$: For symmetric cases with $B_y = 0$, a pair of slow shocks SS and SS' are present in the reconnection layer. For weakly asymmetric cases, there exist a rotational discontinuity RD, slow shock SS, contact discontinuity CD, and slow shock SS'. For highly asymmetric cases, the slow shock SS is replaced by a slow expansion wave SE, and we have RD, SE, CD, and SS' in the reconnection layer.

(b) Cases with $B_y \neq 0$: For symmetric cases with $B_y \neq 0$, a pair of rotational discontinuity RD and RD' and a pair of slow shocks SS and SS' are present in the reconnection layer. For weakly asymmetric cases, there exist a rotational discontinuity RD, slow shock SS, contact discontinuity CD, slow shock SS', and rotational discontinuity RD'. For highly asymmetric cases, the slow shock SS is replaced again by a slow expansion wave SE.

(c) The symmetric cases can be applied to the plasma sheet in the magnetotail. Two slow shocks are expected to exist in the reconnection layer.

(d) The asymmetric cases can be applied to the dayside magnetopause-boundary layer. In the general cases in which the magnetic fields in the magnetosheath and magnetosphere are not exactly antiparallel, the reconnection layer consists of RD, SS, CD, SS', and RD'. The rotational discontinuity RD on the sunward side is usually identified as the magnetopause. When the density ratio ρ_s/ρ_m is greater than ~ 10, the slow shock SS is replaced by a slow expansion wave SE. In the case with exactly antiparallel magnetic fields, the rotational discontinuity RD', which is on the inner edge of the boundary layer, will disappear.

Reproduced with permission of the copyright owner. Further reproduction prohibited without permission.

However, a finite resistivity will affect the stability and evolution of the discontinuities in the reconnection layer [e.g., Wu, 1990; Lin et al., 1992; Wu and Kennel, 1992]. In particular, the rotational discontinuity becomes unstable and is disintegrated, and intermediate shocks can exist in the dissipative MHD formulation. In the next chapter, we will solve the Riemann problem by simulating the evolution of an initial current sheet based on the resistive MHD formulation.

Reproduced with permission of the copyright owner. Further reproduction prohibited without permission.

Chapter 3 Structure of Reconnection Layers in the Resistive MHD Model

In this chapter, we study the structure of reconnection layers at the dayside magnetopause and in the tail plasma sheet based on the resistive MHD formulation. We simulate the 1-D Riemann problem for the evolution of an initial current sheet associated with magnetic reconnection. The total pressure (plasma thermal pressure plus magnetic pressure) is assumed constant across the initial current sheet. After magnetic reconnection takes place at the initial current sheet, a non-zero normal component of magnetic field B_x is present, and the initial current sheet evolves into a system of MHD discontinuities and expansion waves.

We will show that in the presence of a finite resistivity, the results obtained from the ideal MHD formulation in Chapter 2 are modified. The steady rotational discontinuities do not exist, and the steady intermediate shocks (IS) and time-dependent intermediate shocks (TDIS) are present in the reconnection layer, playing the role of rotational discontinuity.

In order to understand the existence and role of intermediate shock in the resistive MHD model, we briefly describe the properties and structure of intermediate shocks in Section 3.1. The simulation model is given in Section 3.2, and the simulation results are presented in Section 3.3. The summary for this chapter is given in Section 3.4.

3.1 Intermediate Shocks in the Resistive MHD Formulation

As mentioned in Chapter 2, four types of intermediate shocks can be obtained from the Rankine Hugoniot jump conditions: the 1-3 shock, 1-4 shock, 2-3 shock, and 2-4 shock. At the 1-3 intermediate shock, the upstream normal component of flow velocity is greater than the local fast

Reproduced with permission of the copyright owner. Further reproduction prohibited without permission.

mode speed (super-fast) and the downstream normal flow speed is less than the local intermediate mode speed (sub-intermediate) and greater than the local slow mode speed (super-slow). At the 1-4 intermediate shock, the upstream normal flow speed is super-fast and the downstream normal flow speed is sub-slow. The 2-3 intermediate shock is the shock with a normal flow speed sub-fast and super-intermediate in the upstream region and sub-intermediate and super-slow in the downstream region, while the 2-4 intermediate shock has a normal flow speed sub-fast and super-intermediate upstream region and sub-slow downstream.

However, based on conventional ideal MHD theories, the intermediate shocks had been considered as unstable or nonevolutionary [Germain, 1960; Jeffrey and Taniuti, 1964; Kantrowitz and Petschek, 1966]. One of the arguments is based on the linear stability considerations of the n-dimensional ideal MHD equations. In order for the shock to be evolutionary, there must be $n+1$ characteristics entering the shock and $n-1$ leaving it [e.g., Landau and Lifshitz, 1960]. Note that $n = 7$ for the set of MHD equations in (2.1). A fast shock or slow shock satisfies the linear stability consideration, with eight incoming characteristics and six outgoing characteristics [Jeffrey and Taniuti, 1964]. For the 1-3, 1-4, or 2-4 intermediate shock, the number of outgoing waves is less than six. For the 2-3 shocks, although there are six outgoing waves, the linear perturbations can be separated into two linearly independent subspaces, and the shock evolutionary condition is not satisfied for each subspace. Therefore, solutions of intermediate shocks are not well posed and the intermediate shocks are unstable. In the ideal MHD formulation, only rotational discontinuities can facilitate the rotation of the tangential magnetic field.

However, recent simulation work based on dissipative MHD equations showed that the intermediate shocks can be formed from continuous waves [Wu, 1987; 1990] and that the rotational discontinuities cannot exist [Wu, 1988]. Wu also showed that there are free parameters in the structure of intermediate shocks, and these parameters are related to the resistivity or viscosity in shocks. If a perturbation is impinging on an intermediate shock, the perturbation could be carried away not only by outgoing waves but also by the change of shock structure. Assume

Reproduced with permission of the copyright owner. Further reproduction prohibited without permission.

that the tangential magnetic field of a steady intermediate shock is in the z direction and the shock normal is in the x direction. The structure of a resistive intermediate shock is related to the parameter $I_y = \int B_y dx$, where the integration is from downstream to upstream along the normal direction x, and different values of I_y are determined by different values of resistivity [Hau and Sonnerup, 1989; Kennel et al., 1990].

Figure 3.1a sketches the hodogram of the tangential magnetic field for 1-3 and 2-3 resistive intermediate shocks. The upstream and downstream magnetic fields for the 1-3 intermediate shocks are marked by, respectively, circled numbers 1 and 3 on the B_z axis. The upstream and downstream magnetic fields of the 2-3 intermediate shocks are indicated by circled numbers 2 and 3, respectively. The arrow on each curve indicates the direction from upstream to downstream. As shown by the dashed curves in Figure 3.1a, these exist a family of resistive 1-3 intermediate shocks with the same upstream and downstream states. Each 1-3 intermediate shock has a certain value of of I_y and corresponds to a certain resistivity. On the other hand, for given upstream and downstream states, a family of 2-3 intermediate shocks have only two solutions with $I_y = \pm I_{ymax}$, where I_{ymax} is the maximum of I_y in the 1-3 shock family, as shown by the solid curve in Figure 3.1a. The hodogram of tangential magnetic field for the 1-2 fast shock, which has $I_y = 0$, is also shown in Figure 3.1a.

Wu [1988] found in a resistive MHD simulation that the rotational discontinuity is unstable and disintegrated into several wave modes due to the diffusion of the transverse magnetic field in the discontinuity. On the other hand, there exists a localized time-dependent structure, across which the magnetic field is non-coplanar, the magnetic field strength is not conserved, and the plasma density increases. The normal component of flow speed is super-intermediate upstream of this structure and sub-intermediate downstream. Since the shock coplanarity condition is violated in this structure, the RH conditions for steady shocks are not satisfied. The structure has been called the time-dependent intermediate shocks (TDIS) [e.g., Wu, 1988, 1990], since it evolves with time and looks like a shock in any finite time. Recently, Wu and Kennel [1992] found a

Reproduced with permission of the copyright owner. Further reproduction prohibited without permission.

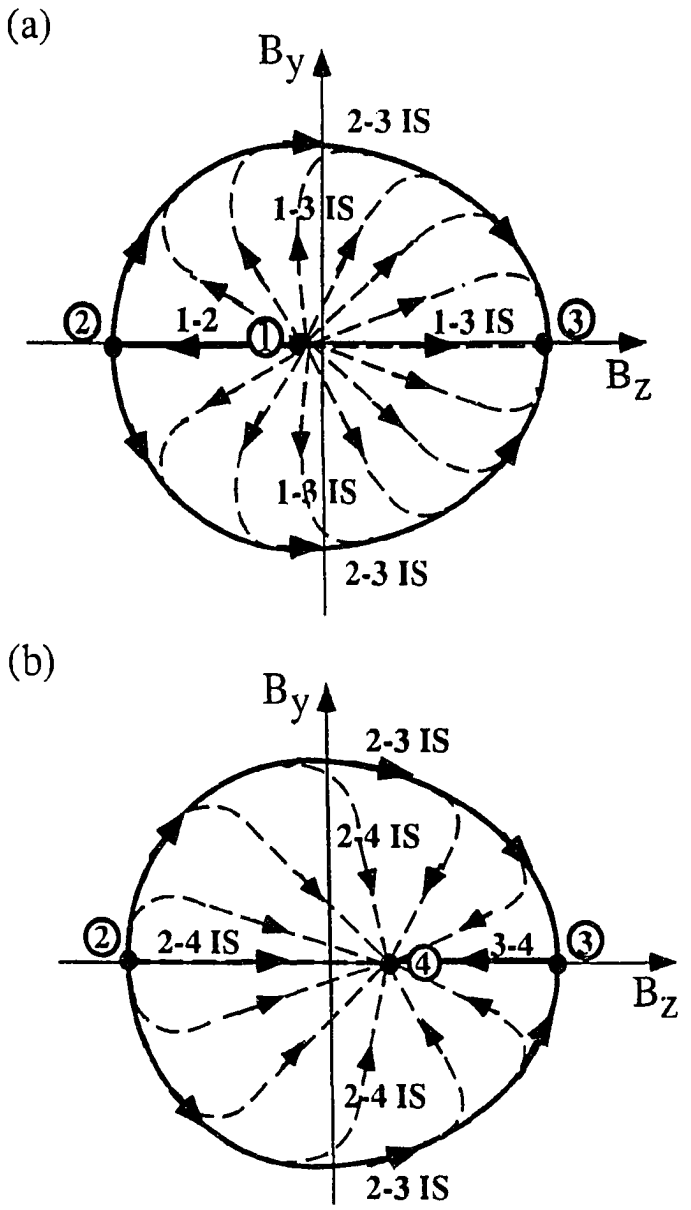

Figure 3.1 Hodograms of tangential magnetic fields in (a) 1-3 and 2-3 resistive intermediate shocks and the 1-2 fast shock and (b) 2-4 and 2-3 resistive intermediate shocks and the 3-4 slow shock.

Reproduced with permission of the copyright owner. Further reproduction prohibited without permission.

quantitative description of time-dependent intermediate shocks in the small-amplitude limit: 2-3 time-dependent intermediate shocks evolve as a self-similar structure whose strength decreases as $1/\sqrt{t}$ and whose width increases as $\sqrt{t}$. Such similarity of the 2-3 time-dependent intermediate shocks has also been discussed by Lin et al. [1992]. Since these time-dependent intermediate shocks approach in the long-time limit the classical rotational discontinuity of ideal MHD, with equal field strengths and plasma densities on either side, one may also call it a time-dependent rotational discontinuity (TDRD) [Lin et al., 1992; Lin and Lee, 1993].

We will show in this chapter that in the resistive MHD formulation, intermediate shocks and time-dependent intermediate shocks may be present in the reconnection layer based on the resistive MHD formulation. The similarity of the time-dependent intermediate shocks will also be examined.

3.2 Simulation Model

In our study, the initial current sheet separates two uniform plasma regions. These two plasma regions have antiparallel magnetic field components in the z direction and a common guide field in the y direction. The normal to the current sheet is in the x direction. Initially, the total pressure $(P + P_B)$ is assumed constant everywhere, where P is the plasma thermal pressure and $P_B = B^2/2\mu_0$ is the magnetic pressure. After the onset of magnetic reconnection, a non-zero normal component of the magnetic field, $B_n = B_x$, is present. We simulate the evolution of the initial current sheet in the presence of the normal magnetic field component B_n and hence study the structure of the reconnection layer.

3.2.1 Basic Equations

Reproduced with permission of the copyright owner. Further reproduction prohibited without permission.

The resistive MHD fluid equations used in our simulation are

$$\frac{\partial \rho}{\partial t} + \nabla \cdot (\rho \mathbf{V}) = 0 \tag{3.1a}$$

$$\frac{\partial (\rho \mathbf{V})}{\partial t} + \nabla \cdot [(P + \frac{B^2}{2\mu_0})\mathbf{I} + \rho \mathbf{V}\mathbf{V} - \frac{\mathbf{B}\mathbf{B}}{\mu_0}] = 0 \tag{3.1b}$$

$$\frac{\partial \epsilon_T}{\partial t} + \nabla \cdot [(\frac{\rho V^2}{2} + \frac{P}{\gamma - 1} + P)\mathbf{V} + \frac{1}{\mu_0}\mathbf{E} \times \mathbf{B}] = 0 \tag{3.1c}$$

$$\frac{\partial \mathbf{B}}{\partial t} = -\nabla \times \mathbf{E} \tag{3.1d}$$

$$\nabla \cdot \mathbf{B} = 0 \tag{3.1e}$$

with

$$\epsilon_T = \frac{1}{2}\rho V^2 + \frac{1}{\gamma - 1}P + \frac{1}{2\mu_0}B^2 \tag{3.2}$$

and

$$\mathbf{E} = -\mathbf{V} \times \mathbf{B} + \eta \mathbf{J} \tag{3.3}$$

where η is the electrical resistivity, and ρ, P, $\mathbf{V}$, $\mathbf{B}$, $\mathbf{E}$, $\mathbf{J}$, and ϵ_T are, respectively, the plasma mass density, pressure, flow velocity, magnetic field, electric field, current density, and total energy, as defined in Chapter 2. In our simulation, the resistivity η is chosen to be a constant.

3.2.2 Initial Conditions, Boundary Condition, and Normalization

Assume that the initial current sheet is located at $x = 0$. For the dayside magnetopause, the magnetosheath is assumed to be in the region with $x < 0$ and the magnetosphere in the region

Reproduced with permission of the copyright owner. Further reproduction prohibited without permission.

with $x > 0$. Let the subscript "s" denote the magnetosheath quantities and "m" the magnetospheric quantities. The initial z-component magnetic field and plasma temperature are given by

$$B_{z0}(x) = \frac{1}{2}(B_{zm} + B_{zs}) + \frac{1}{2}(B_{zm} - B_{zs})\tanh(x/\delta) \tag{3.4}$$

$$T_0(x) = \frac{1}{2}(T_m + T_s) + \frac{1}{2}(T_m - T_s)\tanh(x/\delta) \tag{3.5}$$

where δ is the half-width of the initial current sheet. The magnetic field strength is given by

$$B_0(x) = \frac{1}{2}(B_m + B_s) + \frac{1}{2}(B_m - B_s)\tanh(x/\delta) \tag{3.6}$$

and the profile of initial y component magnetic field is determined by $B_{y0}(x) = [B_0(x)^2 - B_{z0}(x)^2 - B_x^2]^{1/2}$. Note that for some cases we assume $B_{y0}(x) = 0$ everywhere in the simulation domain and the profile of magnetic field strength is determined by $B_0(x) = [B_{z0}(x)^2 + B_x^2]^{1/2}$. The profile of initial plasma thermal pressure P_0 is determined by total pressure balance

$$P_0(x) + B_0(x)^2/2\mu_0 = P_m + B_m^2/2\mu_0 \tag{3.7}$$

The initial profile of plasma density is then determined by the profiles of T_0 and P_0. In our simulation, the conditions $B_s < B_m$, $T_s < T_m$, and $\rho_s > \rho_m$ are used for the dayside magnetopause. The initial plasma flow velocity is assumed zero everywhere. According to $\nabla \cdot \mathbf{B} = 0$, B_x is a constant in the 1-D simulation. In our calculation, $B_x = 0.25B_{zm}$ is used.

In our simulation, a free boundary condition with $\partial/\partial x = 0$ for each physical quantity is used at $x = \pm L_x/2$, where L_x is the length of the simulation domain. The spatial grid size is $\Delta x = 0.2\delta$, and the number of gird points is 2000 -- 4000. For the dayside reconnection layer, the magnetic field is expressed in units of B_m, the plasma density in ρ_m, the temperature in T_m, the plasma thermal pressure in P_m, the spatial coordinate in δ, and the current density in $B_m/(\mu_0\delta)$. The velocity is expressed by the Alfven speed in the magnetosphere, $V_{Am} \equiv B_m/\sqrt{\mu_0\rho_m}$, and the time is expressed by $t_{Am} \equiv \delta/V_{Am}$. The resistivity is expressed in units of $\eta_m \equiv v_{Am}\delta/\mu_0$.

Reproduced with permission of the copyright owner. Further reproduction prohibited without permission.

For the tail plasma sheet, the initial profiles of physical quantities are set up in the same way as for the dayside magnetopause, except equal plasma densities and magnetic field strengths are used. The normalizations of physical quantities are the same as those for the dayside magnetopause, except that the lobe quantities are used as the normalization units. In the following we express the physical quantities in normalized forms.

3.2.3 Numerical Scheme

Write the component equations of (3.1) -- (3.3) in a conservative form

$$\frac{\partial}{\partial t}\rho = \frac{\partial}{\partial x}(\rho V_x) = 0 \tag{3.8a}$$

$$\frac{\partial}{\partial t}(\rho V_x) + \frac{\partial}{\partial x}(\rho V_x^2 + P + \frac{B^2}{2}) = 0 \tag{3.8b}$$

$$\frac{\partial}{\partial t}(\rho V_y) + \frac{\partial}{\partial x}(\rho V_x V_y - B_x B_y) = 0 \tag{3.8c}$$

$$\frac{\partial}{\partial t}(\rho V_z) + \frac{\partial}{\partial x}(\rho V_x V_z - B_x B_z) = 0 \tag{3.8d}$$

$$\frac{\partial}{\partial t}B_y + \frac{\partial}{\partial x}(V_x B_y - V_y B_x - \eta\frac{\partial}{\partial x}B_y) = 0 \tag{3.8e}$$

$$\frac{\partial}{\partial t}B_z + \frac{\partial}{\partial x}(V_x B_z - V_z B_x - \eta\frac{\partial}{\partial x}B_z) = 0 \tag{3.8f}$$

$$\frac{\partial}{\partial t}\epsilon_T + \frac{\partial}{\partial x}[(\epsilon_T + P + \frac{B^2}{2})V_x - (B_x V_x + B_y V_y + B_z V_z)B_x - \eta(B_z\frac{\partial}{\partial x}B_z + B_y\frac{\partial}{\partial x}B_y)] = 0 \tag{3.8g}$$

Each of these component equations can be written in the form

$$\frac{\partial A}{\partial t} + \frac{\partial F_A}{\partial x} = 0 \tag{3.9}$$

where F_A is the flux associated with quantity A.

We use an explicit two-step Lax-Wendroff scheme [Lax and Wendroff, 1960; Richtmyer, 1962; Richtmyer and Morton, 1967] to solve the resistive MHD equation (3.8), which can be

Reproduced with permission of the copyright owner. Further reproduction prohibited without permission.

written in the form of (3.9). Let the value of A at the nth time interval and the jth grid point be A_j^n. The quantity A is advanced through two steps for each time interval Δt. For example, to advance A at the jth grid point from the nth to the $(n+1)$th time interval, we use

$$A_{j+1/2}^{n+1/2} = \frac{1}{2}(A_j^n + A_{j+1}^n) - \frac{\Delta t}{2\Delta x}[(F_A)_{j+1}^n - (F_A)_j^n] \tag{3.10}$$

$$A_j^{n+1} = A_j^n - \frac{\Delta t}{\Delta x}[(F_A)_{j+1/2}^{n+1/2} - (F_A)_{j-1/2}^{n+1/2}] \tag{3.11}$$

This scheme time-centres the integration by defining temporary or intermediate values at the half time step $t^{n+1/2}$, as given in equation (3.10). Numerical diffusion has been introduced into the scheme through the term $\frac{1}{2}(A_j^n + A_{j+1}^n)$ in equation (3.10) to stablize the computation. The two-step Lax-Wendroff scheme is accurate to the second-order in time, and the Courant-Friedrichs-Lewy condition

$$\Delta t \leq \Delta x / |V_{max}| \tag{3.12}$$

must be satisfied to make the scheme stable, where V_{max} is the maximum of the flow speed and wave mode speeds in the simulation system.

3.3 Simulation Results

We have simulated many cases, and the results are summarized in Table 3.1. In the following, we show the simulation results for six typical cases. In Cases 1, 2, and 3, the tangential magnetic fields on the two sides of initial current sheet are exactly antiparallel ($B_y = 0$). Case 1 is a symmetric case, with equal plasma densities and magnetic field strengths on the two sides of the initial current sheet. Case 2 has a small asymmetry in plasma density. Case 3 is a highly asymmetric case, in which both plasma density and magnetic field are asymmetric. In Cases 4, 5, and 6, the guide field $B_y \neq 0$ on the two sides of the initial current sheet. The symmetric cases can be applied to the tail plasma sheet, whereas the asymmetric cases can be applied to the dayside magnetopause.

Reproduced with permission of the copyright owner. Further reproduction prohibited without permission.

The ideal MHD results of Cases 1, 2, 4, and 5 have been shown in Chapter 2. We will compare the results obtained from the resistive MHD simulation and from the ideal MHD formulation for these cases.

3.3.1 Case 1: Symmetric Case with $B_y = 0$

Figure 3.2 shows the simulation results of Case 1, which has equal plasma density and magnetic field strength and antiparallel magnetic fields on the two sides of the initial current sheet. The simulation results shown are in the region from $x = -200\delta$ to $x = 200\delta$, with a total system length of 2000 grid points. In the calculation, the resistivity is chosen as a constant in the simulation domain with $\eta = 0.039$. It is found for the case with an initial guide field $B_{y0}(x) = 0$ that as the system evolves according to equations (3.1), $B_y(x, t)$ remains zero everywhere.

The left column of Figure 3.2 shows spatial profiles of the tangential magnetic field components (B_y and B_z), plasma density, thermal and magnetic pressures (P and P_B) at $t = 889$. As predicted by the ideal MHD formulation and found in 2-D MHD simulations [Shi and Lee, 1990], a Petschek-like structure is formed. Two symmetric slow shocks SS and SS' are present in the reconnection layer at $x = -122$ and $x = 122$. Let the subscripts "1" and "2" denote the quantities upstream and downstream of a discontinuity, respectively. The upstream shock normal angle for each slow shock is $\theta_{nB1} = 74.1^o$, the upstream plasma beta is $\beta_1 = 0.208$, and the upstream intermediate wave speed is 0.258. The upstream normal flow speed in the shock frame is found to be $v_{n1} = 0.258$, indicating an intermediate Mach number $M_I = 1.0$. Both shocks reach a steady state corresponding to a switch-off shock, with $R_{v_n} = 0.497$, $R_\rho = 2.012$, $R_{B_t} = 0$, and $R_p = 5.82$, where R_ρ, R_{v_n}, R_{B_t} and R_p are the ratios of plasma densities, normal components of flow velocities, tangential magnetic fields and plasma thermal pressures across the shock. It is found that the result of Case 1 is exactly the same as that obtained from the ideal MHD formulation.

Reproduced with permission of the copyright owner. Further reproduction prohibited without permission.

Table 3.1 Structure of Reconnection Layer

Symmetry Property \ B_y	$B_y = 0$	$B_y \neq 0$
Symmetric	SS+SS'	TDIS+SS+SS'+TDIS'
Weakly Asymmetric	IS+CD+SS'	TDIS+SS+CD+SS'+TDIS'
Moderately Asymmetric	IS+SE+CD+SS'	TDIS+SE/SS+CD+SS'+TDIS'
Highly Asymmetric	IS+SE+CD+SS'	TDIS+SE+CD+SS'+TDIS'

Note:

(1) CD: Contact Discontinuity
IS: Intermediate Shock
TDIS: Time-Dependent Intermediate Shock
SS: Slow Shock
SE: Slow Expansion Wave
SE/SS: Slow Expansion Wave in early times and Slow Shock in later times.

(2) The width of TDIS increases as $t^{1/2}$ and the strength decreases as $t^{-1/2}$.

(3) In addition, two fast expansion waves are also present, but they quickly propagate out of the reconnection layer.

Table 3.1 Structure of reconnection layer in the resistive MHD model.

Reproduced with permission of the copyright owner. Further reproduction prohibited without permission.

The shock width can be obtained by measuring the distance between the two positions where $|dB_z/dx|$ equals 30% of its maximum value in the transition region of the shock. It is found that the shock width is on the order of $\sim 2\eta/(v_{n1} - v_{n2})$, which is the same as the estimation from the viscous Burger's equation [Whitham, 1974]. The structure with a density variation at $x = 0$, as seen in Figure 3.2, is caused by the finite width of initial current sheet. Note that the two fast expansion waves, which propagate ahead of the two slow shocks, have moved out of the simulation domain and are not shown in the plot.

The positions of the slow shocks are plotted as a function of time in the right plot of Figure 3.2. These positions are identified by tracking the local maximums of $|\partial B_z/\partial x|$. The two slow shocks are found to have a constant width and propagate with constant speed.

3.3.2 Case 2: Weakly Asymmetric Case with $B_y = 0$

Case 2 is an asymmetric case with $\rho_s = 2\rho_m$, $B_{zs} = -B_{zm}$ and $B_{y0}(x) = 0$. A relatively large resistivity, $\eta = 0.098$, was used in this case. The simulation result is shown in Figure 3.3. An intermediate shock IS is present on the magnetosheath side (lefthand side) of the resulting reconnection layer. As shown in the left column of Figure 3.3, at $t = 740$ the intermediate shock is located at $x = -119.8$. On the magnetospheric side (righthand side), a slow shock SS' is located at $x = 88.8$. A contact discontinuity CD at $x = 2.6$ separates the two shocks IS and SS'. The intermediate shock and slow shock satisfy the coplanarity condition.

At the intermediate shock IS, $\theta_{nB1} = 74.1°$, $\beta_1 = 0.208$, and the wave speeds for the fast, intermediate, and slow waves are, respectively, $C_{F1} = 0.719$, $C_{I1} = 0.182$ and $C_{SL1} = 0.0708$ in the upstream region of intermediate shock, and $C_{F2} = 0.572$, $C_{I2} = 0.134$ and $C_{SL2} = 0.131$ in the downstream region. The normal flow speeds in the shock frame are 0.190 upstream and 0.103 downstream. Therefore, the upstream flow speed is sub-fast and super-intermediate while the downstream flow speed is sub-slow. The tangential magnetic field reverses sign across the intermediate shock. The jump relations across the intermediate shock

Reproduced with permission of the copyright owner. Further reproduction prohibited without permission.

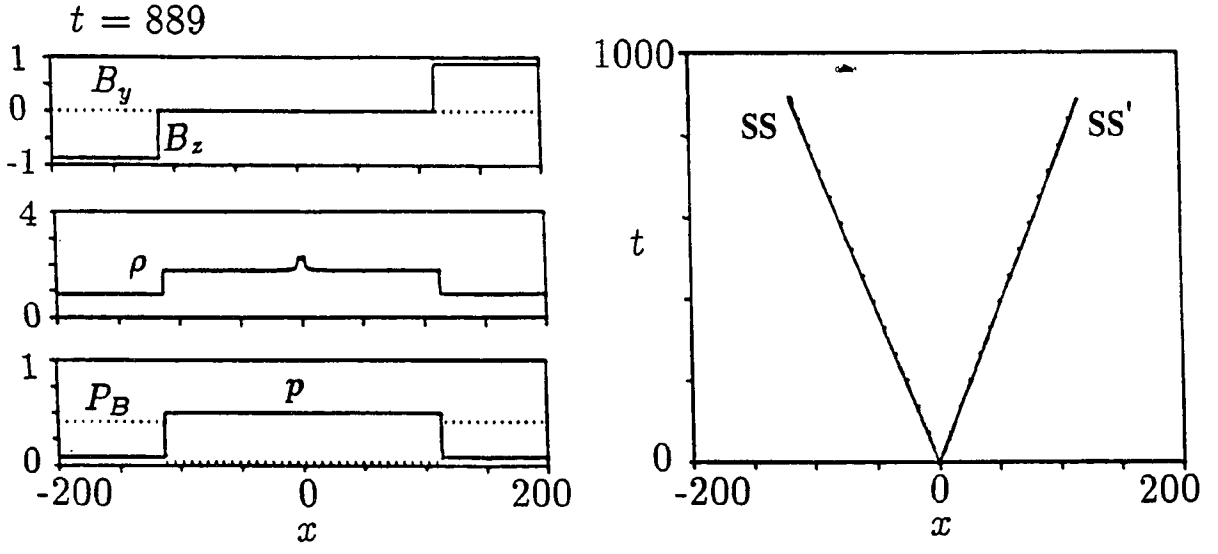

Figure 3.2 Structure of reconnection layer in Case 1, the symmetric case with $B_{y0}(x) = 0$. The right plot shows the positions of the discontinuities as a function of time. The left column shows, respectively, spatial profiles of B_y, B_z, ρ, P, and P_B at $t = 889$.

Reproduced with permission of the copyright owner. Further reproduction prohibited without permission.

are $R_{v_n} = 0.539$, $R_\rho = 1.855$, $R_{B_t} = -0.212$, and $R_p = 5.609$. This is a steady 2-4 intermediate shock with $B_y(x) = 0$. The slow shock SS', which has an upstream intermediate Mach number $M_I = 0.928$, also satisfies the Rankine-Hugoniot conditions. The coplanar intermediate shock IS and slow shock SS' in Case 2 are in a steady state with a constant width which is $\sim 2\eta/(v_{n1} - v_{n2})$. The right column of Figure 3.3 shows the positions of the intermediate shock, the contact discontinuity, and the slow shocks in the xt plane. The contact discontinuity slowly diffuses as time goes on.

The simulation result of Case 2 is different from the result obtained from the ideal MHD formulation. In the ideal MHD result of Case 2, which is shown in Figure 2.4 of Chapter 2, a rotational discontinuity, instead of the intermediate shock, bounds the reconnection layer from the magnetosheath side. Moreover, in the ideal MHD solution of Case 2 there exists a slow shock propagating on the lefthand side of the contact discontinuity CD, across which the plasma density increases. However, in the resistive MHD simulation, this slow shock does not exist, and it is across the intermediate shock IS that the plasma density increases.

3.3.3 Case 3: Highly Asymmetric Case with $B_y = 0$

Case 3 is a highly asymmetric case, in which the magnetic fields in the magnetosheath and magnetosphere are assumed exactly antiparallel, with $B_{ys} = B_{ym} = 0$. Other parameters in Case 3 are given as: $B_{zs} = -0.7B_{zm}$, $\rho_s = 10\rho_m$, $T_s = 0.339T_m$, and $\beta_m = 0.2$. In this case, the Alfven speed in magnetosheath, V_{As}, is equal to $0.228V_{Am}$. We assume that the initial magnetic field strength increases smoothly from the magnetosheath to the magnetosphere according to equation (3.6). The plasma density (temperature) smoothly decreases (increases) from the magnetosheath to the magnetosphere. The tangential magnetic field has a righthand rotation from the magnetosheath to the magnetosphere, with a rotation angle of 180^o.

Figure 3.4 shows the spatial profiles of B_z and ρ of Case 3 in a time series from $t = 0$ to $t = 1694$. In the calculation, the resistivity is chosen as $\eta = 0.039$. Due to the large asymmetry

Reproduced with permission of the copyright owner. Further reproduction prohibited without permission.

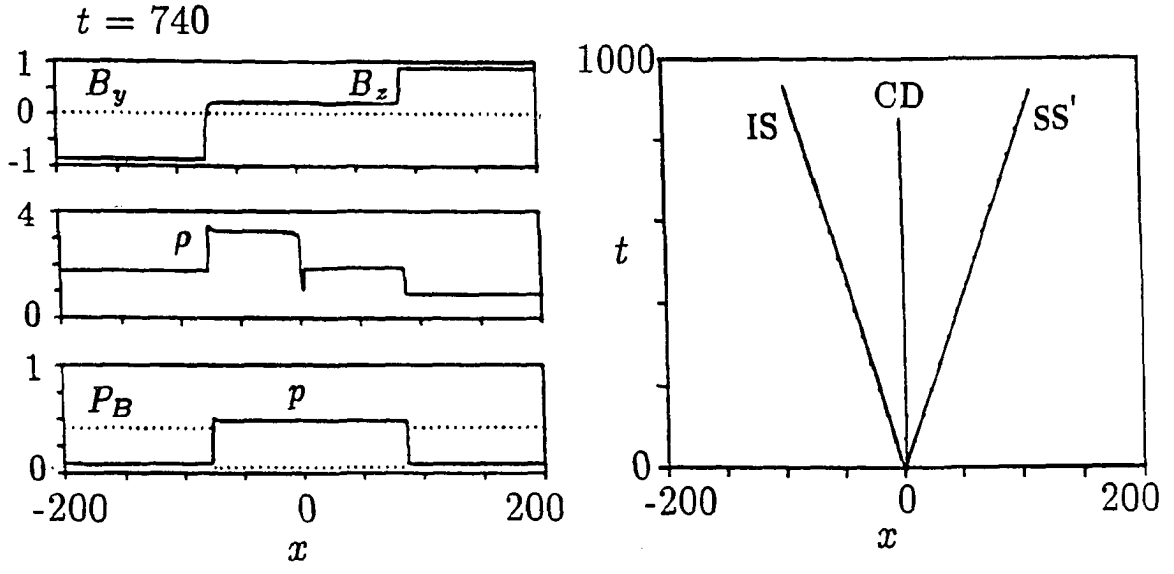

Figure 3.3 Same as Figure 3.2 with $B_{y0}(x) = 0$, except for a case with a small asymmetry in plasma density.

Reproduced with permission of the copyright owner. Further reproduction prohibited without permission.

in plasma density and magnetic field, a slow expansion wave appears on the magnetosheath. As shown in Figure 3.4, an intermediate shock IS and a slow expansion wave SE propagate on the magnetosheath side of the reconnection layer, an Alfven wave pulse AW' and a slow shock SS' on the magnetospheric side, and a contact discontinuity CD is found at the center of the reconnection layer. The current density is mainly concentrated at the intermediate shock IS on the magnetosheath side. Besides, two fast expansion waves (F and F') are observed to propagate ahead of the intermediate shock and the Alfven wave, respectively, toward the simulation boundary.

The simulation results at $t = 821$ are shown in Figure 3.5. The left column of the figure shows hodogram of the tangential magnetic field and spatial profiles of the plasma density and magnetic field strength, while the right column shows spatial profiles of the tangential components of magnetic field (B_y and B_z), tangential components of plasma flow velocity (V_y and V_z), plasma temperature and thermal pressure.

The intermediate shock IS bounding the reconnection layer from the magnetosheath side ranges from $x = -58.1$ (upstream) to $x = -54.8$ (downstream). The upstream physical quantities of this intermediate shock are marked by a and the downstream quantities by c. It is found that the y component of the magnetic field is zero both upstream and downstream of the shock, while B_z switches sign across the shock. The upstream shock normal angle $\theta_{nB1} = 69.3^o$, and the upstream plasma beta is $\beta_1 = 1.32$. The wave speeds of the fast, intermediate, and slow mode are, respectively, $C_{F1} = 0.317$, $C_{I1} = 0.0788$, and $C_{SL1} = 0.0580$ in the upstream region, and $C_{F2} = 0.271$, $C_{I2} = 0.0698$, and $C_{SL2} = 0.06770$ in the downstream region. The normal component of plasma flow velocity relative to the shock is $v_{n1} = 0.0811$ in the upstream region and $v_{n2} = 0.0637$ in the downstream region. Thus at this intermediate shock, the normal flow speed is sub-fast and super-intermediate in the upstream region and sub-slow in the downstream region. The intermediate shock IS is a steady 2-4 intermediate shock with an upstream intermediate Mach number $M_I = 1.029$.

Reproduced with permission of the copyright owner. Further reproduction prohibited without permission.

Reproduced with permission of the copyright owner. Further reproduction prohibited without permission.

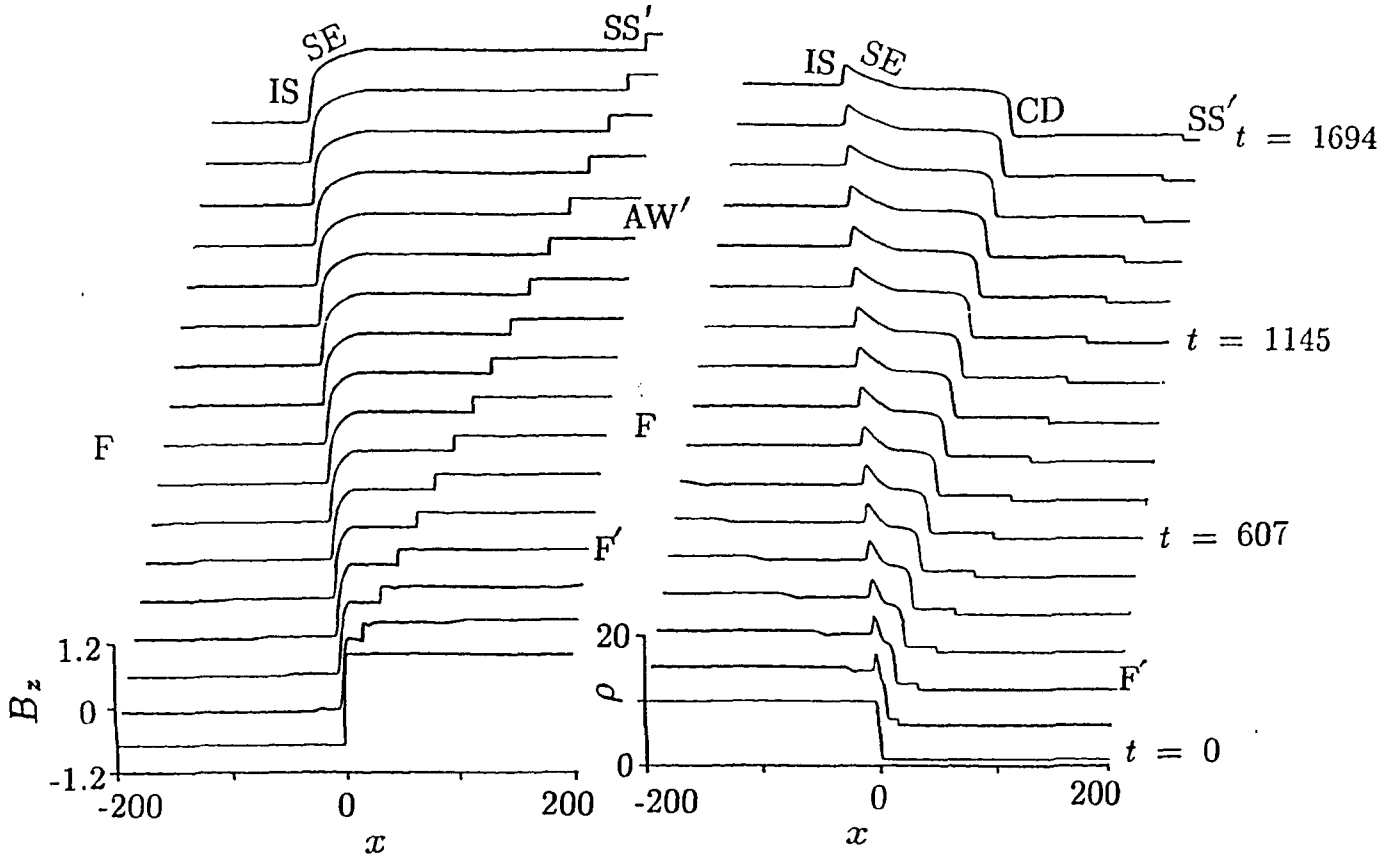

Figure 3.4 Spatial profiles of B_z and ρ obtained from the resistive MHD simulation of Case 3 at different times. An intermediate shock (IS), a slow expansion wave (SE), a contact discontinuity (CD), a slow shock (SS'), and an Alfven wave pulse (AW') are observed in the reconnection layer. Two weak fast expansion waves (F and F') are also observed.

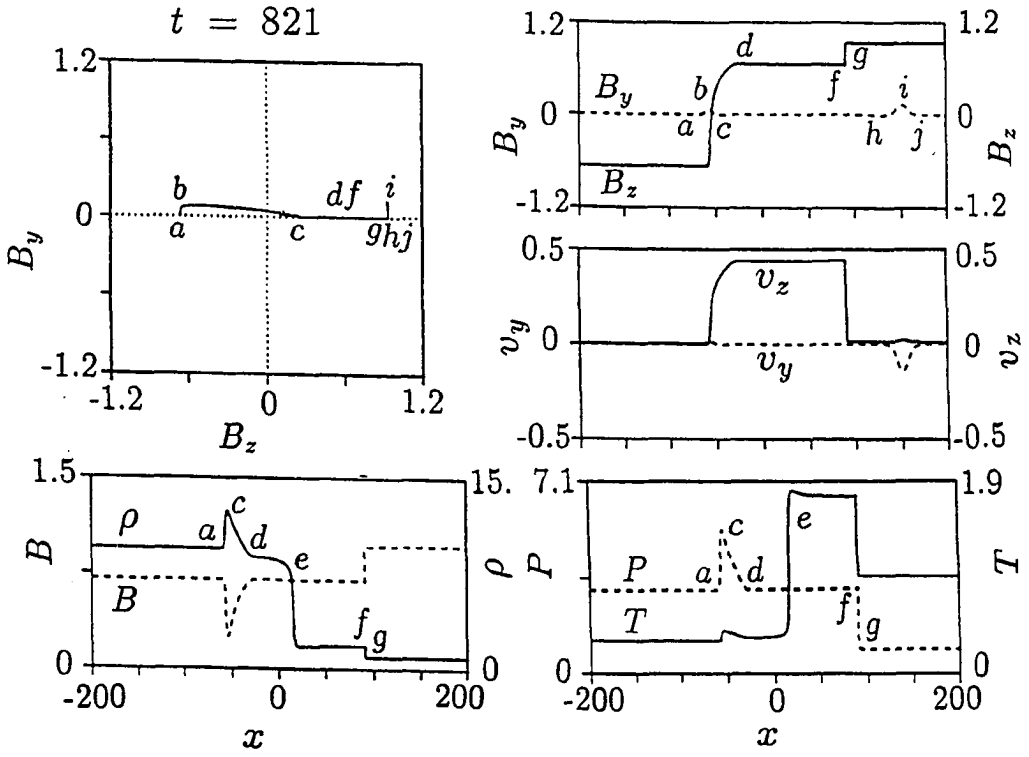

Figure 3.5 Resistive MHD simulation result of Case 3 at $t = 821$ hodogram of the tangential magnetic field and spatial profiles of ρ, B, B_y, B_z, V_y, V_z, T, and P.:

Reproduced with permission of the copyright owner. Further reproduction prohibited without permission.

As seen from the hodogram in Figure 3.5, across this coplanar 2-4 intermediate shock from state a to state c, the tangential magnetic field first goes along a nearly circular arc (ab) around the origin in the B_y-B_z plane, and then evolves to the downstream state along a nearly straight line (bc). This is a 2-4 intermediate shock with $B_y \neq 0$ in the shock transition layer. Such a structure is different from the 2-4 intermediate shock in Case 2, in which $B_y(x) = 0$ everywhere in the shock transition layer. This is due to the existence of a finite B_y in the transition region of initial current sheet. As time passes, this coplanar intermediate shock is found to have a constant width and a steady structure.

The intermediate shock is followed by the slow expansion wave SE whose upstream state is labeled by c and downstream by d. As shown in the hodogram of tangential magnetic field, B_y remains zero in this expansion wave, while B_z is positive and increases across the wave. The width of the expansion wave keeps increasing with time. The plasma density, temperature, and thermal pressure decrease across the expansion wave.

On the other hand, there exists an Alfven wave pulse AW' bounding the reconnection layer from the magnetospheric side, as seen in the region between the states marked by j and h in Figure 3.5. The existence of this wave is due to the non-zero B_y in the transition region of initial current sheet. This wave propagates to the magnetospheric side. The magnetic field strength and plasma density are conserved through this wave. Note that the Alfven speed in the magnetosphere is higher than that in the magnetosheath. According to the Walen relation, which relates the plasma flow velocity to the Alfven velocity, the amplitude of v_y pulse carried by the Alfven wave is very large compared to that carried by the intermediate shock ac on the magnetosheath side.

The slow shock SS' exists at $x = 90.8$; this slow shock propagates toward the magnetospheric side behind the Alfven wave. Across the slow shock, the plasma density and temperature increase from the values indicated by g (upstream) to those indicated by f (downstream), while the magnetic field strength decreases. At this slow shock, $M_1 = 0.686$, $\theta_{nB1} = 75.06°$, and $\beta_1 = 0.206$. The component B_y remains zero through the shock, as seen from the hodogram

Reproduced with permission of the copyright owner. Further reproduction prohibited without permission.

in Figure 3.5. The ratio of magnetic field strength, plasma density, pressure, and normal flow speed are, respectively, $R_B = 0.724$, $R_\rho = 1.938$, $R_P = 3.459$, and $R_{v_n} = 0.516$. The Rankine-Hugoniot conditions for slow shock are satisfied. This slow shock is found to have a constant width as time passes.

Between the slow shock SS' and the slow expansion wave SE in Figure 3.5, there exists a contact discontinuity CD at $x = 15.3$, as marked by e. The contact discontinuity matches the difference in plasma densities on the two sides, and also matches the high temperature downstream of the slow shock on the magnetospheric side and the low temperature at the slow expansion wave on the magnetosheath side.

3.3.4 Case 4: Symmetric Case with $B_y \neq 0$

In Cases 4 -- 6, the tangential magnetic fields on the two sides of initial current sheet are not exactly antiparallel ($B_y \neq 0$). In Case 4, the magnetic field and plasma density on the two sides of the initial current sheet are symmetric. We assume a constant initial guide field $B_{y0}(x) = B_{zm}$ in this case.

The results of Case 4 are shown in Figure 3.6. Four discontinuities ($TDIS + SS + SS' + TDIS'$) can be identified. At the discontinuity $TDIS$, the upstream and downstream magnetic fields of discontinuity are non-coplanar with the normal vector. The rotation angle of tangential magnetic field across this discontinuity is 45°. However, unlike the ideal MHD result in Figure 2.7, this structure is not a rotational discontinuity. The plasma density and pressure increase and the magnetic field strength decreases across this discontinuity. The upstream normal flow speed is sub-fast and super-intermediate, and the downstream normal flow speed is sub-intermediate and super-slow. This structure keeps evolving with time and is a 2-3 time-dependent intermediate shock. The structure behind the time-dependent intermediate shock ($TDIS$) is a slow shock (SS), across which the magnetic field strength decreases and the plasma density and pressure increase. The time-dependent intermediate shock $TDIS'$ and slow shock SS' on the righthand

Reproduced with permission of the copyright owner. Further reproduction prohibited without permission.

side of the reconnection layer are identical to $TDIS$ and SS on the lefthand side. Positions of the four discontinuities are shown as a function of time in the right plot of Figure 3.6.

It is found that the strength of 2-3 time-dependent intermediate shocks decreases with time and the thickness increases. As $t \rightarrow \infty$, the time-dependent intermediate shock gradually evolves to a rotational discontinuity across which the magnetic field strength and plasma density are conserved. As a result of the evolution of time-dependent intermediate shocks, the strength of slow shocks behind the time-dependent intermediate shocks also varies with time. The similarity of the time-dependent intermediate shock will be examined in Section 3.4.

3.3.5 Case 5: Weakly Asymmetric Case with $B_y \neq 0$

In Case 5, we set $\rho_s = 2\rho_m$, $B_{zs} = -B_{zm}$, $B_{y0}(x) = B_{zm}$, and $\eta = 0.039$. The result at $t = 546$ is shown in the left column of Figure 3.7. Five discontinuities ($TDIS + SS + CD + SS' + TDIS'$) can be identified in the spatial profiles. The discontinuity $TDIS$, which bounds the reconnection layer from the magnetosheath side, is a 2-3 time-dependent intermediate shock. At $TDIS$, $\theta_{nB1} = 79.59°$, $\beta_1 = 0.2$. The fast, intermediate, and slow wave speeds are, respectively, $C_{F1} = 0.749$, $C_{I1} = 0.125$, and $C_{SL1} = 0.0478$ in the upstream region and $C_{F2} = 0.744$, $C_{I2} = 0.124$, and $C_{SL2} = 0.050$ in the downstream region. The upstream normal flow speed ($v_{n1} = 0.126$) is sub-fast and super-intermediate, and the downstream normal flow speed ($v_{n2} = 0.124$) is sub-intermediate and super-slow. The discontinuity at $x = -55$ is a slow shock (SS), across which the plasma density increases and magnetic field decreases. The 2-3 time-dependent intermediate shock $TDIS'$ bounds the reconnection layer from the magnetospheric side. A slow shock SS' follows $TDIS'$ propagating to the magnetosphere side. A contact discontinuity is located at $x = 1$. Positions of the five discontinuities as a function of t are shown in the right plot of Figure 3.7. The resistive MHD simulation result is different from the ideal MHD result. The rotational discontinuities RD and RD' in Figure 2.8 are replaced by the time-dependent intermediate shocks $TDIS$ and $TDIS'$, respectively.

Reproduced with permission of the copyright owner. Further reproduction prohibited without permission.

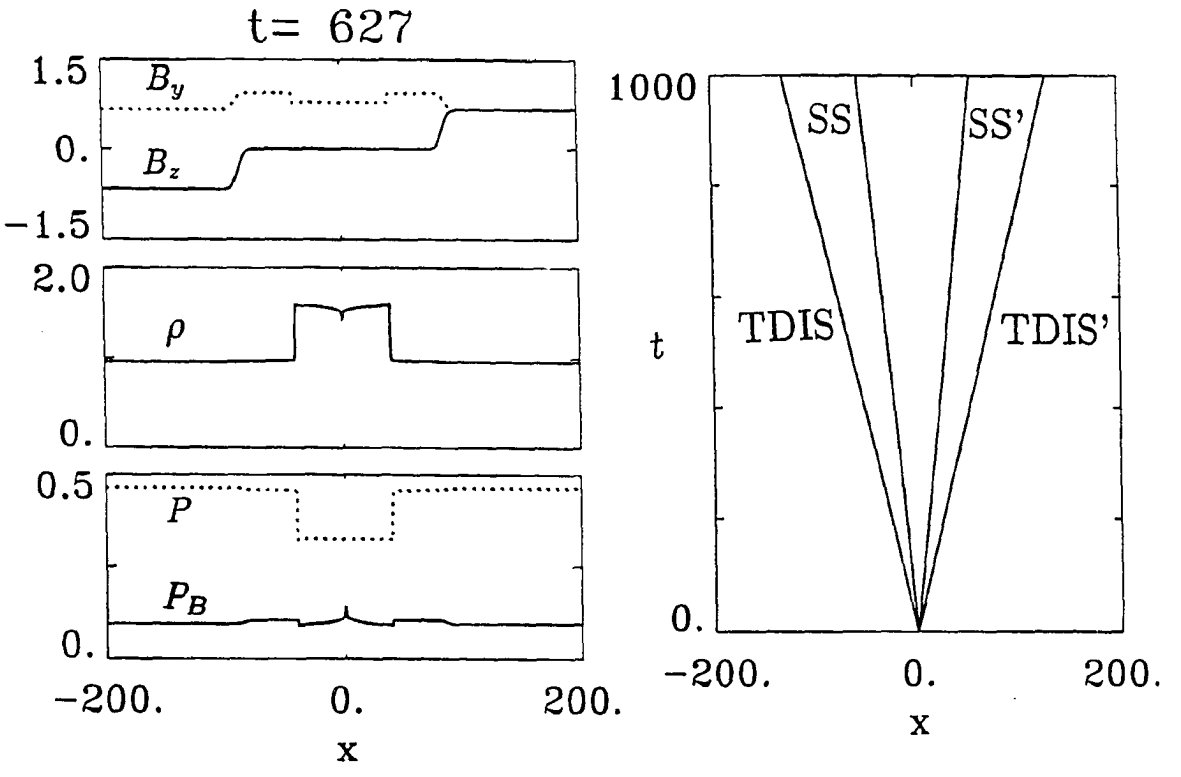

Figure 3.6 Same as Figure 3.2, except for a symmetric case with $B_{y0} \neq 0$.

Reproduced with permission of the copyright owner. Further reproduction prohibited without permission.

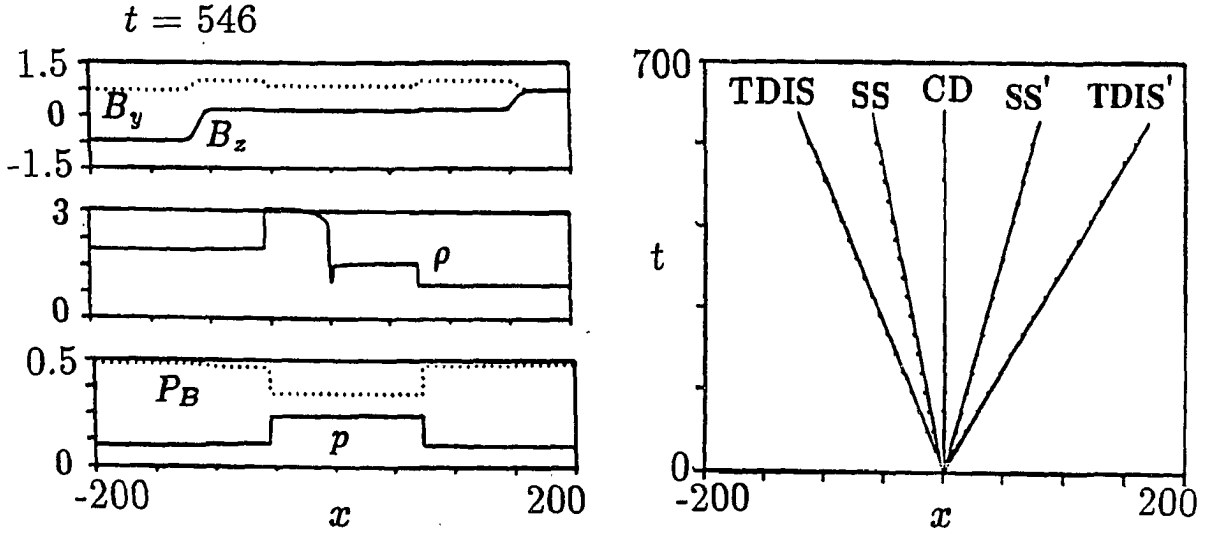

Figure 3.7 Same as Figure 3.2, except for a weakly asymmetric case with $B_{y0}(x) \neq 0$.

Reproduced with permission of the copyright owner. Further reproduction prohibited without permission.

3.3.6 Moderately and Highly Asymmetric Cases with $B_y \neq 0$

Case 6 is a moderately asymmetric case in which the guide fields in the magnetosheath and magnetosphere are not zero. The initial parameters for Case 6 are: $B_{zs} = -0.9B_{zm}$, $B_{ys} = B_{ym} = 0.3B_{zm}$, $\rho_s = 10\rho_m$, $T_s = 0.182T_m$, $\beta_m = 0.2$, and $\eta = 0.039$. In this case, $V_{As} = 0.289V_{Am}$. The angle between the tangential magnetic fields in the magnetosheath and in the magnetosphere is 145°.

Figure 3.8 shows the evolution of B_z and ρ of Case 6 in a time sequence from $t = 0$ to $t = 4323$. In early times, there are five discontinuities and waves in the reconnection layer: a time-dependent intermediate shock ($TDIS$), a slow expansion wave (SE), a contact discontinuity (CD), a slow shock (SS'), and a weak time-dependent intermediate shock ($TDIS'$). In later times with $t > 1574$, the time-dependent intermediate shock $TDIS$ on the magnetosheath side is found to split into a new time-dependent intermediate shock and a slow shock, while the slow expansion wave SE decays with time. The new time-dependent intermediate shock and its neighbouring slow shock gradually separate as time passes.

Figure 3.9 shows the hodogram of tangential magnetic field and the profiles of magnetic field and plasma quantities at $t = 690$. As seen in the figure, $TDIS$ (from upstream state a to downstream state b), SE (from b to c), CD (around state d), SS' (from f to e), and $TDIS'$ (from i to g) are formed in the resulting reconnection layer. The time-dependent intermediate shock $TDIS$ can be identified as the magnetopause. The wave speeds of the fast, intermediate, and slow modes upstream of $TDIS$ are, respectively, $C_{F1} = 0.326$, $C_{I1} = 0.0761$, and $C_{SL1} = 0.0399$, and those in downstream region are $C_{F2} = 0.265$, $C_{I2} = 0.0643$, and $C_{SL2} = 0.0549$. The normal flow speeds relative to $TDIS$ are found to be $v_{n1} = 0.0834$ (upstream) and $v_{n2} = 0.0615$ (downstream). The magnetic field strength, plasma density, and temperature are not conserved across $TDIS$. Since the physical quantities downstream of $TDIS$ vary with time, the slow expansion wave SE behind it also evolves with time. The time-dependent

Reproduced with permission of the copyright owner. Further reproduction prohibited without permission.

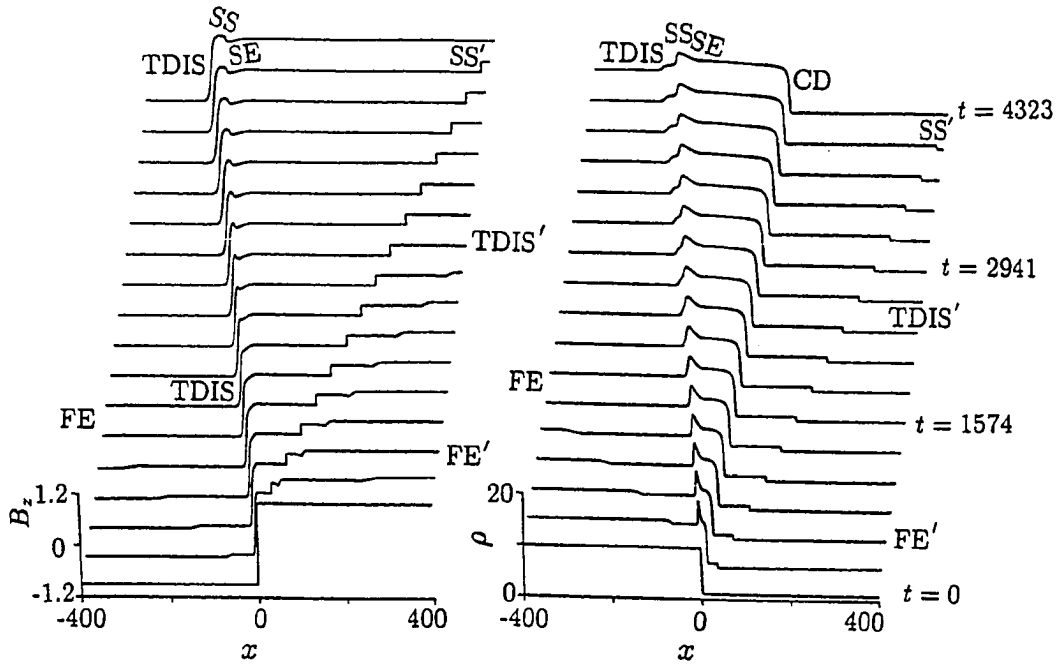

Figure 3.8 Same as Figure 3.5, except for Case 6, an asymmetric case with $B_{ys} = B_{ym} \neq 0$.

Reproduced with permission of the copyright owner. Further reproduction prohibited without permission.

intermediate shock $TDIS$ gradually evolves to a structure with a new time-dependent intermediate shock plus a slow shock.

Figure 3.10 shows the profile of the structures ab and bc at a later time, $t = 4909$. The hodogram of the tangential magnetic field and the spatial profiles of B_y, B_z, B and ρ are plotted. At this stage, $TDIS$ (ab) has evolved to a new time-dependent intermediate shock (aa') and a slow shock $(b'b)$. The width of this system has increased greatly as compared with the structure at $t = 690$. The new time-dependent intermediate shock is found to have $C_{F1} = 0.326$, $C_{I1} = 0.0761$, $C_{SL1} = 0.0399$, $C_{F2} = 0.306$, $C_{I2} = 0.0722$, $C_{SL2} = 0.0458$, $v_{n1} = 0.0776$, and $v_{n2} = 0.0713$. This structure with $C_{I1} < v_{n1} < C_{F1}$ and $C_{SL2} < v_{n2} < C_{I2}$ is a 2-3 time-dependent intermediate shock. Furthermore, the width of $TDIS$ increases with time, and the strength decreases. The magnetic field strength at a' increases gradually toward that at a. Thus the time-dependent intermediate shock evolves toward a rotational discontinuity, across which the magnetic field strength and the plasma density do not change. On the other hand, as the slow shock downstream of the 2-3 time-dependent intermediate shock is developed, the slow expansion wave SE becomes weaker, and the values of physical quantities at point b approach that at c.

The time-dependent intermediate shock $TDIS'$ (ig) on the magnetospheric side is also a 2-3 time-dependent intermediate shock. The rotation angle of tangential magnetic field across $TDIS'$ is small, and the jumps in density and magnetic field strength are also small. Behind $TDIS'$ is the slow shock SS' (fe). Our simulation indicates that at this slow shock, $\theta_{nB1} = 75.62^o$, $\beta_1 = 0.205$, and $M_{I1} = 0.670$. The jump relations of physical quantities across this slow shock are found to be $R_B = 0.741$, $R_\rho = 1.908$, and $R_P = 3.327$. They are found to satisfy the RH conditions.

We have also simulated several cases in which the angle Φ_{B0} between the tangential magnetic fields on the two sides of initial current sheet is set to 30^o, 60^o, 90^o, 135^o, 165^o, and

Reproduced with permission of the copyright owner. Further reproduction prohibited without permission.

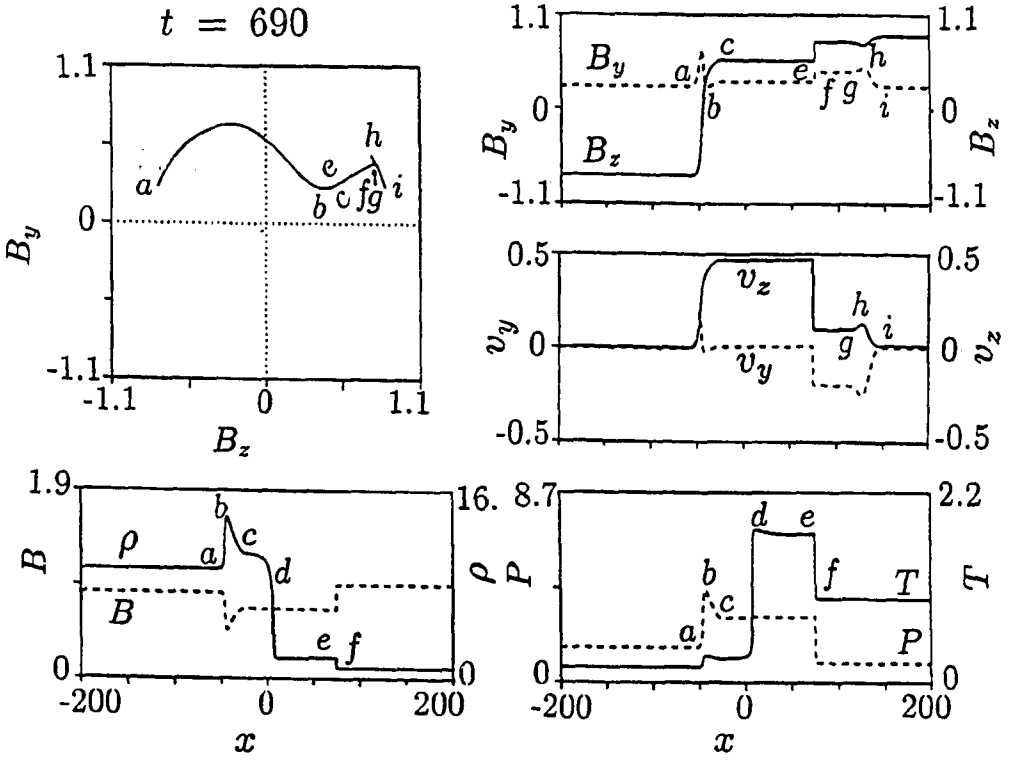

Figure 3.9 Same as Figure 3.6, except for Case 6, an asymmetric case with $B_{ys} = B_{ym} \neq 0$.

Reproduced with permission of the copyright owner. Further reproduction prohibited without permission.

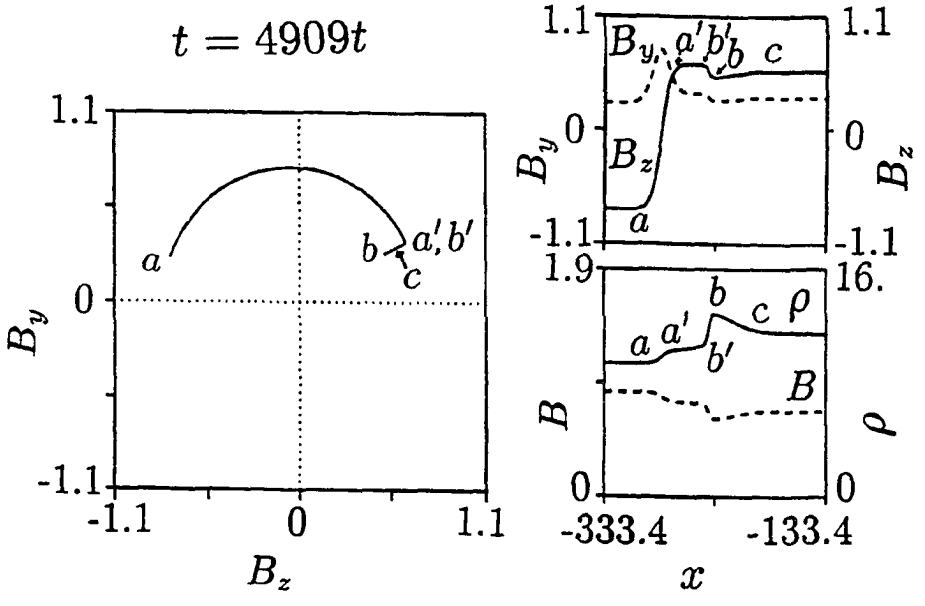

Figure 3.10 MHD simulation result of Case 6 at $t = 4909$.

Reproduced with permission of the copyright owner. Further reproduction prohibited without permission.

178^o, respectively. It is found that the time-dependent intermediate shocks bound the dayside reconnection layer, similar to the results in Cases 5 and 6.

For cases with a larger asymmetry in magnetic field and plasma density, we have five discontinuities $TDIS + SE + CD + SS' + TDIS'$ in the reconnection layer. The slow expansion wave SE does not vanish as $t \rightarrow \infty$, and the slow shock does not appear on the magnetosheath side of the reconnection layer.

3.5 Similarity of the 2-3 Time-Dependent Intermediate Shock

We now examine the similarity of 2-3 time-dependent intermediate shocks. Figure 3.11 shows the evolution of the time-dependent intermediate shock $TDIS$ in Case 5. In the upper panel, we present the spatial profile of B_z at $t = 546$. The leading edge, center, and trailing edge of the left TDIS are indicated by a, b, and c, respectively. Let $s = x - (C_{f1} + V_{x1})t$. Here $C_{f1} = 0.125$ and $V_{x1} = -0.028$ are, respectively, the upstream intermediate wave speed and flow speed. In the lower panel, we plot the position s as a function of $\sqrt{t}$ for the leading edge, center, and trailing edge of the TDIS, as indicated in the figure. The center of TDIS is determined by the local maximum of $|\partial B_z/\partial x|$, and the two edges are defined by the locations where $|\partial B_z/\partial x|$ equals to 0.01 of its maximum value at the shock. The center of the TDIS is best fit by the straight line $s = -0.00669\sqrt{t}$. The two edges are plotted against $\sqrt{t}$ as straight lines, indicating the shock width expands as $\sqrt{t}$. We have also examined other 2-3 time-dependent intermediate shocks obtained in our simulations and found the similarity as shown in Figure 3.11. Such similarity of the 2-3 time-dependent intermediate shocks have also been found by Wu and Kennel [1992] in the small-amplitude limit.

Moreover, the strength of 2-3 time-dependent intermediate shock gradually decreases with time. As $t \rightarrow \infty$, the 2-3 time-dependent intermediate shock gradually evolves to a rotational discontinuity with equal field strengths and densities on either side. This rotational discontinuity has

Reproduced with permission of the copyright owner. Further reproduction prohibited without permission.

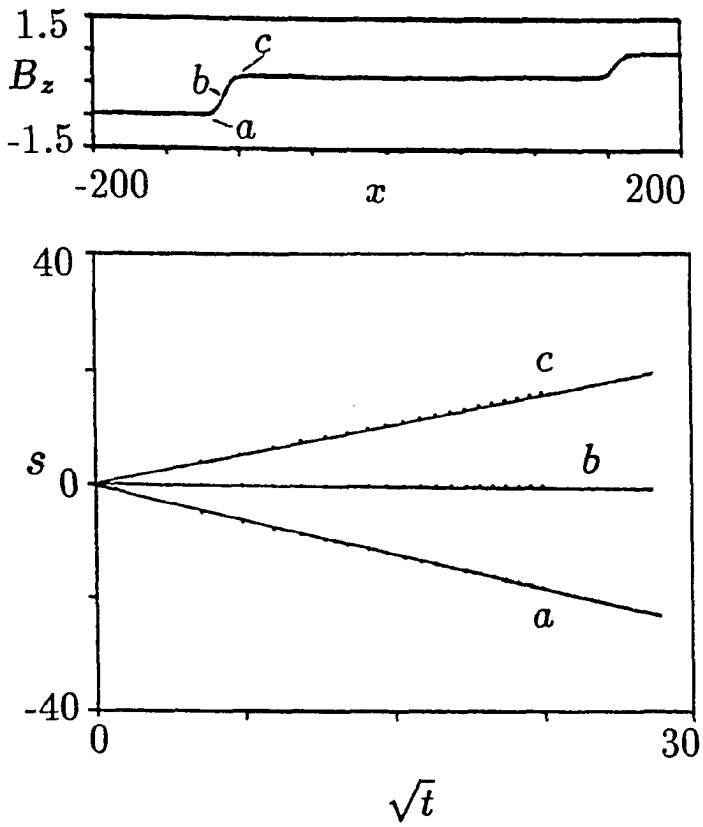

Figure 3.11 The lower panel plots the position s as a function of $\sqrt{t}$ for the leading edge (a), center (b), and trailing edge (c) of the left time-dependent intermediate shock $TDIS$ in Case 5. The upper panel shows the B_z profile at $t = 546$.

Reproduced with permission of the copyright owner. Further reproduction prohibited without permission.

an infinite width. The 2-3 time-dependent intermediate shock can also be called a time-dependent rotational discontinuity (TDRD) [Lin et al., 1992]. However, a steady rotational discontinuity with a finite width does not exist in finite time. It is also found that for cases with $B_y \neq 0$ on the two sides of the initial current sheet, the structure of the reconnection layer approaches the solution of the ideal MHD formulation as $t \rightarrow \infty$.

3.6 Summary

In this chapter, we have studied the structure of the reconnection layer based on a 1-D resistive MHD model. Steady intermediate shocks, time-dependent intermediate shocks, slow shocks, slow expansion waves, contact discontinuity, and Alfven wave may be present in the reconnection layer. A summary of our simulation results is given in Table 3.1.

The resistive MHD results are different from the ideal MHD formulation results. In particular, steady intermediate shocks and time-dependent intermediate shocks are found to bound the reconnection layer. The intermediate shocks, replacing rotational discontinuities, play the role of changing the direction of the magnetic field. The steady intermediate shock may be present in the cases with exactly antiparallel magnetic fields ($B_y = 0$) on the two sides of the initial current sheet, while time-dependent intermediate shocks are present in the cases with $B_y \neq 0$.

The main results are summarized below.

(a) Cases with $B_y = 0$: For symmetric cases with $B_y = 0$, a pair of slow shocks SS and SS' are present in the reconnection layer. For weakly asymmetric cases, there exist a steady intermediate shock IS, a contact discontinuity CD, and a slow shock SS'. For highly asymmetric cases, a slow expansion wave SE is present behind the intermediate shock IS, and we have IS, SE, CD, and SS' in the reconnection layer.

(b) Cases with $B_y \neq 0$: For symmetric cases with $B_y \neq 0$, a pair of time-dependent intermediate shocks $TDIS$ and $TDIS'$ and a pair of slow shocks SS and SS' are present in

Reproduced with permission of the copyright owner. Further reproduction prohibited without permission.

the reconnection layer. For weakly asymmetric cases, there exist a time-dependent intermediate shock $TDIS$, a slow shock SS, a contact discontinuity CD, a slow shock SS', and a weaker time-dependent intermediate shock $TDIS'$. For highly asymmetric cases, the slow shock SS is replaced by a slow expansion wave SE.

(c) The width of the 2-3 time-dependent intermediate shock obtained from our simulations expands self-similarly as $\sqrt{t}$. As the time $t \rightarrow \infty$, the time-dependent intermediate shock gradually evolves to a rotational discontinuity in which the plasma density and magnetic field strength are conserved. However, in the resistive MHD formulation, a steady rotational discontinuity with a finite width does not exist.

(d) The symmetric cases can be applied to the plasma sheet in the magnetotail. Two slow shocks are expected to exist in the reconnection layer. The asymmetric cases can be applied to the dayside magnetopause-boundary layer. In the cases in which the magnetic fields in the magnetosheath and magnetosphere are not exactly antiparallel, the reconnection layer consists of $TDIS$, SS/SE, CD, SS', and $TDIS'$. The time-dependent intermediate shock $TDIS$ can be identified as the magnetopause. In the cases with exactly antiparallel magnetic fields, the magnetopause $TDIS$ is replaced by a steady intermediate shock, and the boundary layer $TDIS'$ will disappear.

The results obtained from the resistive MHD formulation are modified if the kinetic effects of particles are considered. We will show in the next chapter that in the particle simulations, the time-dependent intermediate shocks can evolve quickly to a rotational discontinuity.

Reproduced with permission of the copyright owner. Further reproduction prohibited without permission.

Chapter 4 Structure of the Dayside Reconnection Layer in Hybrid Model

In the previous two chapters, we have studied the structure of reconnection layer based on the ideal MHD formulation and a resistive MHD model. However, the magnetospheric plasma is collisionless and the kinetic effects of particles on the structure of reconnection layer must be considered. The kinetic effects can be studied by particle simulations.

In this chapter, the structure of the reconnection layer at the dayside magnetopause is studied on the basis of a hybrid model in which the ions are treated as individual particles and electrons are treated as a fluid. We simulate the 1-D Riemann problem for the evolution of a magnetopause current sheet associated with the magnetic reconnection. The structure of slow shocks in the magnetotail reconnection layer will be studied in Chapter 5 based on hybrid simulations.

Although the rotational discontinuity does not exist in the resistive MHD simulation, the problem whether the rotational discontinuity can have a stable structure in a kinetic model is still in debate. Rotational discontinuities and intermediate shocks have been intensively studied by hybrid simulations. Stable structures of rotational discontinuities are found to exist in the simulations by Swift and Lee [1983], Lee et al. [1989a], Richter and Scholer [1989], Goodrich and Cargill [1991], Krauss-Varban [1993], and Vasquez and Cargill [1993]. On the other hand, Wu and Hada [1991a] claimed that the initial given rotational discontinuity is unstable and evolves to an intermediate shock and other waves. However, in all the simulations mentioned above, the initial profiles of the plasma density and magnetic field were set up as a rotational discontinuity; these authors did not study how various discontinuities are formed as a result of the evolution of magnetopause current sheet.

Reproduced with permission of the copyright owner. Further reproduction prohibited without permission.

It will be shown in this chapter that the structure of a reconnection layer obtained in hybrid simulations is different from that in resistive MHD simulations. In particular, in hybrid simulations the time-dependent intermediate shock quickly evolves to a steady rotational discontinuity with a constant width. Across the rotational discontinuity, the plasma density and magnetic field strength are not conserved due to the presence of pressure anisotropy. In addition, the contact discontinuity does not appear in the reconnection layer, and the slow shocks and expansion waves are modified as compared with those obtained in resistive MHD simulations.

In Section 4.1, we describe the simulation model. The simulation results are given in Sections 4.2 and 4.3. In Section 4.4, we compare our hybrid simulation results with satellite observations at the dayside magnetopause. Finally, a summary is given in Section 4.5.

4.1 Simulation Model

In our hybrid simulation, an initial current sheet which separates two uniform plasma regions is located at $x = 0$. As described in Chapter 3, the two plasma regions have antiparallel magnetic field components in the z direction and a common guide magnetic field in the y direction. The initial profiles of the z-component magnetic field, temperature, magnetic field strength, and plasma pressure are given by equations (3.3) -- (3.7), respectively, as in the resistive MHD simulations. Across the initial current sheet, the magnetic field strength and temperature increases smoothly from the magnetosheath to the magnetosphere, while the plasma density and pressure decreases smoothly.

The hybrid code used in this study is the one described by Swift and Lee [1983]. In the hybrid model, ions are treated as discrete particles moving in a self-consistent electromagnetic field, and electrons are treated as a massless fluid. Charge neutrality is assumed in calculations.

Let the subscript "s" denote physical quantities in the magnetosheath and "m" denote quantities in the magnetosphere. In the simulation, the length per cell is $0.158\lambda_{im}$, where the

Reproduced with permission of the copyright owner. Further reproduction prohibited without permission.

magnetospheric ion inertial length $\lambda_m = c/\omega_{pim}$, c is the speed of light, and ω_{pim} is the ion plasma frequency in the magnetosphere. The system length used in our study is 4000 -- 6000 cells. Two buffer zones are set up at the two ends of the simulation domain. These boundaries are located far from the resulting discontinuities in reconnection layer so that the main structure of the reconnection layer is not influenced by the boundary. The simulation results in this chapter show only the central part of the whole simulation domain.

The ion number density per cell, N, on the magnetospheric side (low plasma density side) is $N_m = 25$, and the number density on the magnetosheath side is $N_s = 100$ -- 750. The initial current sheet, which is at the center of simulation domain, has a half-width of $2\lambda_m$. The normal component of magnetic field is 0.25 B_{zm}. In the hybrid simulation, time is expressed in units of Ω_m^{-1}, where $\Omega_m = eB_m/m_ic$ is the ion cyclotron frequency in the magnetosphere, e is the elementary charge, and m_i is the ion mass. The velocity is expressed in the magnetospheric Alfven speed V_{Am}, the spatial coordinate is expressed in λ_m, the magnetic field is expressed in B_m, and the temperature is expressed in T_m.

We have simulated many cases for the dayside reconnection layer. Two typical cases are presented in this chapter. In Case 1, the tangential magnetic fields in the magnetosheath and in the magnetosphere are exactly antiparallel with $B_{ys} = B_{ym} = 0$. Case 1 corresponds to Case 3 in the resistive MHD simulation of Chapter 3. In Case 2, the guide fields B_{ys} and B_{ym} are not zero, with $B_{ys} = B_{ym} = 0.3B_{zm}$. Case 2 corresponds to Case 6 of Chapter 3.

4.2 Case 1 with Zero Guide Field ($B_y = 0$)

In Case 1, the guide fields (B_y) in the magnetosheath and magnetosphere are set to zero. The initial conditions of Case 1 are: $B_{zs} = -0.7B_{zm}$, $B_{ys} = B_{ym} = 0$, $T_s = 0.339T_m$, $N_s = 10N_m$, and $\beta_m = 0.2$. The initial tangential magnetic field has a righthand rotation from the magnetosheath to the magnetosphere, with a rotation angle of 180°. The Alfven speed

Reproduced with permission of the copyright owner. Further reproduction prohibited without permission.

in magnetosheath, V_{As}, equals $0.228V_{Am}$. The ion cyclotron frequency in the magnetosheath is $\Omega_s = 0.724\Omega_m$. For the magnetospheric magnetic field with $B \sim 50\gamma$, the ion cyclotron frequency $\Omega_m \sim 4.3s^{-1}$. Thus $t = 600\Omega_m^{-1}$ corresponds to $t = 140s$. At $t = 0$, the plasma thermal pressure is assumed isotropic everywhere. The simulations have been performed for cases with the initial temperature ratio $T_e/T_i = 0$, 0.2, and 0.5 at $t = 0$, where T_e and T_i are the electron and ion temperature, respectively. Results for these cases show no qualitative difference. Here we show results corresponding to $T_e = 0$. The resistive MHD simulation results for this case have been shown in Case 3 of Chapter 3.

4.2.1 Overall Structure of the Reconnection Layer

Figure 4.1 shows the evolution of B_z and N in a time sequence from $t = 0$ to $t = 618\Omega_m^{-1}$. The system length shown in the figure is $240\lambda_m$. In this case the ion inertial length in the magnetosheath is $\lambda_s = 0.316\lambda_m$. In early times of the simulation run, two fast expansion waves are observed to propagate away from initial current sheet along the trajectory pp' and uu', respectively, as indicated in Figure 4.1. The fast expansion waves are identified by a decrease in N and an increase in B_z. Similar to the MHD simulation result shown in Figure 3.5, an intermediate shock is found to propagate on the magnetosheath side along qq' in Figure 4.1. At this intermediate shock, the B_z profile has a large ramp, N dips significantly in the shock transition region, and plasma is accelerated. It is found that magnetosheath-like plasmas with a high flow speed are present earthward of the intermediate shock. The electric current in the reconnection layer is concentrated mainly at the intermediate shock, which is observationally identified as the magnetopause. An Alfven wave is observed on the magnetospheric side as identified by a B_z pulse, propagating along ss'.

However, unlike the MHD simulation result for this case, there appears no contact discontinuity in the boundary layer because of the mixing of particles from the magnetosheath side and from the magnetospheric side. Note that the boundary layer is defined as the region containing

Reproduced with permission of the copyright owner. Further reproduction prohibited without permission.

both the magnetosheath and the magnetospheric plasmas. Across the boundary layer between the intermediate shock qq' and the front rr' in Figure 4.1, the plasma density decreases from the magnetosheath value to the magnetospheric value. Similar to the density profile at the expansion wave in the MHD simulation result in Figure 3.5, the plasma density in the boundary layer earthward of the intermediate shock decreases with a corresponding increase in the magnetic field strength. However, the slow expansion wave behind the intermediate shock is strongly modified as compared with that in the MHD simulation. In addition, no clear shock front can be identified for the slow shock on the magnetosheath side.

4.2.2 *Steady Intermediate Shock at the Magnetopause*

We now examine the simulation result of Case 1 in detail. The result at $t = 464\Omega_m^{-1}$ are shown in Figure 4.2. The left column of the figure shows, from the top to the bottom, hodogram of the tangential magnetic field and spatial profiles of the ion number density and tangential magnetic field components, respectively. The right column shows spatial profiles of the ion temperatures perpendicular and parallel to the local magnetic field ($T_\perp$ and $T_\parallel$) and tangential components of ion flow velocity (V_{iy} and V_{iz}), respectively.

Across the intermediate shock the tangential magnetic field has a righthand rotation and B_z switches sign, changing from state a to state b. The magnetic fields upstream and downstream are coplanar with the normal direction. A strong electric current is also observed in the shock. The downstream value of magnetic field strength is found to be slightly smaller than the upstream value, and the ion number density downstream of the shock is slightly greater than that upstream. Let the subscripts "1" and "2" denote the physical quantities upstream and downstream of a discontinuity, respectively. A close examination indicates $R_N \simeq 1.01$ and $R_B \simeq 0.93$ at this intermediate shock, where $R_N = N_2/N_1 = \rho_2/\rho_1$ and $R_B = B_2/B_1$. The plasma pressure is found to

Reproduced with permission of the copyright owner. Further reproduction prohibited without permission.

Reproduced with permission of the copyright owner. Further reproduction prohibited without permission.

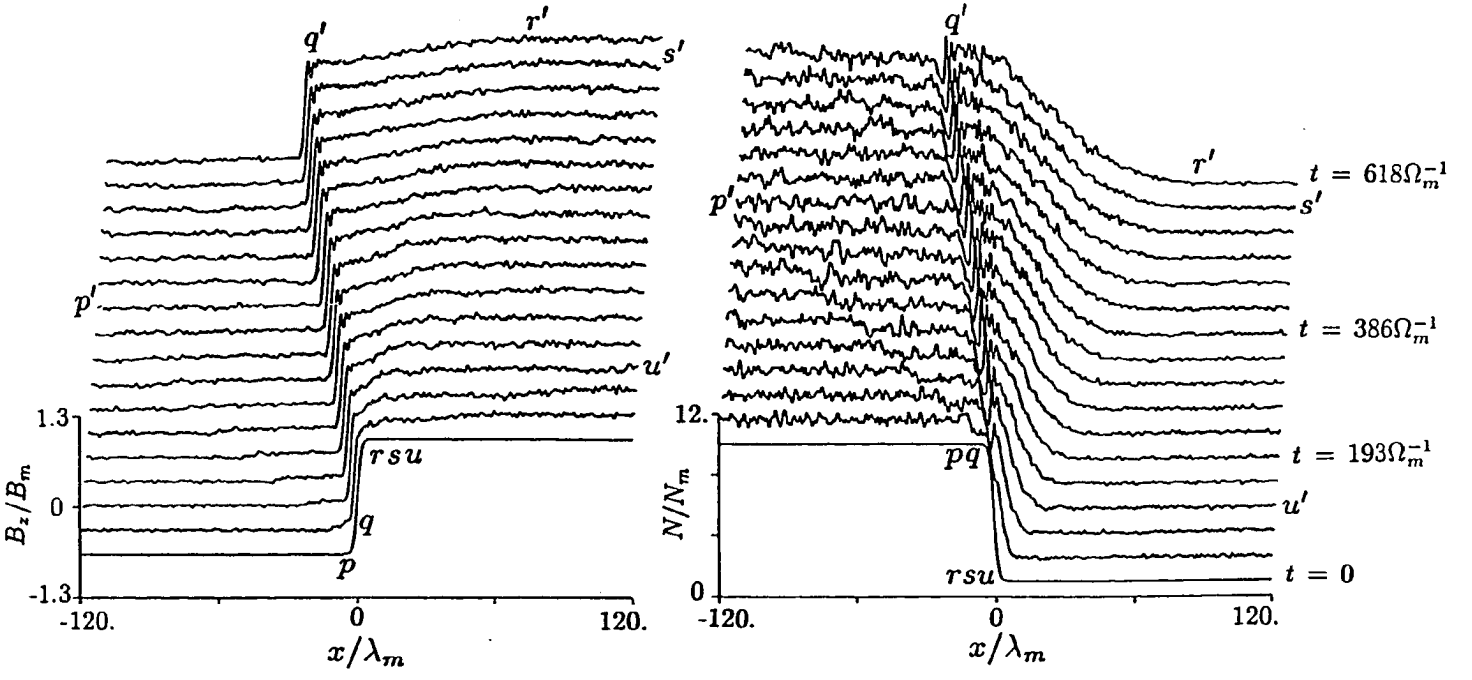

Figure 4.1 Spatial profiles of B_z and N in Case 1 in a time series.

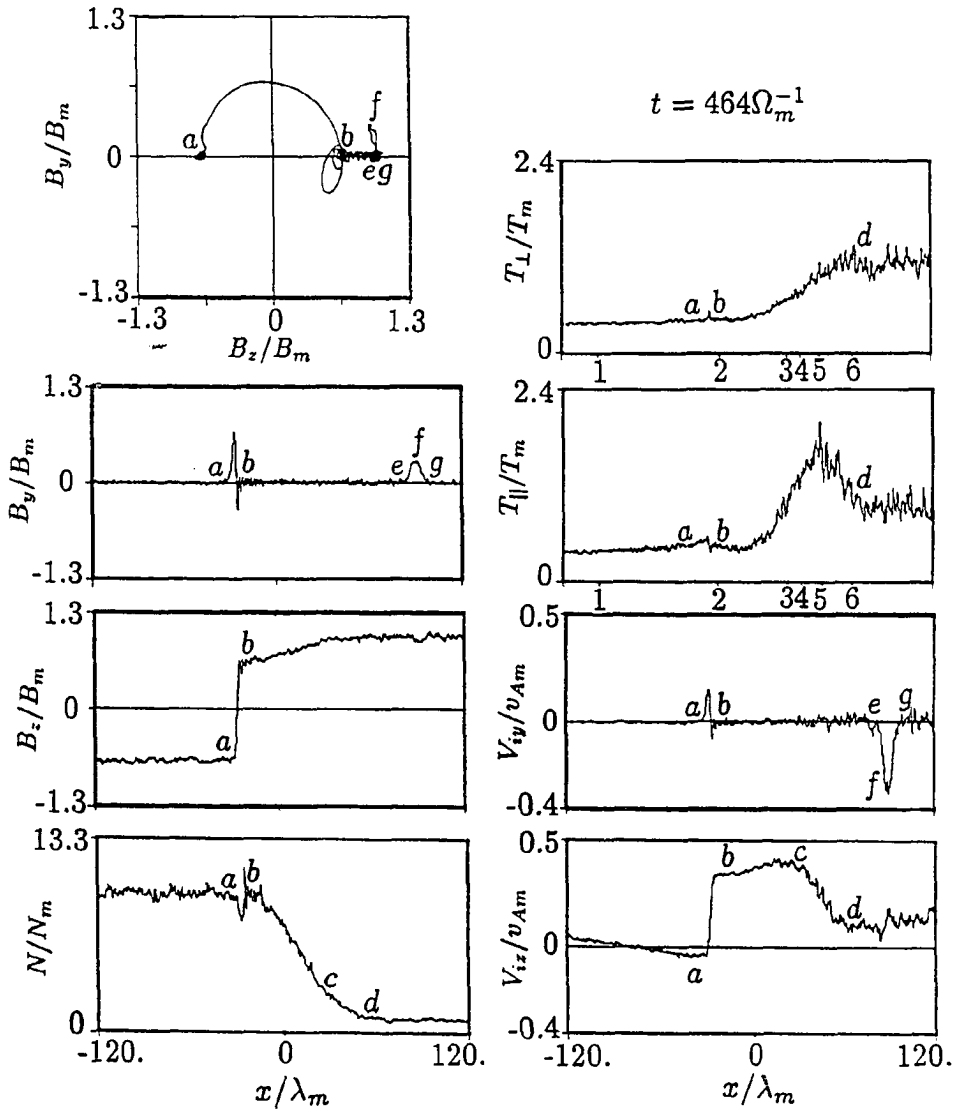

Figure 4.2 Hybrid simulation result of Case 1 at $t = 464\Omega_m^{-1}$. Hodogram of the tangential magnetic field and spatial profiles of B_y, B_z, N, $T_\perp$, $T_\parallel$, V_{iy}, and V_{iz} are shown in the figure.

Reproduced with permission of the copyright owner. Further reproduction prohibited without permission.

be anisotropic in most regions of reconnection layer. With pressure anisotropy, the intermediate mode speed can be written as

$$C_I = C_{I0}(1-\alpha)^{1/2} \tag{4.1}$$

where $C_{I0} = B_x/\sqrt{\mu_0\rho}$ is the intermediate speed in an isotropic plasma, $\alpha = (\beta_{\|} - \beta_{\perp})/2$ is a parameter measuring the pressure anisotropy, $\beta_{\|}$ is the plasma beta parallel to local magnetic field, and $\beta_{\perp}$ is the perpendicular plasma beta. Our calculation indicates that at the intermediate shock, $\theta_{nB1} \simeq 69.2°$, $\beta_1 \simeq 1.4$, $\alpha_1 \simeq 0.11$, $\alpha_2 \simeq 0.04$, $C_{I1} \simeq 0.0798V_{Am}$, $C_{I2} \simeq 0.0827V_{Am}$, and the normal components of flow velocities in the shock frame are $v_{n1} \simeq 0.0814V_{Am}$ and $v_{n2} \simeq 0.0810V_{Am}$. The speed of the shock front is obtained by measuring the time variation of the position with maximum slope of the average B_z in the shock transition region. It is found that the upstream normal flow speed is slightly greater than the local intermediate speed, while the downstream normal flow speed is slightly smaller than the intermediate mode speed. The upstream intermediate Mach number of the intermediate shock is $M_I \simeq 1.02$.

For $B_{y1} = B_{y2} = 0$ and $V_{y1} = V_{y2} = 0$, the RH conditions for MHD discontinuities (shocks) in an anisotropic plasma is given by equation (2.22) and can also be written as

$$[\rho v_x] = 0 \tag{4.2a}$$

$$[v_z B_x - v_x B_z] = 0 \tag{4.2b}$$

$$[\rho v_x v_z - \xi\frac{B_x B_z}{\mu_0}] = 0 \tag{4.2c}$$

$$[\rho v_x^2 + P + \frac{1}{3}(\xi+\frac{1}{2})\frac{B^2}{\mu_0} - \xi\frac{B_x^2}{\mu_0}] = 0 \tag{4.2d}$$

$$[(\frac{1}{2}\rho v^2 + \frac{5}{2}P + \frac{1}{3}(\xi+2)\frac{B^2}{\mu_0})v_x - \xi\frac{B_x B_z}{\mu_0}v_z - \xi\frac{B_x^2}{\mu_0}v_x] = 0 \tag{4.2e}$$

where $\xi = 1-\alpha$, the total ion thermal pressure $P = (P_{\|} + 2P_{\perp})/3$, and the square brackets denote the difference between the upstream and downstream values of physical quantities. It is

Reproduced with permission of the copyright owner. Further reproduction prohibited without permission.

found from the RH conditions (4.2) that the intermediate shock ab in the hybrid simulation of Case 1 is a 2-3 shock. For $\theta_{nB1} = 69.2^o$, $\beta_1 = 1.4$, $\alpha_1 = 0.11$, and $\alpha_2 = 0.04$, the ratios R_N and R_B based on (4.2) as a function of the intermediate Mach number M_I are plotted in Figure 4.3 for both 2-3 and 2-4 intermediate shocks. The dark squares in Figure 4.3 show the values of (R_N, M_I) and (R_B, M_I) obtained from the hybrid simulation for the intermediate shock in Figure 4.1. The extreme case of 2-3 intermediate shocks with $M_I = 1$ is a rotational discontinuity. The jump relations across the rotational discontinuity are indicated by RD in Figure 4.3. It is clearly seen that the intermediate shock obtained in the simulation satisfies the RH jump conditions for the 2-3 intermediate shock with $M_I \simeq 1.02$. On the other hand, the intermediate shock obtained from the MHD simulation for Case 1 is a 2-4 shock as shown in Chapter 3, and the jumps in plasma density and magnetic field strength across the 2-4 shock are relatively strong as compared with those of the 2-3 shock in the hybrid simulation of Case 1. Note that the extreme case of 2-4 intermediate shocks with $M_I = 1$ is a slow switch-off shock, as indicated by SO in Figure 4.3. We have also simulated other cases with $B_{ys} = B_{ym} = 0$ and with various magnetosheath to magnetospheric density and magnetic field ratios at the dayside magnetopause. Similar to Case 1, the results show a 2-4 intermediate shock in MHD simulations and a 2-3 intermediate shock in hybrid simulations.

Moreover, it is found from Figure 4.3 that as M_I decreases toward $M_I = 1$, R_N of the 2-3 intermediate shocks gradually becomes less than 1 and R_B becomes greater than 1. The rotational discontinuity at $M_I = 1$ has $R_N < 1$ and $R_B > 1$, indicating that the plasma density and magnetic field strength on the two sides are not equal. In an anisotropic plasma, the jump conditions across a rotational discontinuity can be written as equation (2.26). These jump conditions are valid for a rotational discontinuity with arbitrary directions of magnetic fields and plasma flow velocities in the upstream and downstream regions. If $\mathbf{B}_1$ is antiparallel to $\mathbf{B}_2$, these jump conditions are the same as the extreme of conditions (4.2) at $M_I = 1$. For a steady rotational discontinuity with $\alpha_1 > \alpha_2$, equation (2.26a) leads to $\rho_2 < \rho_1$, and thus $R_N < 1$. On the other hand, if $\alpha_1 < \alpha_2$, one obtains $R_N > 1$ for rotational discontinuity. For $\beta_1 = 1.4$, $\alpha_1 = 0.11$, and $\alpha_2 = 0.04$,

Reproduced with permission of the copyright owner. Further reproduction prohibited without permission.

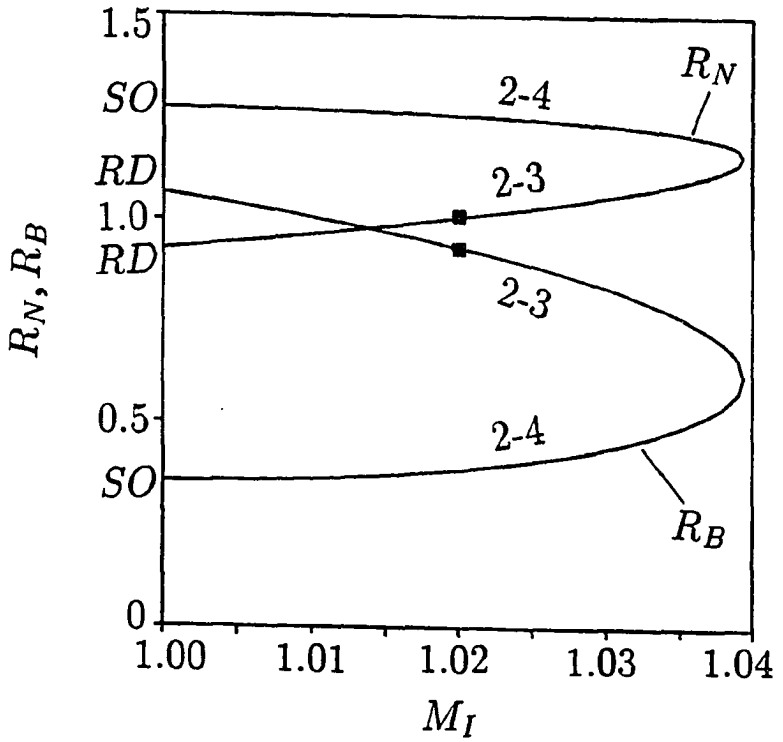

Figure 4.3 The ratios R_N and R_B as a function of M_I based on the Rankine-Hugoniot conditions for the 2-3 and 2-4 intermediate shocks. RD denotes the ration corresponding to a rotational discontinuity, and SO indicates the solutions of a switch-off shock. In the calculation, $\theta_{nB1} = 69.2^o$ and $\beta_1 = 1.4$ are used, and the plasma pressure anisotropy factors are $\alpha_1 = 0.11$ and $\alpha_2 = 0.04$. Two dark squares show the ratio R_N and R_B at $M_I = 1.02$ for the intermediate shock obtained from Case 1.

Reproduced with permission of the copyright owner. Further reproduction prohibited without permission.

the jump conditions for rotational discontinuity are $R_N = 0.927$ and $R_B = 1.065$, as plotted in Figure 4.3 at $M_I = 1$.

We have also examined the variation of other physical quantities for the intermediate shock in Figure 4.2 and found that they satisfy the corresponding RH jump conditions very well. The variation of the flow velocity from upstream to downstream nearly equals the variation of the Alfven velocity across the discontinuity. As seen in Figure 4.2, the plasma is accelerated to high speed through the intermediate shock. The V_{iz} profile in Figure 4.2 shows that the plasma flow speed behind the intermediate shock is $V_{iz} \sim 1.7V_{As}$, where V_{As} is the Alfven speed in the magnetosheath.

Figure 4.4a shows the width of the intermediate shock in Case 1 as a function of time. Since the intermediate shock is on the magnetosheath side of reconnection layer, we use magnetosheath quantities for normalizations in the figure. The shock width, D, is expressed in term of the ion inertial length in the magnetosheath, λ_s, while the time is expressed in term of Ω_s^{-1}. The open square at $t = 0$ in the figure represents the width of initial current sheet, and the dark squares indicate the shock width at different times with $t > 0$. The shock width is obtained by measuring the distance between the two locations where dB_z/dx equals 30% of its maximum value at the shock. It is seen that the shock width reaches a value of $\sim 5.4\lambda_s$ in less than $30\Omega_s^{-1}$ and then oscillates around this value in the simulation. The average shock width, $D \sim 5.4\lambda_s$, is smaller than the width of the initial current sheet. Figure 4.4b shows the value of $(\frac{N_2}{N_1})/(\frac{1-\alpha_1}{1-\alpha_2})$ as a function of time for the intermediate shock obtained in Case 1. Since the intermediate shock does not clearly separate from the following slow expansion fan in early times with $t < 55\Omega_s^{-1}$, the upstream and downstream values of physical quantities cannot be clearly identified. The data plotted in Figure 4.4(b) correspond to $t > 55\Omega_s^{-1}$. It is seen that as time passes, the quantity $(\frac{N_2}{N_1})/(\frac{1-\alpha_1}{1-\alpha_2})$ first oscillates with large amplitudes and then, as $t > 170\Omega_s^{-1}$, stays around a

Reproduced with permission of the copyright owner. Further reproduction prohibited without permission.

constant ~ 1.1, which agrees with the RH relations for the 2-3 intermediate shock. Note that for a rotational discontinuity, $(\frac{N_2}{N_1})/(\frac{1-\alpha_1}{1-\alpha_2}) = 1$.

4.2.3 Alfven Wave Pulse at the Inner Edge of Boundary Layer

As described earlier, an Alfven wave pulse is observed to bound the reconnection layer on the magnetospheric side. The upstream and downstream states of the wave are marked by g and e in Figure 4.2, respectively. The magnetic field strength and the plasma density are constant through the Alfven wave. Moreover, it is found that the Alfven wave structure does not diffuse with time. As the structure propagates toward the magnetosphere, the amplitude of the B_y pulse carried by this Alfven wave does not decrease with time, and the amplitude of V_{iy} pulse carried by the wave remains large as time passes.

4.2.4 Non-Existence of Contact Discontinuity

As mentioned earlier, plasmas from the magnetosheath side and from the magnetospheric side mix in the boundary layer region, which is approximately the region between state b and state d in Figure 4.2. The contact discontinuity which is present in the MHD simulation does not exist in the hybrid model because of the plasma mixing.

4.2.5 Modified Slow Expansion Wave and Slow Shock

Due to the non-existence of the contact discontinuity, the slow expansion wave and slow shock in the boundary layer are greatly modified. In Figure 4.2, the ion number density earthward of the intermediate shock decreases and the magnetic field increases toward the magnetospheric side. This profile appears like a slow expansion wave. However, the ion temperatures $T_\perp$ and $T_\parallel$ monotonically increase in this structure, instead of decreasing in an MHD expansion wave. On the other hand, the V_{iz}, N, and B_z profiles between state c and state d show that the plasma is accelerated, the ion number density gradually increases toward the magnetosheath side, and the

Reproduced with permission of the copyright owner. Further reproduction prohibited without permission.

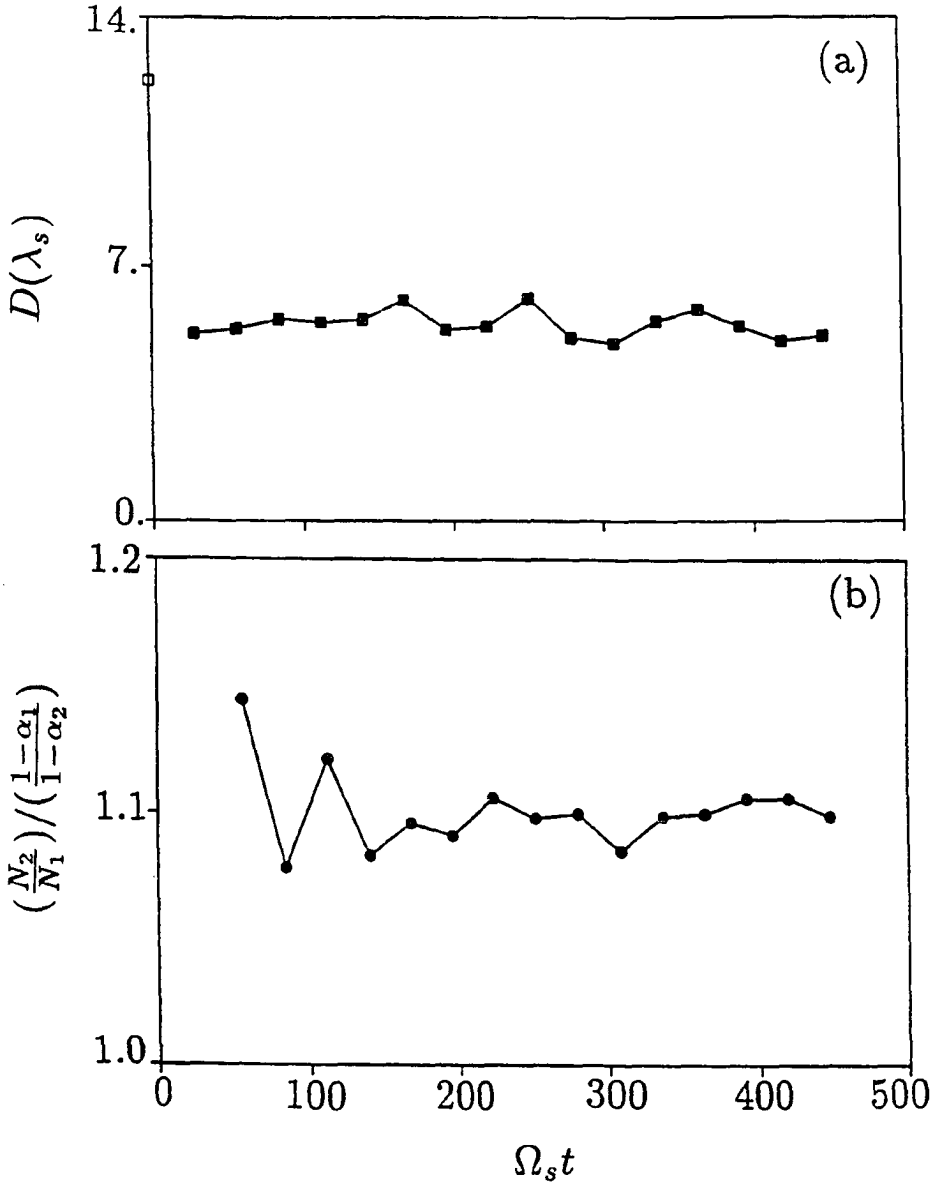

Figure 4.4 (a) The width D and (b) the ratio $(\frac{N_2}{N_1})/(\frac{1-\alpha_1}{1-\alpha_2})$ of the intermediate shock obtained in Case 1 as a function of time.

Reproduced with permission of the copyright owner. Further reproduction prohibited without permission.

magnetic field strength gradually decreases. Compared with the MHD simulation results in Figure 3.6, this structure appears like a slow shock. However, no clear shock front of the slow shock is observed. In addition, the perpendicular temperature decreases across this structure, and the total ion temperature, $T = (T_{\|} + 2T_{\perp})/3$, is also found to decrease from d to c. In the boundary layer, the magnetic field strength and total ion temperature smoothly increase from the magnetosheath side to the magnetospheric side, and the plasma density gradually decreases. These features are different from the results in the MHD simulation of Case 1.

4.2.6 Temperature Anisotropy and D-Shaped Ion Velocity Distribution

As seen in Figure 4.2, there exists a peak in $T_{\|}$ in the boundary layer region, while $T_{\perp}$ monotonically increases from the magnetosheath side to the magnetospheric side. Moreover, $T_{\|} > T_{\perp}$ is observed in the boundary layer. This is caused by the inter-penetration of two groups of ions, the accelerated plasma flow through intermediate shock and the hot ions from the magnetospheric side. Let v_{ix} and v_{iz} denote the x-component and z-component ion velocity, respectively. Figures 4.5a through 4.5f show, respectively, the velocity distributions of ions in the v_{ix}-v_{iz} phase plane at six different positions, 1 through 6, as indicated in the $T_{\|}$ and $T_{\perp}$ plots of Figure 4.2. The arrow in each plot represents the direction of local magnetic field. At position 1, the magnetosheath ions are relatively cold and have not been accelerated, as shown in Figure 4.5a. At site 6, the magnetospheric plasma is hot and the ion velocities spread greatly in the phase space. At position 2, the magnetosheath plasma has been accelerated by the intermediate shock and has a high bulk velocity, as shown in Figure 4.5b. Some hot ions from the magnetosphere are also present. The mixing of the accelerated magnetosheath plasma and the hot magnetospheric plasma is more evident in Figure 4.5c. Note that the ions of magnetosheath origin have a D-shaped distribution with the "D" pointing along the magnetic field, similar to those observed by satellites [Gosling et al., 1990a, b, c; Smith and Rodgers, 1991; Fuselier et al., 1991]. The mixing of plasmas takes place mainly along the magnetic field, leading to the decrease in $T_{\perp}/T_{\|}$. The mixing of

Reproduced with permission of the copyright owner. Further reproduction prohibited without permission.

two plasmas is also observed at position 4 and position 5. At position 5, $T_{\|}$ reaches a maximum. Earthward of this peak, the ion velocity distribution becomes dominated by the magnetospheric hot ions, and finally reaches the state at position 6. Note that the ions plotted in Figures 4.5a -- 4.5c come from two cells, whereas the ions in Figures 4.5d -- 4.5f are obtained from 8 cells so that there are enough data points to show the ion velocity distribution.

We have also run two cases in which the initial plasma density and magnetic field are the same as those in Case 1, except that an initial temperature anisotropy with $T_{\perp 0}/T_{\|0} = 1.2$ and 1.5 are imposed everywhere in the simulation domain, respectively. Similar to Case 1, the resulting reconnection layer consists of an intermediate shock on the magnetosheath side, an Alfven wave pulse on the magnetospheric side, and between them a transition region where the plasma density (magnetic field strength) monotonically decreases (increases). A decrease in $T_{\perp}/T_{\|}$ and a peak in $T_{\|}$ are observed in the boundary layer. Moreover, it is found that the ratio $T_{\perp}/T_{\|}$ in the boundary layer increases with $T_{\perp 0}/T_{\|0}$ and that $T_{\perp}/T_{\|} > 1$ in the boundary layer if $T_{\perp 0} > T_{\|0} > 1.5$.

However, if the speed of the magnetosheath plasma flow accelerated by the intermediate shock is much smaller than the thermal speed of the hot magnetospheric plasma, the peak in $T_{\|}$ may not exist in the boundary layer. For example, we have simulated a case with $\beta_m = 0.2$, $B_{zs} = 0.7B_{zm}$, and $N_s = 50N_m$. It is found that $T_{\perp}/T_{\|}$ decreases in the boundary layer, similar to Case 1. However, the peak in $T_{\|}$ does not exist, and that both $T_{\|}$ and $T_{\perp}$ monotonically increase from the magnetosheath side to the magnetospheric side in the boundary layer.

4.3 Case 2 with a Finite Guide Field ($B_y \neq 0$)

We now study Case 2 in which the tangential magnetic fields in the magnetosheath and in the magnetosphere are not antiparallel. The guide fields in the magnetosheath and magnetosphere are not zero. The initial conditions for Case 2 are: $B_{zs} = -0.9B_{zm}$, $B_{ys} = B_{ym} = 0.3B_{zm}$, $T_s = 0.182T_m$, $N_s = 10N_m$, and $\beta_m = 0.2$. In this case, $V_{As} = 0.289V_{Am}$. The angle

Reproduced with permission of the copyright owner. Further reproduction prohibited without permission.

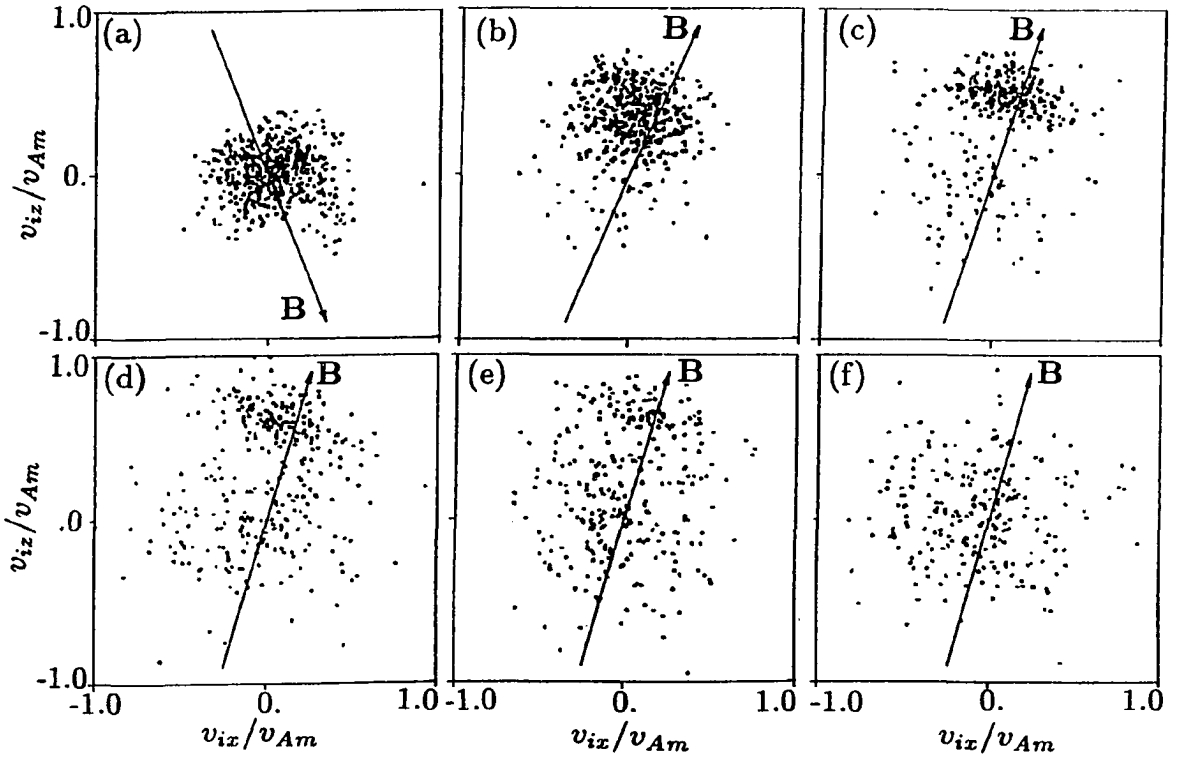

Figure 4.5 Ion velocities in the v_{ix}-v_{iz} phase plane obtained from Case 1. The plots in (a) -- (f) correspond to the results for six different positions in the reconnection layer as indicated in Figure 4.2.

Reproduced with permission of the copyright owner. Further reproduction prohibited without permission.

between the tangential magnetic fields in the magnetosheath and in the magnetosphere is 145^o. In addition, we set $T_e = 0$, $P_{\perp m} = P_{\parallel m}$, and $P_{\perp s} = P_{\parallel s}$. Note that the resistive MHD simulation results for this case have been shown in Case 6 of Chapter 3.

4.3.1 Overall Structure of the Reconnection Layer

Figure 4.6 plots the spatial profiles of B_z and N in a time series from $t = 0$ through $t = 644\Omega_m^{-1}$. Note that $\Omega_s = 0.914\Omega_m$ in this case. Similar to the MHD result in Figure 3.10, two fast waves are observed to propagate away from the main reconnection layer very quickly, along pp' and uu', respectively. However, the main structure of the reconnection layer is quite different from that in the resistive MHD simulation. Two rotational discontinuities, propagating along qq' and ss' respectively, are found to bound the reconnection layer. It is interesting to note that at $t \geq 402\Omega_m^{-1}$, a new fast wave appears upstream of the rotational discontinuity on the magnetosheath side and propagates along ww'. In the region between these two rotational discontinuities, particles from both sides mix, ion number density smoothly decreases from the magnetosheath side to the magnetospheric side. Similar to the results in Case 1, there exists no contact discontinuity in the boundary layer and no clear slow shock front can be identified.

4.3.2 Rotational Discontinuities Bounding the Reconnection Layer

Figure 4.7 shows the hodogram of tangential magnetic field and the profiles of magnetic field and plasma quantities at $t = 483\Omega_m^{-1}$. As seen in the figure, a rotational discontinuity with upstream state marked by a and downstream by b is formed on the magnetosheath side, and another rotational discontinuity whose upstream state is labeled by g and downstream by e is on the magnetospheric side. The current density in the reconnection layer is found to be concentrated mainly at the rotational discontinuity ab. The profile of V_{iz} shows the presence of high-speed plasma flow earthward from the main rotational discontinuity at the magnetopause. The plasma flow speed is $V_{iz} \sim 2V_{As}$.

Reproduced with permission of the copyright owner. Further reproduction prohibited without permission.

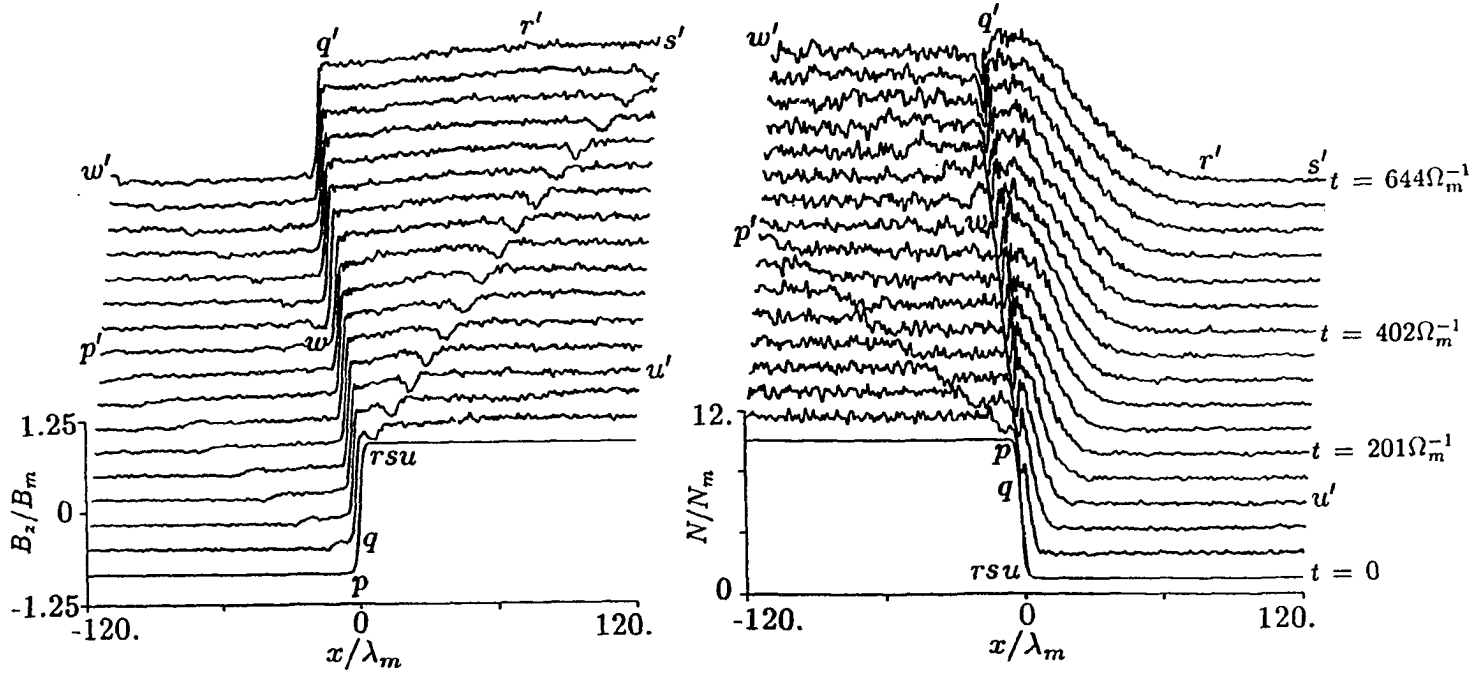

Figure 4.6 Time-series plots of B_z and N for Case 2.

Reproduced with permission of the copyright owner. Further reproduction prohibited without permission.

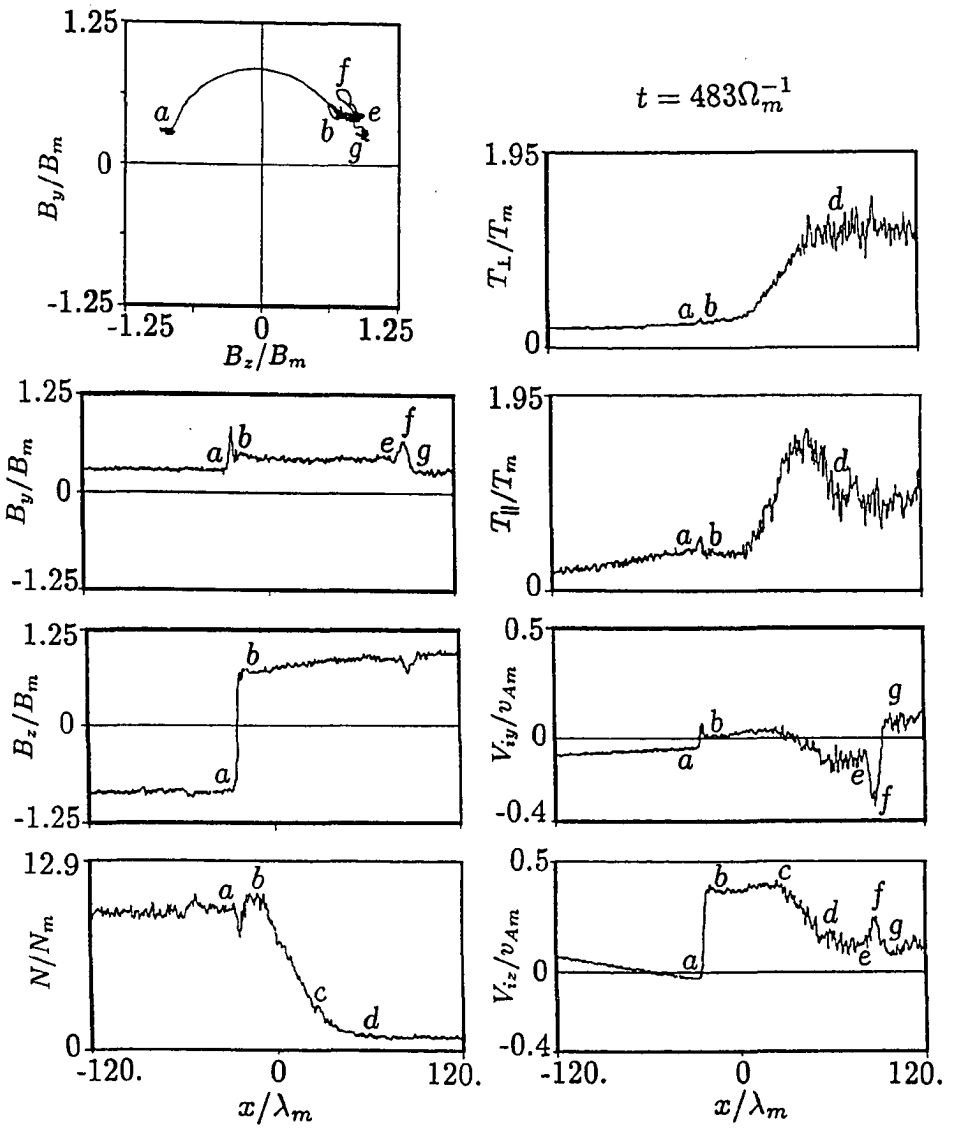

Figure 4.7 Simulation result at $t = 483\Omega_m^{-1}$ in Case 2. Hodogram of the tangential magnetic field and spatial profiles of physical quantities are shown in the figure.

Reproduced with permission of the copyright owner. Further reproduction prohibited without permission.

In order to show that ab is indeed a rotational discontinuity, we now examine the jumps of physical quantities across this discontinuity. The tangential magnetic field has a righthand rotation from upstream to downstream across the discontinuity. The rotation angle of the tangential magnetic field is less than 180^o. Thus the magnetic fields upstream and downstream of the discontinuity are not coplanar with the normal direction. With $\alpha_1 \simeq 0.150$ and $\alpha_2 \simeq 0.195$ obtained in the simulation, the intermediate mode speeds upstream and downstream of this discontinuity are found to be, respectively, $C_{I1} \simeq 0.0735 V_{Am}$ and $C_{I2} \simeq 0.0696 V_{Am}$. The plasma normal flow speeds are found to be $v_{n1} \simeq 0.0714 V_{Am}$ and $v_{n2} \simeq 0.0683 V_{Am}$. The jumps in magnetic field strength and ion number density across the discontinuity in simulation are found to be $R_B \simeq 0.973$ and $R_N \simeq 1.055$.

In Figure 4.8a we plot the variation of C_I/C_{I0} as a function of α, based on equation (4.1). The dark square in the figure corresponds to the upstream value $(\alpha_1, v_{n1}/C_{I01}) = (0.15, 0.896)$ for the rotational discontinuity obtained from the simulation, and the open square corresponds to the downstream value $(\alpha_2, v_{n2}/C_{I20}) = (0.195, 0.88)$, where $C_{I01} = B_x/\sqrt{\mu_0 \rho_1}$ and $C_{I02} = B_x/\sqrt{\mu_0 \rho_2}$. It is seen that the normal flow speeds upstream and downstream of the discontinuity are nearly the local intermediate speeds, which are the normal components of the local Alfven velocities. On the other hand, Figures 4.8b and 4.8c show the ratios R_B and R_N for rotational discontinuities as a function of α_1 based on the RH jump condition in equation (2.26). The perpendicular plasma beta used in the calculation is $\beta_{\perp 1} = 0.50$, which is the observed value for the discontinuity ab in Figure 4.7. The different curves in each plot correspond to the solutions for different values of α_2, as indicated in the plots. The solid curve in each plot shows the solutions corresponding to the observed value $\alpha_2 = 0.195$. The observed values of R_B and R_N with $\alpha_1 = 0.15$ for the discontinuity ab in the simulation are also shown as dark squares. It is found that the observed values of R_B and R_N satisfy the RH conditions for the rotational discontinuity

Reproduced with permission of the copyright owner. Further reproduction prohibited without permission.

with $\alpha_1 = 0.15$ and $\alpha_2 = 0.195$ very well. We have also examined the jumps at this rotational discontinuity for other physical quantities, and found they satisfy the RH conditions very well.

The width of the rotational discontinuity ab in our simulation is shown in Figure 4.9a as a function of time. It is seen that in early times the width of the discontinuity fluctuates and the mean width gradually decreases with time. Then in later times the width is steady around a value of $\sim 5\lambda_s$. The solid line in Figure 4.9b shows the value of $(\frac{N_2}{N_1})/(\frac{1-\alpha_1}{1-\alpha_2})$ for this rotational discontinuity as a function of time. It is seen that in early times $(\frac{N_2}{N_1})/(\frac{1-\alpha_1}{1-\alpha_2})$ is greater than 1, as in a time-dependent intermediate shock, and fluctuates greatly. In later times, the value of $(\frac{N_2}{N_1})/(\frac{1-\alpha_1}{1-\alpha_2})$ stays around 1, which corresponds the the value obtained from the RH conditions for a rotational discontinuity. Thus the steady rotational discontinuity is formed in about $300\Omega_s^{-1} \sim 75s$ in this case. Note that $\beta_s = 0.6$ for this rotational discontinuity. The dashed line in Figure 4.9 shows the value of $(\frac{N_2}{N_1})/(\frac{1-\alpha_1}{1-\alpha_2})$ for a rotational discontinuity formed in the case with $\beta_s = 0.2$. The rotation angle of tangential magnetic field across this discontinuity is nearly the same as that across the rotational discontinuity in Case 2. It is seen that the steady rotational discontinuity is formed more slowly than that with $\beta_s = 0.6$.

On the magnetospheric side, there is another rotational discontinuity ge. Across this discontinuity, the tangential magnetic field slightly changes direction, and the ion number density, plasma temperature, and magnetic field strength are nearly constant. A large-amplitude V_{iy} pulse is associated with this rotational discontinuity. This rotational discontinuity also quickly reaches a steady structure in our simulation.

We have also simulated several cases in which the angle between the tangential magnetic fields on the two sides of initial current is set to $50°$, $90°$, $130°$, and $170°$, respectively. It is found that rotational discontinuities bound the reconnection layer, similar to the result in Case 2.

Based on resistive MHD formulations, the rotational discontinuity does not form in finite time. The intermediate mode discontinuities may either be an intermediate shock or a time-dependent intermediate shock, whose width expands with time. However, in hybrid simulations, the steady

Reproduced with permission of the copyright owner. Further reproduction prohibited without permission.

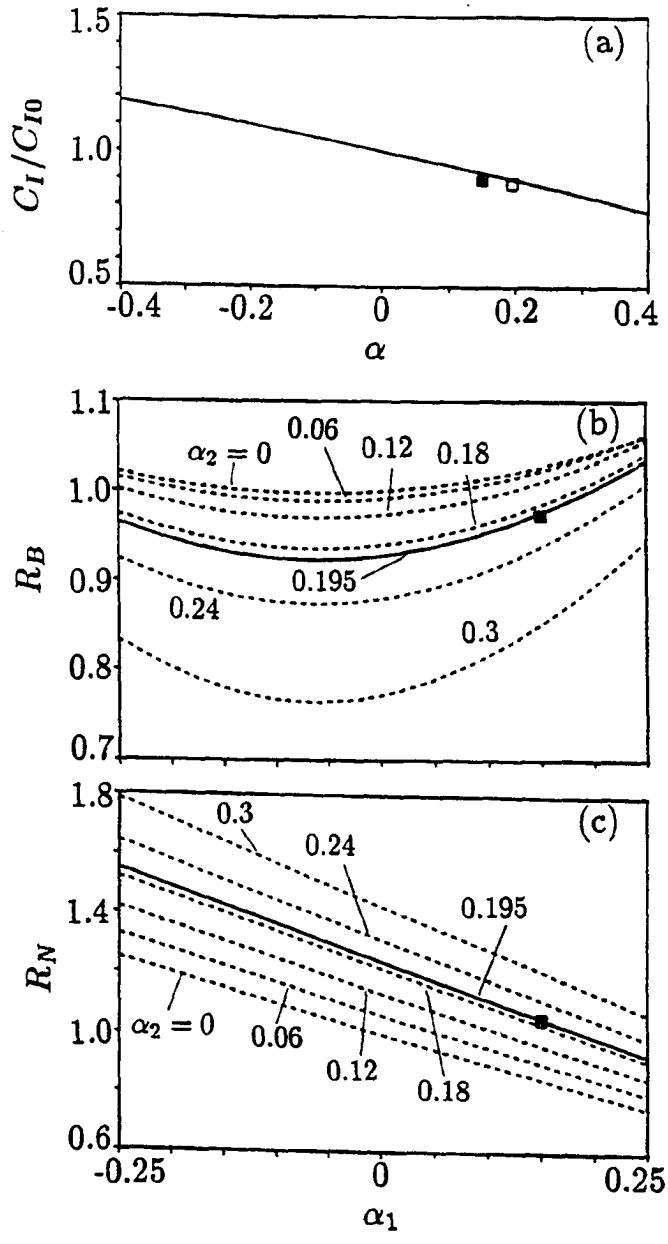

Figure 4.8 (a) The quantity C_I/C_{I0} as a function of α. The dark square corresponds to the upstream value (α_1, v_{n1}/C_{I01}) for the rotational discontinuity on the magnetosheath side in Case 2, and the open square corresponds to the downstream value (α_2, v_{n2}/C_{I02}). (b) The ratio R_B and (c) the ratio R_N as a function of α_1 obtained from the RH conditions for rotational discontinuities with $\beta_{\perp 1} = 0.5$. Different curves in the figure correspond to the solutions with different values of α_2. The dark squares at $\alpha_1 = 0.15$ show the observed values of R_B and R_N for the rotational discontinuity on the magnetosheath side.

Reproduced with permission of the copyright owner. Further reproduction prohibited without permission.

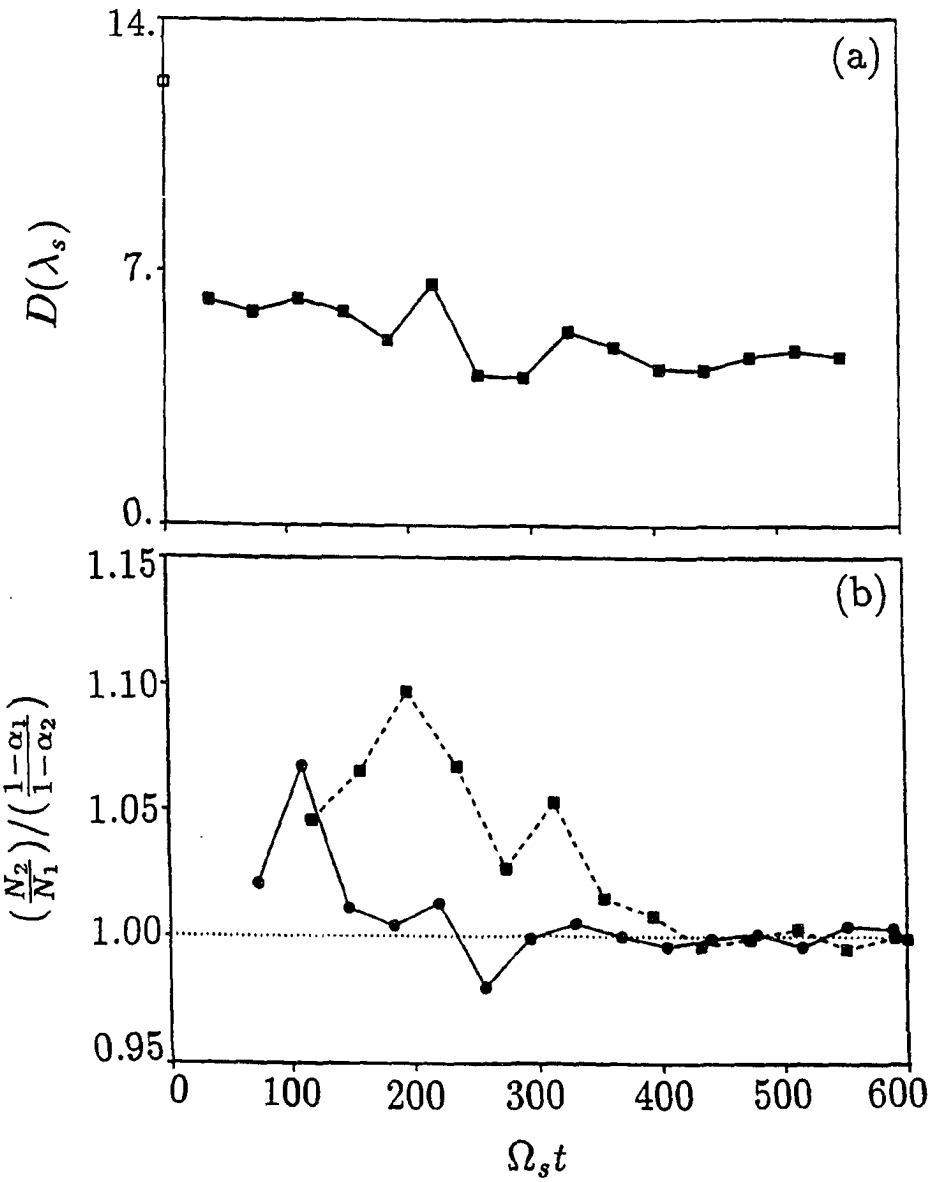

Figure 4.9 (a) The width D and (b) the ratio $(\frac{N_2}{N_1})/(\frac{1-\alpha_1}{1-\alpha_2})$ of the rotational discontinuity in Case 2 as a function of time are shown by the solid curves. The upstream plasma beta is $\beta_1 = 0.6$. For comparison, the dashed curve shows the ratio $(\frac{N_2}{N_1})/(\frac{1-\alpha_1}{1-\alpha_2})$ for the rotational discontinuity in the case with $\beta_1 = 0.2$.

Reproduced with permission of the copyright owner. Further reproduction prohibited without permission.

rotational discontinuity can be quickly formed from a time-dependent intermediate shock, as shown in Figure 4.9. The existence of steady structure of rotational discontinuity in hybrid simulations has been reported by several authors [e.g., Swift and Lee, 1983; Lee et al., 1989a; Richter and Scholer, 1989; Goodrich and Cargill, 1991]. In their simulations, the initial profiles of magnetic field and plasma quantity were determined by the RH conditions for a rotational discontinuity or an intermediate shock. As discussed by Lee et al. [1989a], trapped particles in rotational discontinuity can prevent the discontinuity from diffusing with time, resulting in the occurrence of steady structure of rotational discontinuity. However, the previous authors did not check the RH jump conditions for rotational discontinuities or intermediate shocks and nor did they consider the effect of pressure anisotropy presented in the simulations. Wu and Hada [1991a,b] have used hybrid simulations to show that an intermediate shock can be formed from a simple wave, and that an initial rotational discontinuity evolves to a 2-3 steady intermediate shock or time-dependent intermediate shock. Their simulations were limited to low to medium ion beta and the RH jump conditions were not checked in their paper. In the presence of pressure anisotropy, as occurred in their simulations, a density increase may not mean a shock. On the other hand, we have shown in this chapter that the 2-3 time-dependent intermediate shocks can quickly evolve to a rotational discontinuity, as illustrated in Figure 4.9. The evolution may take a longer time if the ion beta is low. The formation of rotational discontinuity is also observed for cases with $\eta^* \neq 0$.

4.3.3 Structure between Two Rotational Discontinuities

Between the two rotational discontinuities is the region where plasma from the magnetosheath side mixes with that from the magnetospheric side. Similar to the result in Case 1, there exists no contact discontinuity in this boundary layer. The magnetic field strength and perpendicular ion temperature gradually increase from the magnetosheath side to the magnetospheric side, while the ion number density gradually decreases. No clear slow shock can be identified. The total ion temperature is also found to increase monotonically toward the magnetospheric side. A decrease

Reproduced with permission of the copyright owner. Further reproduction prohibited without permission.

in $T_\perp/T_\parallel$ is also observed in the boundary layer. A D-shaped ion velocity distribution is obtained in the boundary layer.

4.4 Comparison with Observations

4.4.1 Observations of Rotational Discontinuity and High-Speed Flow in the Dayside Magnetopause-Boundary Layer

Layered structure associated with magnetic reconnection have been observed at the dayside magnetopause. Satellite observations indicate that the magnetopause current layer is frequently a rotational discontinuity, where the magnetic field changes from the magnetosheath to the magnetosphere, and high-speed plasma flow is present in the dayside boundary layer [e.g., Paschmann et al., 1979; Sonnerup et al., 1981; Berchem and Russell, 1982].

Figure 4.10 shows an ISEE-1 observation of dayside magnetopause-boundary [Paschmann et al., 1979; Sonnerup et al., 1981; Rijnbeek et al., 1988]. Figure 4.10a shows the profiles of the magnitude of tangential magnetic field (B_t), azimuthal angle of the tangential magnetic field ($\alpha_B = tan^{-1}(B_M/B_L)$), plasma pressure P (the lowest dark trace in the third panel), plasma beta (β), proton number density (N_p), proton temperature (T_p), magnitude of tangential flow velocity (V_t), and azimuthal angle of the flow velocity (α_V). The lightest trace in the third panel shows the profile of magnetic pressure ($P_B = B_t^2/2\mu_0$), and the top line shows the profile of total pressure ($P + P_B$). Figure 4.10b shows hodograms of the magnetic field in the L-M plane and L-N plane during the interval 0:39 UT -- 0.46 UT, where the N-direction represents the normal to the magnetopause, and L and M point, respectively, northwards and dawnwards along the plane of the magnetopause.

Reproduced with permission of the copyright owner. Further reproduction prohibited without permission.

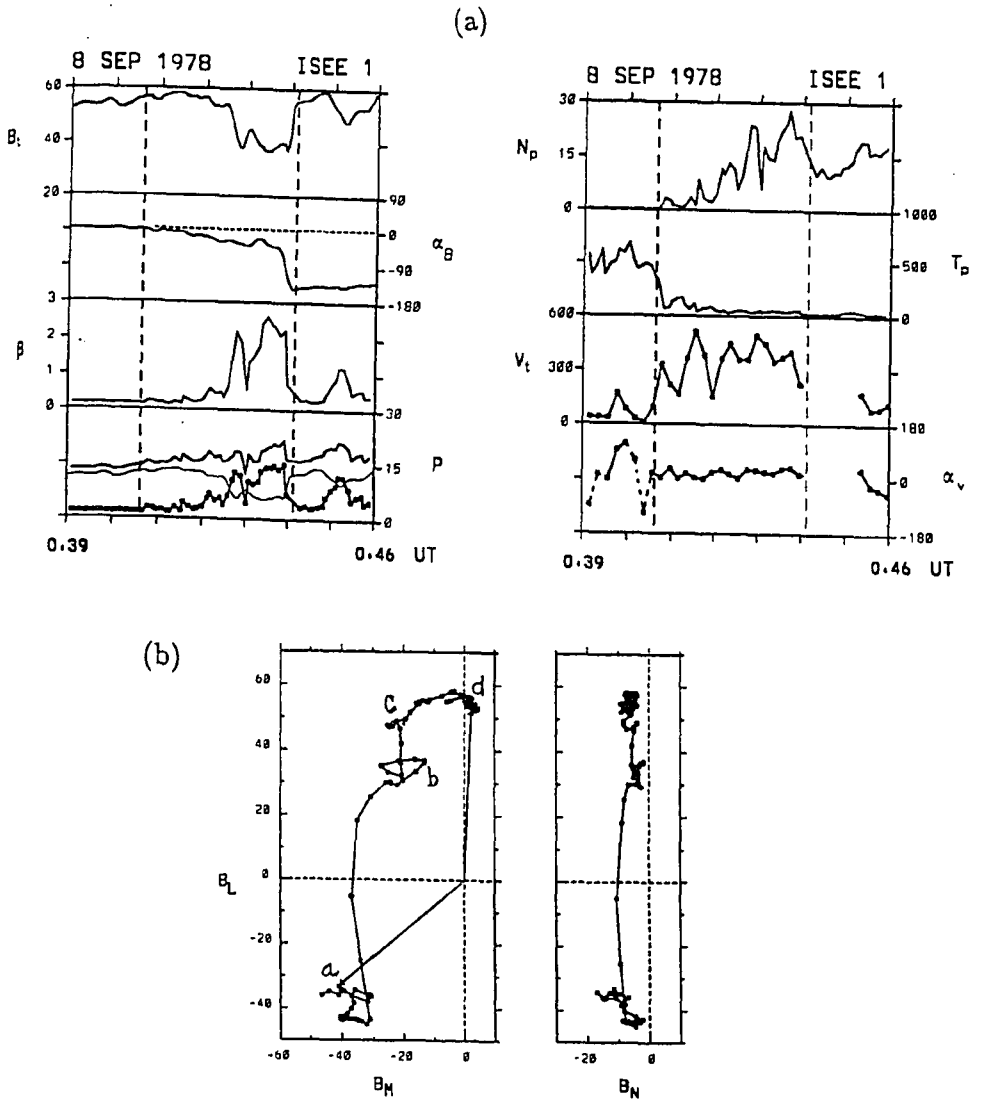

Figure 4.10 ISEE-1 observation of the dayside magnetopause-boundary layer on 8 September 1978. (a) Spatial profiles of physical quantities as described in the text. The reconnection layer is located between the two vertical dashed lines. The satellite crossing corresponding to the magnetopause is indicated by the right vertical dashed line. (b) Hodogram of the magnetic field [Paschmann et al., 1979; Rijnbeek et al., 1988].

Reproduced with permission of the copyright owner. Further reproduction prohibited without permission.

The reconnection layer, or the magnetopause-boundary layer associated with magnetic reconnection, can be identified using the field angle α_B. In Figure 4.10b, the value of α_B changes from 0^o in the magnetosphere to $\sim -145^o$ in the magnetosheath. The edges of reconnection layer are indicated by the two vertical dashed lines in Figure 4.10b [Rijnbeek et al., 1988], and the crossing of the magnetopause is indicated by the right vertical dashed line where α_B has a fairly sharp gradient. A large plasma flow speed, peaking at $450 km/s$, is observed throughout the boundary layer. Across the boundary layer, the ion number density decreases from the magnetosheath to the magnetosphere, and the plasma temperature increases monotonically from the magnetosheath to the magnetosphere.

It is seen from the hodograms in Figure 4.10a that the normal component of magnetic field B_N is non-zero and almost remains constant during the magnetopause-boundary layer crossing. The tangential magnetic field changes from the magnetosheath value (a) to the magnetospheric value (d). The field first rotates from the magnetosheath field at point a to point b, increases the magnitude b to c, and finally rotates from c to the magnetospheric field at d. The major rotations ab is found to be associated with a rotational discontinuity at the magnetopause [Paschmann et al., 1979; Sonnerup et al., 1981].

4.4.2 *Observations of Ion Distribution in the Dayside Boundary Layer*

Observations of electron and ion distributions in the boundary layer region also indicate the presence of layered structure, which is associated with the magnetic reconnection [Gosling et al., 1990a, b, c]. Through the process of dayside magnetic reconnection, the magnetosheath plasma penetrates across the magnetopause into the boundary layer. Measurements made during accelerated flow events in magnetic reconnections reveal separate electron and ion edges to the dayside boundary layer [Gosling et al., 1990b]. Moreover, a D-shaped ion distribution is observed in the dayside boundary layer [Gosling et al., 1990a, b, c; Smith and Rodgers, 1991; Fuselier et al., 1991].

Reproduced with permission of the copyright owner. Further reproduction prohibited without permission.

Figure 4.11 shows a series of three-second snapshots of ion velocity distribution functions obtained by ISEE 2 during a crossing of the dayside [Gosling et al., 1990a, c]. The distributions are shown as contours of constant phase-space density separated logarithmically. The sunward direction is to the left and the duskward direction is to the bottom. The numbers on the dotted circles indicate the velocity scale in km/s. The distribution of hot magnetospheric ions is shown in the top plot, and that of a denser and colder magnetosheath ion population is shown in the bottom plot. The middle plot shows the distribution of boundary layer ions, and the vector drawn represent the direction of magnetic field on the x-y plane.

Both relatively cool ions of magnetosheath origin and hot ions of the magnetosphere were present in the boundary layer. The dense beam of ions in the middle plot with bulk speed of about $500km/s$ and with both earthward ($V_x < 0$) and dawnward $V_y < 0$ components is the transmitted magnetosheath population, while the much hotter and nearly isotropic ions are those associated with the magnetospheric plasma. The transmitted ions in the boundary layer region has a characteristic "D" shape (with the "D" pointing along the magnetic field). Such D-shaped distribution has been predicted by Cowley [1982] and also reported by Smith and Rodgers [1991]. Observations of magnetospheric ions and magnetosheath ions in the boundary layer region have also been reported by Scholer et al. [1981] and Fuselier et al. [1991].

4.4.3 Comparison Between Hybrid Simulations and Satellite Observations

In this chapter, we find by hybrid simulations that the discontinuity bounding reconnection layer on the magnetosheath side is usually a rotational discontinuity. The current density in the magnetopause-boundary layer region is mainly concentrated at the rotational discontinuity, and the plasma is accelerated by the rotational discontinuity. The mixing of the accelerated magnetosheath plasma and the magnetospheric plasma is observed in the boundary layer. These features of the reconnection layer obtained in our simulation are consistent with observations at the dayside magnetopause. Moreover, our hybrid simulation results shown in Figure 4.7 look very similar to

Reproduced with permission of the copyright owner. Further reproduction prohibited without permission.

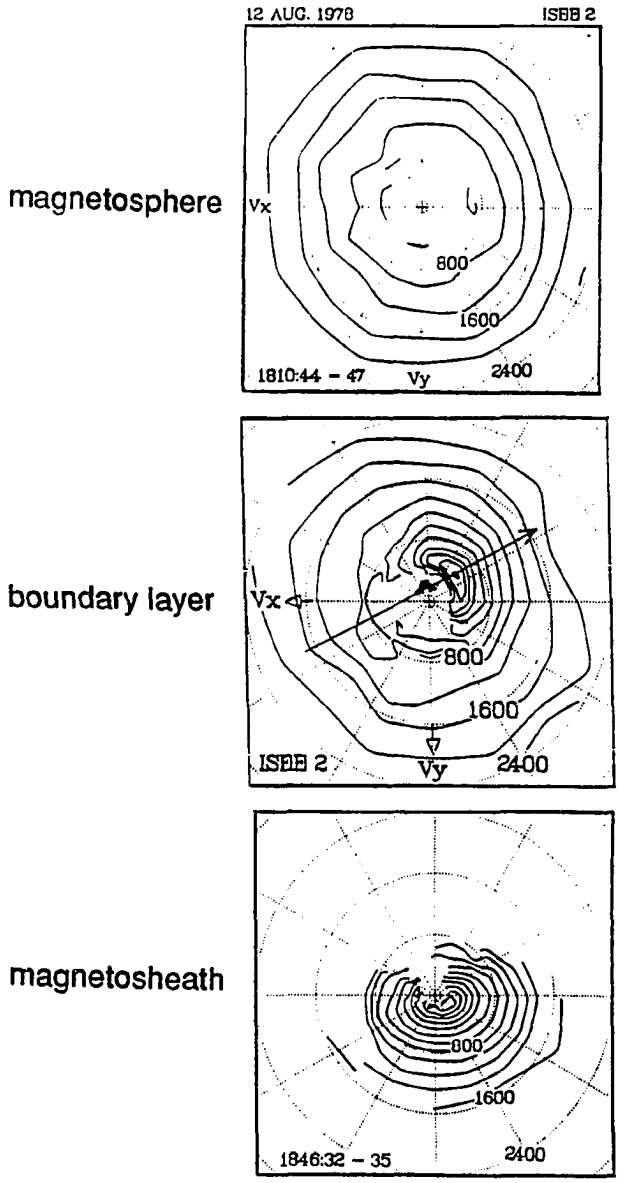

Figure 4.11 A series of three-second snapshots of ion velocity distribution functions obtained by ISEE 2 during an outward crossing of the dayside magnetopause-boundary layer on August 12, 1978. The top, middle, and bottom plots show the ion velocity distributions in the magnetosphere, boundary layer, and magnetosheath, respectively. A D-shaped distribution is observed in the dayside boundary layer [Gosling et al., 1990a, c].

Reproduced with permission of the copyright owner. Further reproduction prohibited without permission.

the observed structure of the dayside magnetopause-boundary layer shown in Figure 4.10. A large magnetic field rotation is found at the magnetopause, a small magnetic field rotation is at the inner edge of boundary layer, a high-speed plasma flow is present in the boundary layer, the ion density decreases and the ion temperature increases from the magnetosheath to the magnetosphere.

We have found in our hybrid simulations that a mixing of hot magnetospheric plasma and cold magnetosheath ion beam is present in the boundary layer region. ISEE 1 and 2 spacecraft have obtained the mixing of the magnetosheath and magnetospheric plasmas in the boundary layer [Gosling et al., 1990a, b, c; Smith and Rodgers, 1991; Fuselier et al., 1991]. The observed ion velocity distributions in Figure 4.11 are very similar to the distributions obtained in our hybrid simulations in Figure 4.5. In particular, the ion velocity distribution in Figure 4.5c shows the presence of a D-shaped distribution for ions of magnetosheath origin, similar to the observed D-shaped distribution in Figure 4.11.

4.5 Summary

In this chapter, we have studied the structure of dayside reconnection layer based on hybrid simulations. It is found that unlike resistive MHD simulations shown in Chapter 3, steady rotational discontinuities are quickly formed from the time-dependent intermediate shocks, the contact discontinuity does not exist, and the slow shocks and slow expansion waves are modified. A D-shaped ion velocity distribution is obtained in the dayside reconnection layer. The main results are listed below.

(a) For cases in which the tangential magnetic fields on the two sides of the dayside magnetopause current sheet are not antiparallel ($B_y \neq 0$), a rotational discontinuity across which the tangential magnetic field rotates a large angle is found to bound the reconnection layer on the magnetosheath side. Although the rotational discontinuity appears like a time-dependent

Reproduced with permission of the copyright owner. Further reproduction prohibited without permission.

intermediate shock in early times, a steady rotational discontinuity with a constant width is quickly formed.

(b) In the case with antiparallel tangential magnetic fields in the magnetosheath and magnetosphere ($B_y = 0$), a 2-3 steady intermediate shock is found to bound the reconnection layer on the magnetosheath side.

(c) Due to the mixing of plasmas from the magnetosheath side and from the magnetospheric side along magnetic field lines, the contact discontinuity does not exist in the reconnection layer, no clear slow shock front can be identified, and the slow expansion waves are strongly modified.

(d) Due to the mixing of the accelerated magnetosheath plasma and the hot magnetospheric plasma, the ratio $T_\perp/T_\parallel$ is reduced in the boundary layer region.

(e) A D-shaped distribution in ion velocity space is found to be present in the boundary layer. The D-shaped ion distributions have been observed by satellites.

(f) An Alfven wave pulse or a rotational discontinuity with a small rotation angle of magnetic field is found to bound the reconnection layer on the magnetospheric side. A large-amplitude V_{iy} pulse is observed in the Alfven wave pulse or the rotational discontinuity.

Reproduced with permission of the copyright owner. Further reproduction prohibited without permission.

Chapter 5 Structure of Slow Shocks in the Magnetotail Reconnection Layer in Hybrid Model

5.1 Introduction

In the magnetotail, the plasma density is symmetric with respect to the equatorial plane, and the magnetic fields in the two lobes are approximately antiparallel to each other with $B_y \simeq 0$. According to our studies in Chapters 2 and 3, two slow shocks are formed in the plasma sheet boundary layer as a result of magnetic reconnection. ISEE-3 deep-tail observations showed that the plasma and field data in the lobe-plasma sheet boundary layer are often consistent with the structure of a slow shock [Feldman et al., 1984; Smith et al., 1984; Schwartz et al., 1987]. In this chapter, we study the evolution and structure of slow shocks based on hybrid simulations.

Based on the two-fluid theory, which includes the Hall current associated with the ion inertia, the resistive slow shocks with a subsonic upstream normal flow speed should present a lefthand circularly polarized wave in the downstream region [Coroniti, 1971]. The structures of slow shocks have also been studied by hybrid simulations for switch-off shocks which has an intermediate Mach number $M_I = 1$ [Swift, 1983; Winske et al., 1985]. The results show the existence of large-amplitude rotational trailing wavetrains. However, the theoretically predicted wavetrains have not been found in the magnetotail observations [e.g., Feldman et al., 1984]. Coroniti et al. [1988] further found that the anomalous resistivity associated with the observed low-frequency waves in the magnetotail is too small to damp the wavetrain. Further simulation studies of slow shocks have also been reported by Lee et al. [1989b] and Omidi and Winske [1989; 1990].

Reproduced with permission of the copyright owner. Further reproduction prohibited without permission.

In symmetric configurations, switch-off slow shocks are found to be formed in the 1-D Riemann problem associated with magnetic reconnection, as shown in Chapters 2 and 3. However, the 2-D MHD simulations of magnetic reconnection in the magnetotail by Lee et al. [1989b] suggested that slow shocks formed in most regions of the magnetotail are non-switch-off shock with $M_I < 0.98$. Most slow shocks observed in the magnetotail are also non-switch-off shocks with $M_I < 0.98$ [e.g., Schwartz, 1987]. The presence of non-switch-off shocks is probably associated with the presence of plasmoid, which can exert a finite pressure-gradient force to slow down the outflowing plasma in the reconnection process.

In this chapter, we study the structure and ion heating of slow shocks based on hybrid simulations. Structures of switch-off ($M_I = 1$) and non-switch-off ($M_I < 1$) slow shocks are simulated. It will be shown that there exists a critical number M_c such that for slow shocks with an intermediate Mach number in the range $1 \geq M_I \geq M_c$, a long large-amplitude rotational wavetrain appears in the downstream region, while for slow shocks with $M_I < M_c$, the downstream rotational wave is damped within a fraction of one wavelength. The critical Mach number M_c depends on the shock normal angle θ_{nB} and the upstream plasma beta β_1. Furthermore, the existence of the critical intermediate Mach number M_c in slow shocks is related to chaotic ion orbits in the downstream wave field: for $M_I < M_c$, the particle orbits are chaotic, leading to a rapid heating of ions and a rapid damping of coherent waves.

In Section 5.2, we briefly describe satellite observations of slow shocks in the tail plasma sheet. Structure of slow shocks in the two-fluid theory is discussed in Section 5.3. In Section 5.4, we present our hybrid simulation results of slow shocks. In Sections 5.5 and 5.6, we study the particle motions in the circularly polarized electromagnetic wave with the propagation oblique to the downstream magnetic field. Under certain conditions, particle motion in a coherent wave field may become chaotic [Ford and Lunsford, 1970; Karney, 1978; Smith and Kaufman, 1978; Terasawa and Nambu, 1989; Buti, 1990]. Particles with highly chaotic orbits lead to the damping of coherent wave in slow shocks. The summary of this chapter is given in Section 5.7.

Reproduced with permission of the copyright owner. Further reproduction prohibited without permission.

5.2 Satellite Observations of Slow Shocks in the Tail Plasma Sheet-Boundary Layer

Slow shocks have been observed by ISEE-3 in the deep magnetotail ($\sim 200R_E$) [Feldman et al., 1984, 1985; Smith et al., 1984; Schwartz et al., 1987]. Figure 5.1 shows an ISEE-3 observation of slow shocks in the magnetotail [Feldman et al., 1984]. Profiles of the electron density (N_e), plasma flow speed (V_x), electron temperature (T_e), heat flux (Q_e), magnetic field strength (B), azimuthal angle (Φ) and polar angle (Θ) of magnetic field are plotted in the figure. The crossing of plasma sheet is indicated by the hatched region, and the quantities of north and south lobes are shown, respectively, on the lefthand side and righthand side of the plasma sheet.

Across two slow shocks, the plasma flow speed, density, temperature, and heat flux increase from lobe values to the plasma sheet value, while the magnetic field strength decreases. The plasma flow speed in the plasma sheet, which is downstream of the slow shocks, is $\sim$ 600 -- $900 km/s$. The lobe magnetic field energy is converted into plasma thermal and flow energy in the plasma sheet. The azimuthal angle of magnetic field varies from $\sim 0^\circ$ in the north lobe to $\sim 180^\circ$ in the south lobe, indicating the the guide field $B_y \sim 0$. The Rankine-Hugoniot conditions of slow shock are found to be satisfied.

However, one feature that is not observed is the large-amplitude rotational wavetrains in downstream region which are expected to exist based on the two-fluid theory [Coroniti, 1971]. The small variation of magnetic azimuthal angle Φ shown in Figure 5.1 indicates the absence of a large rotational wavetrain in downstream regions of slow shocks.

Coroniti et al. [1988] examined electric and magnetic wave spectra for three magnetotail slow shocks observed by ISEE-3 to determine if the ion-acoustic or lower-hybrid waves are sufficient to damp the slow shock wavetrains. They found that the observed wave amplitudes are too small to damp the wavetrains.

Reproduced with permission of the copyright owner. Further reproduction prohibited without permission.

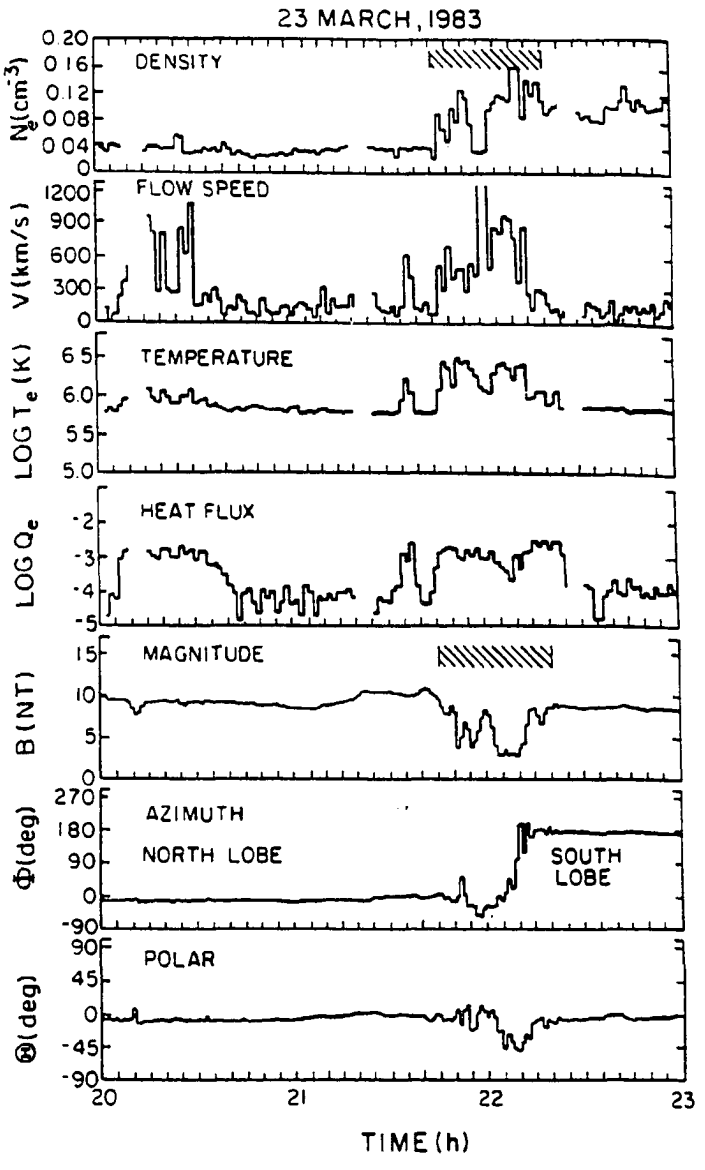

Figure 5.1 ISEE-3 observation of slow shocks in a crossing of tail plasma sheet-boundary layer on 23 March 1983. The electron density N_e, tailward component of the bulk speed V_x, temperature T_e, and heat flux Q_e, along with the polar coordinates (in the GSE frame) of the magnetic field vector (B, Θ, Φ) are shown. The crossing of plasma sheet is indicated by the hatched region, and the two slow shocks are located at the plasma sheet boundaries. Large-amplitude rotational trailing wavetrains predicted by two-fluid theory are not observed [Feldman et al., 1984].

Reproduced with permission of the copyright owner. Further reproduction prohibited without permission.

5.3 Wavetrains in Slow Shocks: Two-Fluid Formulation

In the ideal MHD formulation, the slow shock is a thin layer without a structure. In the resistive MHD formulation, the width of slow shock transition is determined by the resistivity. In the two-fluid formulation, which includes the ion inertia effect or Hall effect, slow shocks can exhibit a dispersive structure.

For the slow wave with a wavelength on the order of the ion gyroradius, or with a wave frequency $\omega \simeq \Omega_i cos\theta$, where Ω_i is the ion cyclotron frequency and θ is the wave propagation angle, the wave is lefthand (ion sense) polarized, and the wave speed decreases with an increasing wave number k due to the ion inertia. On the other hand, the fast wave is righthand (electron sense) polarized and the wave speed increases as the wave number increases. Figure 5.2 sketches the dispersion relations for (a) a slow mode wave and (b) a fast mode wave based on the two-fluid formulation. It is seen that due to the ion inertia effect, the slow wave speed at high wave number is smaller than its MHD characteristic speed, which corresponds to the speed at $k = 0$, whereas the fast mode wave at high wave number has a speed greater than the MHD speed. As a result, the lefthand polarized wave may stand in the downstream region of a slow shock, and the righthand whistler wave may propagate in the upstream region of a fast shock [e.g., Tidman and Krall, 1971]. Two-fluid theory has been used to study the dispersive structure of shocks. Indeed, Coroniti [1971] found, based on a two-fluid theory including the ion inertia and resistivity, that slow shocks have a trailing wavetrain in downstream region, and the trailing waves are lefthand circularly polarized.

We have simulated the dispersive structure of slow shocks based on the two-fluid equations. Figure 5.3a shows the simulation results for a non-switch-off slow shock with $\theta_{nB} = 75^o$, $M_I = 0.96, \beta_1 = 0.1$, and $(c/\omega_{pi})/\lambda_r = 50$, where ω_{pi} is the upstream ion plasma frequency, c/ω_{pi} is the upstream ion inertial length, $\lambda_r = \eta/\mu_0 C_{I1}$ is the resistive length, and η is resistivity. The hodogram of tangential magnetic field and the spatial profiles of tangential magnetic field components and plasma density are presented. In the figure, z is in the shock normal direction.

Reproduced with permission of the copyright owner. Further reproduction prohibited without permission.

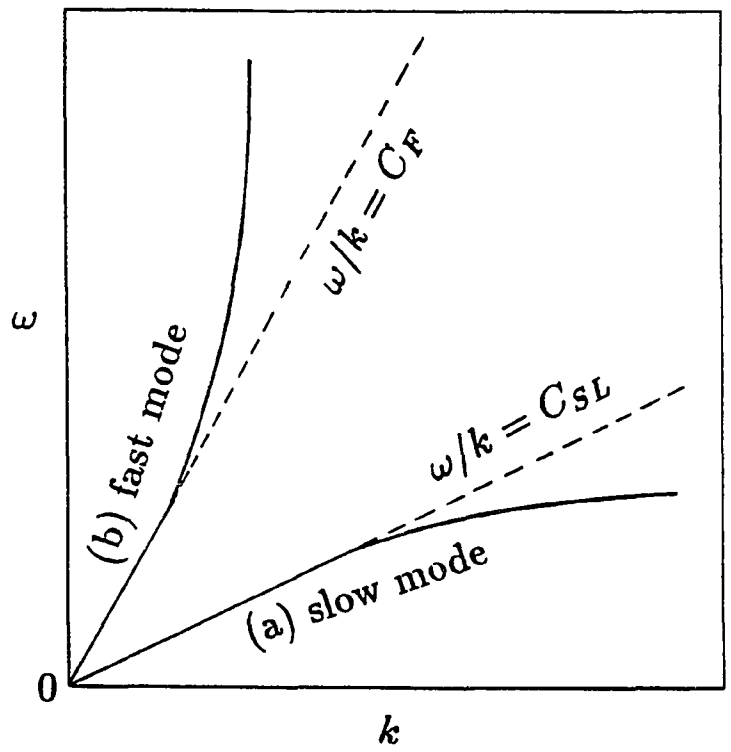

Figure 5.2 Sketches of two-fluid dispersion relations for (a) a slow wave and (b) a fast wave.

Reproduced with permission of the copyright owner. Further reproduction prohibited without permission.

The normal component of magnetic field, B_z, is negative. It is seen that the slow shock has a lefthand circularly polarized trailing wavetrain in the downstream region. The wavetrain is gradually damped by the resistivity. The wavelength right behind the shock front is on the order of 2π times of downstream ion Lamour radius, which is approximately $10.5c/\omega_{pi}$. The simulation results for a fast shock with $\theta_{nB} = 45°$, $M_I = 2$, $\beta_1 = 0.1$, and $(c/\omega_{pi})/\lambda_r = 10$ are shown in Figure 5.3b for comparison. It is seen that the fast shock has a leading wavetrain in the upstream region.

Although the two-fluid theory can describe the shock structures with dispersive waves, it cannot provide the dissipation in collisionless plasma. In order to understand the dissipation mechanism in a collisionless shock, it is important to carry out the study based on kinetic formulation. In the next section, we present the simulation results of slow shocks by using a hybrid code.

5.4 Hybrid Simulations of Slow Shocks

In this section, we use hybrid simulations to study the structure and the dissipation mechanism of collisionless slow shocks. In order to understand the physics of the downstream waves, we have carried out a systematic parameter search for slow shocks. The initial profile in our simulation includes a finite transition region linking two uniform regions determined by the Rankine-Hugoniot conditions of slow shocks. The parameter ranges used in our simulations are : $30° \leq \theta_{nB} \leq 75°$, $M_I \leq 1$, $0 < \beta_1 < 2$, and $0 \leq T_{e1}/T_{i1} \leq 3.5$, where T_{i1} and T_{e1} are the upstream ion temperature and electron temperature, respectively. Note that $T_{e1}/T_{i1} \leq 1.0$ and $\beta_1 < 1$ in the magnetotail [e.g., Schwartz et al., 1987].

We show two typical cases of slow shocks. Case 1 is a switch-off shock with $M_I = 1$, and Case 2 is a non-switch-off shock with $M_I = 0.96$

5.4.1 Case 1: Switch-Off Shock ($M_I = 1$)

Reproduced with permission of the copyright owner. Further reproduction prohibited without permission.

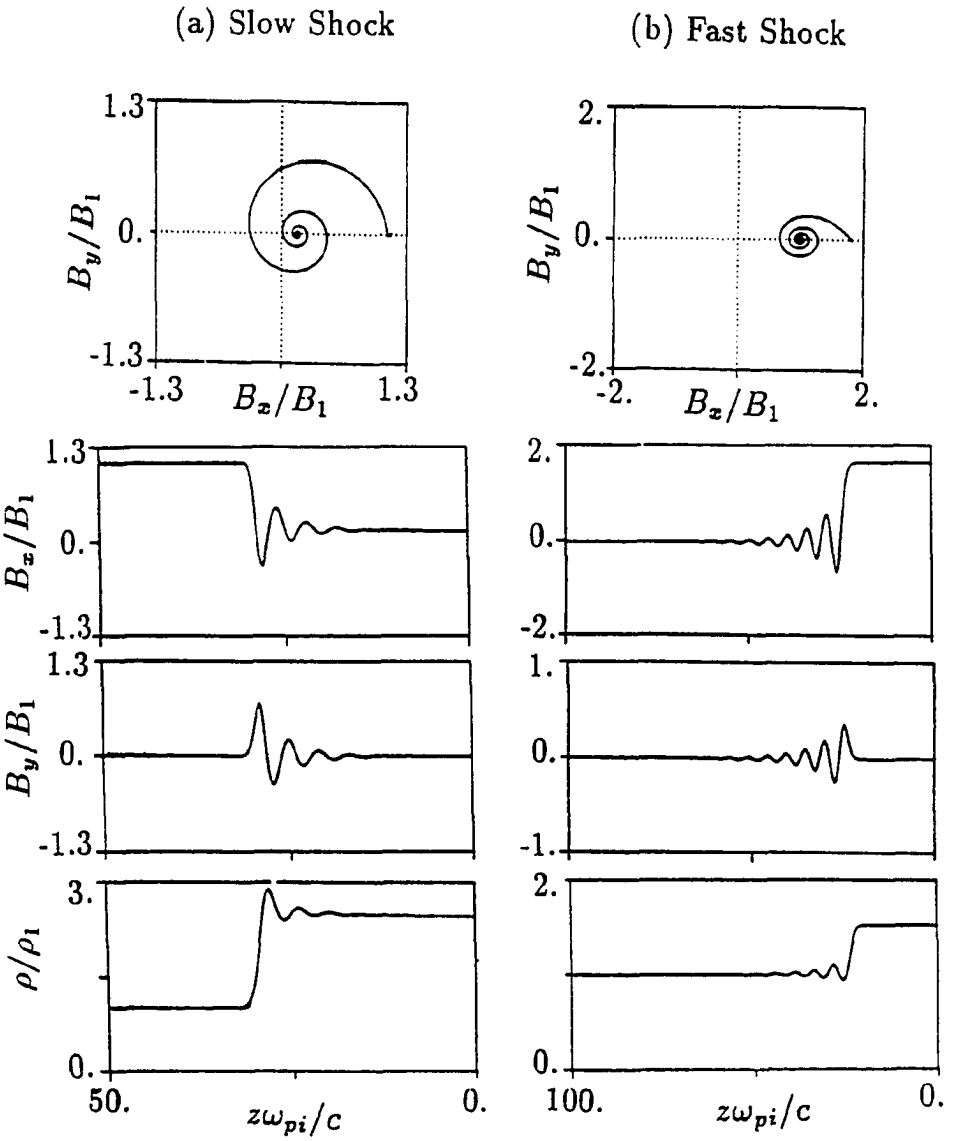

Figure 5.3 Two fluid solutions of MHD shocks. The hodogram of tangential magnetic field and the spatial profiles of the tangential magnetic field components (B_y and B_z) and plasma density (ρ) are presented. (a) A slow shock with $\theta_{nB} = 75°$, $M_I = 0.96$, $\beta_1 = 0.1$, and $(c/\omega_{pi})/\lambda_r = 50$. (b) A fast shock with $\theta_{nB} = 45°$, $M_I = 2$, $\beta_1 = 0.1$, and $(c/\omega_{pi})/\lambda_r = 10$. Quantities B_1 and ρ_1 are the upstream magnetic field strength and upstream plasma density, respectively.

Reproduced with permission of the copyright owner. Further reproduction prohibited without permission.

The upstream plasma beta of the slow switch-off shock in Case 1 is $\beta_1 = 0.1$, the shock normal angle is $\theta_{nB1} = 75^o$, and the electron to ion temperature ratio is $T_e/T_i = 0$. The intermediate Mach number of the switch-off shock is $M_I = 1$. The normal magnetic field component $B_n = B_z$ is chosen to be negative and remains constant in the simulation.

Figure 5.4 shows the hodogram of tangential magnetic field, and the spatial profiles of tangential magnetic field components (B_x and B_y), ion number density N, and perpendicular temperature $T_\perp$ for the switch-off shock at $t = 575\Omega_1^{-1}$. Here, Ω_1 is the upstream ion cyclotron frequency. It is seen from B_x and B_y profiles that a large-amplitude coherent wavetrain is present in the downstream region ($z\omega_{pi}/c \leq 84$) of the slow shock. The tangential magnetic field in the downstream wave exhibits several 360^o rotations, as shown in the hodogram, indicating the presence of rotational wavetrain. The perpendicular temperature $T_\perp$ gradually increases across the rotational wavetrain to the downstream value. The gradual increase of $T_\perp$ may be related to the ion cyclotron damping [Swift, 1983].

The shock evolution processes in the simulation can be briefly described as follows. The lefthand circularly polarized wave first appears and grows from the downstream end of the shock transition region, and the wave amplitude B_w increases with time, finally reaching the value $B_{w0} = B_{t1} - B_{t2}$. Here B_{t1} and B_{t2} are, respectively, the magnitudes of upstream and downstream tangential magnetic field components. The wave length λ_0 is approximately $2\pi R_{c2}$, where R_{c2} is the downstream ion Lamour radius. The simulation results show that the rotational wave is nearly phase standing in the shock frame.

5.4.2 Case 2: Non-Switch-Off Shock with $M_I = 0.96$

We now study the structure of slow shock in Case 2 with $M_I = 0.96$, $\theta_{nB1} = 75^o$, $\beta_1 = 0.1$, and $T_e/T_i = 0$. The simulation results are shown in Figure 5.5. The tangential magnetic field does not show a 360^o rotation, as seen in the magnetic field hodogram. Comparing with the switch-off shock in Case 1, it is clear that the downstream circularly-polarized wavetrain

Reproduced with permission of the copyright owner. Further reproduction prohibited without permission.

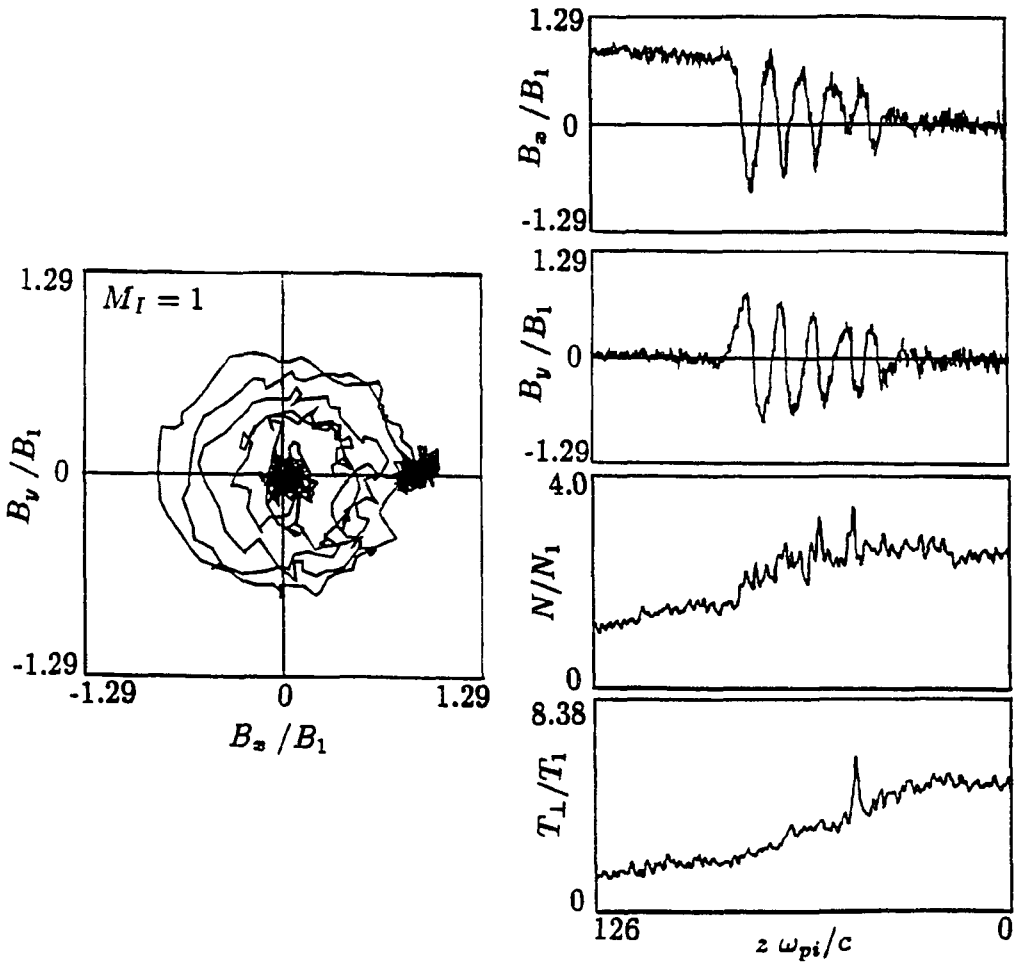

Figure 5.4 Hybrid simulation of the slow switch-off shock with $\theta_{nB} = 75^o$, $\beta_1 = 0.1$, and $M_I = 1$. The hodogram of tangential magnetic field, and the spatial profiles of tangential magnetic field components (B_x and B_y), ion number density N, and perpendicular temperature $T_\perp$ at $t = 575\Omega_1^{-1}$ are shown.

Reproduced with permission of the copyright owner. Further reproduction prohibited without permission.

is damped within $1/4$ wavelength, and the perpendicular temperature $T_\perp$ has a sudden increase at $z \simeq 84c/\omega_{pi}$. We have changed the temperature ratio to $T_{e1}/T_{i1} = 0.5$, 1.0, and 1.5, and found no qualitative difference from the case with $T_e/T_i = 0$.

In the very early time of the simulation for Case 2, a rotational wave with amplitude much less than B_{w0} and with one or less than one rotation is found to appear in the downstream region. This rotational wave is then destroyed to become non-coherent when the wave amplitude exceeds a certain value. The destruction of the coherent wave usually occurs within one wave rotation. In the final quasi-steady state, the downstream wave makes only 1/4 of a rotation, as shown in Figure 5.5.

5.4.3 Existence of the Critical Intermediate Mach Number

Our systematic parameter search of slow shocks indicates that switch-off shocks always exhibit a long large-amplitude rotational wavetrain. However, for given θ_{nB} and β_1, there exists a critical number M_c such that slow shocks with an intermediate Mach number $M_I \leq M_c$ have a long large-amplitude rotational wavetrain and slow shocks with $M_I < M_c$ do not have such a wavetrain. For example, for a magnetotail slow shock with $\theta_{nB} = 75^o$, $\beta_1 = 0.1$, and $T_{e1}/T_{i1} = 0$, the critical number $M_c \sim 0.975$. The simulation results are consistent with observations in the magnetotail, where most slow shocks are found to be non-switch-off shocks with $M_I < 0.98$ and $T_{e1}/T_{i1} < 1$ [Schwartz et al., 1987].

According to our simulation results, the disappearance of large-amplitude rotational wavetrain is accompanied by a rapid increase of the downstream plasma temperature, as shown in Figure 5.5. Therefore, the lack of such waves is directly related to the ion heating process of slow shocks. The purpose of the next two sections is to study the ion heating process in slow shocks based on calculations of ion orbits in the downstream wave field.

Reproduced with permission of the copyright owner. Further reproduction prohibited without permission.

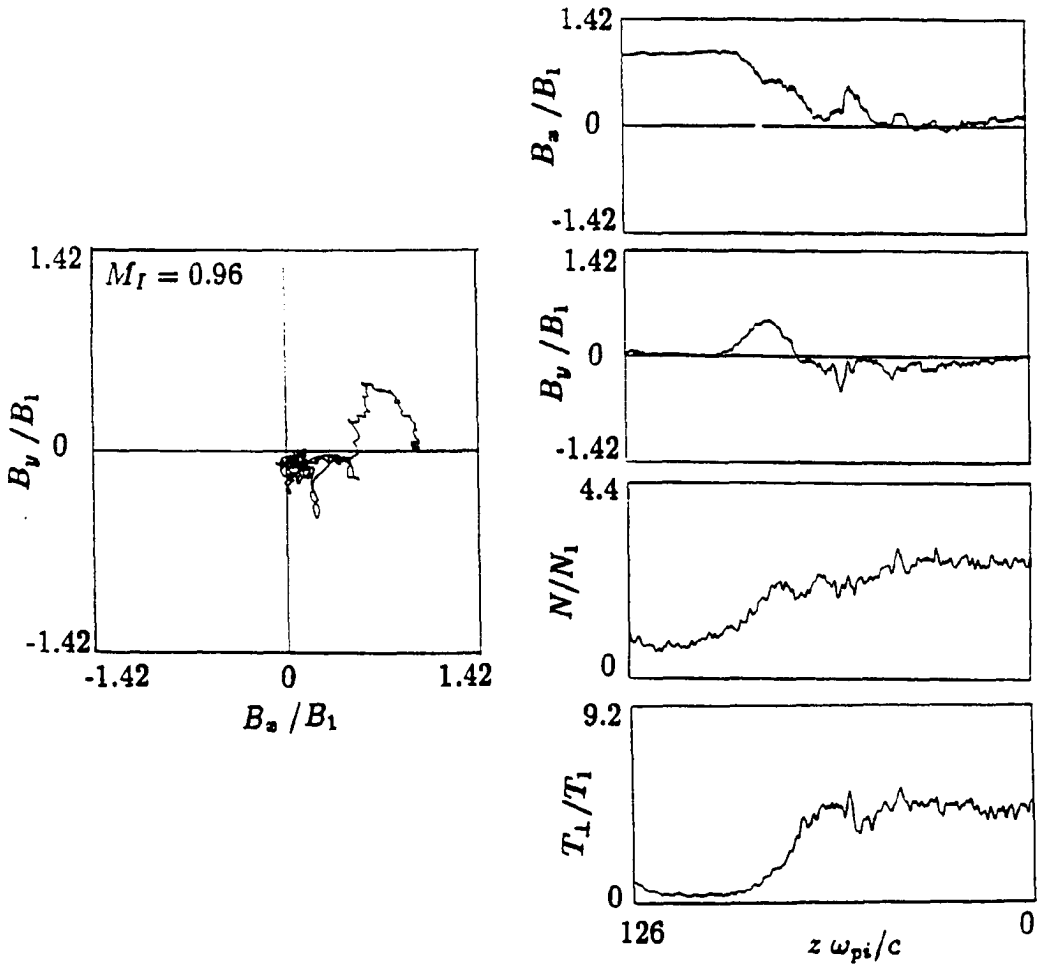

Figure 5.5 Same as Figure 5.4, except for the non-switch-off shock with $M_I = 0.96$.

Reproduced with permission of the copyright owner. Further reproduction prohibited without permission.

5.5 Onset of Chaos: Resonance Overlapping Theory

To investigate the ion heating mechanism of slow shocks, we first assume that a circularly-polarized downstream wave exists, as obtained from the two-fluid theory. Then we study the interaction between particles, which are originally injected from upstream, and the downstream wave. Consider a left-hand polarized electromagnetic wave, which propagates at an angle α' to the averaged local magnetic field $\mathbf{B}_0$ in the downstream side, and has a perturbed magnetic field $\mathbf{B}_w$ in the plane transverse to the wave vector $\mathbf{k}$. In the calculation of ion orbits, we let $\mathbf{B}_0$ be in the z-direction, $\mathbf{k}$ in the yz plane, and $\alpha = 180^o - \alpha'$, for convenience. Note that the coordinate system used here is different from that has been used in the hybrid simulations of slow shocks in Section 5.4. In such a coordinate system, $\alpha = 0^o$ corresponds to a switch-off shock. According to our simulation results, the wave field may be written in the form

$$\mathbf{B}_w = -\mathbf{e}_x B_w \sin\phi + (\mathbf{e}_x \times \mathbf{e}_k) B_w \cos\phi \tag{5.1}$$

where $\mathbf{e}_x$ and $\mathbf{e}_k$ are, respectively, the unit vectors in the x direction and the k direction, $\phi = \mathbf{k} \cdot \mathbf{r}$, and $\mathbf{r}$ is the position in the de Hoffmann-Teller (HT) frame. Our simulations indicate that the electric field is very small. For simplicity, we neglect the electric field in the following discussions. Our study shows that the inclusion of a convection electric field does not significantly modify the results. The equation of motion for a single particle in such a wave field is

$$m\frac{d\mathbf{v}}{dt} = q\mathbf{v} \times (\mathbf{B}_0 + \mathbf{B}_w) \tag{5.2}$$

In this section, we take a look at the particle behavior analytically. In the electromagnetic field, the most elementary interaction process between wave and particle is the cyclotron resonances. The nonlinear effect may be related to these resonances. For a particle in the linear small-amplitude wave, the resonance condition is

$$-k_z v_z/\Omega_0 + n = O(\epsilon) \tag{5.3}$$

where $\Omega_0 = qB_0/mc$, n is an integer, and $\epsilon << 1$.

Reproduced with permission of the copyright owner. Further reproduction prohibited without permission.

The particle resonant orbits can be obtained by assuming the wave amplitude is small. For a nonresonant particle, the particle orbit can be solved by integrating the equations of motion along the unperturbed trajectory. The first-order correction terms oscillate rapidly in time. For a resonant particle, the zero-order orbit varies slowly in time, and there is a more rapid oscillatory motion superposed on the zero-order orbit. By using the secularity-free perturbation theory with an accuracy to the first order in wave amplitude, a constant of motion at the nth resonance can be obtained as [Palmadesso, 1972]:

$$W_n = \frac{1}{2}m(\tilde{v}_z - n\Omega_0/k_z)^2 + A_n\cos\tilde{\Phi}_n \tag{5.4}$$

where $A_n = -(q/k_z)\tilde{v}_\perp B_w[(n\Omega_0/k_\perp\tilde{v}_\perp)J_n(\tilde{u}_\perp) + \cos\alpha J_n'(\tilde{u}_\perp)]$. Here tilde stands for the quantities varying on the slow time scale, $\tilde{v}_z$ and $\tilde{v}_\perp$ are, respectively, the components of average velocity parallel and perpendicular to the magnetic field $\mathbf{B}_0$, and J_n is the nth order Bessel function with the argument $\tilde{u}_\perp = k_\perp\tilde{v}_\perp/\Omega_0$. The prime denotes the derivative, $J_n' = dJ_n/d\tilde{u}_\perp$. Finally, $\tilde{\Phi}_n = (k_z\tilde{v}_z - n\Omega_0)t + \tilde{\chi}_n$, where $\tilde{\chi}_n = \tilde{\phi} + n(\tilde{\psi} + \pi/2) - u_{\perp 0}\cos\psi_0$, the phase-angle ψ is defined as $\tan^{-1}(v_y/v_x)$, and $u_{\perp 0}$ and ψ_0 stand for the values at $t = 0$.

The slowly changing or average ion motion as described by equation (5.4) can be illustrated in the $\tilde{\Phi}$-$\tilde{v}_z$ plane, where $\tilde{\Phi}$ is used to represent $\tilde{\Phi}_n$ with various number of n. Some contours are schematically sketched in Figure 5.6, where a trapped particle orbit, an untrapped orbit, and a separatrix are illustrated for the contours of the nth resonance. Note that the trapping width, which is defined as the maximum deviation of $k_z\tilde{v}_z/\Omega_0$ on separatrix from the line $k_z\tilde{v}_z/\Omega_0 = n$ for the nth resonance, may be different for different values of n. The onset of stochasticity may be caused by the overlapping of particle resonance orbits [Smith and Kaufman, 1978]. The condition for resonance overlapping is estimated as

$$2[|D_n|^{1/2} + |D_{n+1}|^{1/2}]^2 > 1 \tag{5.5}$$

where $D_n = 2C_1 n\cot\alpha J_n(\tilde{u}_\perp) + 2C_1\cos\alpha(k_z\tilde{v}_\perp/\Omega_0)J_n'(\tilde{u}_\perp)$ and the normalized wave

Reproduced with permission of the copyright owner. Further reproduction prohibited without permission.

amplitude $C_1 = B_w/B_0$. Thus given α and the initial particle velocity, one can find from equation (5.5) a critical number C_{1c} such that the particle orbits may overlap if $C_1 \geq C_{1c}$.

The criterion (5.5) provides only an approximate estimate for the condition of chaos. The consideration of the secondary resonances and even the width of the separatrix in particle resonant orbits may lead the critical number C_{1c} to a much smaller value [Lichtenberg and Lieberman, 1983].

We now use the criterion given by equation (5.5) to estimate the condition for the occurrence of chaotic particle motion in the downstream wave of a slow shock. The particle velocities are chosen as those of the incident particle from the upstream side in the HT frame plus the thermal velocities of the upstream plasma. Because the thermal velocity has the components parallel and perpendicular to the upstream magnetic field, the calculations should be carried out for each case, and the result should be the average of all these possible cases. We have calculated the critical number C_{1c} with the particle incident speed v_0 given as $kv_0/\Omega_0 \simeq 1.5$, which corresponds to slow shocks with $\theta_{nB} = 75^o$ and $\beta_1 = 0.1$. It can be shown that $D_n = 0$ for $\alpha = 0^o$, and hence the switch-off shocks ($\alpha = 0^o$) cannot have the overlapping resonances.

We have calculated the results for $n = 0, -1$, and 1, respectively. Because $kv_0/\Omega_0 \simeq 1.5$ for the slow shocks considered, there is no need to calculate the overlapping conditions for $n < -1$ or $n > 1$. The results for $n = -1$ are shown by the dashed curve in Figure 5.7. The abscissa of the figure is α, and the corresponding values of M_I for slow shocks with $\theta_{nB} = 75^o$ and $\beta_1 = 0.1$. In obtaining the relation between α and M_I, we assume $\mathbf{B}_0 = \mathbf{B}_2$, where $\mathbf{B}_2$ is the downstream magnetic field of each slow shock obtained by the Rankine-Hugoniot conditions. Furthermore, the resultant critical numbers with $n = 0$ are very close to those of $n = -1$, whereas for $n = 1$, C_{1c} is higher.

Note that there are analytical solutions for particle motions in the wave field with $\alpha = 0^o$. Let the normalized velocity of a particle be $\mathbf{v}^* = |k_z|\mathbf{v}/\Omega_0$ ($= k\mathbf{v}/\Omega_0$ for $\alpha = 0^o$), the normalized

Reproduced with permission of the copyright owner. Further reproduction prohibited without permission.

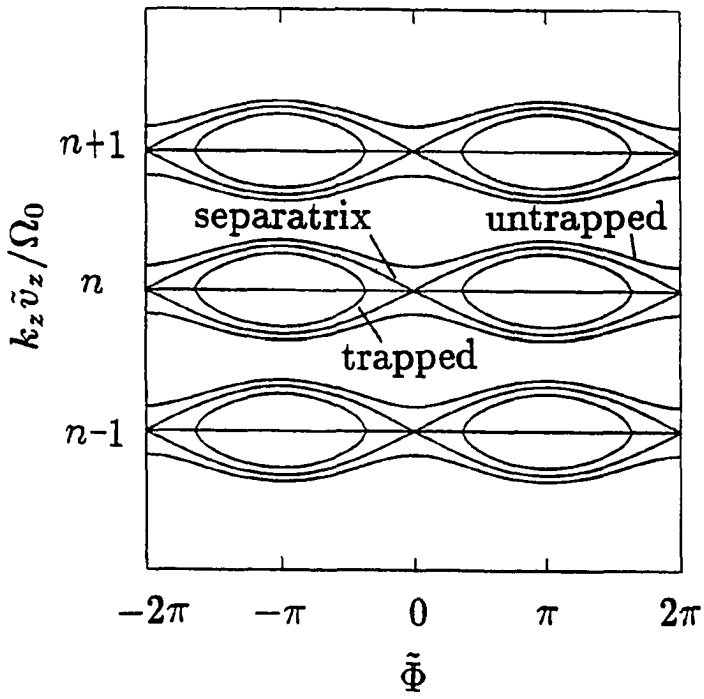

Figure 5.6 A sketch of particle trajectories on the $\tilde{\Phi}$-$\tilde{v}_z$ plane in a small-amplitude wave.

Reproduced with permission of the copyright owner. Further reproduction prohibited without permission.

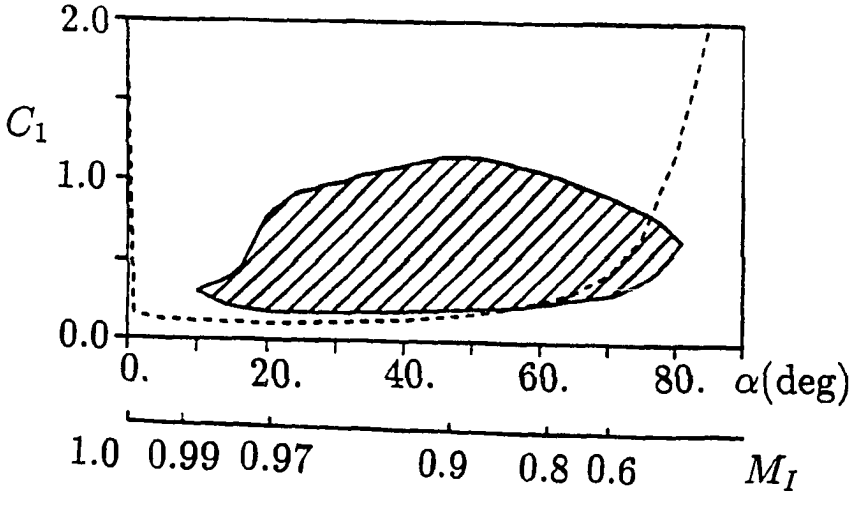

Figure 5.7 The highly chaotic region in which the particle motions become stochastic within one wavelength is shown by the shaded area. The quantity $C_1 = B_w/B_0$ is the normalized wave amplitude. The area above the dashed line is the chaotic region as predicted by the resonance overlapping theory.

Reproduced with permission of the copyright owner. Further reproduction prohibited without permission.

time be $t^* = \Omega_0 t$. From the Lagrangian formulation, the following constants of motion can be obtained

$$v_x^{*2} + v_y^{*2} + v_z^{*2} = a_1 \tag{5.6a}$$

$$v_y^* - C_1 \cos\phi - x^* = a_2 \tag{5.6b}$$

$$v_x^* + C_1 \sin\phi + y^* = a_3 \tag{5.6c}$$

$$\frac{1}{2} v_z^{*2} - C_1 (v_x^* \sin\phi - v_y^* \cos\phi) - v_z^* = a_4 \tag{5.6d}$$

where a_1, a_2, a_3, and a_4 are constants. One can then obtain the following equation for v_z^*

$$\int \frac{dv_z^*}{f(v_z^*)} - t^* = a_6 \tag{5.7}$$

where $f(v_z^*) = \pm[\frac{1}{4} v_z^{*4} - v_z^{*3} + (1 - C_1^2 - a_4) v_z^{*2} + 2a_4 v_z^* + a_5]^{1/2}$, and a_5 and a_6 are constants. For given wave amplitude and propagation angle, the six constants, a_1 through a_6, are determined by the initial position and velocity of the particle. The integral in equation (5.7) is an elliptic integral, whose solution can be expressed in terms of elliptic functions [e.g., Goldstein, 1951]. With v_z^* solved by (5.7), the quantity $\phi = kz$ can be obtained by the time integration of v_z^*, and other quantities are solved from (5.6a) -- (5.6d). By this procedure the analytical solution for $\alpha = 0°$ is obtained is found to be periodic.

It is seen from Figure 5.7 that the particle resonant orbits may overlap even for $M_I = 0.99$. However, we notice that the condition (5.5) gives only the lower bound but not the upper bound (see next section) of chaotic region for a certain α. The particle orbits in a large-amplitude wave cannot be fully estimated by the linear analysis approach. If the wave amplitude is large enough, the particle motion will be dominantly determined by periodic wave, and the particle may resume

Reproduced with permission of the copyright owner. Further reproduction prohibited without permission.

the regular motion. For example, let us consider an extreme case with $C_1 \rightarrow \infty$. The particle motion in phase space is found to be on the curve

$$\frac{1}{2}(kv_z/\Omega_w)^2 - a_1' sin(\phi - a_2') = a_3' \tag{5.8}$$

with

$$a_1' = (k/\Omega_w)[\Omega_w^2/k^2 + v_{x0}^2 + v_{y0}^2 + 2(\Omega_w/k)(v_{x0}\sin\phi_0 - v_{y0}\cos\phi_0)]^{1/2} \tag{5.9a}$$

$$a_2' = \tan^{-1}\frac{v_{y0} - (\Omega_w/k)\cos\phi_0}{v_{x0} + (\Omega_w/k)\sin\phi_0} \tag{5.9b}$$

where $\Omega_w = qB_w/mc$, a_3' is a constant, and the subscript "0" denotes the values at $t = 0$. Thus the motion is periodic and not chaotic. Furthermore, the condition (5.5) cannot give us the criterion under which the orbits of a group of particles spread chaotically within one wavelength, which corresponds to the simulation results of slow shocks with $M_f < M_c$.

5.6 Particle Orbits Obtained by Numerical Integration

In this section, we use the numerical integration approach to solve the particle orbits and search for the condition for the occurrence of chaotic particle motion. For a particle in regular motion, its trajectory in phase space is periodic or quasi-periodic, whereas the orbit of a particle in chaotic motion present random patterns. In general, a particle in regular motion will be on smooth curves when mapped into the Poincare surface of section in the phase space. On the other hand, if the mapping is scattered, the system is chaotic. Another way to distinguish the chaos from the regular motion is that a chaotic system is very sensitive to the initial conditions. For chaotic motions, two orbits initially very close in the phase space may separate exponentially with time [e.g., Ford and Lunsford, 1970].

Reproduced with permission of the copyright owner. Further reproduction prohibited without permission.

Equation (5.2) can be written in component forms as

$$\frac{dv_x^*}{dt^*} = v_y^*(1 + C_1 \sin\alpha\cos\phi) - C_1 v_z^* \cos\alpha\cos\phi \qquad (5.10a)$$

$$\frac{dv_y^*}{dt^*} = -C_1 v_z^* \sin\phi - v_x^*(1 + C_1 \sin\alpha\cos\phi) \qquad (5.10b)$$

$$\frac{dv_z^*}{dt^*} = C_1 v_x^* \cos\phi\cos\alpha + C_1 v_y^* \sin\phi \qquad (5.10c)$$

$$\frac{d\phi}{dt^*} = v_z^* - v_y^* \tan\alpha \qquad (5.10d)$$

For given C_1, α, initial value of ϕ, and initial velocity, one can integrate equations (5.10) to obtain particle trajectories. The integration scheme utilizes the 6-order Runge-Kutta-Verner method. A typical integration time step is $\Delta t = 0.05\Omega_0^{-1}$ The Hamiltonian has been used to examine the accuracy of the integration, which is accurate to 10^{-5} at $t = 5000\Delta t$.

According to the discussion in Section 5.5, for a particle in resonant motion, the variation of velocity v_z^* $(= |k_z|v_z/\Omega_0)$ should be on a certain resonant orbit and be periodic in time. If the resonance overlapping condition is satisfied, the particle motion is chaotic and v_z^* jump stochastically in a certain range as time passes. In order to see the chaotic particle motion as a result of the overlapping of particle resonance orbits, we show in Figure 5.8 our calculation results for a case with $\alpha = 30^o$ and $kv_0/\Omega_0 = 2.6$, where v_0 is the initial speed of the particle. The variation of v_z^* as a function of t^* is plotted for $C_1 = 0.095$ and $C_1 = 0.12$, respectively, in the figure. Initially, the particle is incident into to the wave field with a velocity antiparallel to the total local magnetic field, $\mathbf{B} = \mathbf{B}_0 + \mathbf{B}_w$, at the position $\phi = 0$. It is seen that for $C_1 = 0.095$, the particle motion shows a periodic pattern, with a high-frequency oscillatory motion superposed on an average orbit. However, for $C_1 = 0.12$, v_z randomly jumps in the range between $|k_z|v_z/\Omega_0 \sim -1$ and $|k_z|v_z/\Omega_0 \sim +2$, indicating a stochastic motion resulting from the overlapping of particle resonant orbits. Through this process, the particles in a plasma can be

Reproduced with permission of the copyright owner. Further reproduction prohibited without permission.

greatly heated. It is interesting to note that the critical number C_{1c} in this case estimated from the the criterion (5.5) is $C_{1c} \sim 0.12$.

As mentioned earlier, the qualitative difference between particles in regular motion and in chaotic motion can also be shown by calculating the separation of two particles in phase space. Let the particle incident speed v_0 satisfies $kv_0/\Omega_0 \simeq 1.5$, which is associated with slow shocks with $\theta_{nB} = 75^o$ and $\beta_1 = 0.1$. The three solid curves in Figure 5.9 show the separation in the 4-dimensional phase space, D, of two particles as a function of time t for three cases with $\alpha = 0^o$, 14^o and 20^o, where $D = \| \mathbf{S}_1 - \mathbf{S}_2 \|$, $\mathbf{S}_i = (\phi_i, v^*_{xi}, v^*_{yi}, v^*_{zi})$, and i=1 and 2 stand for the two particles. At $t = 0$, the pair of particles are started from $\phi = 0$ and with velocities approximately antiparallel to the total local magnetic field $\mathbf{B} = \mathbf{B}_0 + \mathbf{B}_w$, as in the simulation of slow shocks, except a minute difference in the incident direction. We choose the initial separation $D = D_0 = 10^{-3}$. We see that D is a linear function of time for $\alpha = 0^o$ ($M_I = 1$), indicating a regular particle motion. On the other hand, the exponential divergence of D in the case with $\alpha = 20^o$ ($M_I = 0.97$) demonstrates a very rapid "forgetting" of initial conditions in the typical chaotic motion, while the exponential curve (dashed) corresponds to $D = D_0 \exp(\sigma \Omega_0 t)$ with $\sigma = 0.2$. The exponential fit is calculated for a time duration longer than $50\Omega_0 t$. The last case with $\alpha = 14^o$ and $\sigma = 0.12$ is associated with $M_I = 0.98$.

Our calculations further indicate that each particle may have several chaotic bands in C_1 for a fixed α. Taking $\alpha = 20^o$, we draw in Figure 5.10 the chaotic bands of two particles, which initially have the same speed ($kv_0 = 1.5$) and same same pitch-angle (20^o), but have phase-angles differing by 90^o. The calculations have been carried out until $\Omega_0 t > 250$. Our results indicate that there are three chaotic bands for particle 1: $0.06 < C_1 < 0.17$; $0.19 < C_1 < 0.55$; and $0.65 < C_1 < 0.76$. Thus the particle resumes regular motion several times as C_1 increases. On the other hand, our phase space plots indicates that if $C_1 > 0.76$, the particle motion is regular and dominated by the external periodic wave field.

Reproduced with permission of the copyright owner. Further reproduction prohibited without permission.

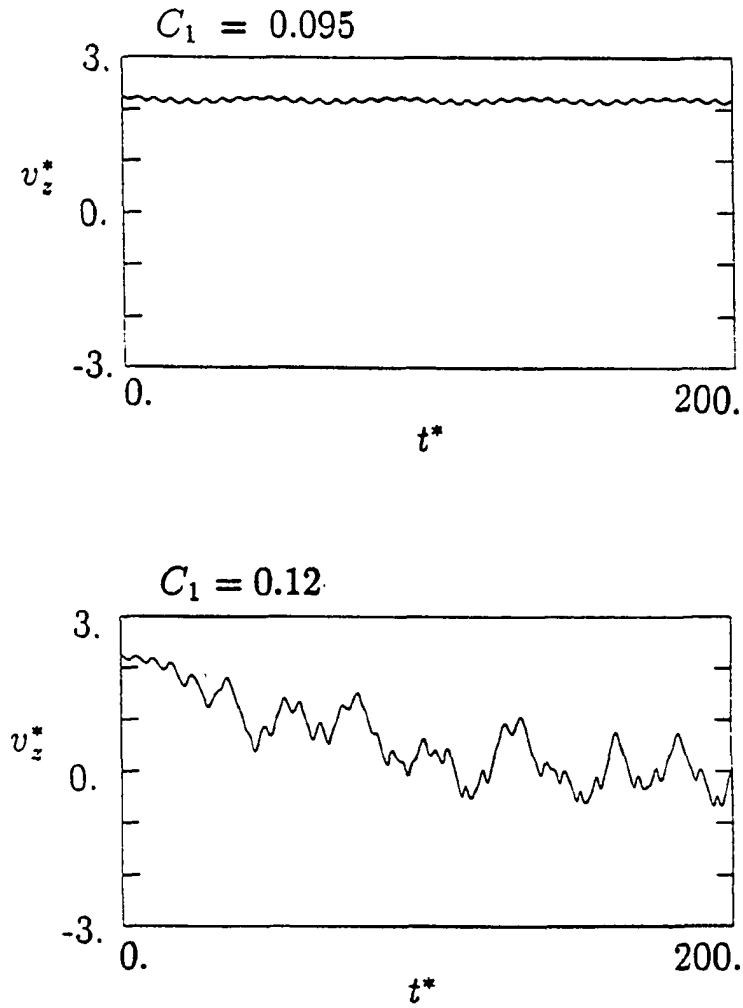

Figure 5.8 Variation of v_z^* as a function of t^* for $C_1 = 0.095$ and $C_1 = 0.12$, respectively. The wave propagation angle is 30^o, and the initial particle speed is given by $kv_0/\Omega_0 = 2.6$.

Reproduced with permission of the copyright owner. Further reproduction prohibited without permission.

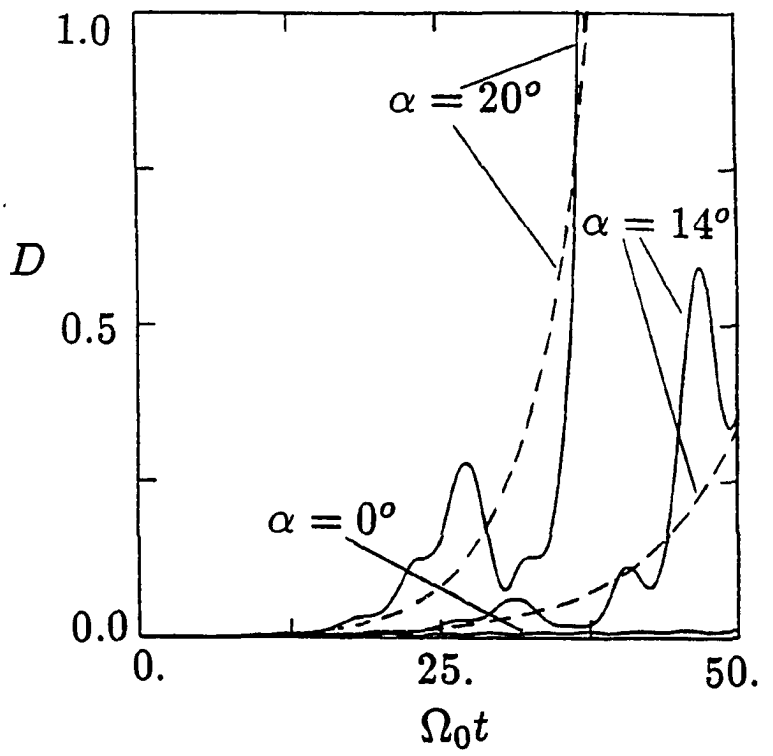

Figure 5.9 The solid lines represent the separation of two particles in the 4-dimensional phase space, D, as a function of time t for three cases with $\alpha = 0°$, $14°$, and $20°$. The dashed lines represent the best fit by an exponential function.

Reproduced with permission of the copyright owner. Further reproduction prohibited without permission.

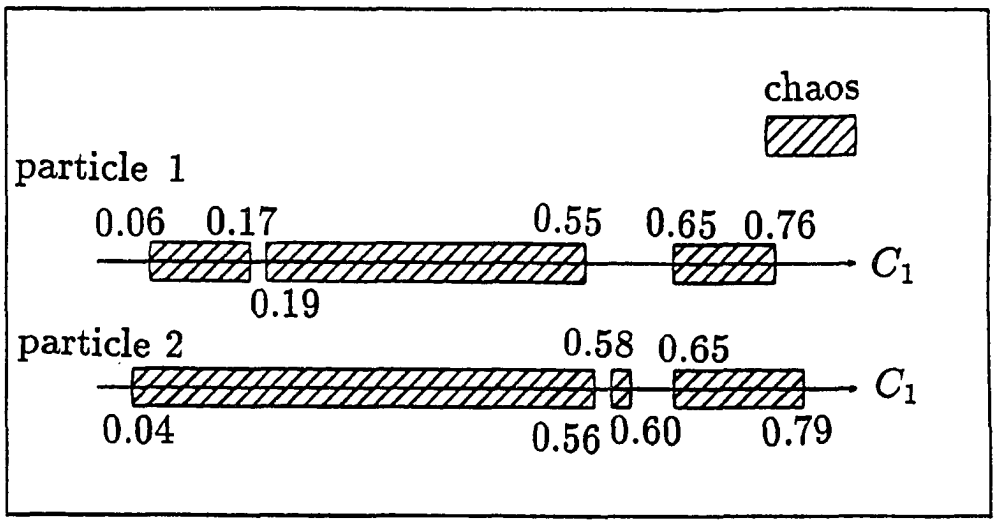

Figure 5.10 Chaotic bands of two particles in the case with $\alpha = 20°$.

Reproduced with permission of the copyright owner. Further reproduction prohibited without permission.

Several examples of phase plane plots for particle 1 are shown in Figure 5.11. Initially the particle is at $\phi = 0$ with $v_z^* = 0$. Figure 5.11(a) shows the surface-of-section plots of the particle velocity for $C_1 = 0.03$, 0.1 and 0.6, respectively. The velocity points are plotted on the v_x^*-v_z^* phase plane whenever ϕ is a multiple of 2π. It is seen that the particle motion is periodic and on a closed curve in phase space for $C_1 = 0.03$ and 0.6, whereas the particle velocity spreads randomly in the phase space for the case with $C_1 = 0.1$. The results of particle 1 in the wave field with $C_1 = 0.181$, 0.25 and 0.66 are shown in Figure 5.11(b) in a different format. Here, the particle trajectory is drawn continuously on the v_x^*-v_z^* phase plane. A periodic motion is seen for the case with $C_1 = 0.181$, whereas the other two cases, with $C_1 = 0.25$ and $C_1 = 0.66$, respectively, exhibit chaotic particle motions.

Particle 2 also has several chaotic bands, as shown in Figure 5.11, and the particle motion is not chaotic if $C_1 > 0.79$. Similar phenomena are observed for particles with other different initial phase-angle. In general, there exists a lower bound and an upper bound in C_1 such that incident particles in this group are generally chaotic when C_1 is between these two values.

We now search for the behavior of a group of 200 incident particles initially with $\phi = 0$. These particles have the same initial speed v_0 with $kv_0/\Omega_0 = 1.5$ and the same pitch-angle (20^o), and their phase angles around the magnetic field line are uniformly distributed from 0^o to 360^o. Our purpose is to find under which conditions the particle trajectories are stochastic within one wavelength after incident in the rotational wave.

Figure 5.12 shows the phase projection of the 200 particles on the v_x^*-v_z^* plane for two cases: case (1) $C_1 = 0.5$ and $\alpha = 10^o$ and case (2) $C_1 = 0.5$ and $\alpha = 20^o$. Initially, the 200 points in phase space are on a closed curve as shown in the plots at $\phi = 0$. When cut at $\phi = 2\pi$, the velocities of the group of particles are found on a smooth curve for the case with $\alpha = 10^o$, whereas the particle orbits spread stochastically in the case with $\alpha = 20^o$. The particles move chaotically within one wavelength in the latter case. In a plasma, a proper distribution of particles is required to provide the current associated with the circularly polarized coherent wave. For

Reproduced with permission of the copyright owner. Further reproduction prohibited without permission.

Reproduced with permission of the copyright owner. Further reproduction prohibited without permission.

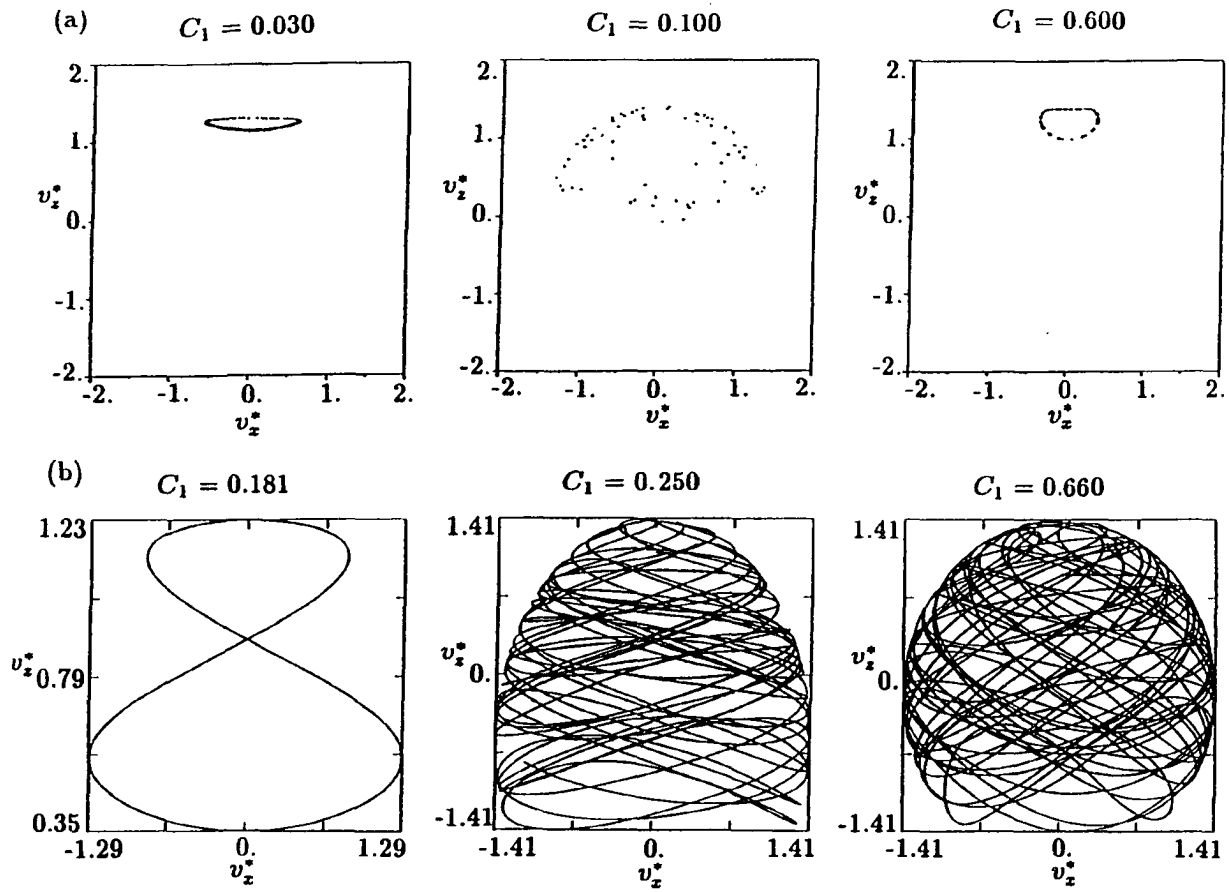

Figure 5.11 Motions of particle 1 on the v_x^*-v_z^* phase plane. (a) Surface of section plots for the cases with, respectively, $C_1 = 0.03$, $C_1 = 0.1$, and $C_1 = 0.6$ whenever ϕ is a multiple of 2π. (b) Particle trajectories in the cases with, respectively, $C_1 = 0.181$, $C_1 = 0.25$, and $C_1 = 0.6$.

particles originally with a proper distribution in a coherent wave field, the onset of chaos causes the occurrence of random particle motions, which changes the current distribution in the system. As a result, the coherent wave cannot be maintained.

The shaded area in Figure 5.7 is the region where this highly chaotic motion condition is satisfied in the α-C_1 plane. We now look for the critical intermediate Mach number of slow shocks with $\theta_{nB} = 75^o$ and $\beta_1 = 0.1$. As shown in Figure 5.7, for $\alpha < 10^o$ ($M_I > 0.985$), there is no highly chaotic motion which is required for the strong damping of downstream waves of slow shocks. For $10^o < \alpha < 16^o$ ($0.985 > M_I > 0.975$), the chaotic region is narrow in C_1. Our simulation of a slow shock with $M_I \simeq 0.98$ shows that the growth of the wave is fast enough to have the wave amplitude increase beyond the upper bound of chaotic region. In this case, the development of chaos is not strong and fast enough to suppress the development of large-amplitude wave before it grows beyond the upper bound. When $\alpha > 16^o$, the chaotic region is wide in C_1, indicating a high probability that the rotational waves can be damped before the waves grow to the upper bound of chaotic region in Figure 5.7. Thus we expect that the critical intermediate Mach number for the damping of wavetrain is $M_c \sim 0.975$, which is consistent with the simulation result. Such a good agreement between simulation and test particle calculation is also observed for other subsonic slow shocks with different θ_{nB} and β_1.

We now examine the ion heating process associated with the non-switch-off shock in Figure 5.5. At $z \simeq 84c/\omega_{pi}$, the strength of the tangential magnetic field in the slow shock with $M_I = 0.96$ undergoes a sudden decrease, and the temperature, $T_\perp$, has a rapid increase. We notice that although the large-amplitude rotation around B_2 no longer exists in a slow shock with $M_I < M_c$, the magnetic field hodogram in this case shows a tendency of rotation around an effective background magnetic field and that this rotational wave is terminated within $1/4$ wavelength. As shown in Figure 5.5, the effective background magnetic field has a magnitude of $1.9B_n$ and $\alpha_{eff} \simeq 60^o$. The normalized wave amplitude is $C_{1eff} \simeq 0.9$. From Figure 5.7, we find that ion orbits are chaotic and ions can be thermalized within one wavelength after

Reproduced with permission of the copyright owner. Further reproduction prohibited without permission.

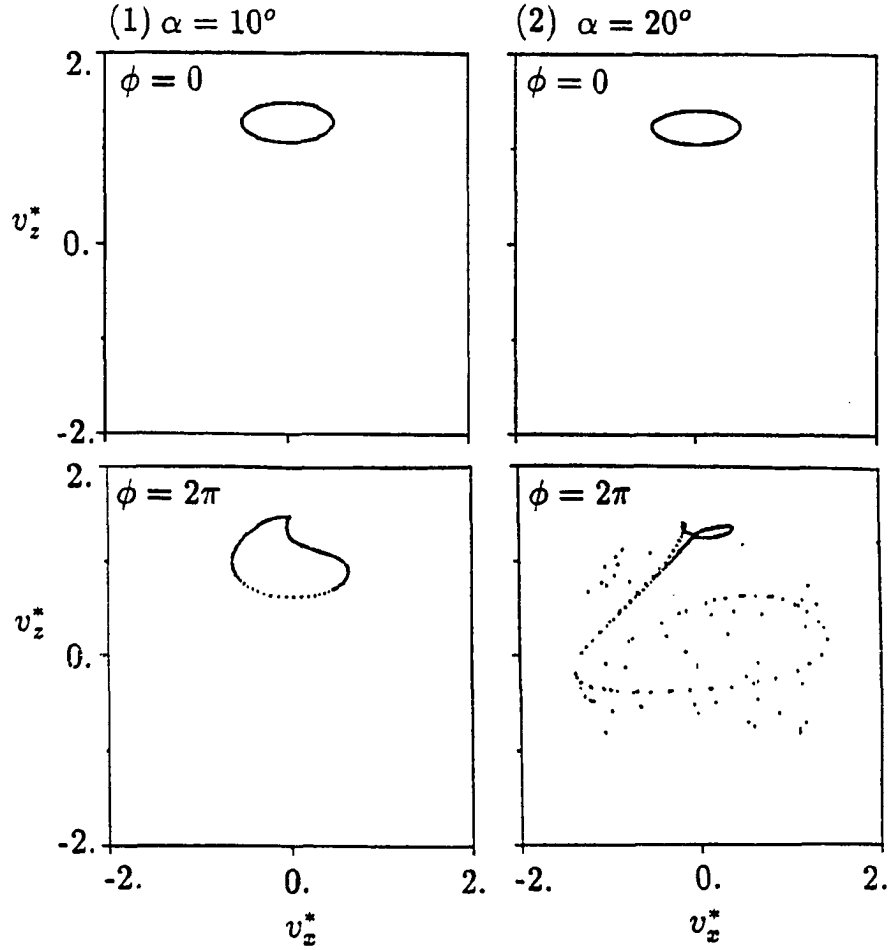

Figure 5.12 Phase projections of 200 particles on the v_x^*-v_z^* plane for two cases case (1) $C_1 = 0.5$ and $\alpha = 10^o$ and case (2) $C_1 = 0.5$ and $\alpha = 20^o$.:

Reproduced with permission of the copyright owner. Further reproduction prohibited without permission.

incidence in this wave field. Furthermore, we found that the region for particles to become chaotic within $1/4$ wavelength is only slightly smaller than the shaded region in Figure 5.7. The chaotic ion heating can occur within 1/4 of one wave rotation, as shown in the case with $M_I = 0.96$ in Figure 5.5. Besides, there are small-amplitude waves in downstream region. They also contribute to the ion heating of slow shocks. On the other hand, our simulation as shown in the $M_I = 1$ case of Figure 5.5 indicates that the growth of ion temperature in shock transition region is very slow since there is no chaotic heating of particles.

5.7 Summary

In this chapter, we have studied the structure of slow shocks in the magnetotail reconnection layer based on hybrid simulations. We then demonstrated that the chaotic particle orbits in the downstream wave field can provide an efficient mechanism for the ion heating in slow shocks.

The two-fluid model shows that the slow shocks have a lefthand circularly-polarized wavetrain standing in the downstream region. However, the hybrid simulations indicate that there exists a critical number, M_c, such that for slow shocks with $M_I \geq M_c$, a large-amplitude rotational wavetrain is present, while for slow shocks with $M_I < M_c$, the downstream rotational wave is damped within a fraction of one wavelength. The results can be used to explain the lack of large-amplitude coherent wave trains downstream of the slow shocks observed in the magnetotail. The obtained value of the critical intermediate Mach number M_c in our simulations is consistent with satellite observations in the magnetotail.

In the hybrid simulations, the lack of coherent wavetrain is related to a rapid ion heating in slow shocks. Both analytical and numerical integration methods are used to study the particle orbits in the downstream wave field associated with slow shocks. The occurrence of chaotic particle orbits in a rotational wave field can lead to a sudden increase of ion temperature in a slow shock. The criterion for the occurrence of highly chaotic ion motions is also obtained. This criterion can

Reproduced with permission of the copyright owner. Further reproduction prohibited without permission.

be used to explain the existence of the critical intermediate Mach number (M_c) observed in the hybrid simulations.

Reproduced with permission of the copyright owner. Further reproduction prohibited without permission.

Chapter 6 Discussion and Summary

In the earth's magnetosphere, magnetic reconnection usually takes place at the dayside magnetopause and in the nightside plasma sheet. Through magnetic reconnection, the magnetic energy can be efficiently converted into kinetic energy, leading to the ejection of high-speed plasma. A layered structure which contains several magnetohydrodynamic (MHD) discontinuities and expansion waves is formed in the high-speed outflow region. This layered plasma structure is called the reconnection layer. The existence of reconnection layers in the dayside magnetopause-boundary layer and the tail plasma sheet have been observed by satellites.

In this thesis, we have systematically studied the structure of reconnection layers at the dayside magnetopause and in the magnetotail. The 1-D ideal MHD model, resistive MHD model, and hybrid model are used to solve the Riemann problem for the evolution of an initial current sheet after the onset of magnetic reconnection.

In the ideal and resistive MHD models, plasma is considered as a continuous fluid and the kinetic effects of individual particles are neglected. The advantage of the ideal MHD model is that exact solutions of the Riemann problem can be obtained. The advantage of the resistive MHD model is that simulations with a high spatial resolution and a low noise level can be carried out as compared to the hybrid model. However, the resistivity used in the resistive MHD model may not be realistic in the collisionless magnetospheric plasma. In the hybrid model, the kinetic effects of ions in collisionless plasma are included. The disadvantage of the hybrid model is that the resolution is lower than that in the resistive MHD model and the noise is higher.

The global structure of reconnection layers in the magnetosphere can be obtained by performing global MHD simulations. However, in order to clearly identify the obtained MHD discontinuities and expansion waves, a very high spatial resolution is required in the global

Reproduced with permission of the copyright owner. Further reproduction prohibited without permission.

simulation. So far the global structure of reconnection layers with high resolution has not been obtained. For example, in previous global MHD simulations of magnetosphere by Lyon et al. [1981] and Ogino et al. [1986], the grid size at the magnetopause is $\sim 1R_E$. In the global simulations of dayside magnetopause by Shi et al. [1990], the grid size is $\sim 0.1R_E$. The typical width of the reconnection layer at the magnetopause is less than $1R_E$, and hence the discontinuities and expansion waves cannot be clearly identified in previous global simulations. On the other hand, in our 1-D MHD simulations, 2000-4000 grid points are used across the reconnection layer, and the MHD discontinuities can be clearly separated and identified.

Our study indicates that five discontinuities and expansion waves may be developed in a reconnection layer. These discontinuities and expansion waves include rotational discontinuities, intermediate shocks, slow shocks, slow expansion waves, and a contact discontinuity. The rotational discontinuities and intermediate shocks change the direction of magnetic field, the slow shocks and slow expansion waves change the magnitude of magnetic field and plasma density, and the central contact discontinuity matches different plasma densities on the two sides. In addition, two fast expansion waves are also present in the solution of Riemann problem, but they quickly propagate out of the reconnection layer. The main results are summarized as follows.

(A) Reconnection Layer in the Ideal MHD Formulation

In Chapter 2, we studied the structure of reconnection layers at the dayside magnetopause and in the tail plasma sheet based on the ideal MHD formulation. It is found that rotational discontinuities, slow shocks, slow expansion waves, and contact discontinuity may be present in the reconnection layer. Symmetric cases in our study correspond to the magnetotail reconnection layer, and asymmetric cases can be applied to the dayside magnetopause-boundary layer.

In the cases with a zero guide field ($B_y = 0$), our study provides an understanding for the transition from Petschek's [1964] model to Levy et al.'s [1964] model, as illustrated in Figure 6.1. In Petschek's symmetric model, two slow shocks are formed in the reconnection layer. The

Reproduced with permission of the copyright owner. Further reproduction prohibited without permission.

structure of the reconnection layer changes qualitatively as the density ratio ρ_m/ρ_s decreases. In the weakly asymmetric cases with $1 > \rho_m/\rho_s > R_c \sim 10$ and $B_m > B_s$, the discontinuities in the reconnection layer are $(RD + SS + CD + SS')$. Here, the prime indicates the discontinuity propagating toward the magnetospheric (low-density) side of the reconnection layer. In the highly asymmetric cases with $\rho_m/\rho_s < R_c$, the structure becomes $(RD + SE + CD + SS')$. As $\rho_m/\rho_s \rightarrow 0$, the slow shock SS' and the contact discontinuity CD disappear, and the reconnection layer contains only RD and SE as in Levy et al.'s model.

For symmetric cases with $B_y \neq 0$, a pair of rotational discontinuities (RD and RD') and a pair of slow shocks (SS and SS') are present in the reconnection layer. For weakly asymmetric cases with $B_y \neq 0$, there exist a rotational discontinuity RD, slow shock SS, contact discontinuity CD, slow shock SS', and rotational discontinuity RD'. For highly asymmetric cases, the slow shock SS is replaced again by a slow expansion wave SE.

(B) Reconnection Layer in Resistive MHD Model and the Role of Intermediate Shocks

In Chapter 3, the structure of the reconnection layer in the magnetosphere was studied on the basis of resistive MHD simulations. We have shown that in the presence of a finite resistivity, the results obtained from the ideal MHD formulation are modified. The steady rotational discontinuities do not exist, and the steady intermediate shocks and time-dependent intermediate shocks are found to bound the reconnection layer, playing the role of a rotational discontinuity. Figure 6.2 provides a summary of the role of the rotational discontinuity, intermediate shock, and time-dependent intermediate shock in the ideal MHD formulation, resistive MHD model, and hybrid model.

For symmetric cases with $B_y = 0$, a pair of slow shocks SS and SS' are present in the reconnection layer, similar to the ideal MHD case. For asymmetric cases with $B_y \neq 0$, the rotational discontinuity RD in the ideal MHD model is replaced by a steady 2-4 intermediate shock IS, as shown in Figure 6.2. For cases with $B_y \neq 0$, the rotational discontinuities RD

Reproduced with permission of the copyright owner. Further reproduction prohibited without permission.

Transition from Petschek's Model to Levy et al.'s Model

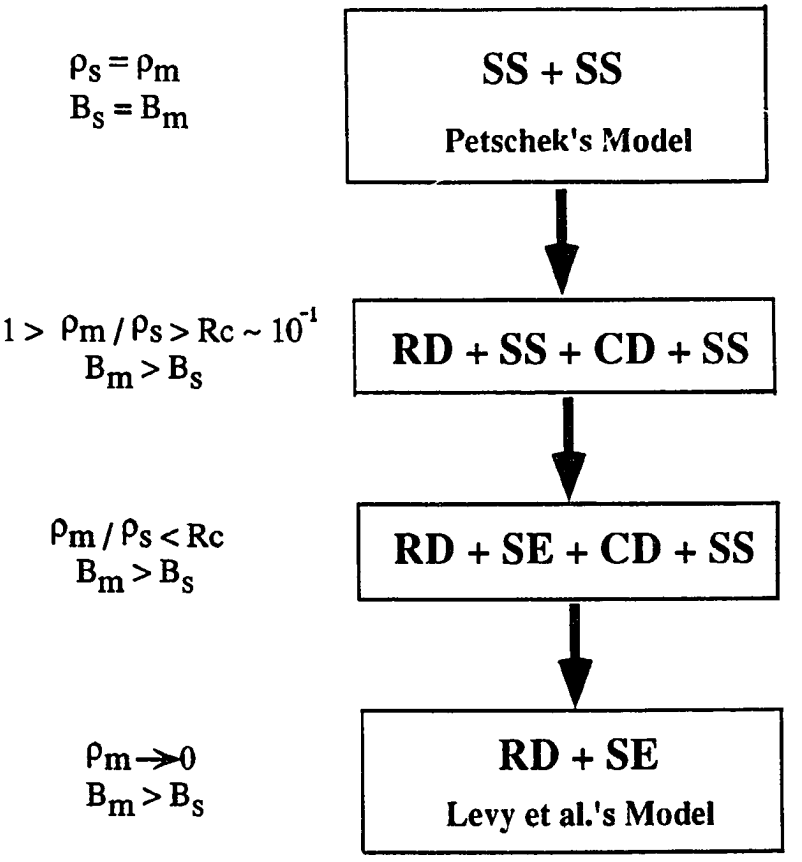

Figure 6.1 Structure of reconnection layer in the ideal MHD formulation with $B_y = 0$. As the density ratio ρ_m / ρ_s decreases, the structure evolves from the symmetric case in the Petschek model to the highly asymmetric Levy et al. model.

Reproduced with permission of the copyright owner. Further reproduction prohibited without permission.

(A) $B_y = 0$ (Antiparallel Magnetic Fields)

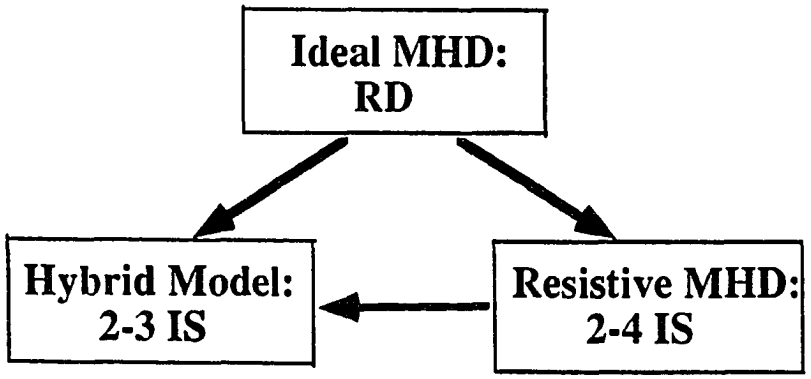

(B) $B_y \neq 0$

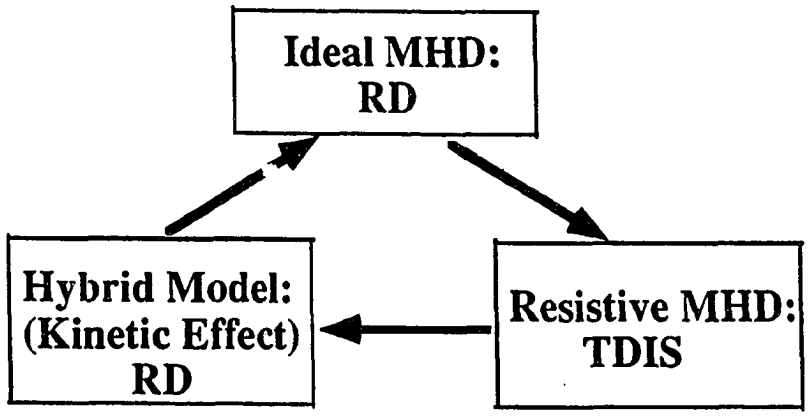

Figure 6.2 Relations among the rotational discontinuity (RD), steady intermediate shock (IS), and time-dependent intermediate shock (TDIS) in the ideal MHD model, resistive MHD model, and hybrid model.

Reproduced with permission of the copyright owner. Further reproduction prohibited without permission.

and RD' in the ideal MHD model are replaced by two 2-3 time-dependent intermediate shocks $TDIS$ and $TDIS'$, respectively.

The width of the 2-3 time-dependent intermediate shock obtained from our simulations expands self-similarly as $\sqrt{t}$. As time $t \rightarrow \infty$, the time-dependent intermediate shock gradually evolves to a rotational discontinuity in which the plasma density and magnetic field strength are conserved. However, in the resistive MHD formulation, a steady rotational discontinuity with a finite width does not exist.

(C) Structure of the Dayside Reconnection Layer in Hybrid Model

In Chapter 4, we studied the reconnection layer at the dayside magnetopause based on hybrid simulations. In the hybrid model, ions are considered as individual particles and electrons as fluid.

It is found that the structure of the reconnection layer obtained in hybrid simulations is different from that in the resistive MHD simulations. As illustrated in Figure 6.2(A), the 2-4 steady intermediate shock in the resistive MHD model is replaced by the 2-3 intermediate shock in the hybrid simulation. The time-dependent intermediate shock quickly evolves to a steady rotational discontinuity because of the particle kinetic effect, as illustrated in Figure 6.2(B). In addition, due to the mixing of plasmas from the magnetosheath side and from the magnetospheric side, the contact discontinuity does not exist, and the slow shocks and expansion waves are strongly modified in the reconnection layer. As a result, the ion temperature (number density) monotonically increases (decreases) in the boundary layer region from the magnetosheath to the magnetosphere.

Due to the mixing of the accelerated magnetosheath plasma and the hot magnetospheric plasma, the ratio $T_\perp/T_\parallel$ is reduced in the boundary layer region. A D-shaped distribution in ion velocity space, which is associated with the transmitted magnetosheath ions, is found to be present in the boundary layer.

(D) Comparison of MHD and Hybrid Simulation Results with Observations

Reproduced with permission of the copyright owner. Further reproduction prohibited without permission.

Rotational Discontinuity and High-Speed Plasma Flow: The presence of high-speed plasma flow in the reconnection layer has been obtained in our hybrid model and MHD models. The resistive MHD model predicts that a steady rotational discontinuity cannot exist. However, our hybrid simulations show that in the general cases rotational discontinuities should be present in the dayside reconnection layer. The rotational discontinuity and high-speed plasma flow have been observed by many satellites in the dayside magnetopause-boundary layer.

Contact Discontinuity: A contact discontinuity is obtained from the ideal MHD formulation and resistive MHD simulations for the dayside reconnection layer. However, our hybrid simulations indicate that the contact discontinuity does not exist in collisionless plasma. As a result, the slow shock and slow expansion wave are modified, and the plasma temperature in the dayside boundary layer increases monotonically from the magnetosheath to the magnetosphere. Satellite observations in the dayside boundary layer also indicate the absence of contact discontinuity and the monotonic increase of plasma temperature.

Temperature Anisotropy and D-Shaped Ion Velocity Distribution: A temperature anisotropy ($T_\perp \neq T_\parallel$) and a D-shaped ion velocity distribution in the reconnection layer have been obtained in our hybrid simulations. These phenomena have been observed in the dayside boundary layer. On the other hand, the temperature anisotropy and ion distributions cannot be obtained from the MHD models.

(E) Slow Shocks in the Magnetotail Reconnection Layer

The magnetotail reconnection layer consists of two slow shocks. In Chapter 5, we studied the structure and ion heating of slow shocks in the magnetotail plasma sheet based on two-fluid simulation and hybrid simulation. The results of our study are summarized in Figure 6.3.

In the ideal MHD formulation, a slow shock is a thin layer without a structure. In the two-fluid formulation, a large-amplitude rotational wavetrain is present in the downstream region of the slow shock.

Reproduced with permission of the copyright owner. Further reproduction prohibited without permission.

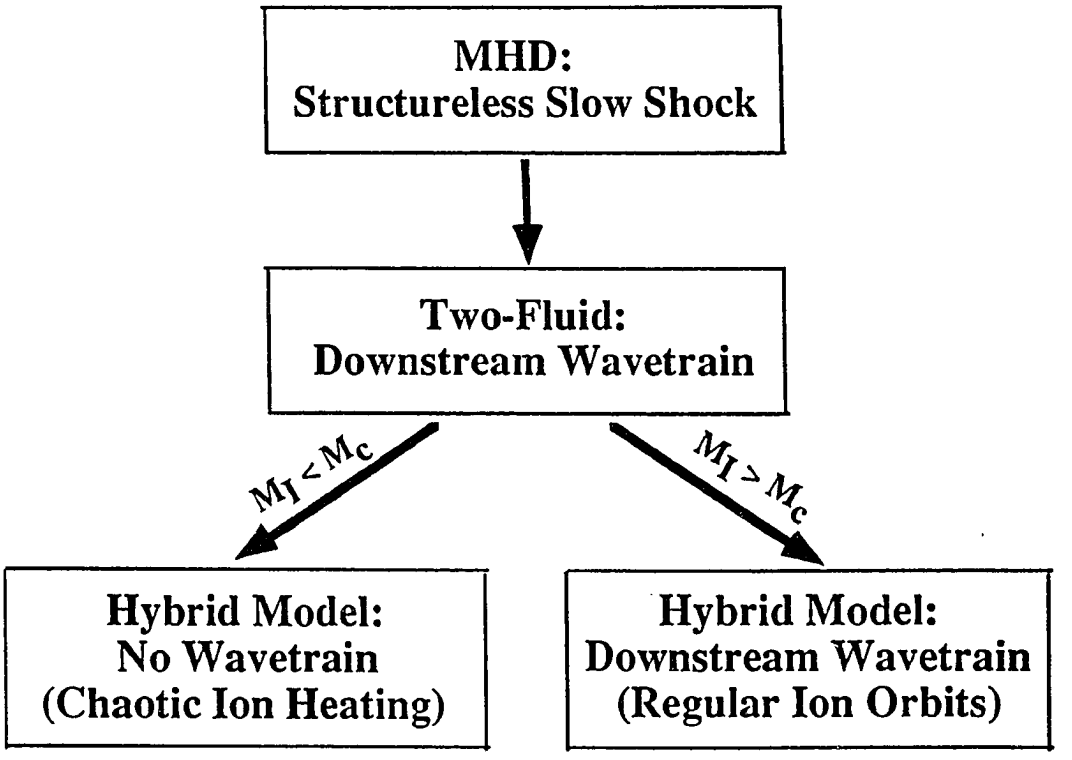

Figure 6.3 Structure of slow shocks in the ideal MHD formulation, two-fluid model, and hybrid model.

Reproduced with permission of the copyright owner. Further reproduction prohibited without permission.

In hybrid simulation, it is found that there exists a critical number M_c such that for slow shocks with an intermediate Mach number in the range $1 \geq M_I \geq M_c$, a long large-amplitude rotational wavetrain appears in the downstream region, while for slow shocks with $M_I < M_c$, the downstream rotational wave is damped within a fraction of one wavelength. The results can be used to explain the lack of large-amplitude coherent wave trains downstream of the slow shocks observed in the magnetotail.

The lack of coherent wavetrain is related to a rapid ion heating in slow shocks. As illustrated in Figure 6.3, the existence of the critical intermediate Mach number M_c in slow shocks is related to chaotic ion orbits in the downstream wave field. For $M_I < M_c$, the particle orbits are chaotic, leading to the rapid heating of ions and the rapid damping of coherent waves. For $M_I > M_c$, the ions have regular orbits in downstream wave field.

The ion heating mechanism and the width of collisionless slow shocks cannot be obtained from MHD models. In the resistive MHD model, the width D of a slow shock is related to the resistivity η by $D \sim 2\eta/(v_{n1} - v_{n2})$, where v_{n1} and v_{n2} are the upstream and downstream plasma normal flow speeds, respectively. However, the resistivity in collisionless plasma cannot be determined from the MHD formulation. The ion heating and shock width can be obtained in our hybrid simulations. For slow shocks with $M_I < M_c$, the chaotic ion heating occurs and the shock width $D \sim R_{c2}$, where R_{c2} is the downstream ion gyroradius. For slow shocks with $M_I > M_c$, the shock transition region is long (~ 10--$50R_{c2}$) due to the presence of the rotational wavetrain.

In summary, we have systematically studied the structure of reconnection layers at the dayside magnetopause and in the magnetotail. The results can explain the presence of rotational discontinuities, high-speed plasma flow, and layered structure observed in the dayside boundary layer and the structure of slow shocks observed in the magnetotail plasma sheet.

Reproduced with permission of the copyright owner. Further reproduction prohibited without permission.

References

Akasofu, S.-I., E. W. Hones, Jr., S. J. Bame, J. R. Asbridge, and A. T. Y. Lui, Magnetotail and boundary layer plasmas at a geocentric distance of $\sim 18R_E$: VELA 5 and 6 observations, *J. Geophys. Res.*, *78*, 7257, 1973.

Akhiezer, A. I., G. J. Lubarski, and R. V. Polovin, The stability of shock waves in magnetohydrodynamics, *Zh. Eksp. Teor. Fiz.*, *35*, 731, 1958.

Akhiezer, A. I., I. A. Akhiezer, R. V. Polovin, A. G. Sitenko, and K. N. Stepanov, *Plasma Electrodynamics, Vol. 1*, Pergamon, Oxford, 1975.

Berchem, J. and C. T. Russell, Magnetic field rotation through the magnetopause: ISEE 1 and 2 observations, *J. Geophys. Res.*, *87*, 8139, 1982.

Biernat, H. K., M. F. Heyn, R. P. Rijnbeek, V. S. Semenov and C. J. Farrugia, The structure of reconnection layers: Application to the Earth's magnetopause, *J. Geophys. Res.*, *1*, 287, 1988.

Buti, B., Nonlinear and chaotic Alfven waves, in *Solar and Planetary Plasma Physics*, ed. B. Buti, World Scientific, Singapore, 1990.

Chao, J. K, Interplanetary collisionless shock waves, *Rep. CSR TR-70-3*, Mass. Inst. of Technol. Cent. for Space Res., Cambridge, Mass., 1970.

Coroniti, F. V., Laminar wave-train structure of collisionless magnetic slow shocks, *Nuclear Fusion*, *11*, 261, 1971.

Coroniti, F. V., F. L. Scarf, C. F. Kennel, B. T. Tsurutani, and E. J. Smith, A search for lower hybrid drift turbulence in slow shocks, *J. Geophys. Res*, *93*, 2553, 1988.

Reproduced with permission of the copyright owner. Further reproduction prohibited without permission.

Cowley, S. W. H., The causes of convection in the Earth's magnetosphere: A review of developments during the IMS, *Rev. of Geophys. and Space Physics*, *20*, 531, 1982.

de Hoffmann F. and E. Teller, Magnetohydrodynamic Shocks, *Phys. Rev.*, *80*, 692, 1950.

Dungey, J. W., Interplanetary magnetic field and the auroral zones, *Phys. Rev. Lett.*, *6*, 47, 1961.

Eastman, T. E., The plasma boundary layer and magnetopause layer of the Earth's magnetosphere, Thesis, *Rep. LA-7842-T*, Los Alamos Sci. Lab., Los Alamos, N.M., June, 1979.

Eastman, T. E. and E. W. Hones, Jr., Characteristics of the magnetospheric boundary layer and magnetopause layer as observed by Imp 6, *J. Geophys. Res.*, *84*, 2019, 1979.

Eastman, T. E., E. W. Hones, Jr., S. J. Bame, and J. R. Asbridge, The magnetospheric boundary layer: Site of plasma, momentum, energy transfer from the magnetosheath into the magnetosphere, *Geophys. Res. Lett.*, *3*, 685, 1976.

Feldman, W. C., S. J. Schwartz, S. J. Bame, D. N. Baker, J. Birn, J. T. Gosling, E. W. Hones, Jr., D. J. McComas, J. A. Slavin, E. J. Smith, and R. D. Zwickl, Evidence for slow-mode shock in the deep geomagnetic tail, *Geophys. Res. Lett.*, *11*, 599, 1984.

Feldman, W. C., D. N. Bakes, S. J. Bame, J. Birn, J. T. Gosling, E. W. Hones, Jr., and S. J. Schwartz, Slow-mode shocks: A semipermanent feature of the distant geomagnetic tail, *J. Geophys. Res.*, *90*, 233, 1985.

Ford, J. and G. H. Lunsford, Stochastic behavior of resonant nearly linear oscillator systems in the limit of zero nonlinear coupling, *Physical Review, A*, *1*, 59, 1970.

Reproduced with permission of the copyright owner. Further reproduction prohibited without permission.

Fuselier, S. A., D. M. Klumpar, and E. G. Shelley, Ion reflection and transmission during reconnection at the earth's subsolar magnetopause, *Geophys. Res. Lett.*, *18*, 139, 1991.

Germain, P., Shock waves and shock-wave structure in magnetofluid dynamics, *Rev. Mod. Phys.*, *32*, 951, 1960.

Goldstein, H., *Classical Mechanics*, Addison-Wesley, Cambridge, Mass, 1951.

Goodrich, C. C. and P. J. Cargill, An investigation of the structure of rotational discontinuities, *J. Geophys. Res.*, *18*, 65, 1991.

Gosling J. T., M. F. Thomsen, S. J. Bame, R. C. Elphic, and C. T. Russell, Plasma flow reversals at the dayside magnetopause and the origin of asymmetric polar cap convection, *J. Geophys. Res.*, *95*, 8073, 1990a.

Gosling, J. T., M. F. Thomsen, S. J. Bame, T. G. Onsager, and C. T. Russell, The electron edge of the low latitude boundary layer during accelerated flow events, *Geophys. Res. Lett.*, *17*, 1833, 1990b.

Gosling, J. T., M. F. Thomsen, S. J. Bame, R. C. Elphic, and C. T. Russell, Cold ion beams in the low latitude boundary layer during accelerated flow events, *Geophys. Res. Lett.*, *17*, 2245, 1990c.

Haerendel, G., G. Paschmann, N. Sckopke, H. Rosenbauer, and P. C. Hedgecock, The frontside boundary layer of the magnetosphere and the problem of reconnection, *J. Geophys. Res.*, *83*, 3195, 1978.

Hapgood, M. A. and D. A. Bryant, Exploring the magnetospheric boundary layer, submitted to *Planetary and Space Science*, 1992.

Reproduced with permission of the copyright owner. Further reproduction prohibited without permission.

Hau, L.-N. and B. U. O. Sonnerup, On the structure of resistive MHD intermediate shocks, *J. Geophys. Res.*, *94*, 6539, 1989.

Heyn, M. F., H. K. Biernat, R. P. Rijnbeek and V. S. Semenov, The structure of reconnection layer, *J. Plasma Phys.*, *40*, 235, 1988.

Hudson, P. D., Rotational discontinuities in an anisotropic plasma, *Planet. Space Sci.*, *19*, 1693, 1971.

Jeffrey, A. and T. Taniuti, *Non-Linear Wave Propagation*, Academic, Orlando, Fla., 1964.

Kantrowitz, A. R. and H. E. Petschek, MHD characteristics and shock waves, in *Plasma Physics in Theory and Application*, ed. W. B. Kunkel, pp. 148-206, MaGraw-Hill, New York, 1966.

Karney, C. F. F., Stochastic ion heating by a lower hybrid wave, *Phys. Fluids.*, *21*, 1584, 1978.

Kennel, C. F., R. D. Blandford, and P. Coppi, MHD intermediate shock discontinuities, Part 1, Rankine-Hugoniot conditions, *J. Plasma Physics*, *42*, 299, 1989.

Kennel, C. F., R. D. Blandford, and C. C. Wu, Structure and evolution of small-amplitude intermediate shock waves, *Phys. Fluids*, *B2 (2)*, 253, 1990.

Krauss-Varban, D., Structure and length scales of rotational discontinuities, *J. Geophys. Res.*, in press, 1993.

Landau, L. D. and E. M. Lifshitz, *Electrodynamics of Continuous Media*, Pergamon Press, 1960.

Lee, L. C., L. Huang and J. K. Chao, On the stability of rotational discontinuities and intermediate shocks, *J. Geophys. Res.*, *94*, 8813, 1989a.

Lee, L. C., Y. Lin, Y. Shi, and B. T. Tsurutani, Slow shock characteristics as a function of distance from the X-line in the magnetotail, *Geophys. Res. Lett.*, *16*, 903, 1989b.

Reproduced with permission of the copyright owner. Further reproduction prohibited without permission.

Levy, R. H., H. E. Petschek and G. L. Siscoe, Aerodynamic aspects of the magnetospheric flow, *AIAA J., 2*, 2065, 1964.

Lin, Y. and L. C. Lee, Chaos and ion heating in a slow shock, *Geophys. Res. Lett., 18*, 1615, 1991.

Lin, Y., L. C. Lee and C. F. Kennel, The role of intermediate shocks in magnetic reconnection, *Geophys. Res. Lett., 19*, 229, 1992.

Lin, Y. and L. C. Lee, Structure of the Dayside Reconnection Layer in Resistive MHD and Hybrid Models, *J. Geophys. Res.*, in press, 1993.

Lichtenberg, A. J. and M. A. Lieberman, *Regular and stochastic motion*, in *Applied mathematical sciences*, edited by F. John et al., Vol. 38, 1983.

Lyon, J. G., S. H. Brecht, J. D. Huba, J. A. Fedder, and P. J. Palmadesso, Computer simulation of a geomagnetic substorm, *Phys. Rev. Lett., 46*, 1038, 1981.

Ogino, T., R. J. Walker, M. Ashour-Abdalla, and J. M. Dawson, An MHD simulation of the effects of the interplanetary magnetic field B_y component on the interaction of the solar wind with the earth's magnetosphere during southward interplanetary magnetic field, *J. Geophys. Res., 91*, 10029, 1986.

Omidi, N. and D. Winske, Structure of slow magnetosonic shocks in low beta plasmas, *Geophys. Res. Lett., 16*, 907, 1989.

Palmadesso, P. J., Resonance. particle trapping, and Landau damping in finite amplitude obliquely propagating waves, *Phys. Fluids, 15*, 2006, 1972.

Paschmann, G., B. U. O. Sonnerup, I. Papamastorakis, N. Sckopke, G. Haerendel, S. J. Bame, J. R. Asbridge, J. T. Gosling, C. T. Russell and R. C. Elphic, Plasma acceleration at the Earth's magnetopause: Evidence for reconnection, *Nature, 282*, 243, 1979.

Reproduced with permission of the copyright owner. Further reproduction prohibited without permission.

Paschmann, G., I. Papamastorakis, W. Baumjohann, N. Sckopke, C. W. Carlson, B. U. O. Sonnerup, and H. Luhr, The magnetopause for large magnetic shear: AMPTE/IRM observations, *J. Geophys., Res., 91*, 11099, 1986.

Petschek, H. E., Magnetic field annihilation, in AAS-NASA Symposium on the Physics of Solar Flares, *NASA Spec. Publ., SP-50*, 425-439, 1964.

Priest, E. R. and T. G. Forbes, New models for fast steady state magnetic reconnection, *J. Geophys. Res., 91*, 5579, 1986.

Priest, E. R and L. C. Lee, Nonlinear magnetic reconnection models with separatrix jets, *J. Plasma Physics, 44*, 337, 1991.

Richter, P. and M. Scholer, On the stability of rotational discontinuities, *Geophys. Res. Lett., 16*, 1257, 1989.

Rijnbeek, R. P., H. K. Biernat, M. F. Heyn, V. S. Semenov, C. J. Farrugia, D. J. Southwood, G. Paschmann, N. Sckopke and C. T. Russell, The structure of the reconnection layer observed by ISEE 1 on 8 September 1978, *Annales Geophys., 7*, 297, 1988.

Rosenbauer, H., H. Grunwaldt, M. D. Montgomery, G. Paschmann, and N. Sckopke, HEOS 2 plasma observations in the distant polar magnetosphere: The plasma mantle, *J. Geophys. Res., 80*, 2723, 1975.

Sato, T., Strong plasma acceleration by slow shocks resulting from magnetic reconnection, *J. Geophys. Res., 84*, 7177, 1979.

Sanchez, E. R., G. L. Siscoe, J. T. Gosling, E. W. Hones, Jr., and R. P. Lepping, Observations of rotational discontinuity-slow expansion fan structure of the magnetotail boundary, *J. Geophys. Res, 95*, 61, 1990.

Reproduced with permission of the copyright owner. Further reproduction prohibited without permission.

Scholer, M., F. M. Ipavich, G. Gloeckler, D. Hovestadt, and B. Klecker, Leakage of magnetospheric ions into the magnetosheath along reconnected field lines at the dayside magnetopause, *J. Geophys. Res.*, *86*, 1299, 1981.

Scholer, M., Asymmetric time-dependent and stationary magnetic reconnection at the dayside magnetopause, *J. Geophys. Res.*, *94*, 15099, 1989.

Schwartz, S. J., M. F. Thomsen, W. C. Feldman, and F. T. Douglas, Electron dynamics and potential jump across slow mode shocks, *J. Geophys. Res.*, *92*, 3165, 1987.

Sckopke, N., G. Paschmann, G. Haerendel, B. U. O. Sonnerup, S. J. Bame, and E. W. Hones, Jr., Structure of the low-latitude boundary layer, *J. Geophys. Res.*, *86*, 2099, 1981.

Shi, Y. and L. C. Lee, Structure of the reconnection layer at the dayside magnetopause, *Planet. Space. Sci.*, *38*, 437, 1990.

Shi, Y., C. C. Wu, and L. C. Lee, Magnetic reconnection patterns at the dayside magnetopause, An MHD simulation study, *J. Geophys. Res.*, *96*, 17627, 1991.

Smith, G. R. and A. N. Kaufman, Stochastic acceleration by an obliquely propagating wave, *Phys. Fluids*, *21*, 2230, 1978.

Smith, E. J., J. A. Slavin, B. T. Tsurutani, W. C. Feldman and S. J. Bame, Slow mode shocks in the Earth's magnetotail: ISEE-3, Geophys. Res. Lett., 11, 1054, 1984.

Smith, M. F. and D. J. Rodgers, Ion distributions at the dayside magnetopause, *J. Geophys. Res.*, *96*, 11617, 1991.

Song, P. and C. T. Russell, Model of the formation of the low-latitude boundary layer for strongly northward interplanetary magnetic field, *J. Geophys. Res.*, *97*, 1411, 1992.

Reproduced with permission of the copyright owner. Further reproduction prohibited without permission.

Song, P., C. T. Russell, N. Lin, R. J. Strangeway, J. T. Gosling, M. Thomson, T. A. Fritz, D. G. Mitchell and R. R. Anderson, Wave and particle properties of the subsolar magnetopause, in *Physics of Space Plasma*, SPI Conference Proceedings and Reprint Series, No. 9, MIT, pp. 463-476, Cambridge, Mass. 1989.

Sonnerup, B. U. O., Magnetic re-connexion in a highly conducting incompressible fluid, *J. Plasma. Phys.*, *4*, 161, 1970.

Sonnerup, B. U. O., Magnetic field reconnection, in *Solar System Plasma Physics, Vol. III*, p45, ed. by C. F. Kennel, L. T. Lanzerotti, and E. N. Parker, North Holland Publishing Company, 1979.

Sonnerup, B. U. O., G. Paschmann, I. Papamastorakis, N. Sckopke, G. Haerendel, S. J. Bame, J. R. Asbridge, J. T. Gosling and C. T. Russell, Evidence for magnetic reconnection at the Earth's magnetopause, *J. Geophys., Res., 86*, 10049, 1981.

Swift, D. W., On the structure of the magnetic slow switch-off shock, *J. Geophys. Res., 88*, 5685, 1983.

Swift, D. W. and L. C. Lee, Rotational discontinuities and the structure of the magnetopause, *J. Geophys. Res., 88*, 111, 1983.

Taniuti, T., A note on the evolutionary condition on hydromagnetic shocks, *Prog. Theor. Phys., 28*, 756, 1962.

Terasawa, T. and M. Nambu, Ion heating and acceleration by magnetosonic waves via cyclotron subharmonic resonance, *Geophys. Res. Lett., 16*, 357, 1989.

Tidman, D. A. and N. A. Krall, *Shock Waves in Collisionless Plasmas*, John Wiley and Sons, Inc., 1971.

Reproduced with permission of the copyright owner. Further reproduction prohibited without permission.

Ugai, M., Self-consistent development of fast magnetic reconnection with anomalous plasma resistivity, *Plasma Phys. Contr. Fusion*, *26*, 1549, 1984.

Van Allen, J. A. and J. Adnan, Observed currents on the Earth's high-latitude magnetopause, *J. Geophys. Res.*, *97*, 6381, 1992.

Vasquez, B. J. and P. J. Cargill, A wave-model interpretation of the evolution of rotational discontinuities, *J. Geophys. Res.*, in press, 1993.

Winske, D., E. K. Stover and S. P. Gary, The structure and evolution of slow mode shocks, *Geophys. Res. Lett.*, *12*, 295, 1985.

Winske, D. and N. Omidi, Electromagnetic ion/ion cyclotron instability at slow shocks, *Geophys. Res. Lett.*, *17*, 2297, 1990.

Whitham, G. B., *Linear and nonlinear waves*, John Wiley, New York, 1974.

Wu, C. C., On MHD intermediate Shocks, *Geophys. Res. Lett.*, *14*, 668, 1987.

Wu, C. C., Effects of dissipation on rotational discontinuities, *J. Geophys. Res.*, *93*, 3969, 1988.

Wu, C. C., Formation, structure, and stability of MHD intermediate shocks, *J. Geophys. Res.*, *95*, 8149, 1990.

Wu, C. C. and T. Hada, On rotational discontinuities in both two-fluid and hybrid models, *J. Geophys. Res.*, *96*, 3755, 1991a.

Wu, C. C. and T. Hada, Formation of intermediate shocks in both two-fluid and hybrid models, *J. Geophys. Res.*, *96*, 3769, 1991b.

Wu, C. C. and C. F. Kennel, Structure and evolution of time-dependent intermediate shocks, *Phys. Rev. Lett.*, *68*, 56, 1992.

Reproduced with permission of the copyright owner. Further reproduction prohibited without permission.

Yan, M., L. C. Lee, and E. R. Priest, Fast magnetic reconnection with small shock angles, *J. Geophys. Res.*, *97*, 8277, 1992.

Yang, C-K. and B. U. O. Sonnerup, Compressible magnetopause reconnection, *J. Geophys. Res.*, *82*, 699, 1977.

Yeh, T. and W. Axford, On the re-connexion of magnetic field lines in conducting fluids, *J. Plasma Phys.*, *4*, 207, 1970.

Reproduced with permission of the copyright owner. Further reproduction prohibited without permission.